



ScuDo
Scuola di Dottorato ~ Doctoral School
WHAT YOU ARE, TAKES YOU FAR



Doctoral Dissertation
Doctoral Program in Material Science and Technologies (32.th cycle)

Study and development of an innovative L-PBF demonstrator and an anti-ice solution based on trabecular structures

Sara Varetti

* * * * *

Supervisors

Prof. Mariangela Lombardi, Academic supervisor
Ing. Fabio Ferrario, Company supervisor

Doctoral Examination Committee:

Prof. Maurizio Vedani, Politecnico di Milano
Prof. Daniel Milanese, Università di Parma
Prof. Elena Bassoli, Università degli Studi di Modena e Reggio Emilia
Prof. Gianluca Rossi, Università degli Studi di Perugia

Politecnico di Torino
October 31, 2019

This thesis is licensed under a Creative Commons License, Attribution - Noncommercial-NoDerivative Works 4.0 International: see www.creativecommons.org. The text may be reproduced for non-commercial purposes, provided that credit is given to the original author.

I hereby declare that, the contents and organization of this dissertation constitute my own original work and does not compromise in any way the rights of third parties, including those relating to the security of personal data.

.....

Sara Varetto
Turin, October 31, 2019

Summary

The work presented in this thesis regards two separate research topics about Laser Powder Bed Fusion (L-PBF) technology, carried out simultaneously over the Ph.D course. The first topic concerns the experimental characterization of samples produced with an innovative L-PBF prototype. The second topic is related to the mechanical and thermal characterization of a real case-study produced with a L-PBF commercial machine.

In the first topic an innovative L-PBF demonstrator, able to processing very large components and with a higher production rate, is presented. The machine was built in the frame of the regional project STAMP by the innovative start-up 3D New Technologies S.r.l. A set of tests was conducted to evaluate the powders to be used for the production and for the optimization of the process parameters of the machine. Initially the samples produced by the machine were made of Stainless Steel 316L powders, because 316L material is simple to produce. The goal is to turn to more complex materials whose production can take advantage of machine innovations, such as aluminum alloys. In Chapter 1 the STAMP project is introduced and the L-PBF technology market is carefully analyzed, in order to justify the technical choices that characterized the innovations of the machine, named LLA-400. The LLA-400 machine tries to respond to the demand for larger and faster L-PBF machines, with greater automation and closer to the concept of industrialization. The Chapter 2 analyzes in detail the innovative solutions adopted for the demonstrator, accompanied by tests to evaluate the functioning of some components such as inert gas blowing. This section describes also the characteristics of different powders for L-PBF: AlSi10Mg powders made with different atomization techniques and 316L commercial powders of LPW Technology Ltd. The 316L powders were used for the specimens produced with the machine in the first trials; Al powders will be used for future jobs. Finally the results of the characterization of the first 316L samples, consisting in single layers, produced by the machine are reported. The fusion defects were analyzed by Optical Microscopy and compared with literature data.

The second topic concerns the characterization of an anti-ice system patented by Politecnico di Torino. The system for the leading edge of the aircraft wings consists of a sandwich panel with a core made of trabecular structure. The entire

panel is made with L-PBF technology. In the Chapter 3 the state-of-art for the trabecular structures produced by L-PBF and the current aircraft anti-ice solutions were analyzed. The anti-ice system produced is an hot air system: it uses the hot air tapped from the engine to maintain the wing surface at a temperature higher than the water freezing point. The characterization of the system was funded by Politecnico di Torino with a Proof of Concept (PoC), that had the goal of carrying the patent from a TRL 1 to a TRL 5, with a prototype. The prototype must demonstrate the functioning of the system and its feasibility with the L-PBF technology. In order to choose the design of the final mock-up, different mechanical and thermal tests on AlSi10Mg and Ti6Al4V specimens were carried out. The specimens were produced with six different cell shapes (Bccz, Rhombic dodecahedron, Octet-truss, Auxetic, Schwartz diamond and Gyroid), three cell sizes and three values of solid volume fraction. In Chapter 4 all the specimens produced for the mechanical and thermal tests were described with their characterization methods. The first mechanical test is the uniaxial compression test of trabecular specimens in AlSi10Mg and Ti6Al4V. On the basis of the results obtained from this test, the characteristics of the specimens for the following tests were chosen. The second test set is the uniaxial compression test on sandwich panel with trabecular core, followed by the 3-point bending tests. The last mechanical test carried out is the fatigue test on some selected specimens. The features, the measures, the pictures and the results of the specimens subjected to mechanical tests are listed in Appendix A, B, C and D. Finally, thermal tests were carried out on the panels, to verify the grade of the heat exchange between the hot air and the panel. Furthermore, thanks to the Optical Microscope images of the specimens, it was possible to analyze the results of the production process with AlSi10Mg and Ti6Al4V materials. For denser cell, such as 3 mm, in particular in the case of samples made by AlSi10Mg, the difficult heat dissipation during the process causes an excessive enlargement of the structure, making these cells not suitable for the final application. The final mock-up with the airfoil of the P180 aircraft of Piaggio was shown in the last section of Chapter 4.

The conclusions of both the topics of the thesis are illustrated in the last chapter (Chapter 5). For the LLA400 machine of the STAMP project the innovations introduced such as preheating and increased productivity have been verified. 316L single layers were produced and some process parameters that allow obtaining a homogeneous melting were identified. For the future, it is necessary to produce larger pieces and to observe the effects of innovations on the quality of the final component. This operation will be performed on all other materials. This will allow to obtain an optimal set of parameters for each type of material processed. In the same chapter the observations on the mechanical and thermal results about the characterization of the trabecular structures are summarized. The best cells shapes are the Schwartz diamond and the Bccz, while the best cell size is 7 mm, that allows a good passage of the air.

Acknowledgements

I would like to acknowledge Prof. Mariangela Lombardi and Ing. Fabio Ferrario for their support in this thesis work.

I want to express my gratitude to 3D New Technologies and the people who work there, which allowed me to experience the working reality of an innovative start-up. Also, thanks to Prof. Paolo Maggiore and its entire research group for involving me in their projects.

Thanks to the workers of Prima Additive, for shared with me their experiences and the laboratory, thanks to Gabriele Imbalzano for the X-ray tomography, and thanks to all the other people who helped me to collect the data presented in this thesis.

In addition to the important formative aspect of the Ph.D, there is another equally important aspect: these three years allowed me to develop human ties with the people with whom I worked and with whom I compared my points of view.

Thanks to all the Ph.D and thesis students who spent time in office 28 and in particular thanks to Carlo, Andrea_Mazza, Andrea C., Roberto, Dario and Piercarlo for creating an environment in which working was very fun.

I would like to acknowledge my colleagues and friends at 3D-NT for the time and the experiences spent together and in particular Livio, Isabella, Salvatore, Simone, Francesco and Gianni.

Thanks to all the very nice staff of Assocam Scuola Camerana and of Fondazione ITS, for making me try to be a teacher and for having welcomed me like a big family.

Finally, thanks to my beloved Lorenzo and my parents, who supported me in all my choices.

Contents

List of Tables	X
List of Figures	XIII
1 Introduction	1
1.1 Metal Additive Manufacturing: technologies overview	1
1.1.1 Powder Bed Fusion (PBF)	3
1.1.2 Direct Energy Deposition (DED)	7
1.2 STAMP Project	8
1.3 PBF technology benchmark	10
1.3.1 PB costs evolution	13
1.3.2 Work chamber size and weight	16
1.3.3 Productivity	17
1.3.4 Process monitoring	20
1.3.5 Inert gas management	21
1.3.6 Powder management	22
1.3.7 Materials and powder	23
1.3.8 Design for Additive Manufacturing	26
1.4 Choice of material: aluminum alloys	28
2 LLA400 Machine	33
2.1 Machine description	33
2.1.1 Building chamber and powder management	35
2.1.2 Powder distribution system, preheating and melting	35
2.1.3 Z axis	37
2.2 Fume blowing and suction system	38
2.3 AlSi10Mg powder characterization	43
2.3.1 Powder 1	45
2.3.2 Powder 2	47
2.3.3 Powder 3	48
2.3.4 Powder 4	49
2.3.5 Final comparison between powders	53

2.4	316L Stainless Steel powder characterization	54
2.5	Experimental tests: single layer	55
3	Trabecular structures	73
3.1	Trabecular structures: state-of-art	73
3.2	Anti-ice systems	77
3.3	Proof Of Concept	81
4	Trabecular structures characterization	85
4.1	Design of the specimens	85
4.1.1	Trabecular specimens for uniaxial compression tests	86
4.1.2	Sandwich panels with trabecular core for uniaxial compression tests	89
4.1.3	Sandwich panels with trabecular core for 3-point bending tests	90
4.1.4	Trabecular specimens for compressive fatigue tests	92
4.1.5	Sandwich panels for thermal tests	93
4.2	Optical Microscope and CT-scan analysis	98
4.2.1	Optical Microscope (OM) analysis	99
4.2.2	CT-scan analysis	104
4.3	Uniaxial compression tests on AlSi10Mg trabecular specimens	107
4.3.1	Bccz specimens	107
4.3.2	Rhombic dodecahedron specimens	112
4.3.3	Octet-truss specimens	115
4.3.4	Auxetic specimens	118
4.3.5	Gyroid specimens	119
4.3.6	Schwartz diamond specimens	121
4.3.7	Comparison between stress-strain curves	123
4.3.8	Comparison with Gibson - Ashby model	128
4.4	Uniaxial compression tests on Ti6Al4V trabecular specimens	132
4.4.1	Bccz specimens	132
4.4.2	Rhombic dodecahedron specimens	134
4.4.3	Octet-truss specimens	135
4.4.4	Auxetic specimens	137
4.4.5	Gyroid specimens	138
4.4.6	Schwartz diamond specimens	140
4.4.7	Comparison between stress-strain curves	142
4.4.8	Comparison with Gibson-Ashby model	142
4.5	Uniaxial compression tests on sandwich panels	146
4.6	3-point bending tests on sandwich panels	150
4.6.1	Long sandwich panels	150
4.6.2	Short sandwich panels	153
4.7	Fatigue tests	156

4.7.1	Rhombic dodecahedron	157
4.7.2	Octet-truss	159
4.7.3	Bccz	162
4.8	Thermal tests on the test bench	163
4.9	POC final prototype	166
5	Conclusions and future developments	169
5.1	STAMP project and LLA400 machine	169
5.2	Proof Of Concept and trabecular structures	170
A	List of specimens	173
A.1	AlSi10Mg specimens for uniaxial compression test	173
A.2	Ti6Al4V specimens for uniaxial compression test	178
A.3	AlSi10Mg sandwich panels for uniaxial compression test	180
A.4	AlSi10Mg sandwich panels for bending tests	181
B	Images of specimens	185
B.1	AlSi10Mg specimens for uniaxial compression test	185
B.2	Ti6Al4V specimens for uniaxial compression test	192
B.3	AlSi10Mg sandwich panels for uniaxial compression test	196
B.4	AlSi10Mg sandwich panels for bending tests	198
B.5	AlSi10Mg specimens for fatigue tests	202
C	Mechanical tests results	205
C.1	Results of uniaxial compression tests on AlSi10Mg trabecular specimens	205
C.2	Results of uniaxial compression tests on Ti6Al4V trabecular specimens	210
C.3	Results of uniaxial compression tests on AlSi10Mg sandwich panels	212
C.4	Results of bending tests on AlSi10Mg sandwich panels	213
C.5	Results of fatigue tests on AlSi10Mg specimens	216
D	Graphs	219
D.1	AlSi10Mg specimens for uniaxial compression test	219
D.2	Ti6Al4V specimens for uniaxial compression test	237
D.3	AlSi10Mg sandwich panels for uniaxial compression test	247
D.4	AlSi10Mg sandwich panels for bending tests	249
	Bibliography	261

List of Tables

1.1	Comparison between AM technologies on the market.	11
1.2	Building chamber size of the PBF machines currently on the market.	17
1.3	Build rate of some PBF machines currently on the market.	18
1.4	Main control systems for the powder bed defects and the melt pool temperature.	20
1.5	Inert gas management for PBF machines currently on the market.	22
1.6	Powder management for PBF machines currently on the market.	23
2.1	Powder types and description.	44
2.2	Powder bed density analysis for AlSi10Mg Powder 1.	45
2.3	Powder bed density analysis for AlSi10Mg Powder 2.	47
2.4	Powder bed density analysis for AlSi10Mg Powder 3.	48
2.5	Powder bed density analysis for AlSi10Mg Powder 4.	51
2.6	Values of D10, D50, D90 and SPAN for all the AlSi10Mg powders.	53
2.7	Values of D10, D50, D90 and SPAN for all the 316L powder.	54
2.8	Energy density for all the samples of the first set.	56
2.9	Energy density for all the samples of the second set.	59
4.1	Factors used to produce sandwich panels for uniaxial compression tests	89
4.2	Factors used to produce sandwich panels for for 3-point bending tests	90
4.3	Factors used to produce specimens for fatigue tests.	93
4.4	Thermal tests setup.	98
4.5	Average relative density experimentally measured for Bccz, Rhombic and Octet specimens for AlSi10Mg and Ti6Al4V.	103
4.6	Results thermal tests.	164
A.1	AlSi10Mg compression specimens with Bccz cells. The identification code of the specimes is: Celle shape - Cell size - Solid volume fraction (nominal) - Serial number	174
A.2	AlSi10Mg compression specimens with Rhombic dodecahedron cells. The identification code of the specimes is: Celle shape - Cell size - Solid volume fraction (nominal) - Serial number	175
A.3	AlSi10Mg compression specimens with Octet-truss cells. The identification code of the specimes is: Celle shape - Cell size - Solid volume fraction (nominal) - Serial number	176

A.4	AlSi10Mg compression specimens with Auxetic, Gyroid and Schwartz diamond cells. The identification code of the specimens is: Celle shape - Cell size - Solid volume fraction (nominal) - Serial number	177
A.5	Ti6Al4V compression specimens with Bccz, Rhombic dodecahedron and Octet-truss cells. The identification code of the specimens is: Celle shape - Cell size - Solid volume fraction (nominal) - Serial number	178
A.6	Ti6Al4V compression specimens with Auxetic, Gyroid and Schwartz diamond cells. The identification code of the specimens is: Celle shape - Cell size - Solid volume fraction (nominal) - Serial number	179
A.7	AlSi10Mg compression sandwich panels with Bccz, Octet-truss and Schwartz diamond cells. The identification code of the specimens is: Celle shape - Cell size - Solid volume fraction (nominal)	180
A.8	AlSi10Mg short sandwich panels for bending test with Bccz, Octet-truss and Schwartz diamond cells. The identification code of the specimens is: Celle shape - Cell size - Solid volume fraction (nominal) - Serial number	182
A.9	AlSi10Mg long sandwich panels for bending test with Bccz, Octet-truss and Schwartz diamond cells. The identification code of the specimens is: Celle shape - Cell size - Solid volume fraction (nominal) - Serial number	183
C.1	AlSi10Mg compression specimens with Bccz cells. The identification code of the specimens is: Celle shape - Cell size - Solid volume fraction (nominal) - Serial number	206
C.2	AlSi10Mg compression specimens with Rhombic dodecahedron cells. The identification code of the specimens is: Celle shape - Cell size - Solid volume fraction (nominal) - Serial number	207
C.3	AlSi10Mg compression specimens with Octet-truss cells. The identification code of the specimens is: Celle shape - Cell size - Solid volume fraction (nominal) - Serial number	208
C.4	AlSi10Mg compression specimens with Auxetic, Gyroid and Schwartz diamond cells. The identification code of the specimens is: Celle shape - Cell size - Solid volume fraction (nominal) - Serial number	209
C.5	Ti6Al4V compression specimens with Bccz, Rhombic dodecahedron and Octet-truss cells. The identification code of the specimens is: Celle shape - Cell size - Solid volume fraction (nominal) - Serial number	210
C.6	Ti6Al4V compression specimens with Auxetic, Gyroid and Schwartz diamond cells. The identification code of the specimens is: Celle shape - Cell size - Solid volume fraction (nominal) - Serial number	211

C.7	AlSi10Mg compression sandwich panels with Bccz, Octet-truss and Schwartz diamond cells. The identification code of the specimes is: Celle shape - Cell size - Solid volume fraction (nominal)	212
C.8	AlSi10Mg short sandwich panels for bending test with Bccz, Octet-truss and Schwartz diamond cells. The identification code of the specimes is: Celle shape - Cell size - Solid volume fraction (nominal) - Serial number	213
C.9	AlSi10Mg long sandwich panels for bending test with Bccz, Octet-truss and Schwartz diamond cells. The identification code of the specimes is: Celle shape - Cell size - Solid volume fraction (nominal) - Serial number	214
C.10	AlSi10Mg specimens for fatigue test with Bccz cell. The identification code of the specimes is: Celle shape - Cell size - Solid volume fraction (nominal) - Serial number	216
C.11	AlSi10Mg specimens for fatigue test with Rhombic dodecahedron cell. The identification code of the specimes is: Celle shape - Cell size - Solid volume fraction (nominal) - Serial number	217
C.12	AlSi10Mg specimens for fatigue test with Octet-truss cell. The identification code of the specimes is: Celle shape - Cell size - Solid volume fraction (nominal) - Serial number	218

List of Figures

1.1	Explicative drawings of a) Stereolithography [104], b) FDM technology [105] and c) LOM technology [106].	2
1.2	Phases for the component creation with PBF technology: a) melting of the layer, b) the lowering of the building platform, c) the movimentation of the rake and d) the creation of the new layer. . .	3
1.3	Explicative drawings of a) SLM [107], b) EBM [108] and c) DED [109].	4
1.4	Effects of residual stresses in two cases: a) failure of the job during the process and b) deformation and cracking of the component after the separation from the platform [169].	5
1.5	a) A particle size distribution for powders designed for EBM technology and b) an example of a SEM image of Ti6Al4V powders [89].	6
1.6	SEM images of an example of Ti6Al4V pre-heated powders [31]. . .	7
1.7	Market shares of the main producers of metal systems in Europe (2014) [138].	10
1.8	Request for components produced for AM divided by each sector [51].	12
1.9	Increase in the number of pieces made with additive technologies from 2011 to 2013 [132].	13
1.10	Evolution of AM production costs from 2013 to 2023 [11].	14
1.11	Subdivision of additive production costs updated to 2013 [11]. . . .	14
1.12	Expected developments for the years after 2013 [11].	15
1.13	Powder distribution systems with a) two containers and b) a hopper [159].	19
1.14	Analysis of the evolution of the powder price of the various metals up to 2020 [11].	26
1.15	Life cycle scheme for a component produced with AM techology [39].	27
1.16	Aerospace bracket produced with SLM technology after topological optimization [52].	28
1.17	Aluminum alloys classifications and their common uses in industries [71].	29
1.18	a) Absorption rate of different materials varying wavelength [118] and b) absorption of Aluminum by varying the temperature [58]. . .	30
1.19	Al-Si binary equilibrium diagram [62].	30

2.1	Machine name: LLA400.	34
2.2	Front view of the LLA400 demonstrator.	34
2.3	Phases for components creation with LLA400 demonstrator: a) creation of the layer with recoater 1, b) movement of lamp carriage and melting of the powder, c) movement of recoater 2 without recoating, d) creation of the new layer with recoater 2.	36
2.4	Front view of the LLA400 demonstrator open.	37
2.5	Two OM images (16X) of single layers of 316L SS with dimensions of 20 mm x 20 mm x 40 μ m produced with a laser power of 300 W and a scanning speed of a) 400 mm/s and b) 200 mm/s with two different problems: a) oxidation and b) fume deposition.	38
2.6	Fumes and lapilli removal system.	39
2.7	N ₂ speed values of the blowing nozzle with a slot of 0.5 mm. The measurements are taken at a) 2 cm, b) 5 cm, c) 7.5 cm and d) 10 cm from the nozzle.	40
2.8	N ₂ speed values of the blowing nozzle with a slot of 0.75 mm. The measurements are taken at a) 2 cm, b) 5 cm, c) 7.5 cm and d) 10 cm from the nozzle.	41
2.9	N ₂ speed values of the blowing nozzle with a slot of 1 mm. The measurements are taken at a) 2 cm, b) 5 cm, c) 7.5 cm and d) 10 cm from the nozzle.	41
2.10	N ₂ speed values of the blowing nozzle with a slot of 1.25 mm. The measurements are taken at a) 2 cm, b) 5 cm, c) 7.5 cm and d) 10 cm from the nozzle.	42
2.11	N ₂ speed values of the blowing nozzle with a slot of 1.5 mm. The measurements are taken at a) 2 cm, b) 5 cm, c) 7.5 cm and d) 10 cm from the nozzle.	42
2.12	Suction speed values of the suction nozzle with a slot of a) 0.5 mm, b) 0.75 mm, c) 1 mm, d) 1.25 mm and e) 1.5 mm.	43
2.13	Particle size distribution in a) number of particles and in b) volume for Powder 1.	45
2.14	SEM images for Powder 1 at magnification of a) 50X, b) 500X, c) 1000X and d) 1800X.	46
2.15	SEM images for Powder 2 at magnification of a) 50X, b) 500X, c) 1000X and d) 2500X.	48
2.16	Particle size distribution in a) number of particles and in b) volume for Powder 3.	49
2.17	SEM images for Powder 3 at magnification of a) 50X, b) 100X, c) 500X, d) 1000X and e)1800X.	50
2.18	Particle size distribution in a) number of particles and in b) volume for Powder 4.	51

2.19 SEM images for Powder 4 at magnification of a) 200X, b) 500X, c) 1000X, d) 1800X and e) 10000X.	52
2.20 Particle size distribution in a) number of particles and in b) volume for 316L powder.	54
2.21 SEM images for 316L powder at magnification of a) 500X and b) 1000X.	55
2.22 Building platform with removable discs.	57
2.23 OM (stereomicroscope) images at 16X magnification of 316L single layers produced with a laser CF1000 and a power of 300 W and a scanning speed of a) 100 mm/s, b) 200 mm/s, c) 300 mm/s, d) 400 mm/s, e) 500 mm/s, f) 600 mm/s, g) 700 mm/s, h), i) 800 mm/s, l) 900 mm/s and m) 1000 mm/s.	58
2.24 316L single layer produced with a laser produced with a laser CS450 and a power of 195 W and a scanning speed of a) 300 mm/s, b) 400 mm/s, c) 500 mm/s and d) 600 mm/s.	61
2.25 316L single layer produced with a laser produced with a laser CS450 and a power of 195 W and a scanning speed of a) 700 mm/s, b) 800 mm/s, c) 900 mm/s and d) 1000 mm/s.	62
2.26 316L single layer produced with a laser produced with a laser CS450 and a power of 195 W and a scanning speed of a) 1100 mm/s, b) 1200 mm/s, c) 1300 mm/s, d) 1400 mm/s and e) 1500 mm/s.	63
2.27 OM (stereomicroscope) images at 35X magnification of 316L single layers produced with a laser CS450 and a power of 195 W and a scanning speed of 300 mm/s.	64
2.28 OM (stereomicroscope) images at 35X magnification of 316L single layers produced with a laser CS450 and a power of 195 W and a scanning speed of 400 mm/s.	65
2.29 OM (stereomicroscope) images at 35X magnification of 316L single layers produced with a laser CS450 and a power of 195 W and a scanning speed of 500 mm/s.	66
2.30 OM (stereomicroscope) images at 35X magnification of 316L single layers produced with a laser CS450 and a power of 195 W and a scanning speed of 600 mm/s.	67
2.31 OM (stereomicroscope) images at 35X magnification of 316L single layers produced with a laser CS450 and a power of 195 W and a scanning speed of 700 mm/s.	67
2.32 OM (stereomicroscope) images at 35X magnification of 316L single layers produced with a laser CS450 and a power of 195 W and a scanning speed of 800 mm/s.	68
2.33 OM (stereomicroscope) images at 35X magnification of 316L single layers produced with a laser CS450 and a power of 195 W and a scanning speed of 900 mm/s.	68

2.34	OM (stereomicroscope) images at 35X magnification of 316L single layers produced with a laser CS450 and a power of 195 W and a scanning speed of 1000 mm/s.	69
2.35	OM (stereomicroscope) images at 35X magnification of 316L single layers produced with a laser CS450 and a power of 195 W and a scanning speed of 1100 mm/s.	69
2.36	OM (stereomicroscope) images at 35X magnification of 316L single layers produced with a laser CS450 and a power of 195 W and a scanning speed of 1200 mm/s.	70
2.37	OM (stereomicroscope) images at 35X magnification of 316L single layers produced with a laser CS450 and a power of 195 W and a scanning speed of 1300 mm/s.	70
2.38	OM (stereomicroscope) images at 35X magnification of 316L single layers produced with a laser CS450 and a power of 195 W and a scanning speed of 1400 mm/s.	71
2.39	OM (stereomicroscope) images at 35X magnification of 316L single layers produced with a laser CS450 and a power of 195 W and a scanning speed of 1500 mm/s.	71
3.1	Ashby diagrams a) strenght vs. density and b) strenght vs. maximum service temperature [6].	73
3.2	Sandwich panel composition.	74
3.3	a) Rhombic dodecahedron [139], b) Tetrakaidecahedron [167] and c) Waire and Phelan structure [174].	75
3.4	a) Schematic image of the four main effect of ice: lift, thrust and drag decreasing and weight increasing. b) Effect of temperature on the amount of SLD in the clouds [80].	77
3.5	a) The classification of the clouds varying the altitude [33] and b) the classification of ice formed on aircrat surfaces [79].	78
3.6	a) Pneumatic de-ice system [130] and b) hot-air anti-ice system.	80
3.7	A scheme of the innovative hot-ait anti-ice system.	82
4.1	DoE for AlSi10Mg compression specimens with a) Bccz, Octet-truss and Rhombic dodecahedron cells and for b) Auxetic, Gyroid and Schwartz diamond cells.	86
4.2	DoE for Ti6Al4V compression specimens with a) Bccz, Octet-truss and Rhombic dodecahedron cells and for b) Auxetic, Gyroid and Schwartz diamond cells.	87
4.3	Setup of the Instron machine for uniaxial compression test on trabecular specimens.	88
4.4	Zwick Roell machine setup for uniaxial compression test on a Octet-truss sandwich panel.	89
4.5	Zwick Roell machine setup for 3-point bending tests on a) a Bccz long panel and b) a Bccz short panel.	90

4.6	Images from ASTM C393/C393M-16 [24] about a) the dimensions of the panels and b) the 3-point load position.	91
4.7	Calculation method of the offset according to ASTM D7250/D7250M-16 [37].	92
4.8	Example of Rhombic panel with cell size of 7 mm and with a solid volume fraction of 25 %.	94
4.9	Section view of the test bench.	95
4.10	Synoptic scheme of the test bench.	96
4.11	Detail view of the measuring equipment: a) convergent duct, b) external skin of the test article, c) divergent duct, d) static outport of the test article and e) infrared thermal camera FLIR. Detail view f) and h) of the junctioning process with high temp silicone and of the test bench g) pre and i) post insulating blanket installation.	97
4.12	OM images of AlSi10Mg compression specimens: a) Oct-3-30 at magnification of 20X and b) Rhom-3-25 at magnification of 16X.	99
4.13	Strut diameter of AlSi10Mg Oct-3-30 from a) CAD model and b) from OM image 20X and of Oct-7-30 from c) CAD model and d) from OM image 8X.	100
4.14	OM images of AlSi10Mg compression specimens at magnification of 8X: a) Bccz-5-30, b) Rhom-5-30, c) Oct-5-30, d) Aux-5-30, e) Gyr-5-25 and f) Sch-5-35.	101
4.15	Rhom-3-25 produced in a) Ti6Al4V and b) AlSi10Mg.	102
4.16	Tomography of AlSi10Mg Bccz specimens in XY plane: a) Bccz-3-30, b) Bccz-5-25, c) and d) Bccz-7-35.	105
4.17	Tomography of Rhombic dodecahedron specimens in XY plane: a) Rhom-5-35 in AlSi10Mg and b) Rhom-5-35 in Ti6Al4V.	106
4.18	Tomography of Octet-truss specimens in XY plane: a) Oct-5-30 in AlSi10Mg and b) Oct-5-30 in Ti6Al4V.	106
4.19	Tomography of Schwartz diamond specimens in XY plane: a) Sch-5-35 in AlSi10Mg and b) Sch-5-35 in Ti6Al4V.	107
4.20	Phases of the compression test on Bccz-3-25-1 specimen.	108
4.21	Tested specimens in different condition: a) Bccz-3-25-1 after the failure of the second plane, b) Bccz-5-30-2 after the failure of the first plane, c) Bccz-5-35-1 continuing the test after the failure of the first plane, d) Bccz-7-25-1 after the failure of the first plane and e) Bccz-7-30-2 after the failure of the first plane.	109
4.22	Stress-strain curves for specimens with Bccz cell and 35 % of solid volume fraction.	110
4.23	Stress-strain curves for specimens with Bccz cell and 5 mm cell size.	111
4.24	Tested specimens in different conditions: a) Rhom-3-25-1 after the failure of the second plane, b) Rhom-5-25-1 after the failure of the first plane and c) Rhom-7-30-2 after the failure of the first plane.	112

4.25	Stress-strain curves for specimens with Rhombic dodecahedron cell and 25% of solid volume fraction.	113
4.26	Stress-strain curves for specimens with Rhombic dodecahedron cell and 7 mm cell size.	114
4.27	Tested specimens in different condition: a) Oct-3-25-2 after the failure of the second plane, b) Oct-5-25-1 after the failure of the first plane and c) Oct-7-35-1 after the failure of the first plane.	115
4.28	Stress-strain curves for specimens with Octet-truss cell and 30% of solid volume fraction.	116
4.29	Stress-strain curves for specimens with Octet-truss cell and 3 mm cell size.	117
4.30	Tested specimens: a) Aux-3-35-1, b) Aux-3-35-5 and c) Oct-7-25-2.	118
4.31	Stress-strain curves for specimens with Auxetic cell.	119
4.32	Tested specimens: a) Gyr-3-30-1, b) Gyr-5-25-2 and c) Gyr-7-35-2.	120
4.33	Stress-strain curves for specimens with Gyroid cell.	121
4.34	Tested specimens: a) Sch-3-25-1, b) Sch-5-35-2 and c) Sch-7-30-1.	121
4.35	Stress-strain curves for specimens with Schwartz diamond cell.	122
4.36	Stress-strain curves for Bccz, Octet-truss and Rhombic dodecahedron specimens with 5 mm and 7 mm cells.	123
4.37	Main effect plot for σ_{\max}	125
4.38	Main effect plot for σ_{02}	125
4.39	Main effect plot for E.	126
4.40	Bar chart of the mechanical results for Bccz, Octet-truss and Rhombic dodecahedron cells.	127
4.41	Bar chart of the mechanical results for Auxetic, Gyroid and Schwartz diamond cells.	128
4.42	Comparison between experimental data for Bccz, Octet and Rhombic cells in AlSi10Mg with the values obtained from Gibson-Ashby model for the same cells in terms of a) σ_{\max} and b) E.	130
4.43	Comparison between experimental data for Auxetic, Gyroid and Schwartz cells in AlSi10Mg with the values obtained from Gibson-Ashby model for the same cells in terms of a) σ_{\max} and b) E.	131
4.44	Tested specimens: a) Bccz-3-30-3, b) Bccz-5-25-2 and c) Bccz-7-35-1.	132
4.45	Stress-strain curves for Ti6Al4V Bccz specimens.	133
4.46	Tested specimens: a) Rhom-3-25-1, b) Rhom-5-35-3 and c) Rhom-7-30-3.	134
4.47	Stress-strain curves for Ti6Al4V Rhombic dodecahedron specimens.	135
4.48	Tested specimens: a) Oct-3-35-1, b) Oct-5-30-2 and c) oct-7-25-3.	136
4.49	Stress-strain curves for Ti6Al4V Octet-truss specimens.	137
4.50	Tested specimens: a) Aux-3-35-1, b) Aux-5-30-2 and c) Aux-7-25-5.	137
4.51	Stress-strain curves for Ti6Al4V Auxetic specimens.	138
4.52	Tested specimens: a) Gyr-3-30-2, b) Gyr-25-2 and c) Gyr-7-35-1.	139

4.53	Stress-strain curves for Ti6Al4V Gyroid specimens.	140
4.54	Tested specimens: a) Sch-3-25-2, b) Sch-5-35-2 and c) Sch-7-30-2. . .	141
4.55	Stress-strain curves for Ti6Al4V Schwartz diamond specimens. . . .	141
4.56	Comparison between experimental data for Bccz, Octet and Rhombic cells in Ti6Al4V with the values obtained from Gibson-Ashby model for the same cells in terms of a) σ_{\max} and b) E.	144
4.57	Comparison between experimental data for Auxetic, Gyroid and Schwartz cells in Ti6Al4V with the values obtained from Gibson-Ashby model for the same cells in terms of a) σ_{\max} and b) E.	145
4.58	Tested sandwich panels: a) Bccz-7-30, b) Oct-7-25 and c) Sch-7-25. . . .	146
4.59	Column chart of compression test results on sandwich panels.	147
4.60	Column chart of compression test results on sandwich panels.	147
4.61	Main effect plot for σ_{\max}	148
4.62	Main effect plot for σ_{02}	149
4.63	Main effect plot for E.	149
4.64	Long sandwich panels after 3-point bending test: a) Bccz-5-30-1 and b) Bccz-7-25-2.	151
4.65	Long sandwich panels after 3-point bending test: a) Oct-5-25-1 and b) Bccz-7-30-1.	152
4.66	Long sandwich panels after 3-point bending test: a) Sch-5-30-2 and b) Sch-7-30-2.	153
4.67	Long sandwich panels after 3-point bending test: a) Bccz-5-30- and b) Bccz-7-25-2.	154
4.68	Long sandwich panels after 3-point bending test: a) Oct-5-30-2 and b) Oct-7-30-1.	155
4.69	Long sandwich panels after 3-point bending test: a) Sch-5-25-1 and b) Sch-7-30-2.	156
4.70	Wohler curves for Rhombic dodecahedron specimens.	157
4.71	Rom-5-25 specimens subjected to fatigue tests with maximum load of: a) 80 % of σ_{02} , b) 60 % of σ_{02} and c) 40 % of σ_{02}	158
4.72	Rom-5-30 specimens subjected to fatigue tests with maximum load of: a) 80 % of σ_{02} , b) 60 % of σ_{02} and c) 20 % of σ_{02}	159
4.73	Rom-7-30 specimens subjected to fatigue tests with maximum load of: a) 80 % of σ_{02} , b) 40 % of σ_{02} and c) 20 % of σ_{02}	159
4.74	Wohler curves for Octet-truss specimens.	160
4.75	Oct-5-25 specimens subjected to fatigue tests with maximum load of: a) 80 % of σ_{02} , b) 60 % of σ_{02} and c) 40 % of σ_{02}	161
4.76	Oct-5-30 specimens subjected to fatigue tests with maximum load of: a) 80 % of σ_{02} , b) 40 % of σ_{02} and c) 20 % of σ_{02}	161
4.77	Oct-7-30 specimens subjected to fatigue tests with maximum load of: a) 80 % of σ_{02} , b) 40 % of σ_{02} and c) 20 % of σ_{02}	162

4.78	Specimens subjected to fatigue tests: a) Bccz-5-25 with 80 % of σ_{02} , b) Bccz-5-30 with 80 % of σ_{02} , c) Bccz-7-30 with 80 % of σ_{02} and d) Bccz-7-30 with 60 % of σ_{02} .	163
4.79	Cross section of a) Bccz and b) Rhombic panels.	164
4.80	Pressure drop, temperature drop and heat transfer for all the panels.	165
4.81	Anti-ice system of Piaggio P180 aircraft.	166
4.82	Mock-up of the anti-ice system designed for Piaggio P180 aircraft and produced with L-PBF.	167
A.1	Measurements of the specimens for compression tests.	173
A.2	Measurements of the sandwich panels for compression tests.	180
A.3	Measurements of the sandwich panels for bending tests.	181
B.1	Lateral and top view of the Bccz AlSi10Mg specimens: a) Bccz-3- 25-1, b) Bccz-3-30-2 and c) Bccz-3-35-1.	185
B.2	Lateral and top view of the Bccz AlSi10Mg specimens: a) Bccz-5- 25-3, b) Bccz-5-30-1 and c) Bccz-5-35-1.	186
B.3	Lateral and top view of the Bccz AlSi10Mg specimens: a) Bccz-7- 25-2, b) Bccz-7-30-1 and c) Bccz-7-35-1.	186
B.4	Lateral and top view of the Rhombic dodecahedron AlSi10Mg spec- imens: a) Rhom-3-25-1, b) Rhom-3-30-1 and c) Rhom-3-35-1.	187
B.5	Lateral and top view of the Rhombic dodecahedron AlSi10Mg spec- imens: a) Rhom-5-25-1, b) Rhom-5-30-1 and c) Rhom-5-35-1.	187
B.6	Lateral and top view of the Rhombic dodecahedron AlSi10Mg spec- imens: a) Rhom-7-25-2, b) Rhom-7-30-2 and c) Rhom-7-35-1.	188
B.7	Lateral and top view of the Octet-truss AlSi10Mg specimens: a) Oct-3-25-6, b) Oct-3-30-3 and c) Oct-3-35-3.	188
B.8	Lateral and top view of the Octet-truss AlSi10Mg specimens: a) Oct-5-25-1, b) Oct-5-30-1 and c) Oct-5-35-1.	189
B.9	Lateral and top view of the Octet-truss AlSi10Mg specimens: a) Oct-7-25-1, b) Oct-7-30-1 and c) Oct-7-35-1.	189
B.10	Lateral and top view of the Auxetic AlSi10Mg specimens: a) Aux- 3-35-3, b) Aux-5-30-1 and c) Aux-7-25-1.	190
B.11	Lateral and top view of the Gyroid AlSi10Mg specimens: a) Gyr-3- 30-3, b) Gyr-5-25-1 and c) Gyr-7-35-2.	190
B.12	Lateral and top view of the Schwartz diamond AlSi10Mg specimens: a) Sch-3-25-3, b) Sch-5-35-1 and c) Sch-7-30-2.	191
B.13	Lateral and top view of the Bccz Ti6Al4V specimens: a) Bccz-3-30-2, b) Bccz-5-25-1 and c) Bccz-7-35-1.	192
B.14	Lateral and top view of the Rhombic dodecahedron Ti6Al4V speci- mens: a) Rhom-3-25-3, b) Rhom-5-35-1 and c) Rhom-7-30-3.	193
B.15	Lateral and top view of the Octet-truss Ti6Al4V specimens: a) Oct- 3-35-3, b) Oct-5-30-3 and c) Oct-7-25-2.	193

B.16 Lateral and top view of the Auxetic Ti6Al4V specimens: a) Aux-3-35-1, b) Aux-5-30-1 and c) Aux-7-25-4.	194
B.17 Lateral and top view of the Gyroid Ti6Al4V specimens: a) Gyr-3-30-13, b) Gyr-5-25-1 and c) Gyr-7-35-1.	194
B.18 Lateral and top view of the Schwartz diamond Ti6Al4V specimens: a) Sch-3-25-1, b) Sch-5-35-4 and c) Sch-7-30-1.	195
B.19 Lateral and top view of the Bccz AlSi10Mg sandwich panels: a) Bccz-5-25 and b) Bccz-5-30.	196
B.20 Lateral and top view of the Bccz AlSi10Mg sandwich panels: a) Bccz-7-25 and b) Bccz-7-30.	196
B.21 Lateral and top view of the Octet-truss AlSi10Mg sandwich panels: a) Oct-5-25 and b) Oct-5-30.	196
B.22 Lateral and top view of the Octet-truss AlSi10Mg sandwich panels: a) Oct-7-25 and b) Oct-7-30.	197
B.23 Lateral and top view of the Schwartz diamond AlSi10Mg sandwich panels: a) Sch-5-25 and b) Sch-5-30.	197
B.24 Lateral and top view of the Schwartz diamond AlSi10Mg sandwich panels: a) Sch-7-25 and b) Sch-7-30.	197
B.25 Lateral and top view of the Bccz AlSi10Mg long sandwich panels: a) Bccz-5-25-2 and b) Bccz-5-30-1.	198
B.26 Lateral and top view of the Bccz AlSi10Mg long sandwich panels: a) Bccz-7-25-1 and b) Bccz-7-30-1.	198
B.27 Lateral and top view of the Octet-truss AlSi10Mg long sandwich panels: a) Oct-5-25-2 and b) Oct-5-30-1.	198
B.28 Lateral and top view of the Octet-truss AlSi10Mg long sandwich panels: a) Oct-7-25-2 and b) Oct-7-30-2.	199
B.29 Lateral and top view of the Schwartz diamond AlSi10Mg long sandwich panels: a) Sch-5-25-2 and b) Sch-5-30-1.	199
B.30 Lateral and top view of the Schwartz diamond AlSi10Mg long sandwich panels: a) Sch-7-25-1 and b) Sch-7-30-1.	199
B.31 Lateral and top view of the Bccz AlSi10Mg short sandwich panels: a) Bccz-5-25-1 and b) Bccz-5-30-2.	200
B.32 Lateral and top view of the Bccz AlSi10Mg short sandwich panels: a) Bccz-7-25-1 and b) Bccz-7-30-1.	200
B.33 Lateral and top view of the Octet-truss AlSi10Mg short sandwich panels: a) Oct-5-25-1 and b) Oct-5-30-1.	200
B.34 Lateral and top view of the Octet-truss AlSi10Mg short sandwich panels: a) Oct-7-25-1 and b) Oct-7-30-1.	201
B.35 Lateral and top view of the Schwartz diamond AlSi10Mg short sandwich panels: a) Sch-5-25-2 and b) Sch-5-30-1.	201
B.36 Lateral and top view of the Schwartz diamond AlSi10Mg short sandwich panels: a) Sch-7-25-2 and b) Sch-7-30-2.	201

B.37 Lateral view of the Bccz AlSi10Mg specimens for fatigue test: a) Bccz-5-25, b) Bccz-5-30 and b) Bccz-7-30.	202
B.38 Lateral view of the Octet-truss AlSi10Mg specimens for fatigue test: a) Oct-5-25, b) Oct-5-30 and b) Oct-7-30.	202
B.39 Lateral view of the Rhombic dodecahedron AlSi10Mg specimens for fatigue test: a) Rhom-5-25, b) Rhom-5-30 and b) Rhom-7-30.	203
D.1 Stress-strain curves of compression test of Bccz-3-25 specimens.	219
D.2 Stress-strain curves of compression test of Bccz-3-30 specimens.	220
D.3 Stress-strain curves of compression test of Bccz-3-35 specimens.	220
D.4 Stress-strain curves of compression test of Bccz-5-25 specimens.	221
D.5 Stress-strain curves of compression test of Bccz-5-30 specimens.	221
D.6 Stress-strain curves of compression test of Bccz-5-35 specimens.	222
D.7 Stress-strain curves of compression test of Bccz-7-25 specimens.	222
D.8 Stress-strain curves of compression test of Bccz-7-30 specimens.	223
D.9 Stress-strain curves of compression test of Bccz-7-35 specimens.	223
D.10 Stress-strain curves of compression test of Rhom-3-25 specimens.	224
D.11 Stress-strain curves of compression test of Rhom-3-30 specimens.	224
D.12 Stress-strain curves of compression test of Rhom-3-35 specimens.	225
D.13 Stress-strain curves of compression test of Rhom-5-25 specimens.	225
D.14 Stress-strain curves of compression test of Rhom-5-30 specimens.	226
D.15 Stress-strain curves of compression test of Rhom-5-35 specimens.	226
D.16 Stress-strain curves of compression test of Rhom-7-25 specimens.	227
D.17 Stress-strain curves of compression test of Rhom-7-30 specimens.	227
D.18 Stress-strain curves of compression test of Rhom-7-35 specimens.	228
D.19 Stress-strain curves of compression test of Oct-3-25 specimens.	228
D.20 Stress-strain curves of compression test of Oct-3-30 specimens.	229
D.21 Stress-strain curves of compression test of Oct-3-35 specimens.	229
D.22 Stress-strain curves of compression test of Oct-5-25 specimens.	230
D.23 Stress-strain curves of compression test of Oct-5-30 specimens.	230
D.24 Stress-strain curves of compression test of Oct-5-35 specimens.	231
D.25 Stress-strain curves of compression test of Oct-7-25 specimens.	231
D.26 Stress-strain curves of compression test of Oct-7-30 specimens.	232
D.27 Stress-strain curves of compression test of Oct-7-35 specimens.	232
D.28 Stress-strain curves of compression test of Aux-3-35 specimens.	233
D.29 Stress-strain curves of compression test of Aux-5-30 specimens.	233
D.30 Stress-strain curves of compression test of Aux-7-25 specimens.	234
D.31 Stress-strain curves of compression test of Gyr-3-30 specimens.	234
D.32 Stress-strain curves of compression test of Gyr-5-25 specimens.	235
D.33 Stress-strain curves of compression test of Gyr-7-35 specimens.	235
D.34 Stress-strain curves of compression test of Sch-3-25 specimens.	236
D.35 Stress-strain curve of compression test of Sch-5-35 specimens.	236
D.36 Stress-strain curves of compression test of Sch-7-30 specimens.	237

D.37 Stress-strain curves of compression test of Bccz-3-30 specimens. . .	237
D.38 Stress-strain curves of compression test of Bccz-5-25 specimens. . .	238
D.39 Stress-strain curves of compression test of Bccz-7-35 specimens. . .	238
D.40 Stress-strain curves of compression test of Rhom-3-25 specimens. . .	239
D.41 Stress-strain curves of compression test of Rhom-5-35 specimens. . .	239
D.42 Stress-strain curves of compression test of Rhom-7-30 specimens. . .	240
D.43 Stress-strain curves of compression test of Oct-3-35 specimens. . . .	240
D.44 Stress-strain curves of compression test of Oct-5-30 specimens. . . .	241
D.45 Stress-strain curves of compression test of Oct-7-25 specimens. . . .	241
D.46 Stress-strain curves of compression test of Aux-3-35 specimens. . . .	242
D.47 Stress-strain curves of compression test of Aux-5-30 specimens. . . .	242
D.48 Stress-strain curves of compression test of Aux-7-25 specimens. . . .	243
D.49 Stress-strain curves of compression test of Gyr-3-30 specimens. . . .	243
D.50 Stress-strain curves of compression test of Gyr-5-25 specimens. . . .	244
D.51 Stress-strain curves of compression test of Gyr-7-35 specimens. . . .	244
D.52 Stress-strain curves of compression test of Sch-3-25 specimens. . . .	245
D.53 Stress-strain curves of compression test of Sch-5-35 specimens. . . .	245
D.54 Stress-strain curves of compression test of Sch-7-30 specimens. . . .	246
D.55 Stress-strain curves of compression test of Bccz sandwich panels. . .	247
D.56 Stress-strain curves of compression test of Octet-truss sandwich panels.	247
D.57 Stress-strain curves of compression test of Schwartz diamond sandwich panels.	248
D.58 σ vs crosshead displacement curves of bending test on Bccz-5-25 short sandwich panels.	249
D.59 σ vs crosshead displacement curves of bending test on Bccz-5-30 short sandwich panels.	249
D.60 σ vs crosshead displacement curves of bending test on Bccz-7-25 short sandwich panels.	250
D.61 σ vs crosshead displacement curves of bending test on Bccz-7-30 short sandwich panels.	250
D.62 σ vs crosshead displacement curves of bending test on Oct-5-25 short sandwich panels.	251
D.63 σ vs crosshead displacement curves of bending test on Oct-5-30 short sandwich panels.	251
D.64 σ vs crosshead displacement curves of bending test on Oct-7-25 short sandwich panels.	252
D.65 σ vs crosshead displacement curves of bending test on Oct-7-30 short sandwich panels.	252
D.66 σ vs crosshead displacement curves of bending test on Sch-5-25 short sandwich panels.	253
D.67 σ vs crosshead displacement curves of bending test on Sch-5-30 short sandwich panels.	253

D.68 σ vs crosshead displacement curves of bending test on Sch-7-25 short sandwich panels.	254
D.69 σ vs crosshead displacement curves of bending test on Sch-7-30 short sandwich panels.	254
D.70 σ vs crosshead displacement curves of bending test on Bccz-5-25 long sandwich panels.	255
D.71 σ vs crosshead displacement curves of bending test on Bccz-5-30 long sandwich panels.	255
D.72 σ vs crosshead displacement curves of bending test on Bccz-7-25 long sandwich panels.	256
D.73 σ vs crosshead displacement curves of bending test on Bccz-7-30 long sandwich panels.	256
D.74 σ vs crosshead displacement curves of bending test on Oct-5-25 long sandwich panels.	257
D.75 σ vs crosshead displacement curves of bending test on Oct-5-30 long sandwich panels.	257
D.76 σ vs crosshead displacement curves of bending test on Oct-7-25 long sandwich panels.	258
D.77 σ vs crosshead displacement curves of bending test on Oct-7-30 long sandwich panels.	258
D.78 σ vs crosshead displacement curves of bending test on Sch-5-25 long sandwich panels.	259
D.79 σ vs crosshead displacement curves of bending test on Sch-5-30 long sandwich panels.	259
D.80 σ vs crosshead displacement curves of bending test on Sch-7-25 long sandwich panels.	260
D.81 σ vs crosshead displacement curves of bending test on Sch-7-30 long sandwich panels.	260

Chapter 1

Introduction

1.1 Metal Additive Manufacturing: technologies overview

Despite the great diffusion of Additive Manufacturing (AM) technologies in the last few years, the basics of the technique date back to the 80s. In this period took place the first production of stereolithography machines, marketed by the 3D System, and whose mechanism is shown in Figure 1.1a. The stereolithography technology consists in the solidification of a liquid photopolymer, such as a resin, layer by layer by a light energy source. The liquid resin is contained in a chamber in which also the building platform is located; at each layer the platform is lowered to the desired thickness and the section of interest is solidified. The process is repeated until the component is completed. The non-solidified resin can be reused for subsequent processing [111]. Simultaneously with the invention of stereolithography, the first generation of acrylate resins were launched. The first stereolithography machines were followed by others from different manufacturers, such as Japan's NTT Data CMET and Sony / D-MEC, accompanied by the commercialization of epoxy resins. Only in 1990 the well-known company Electro Optical Systems (EOS) introduced its stereolithography machine. In the same year Quadrax launched the Mark1000 SL machine, using visible light resins as a raw material. It is necessary to wait until 1991 to see on the market some 3D printing technologies capable of processing materials different than resins, such as the Fused Deposition Modeling (FDM) technology produced by Stratasys, the Laminated Object Manufacturing (LOM) proposed by Helisys and the Solid Ground Curing (SGC) created by Cubital [66]. The FDM technology, illustrated in Figure 1.1b, is currently very widespread on the market, especially in the area of competence of low-cost 3D printing machines, which can produce pieces in some simple-to-treat materials, such as PLA (polylactic acid) and ABS (acrylonitrile-butadiene-styrene) [34, 78]. However, there are

also some machines for industrial use, capable of processing difficult-to-handle materials such as PEEK, Nylon and elastomers [41]. The operating principle is based on the extrusion of a thermoplastic polymer filament. The filament is heated by a resistance up to the softening point and pushed through a nozzle. The material is deposited layer by layer according to the coordinates present in the model (.gcode) [110]. The LOM, schematized in Figure 1.1c, is a technology that showed a much lower spread than the FDM. It consists of overlapping layers of different materials, such as paper, metal or plastic, cut them according to the desired section. It is necessary to glue the different layers together by thermal adhesives, in order to produce the finished component [72, 78]. Many other technologies followed, and they are capable of processing different polymers in different ways.

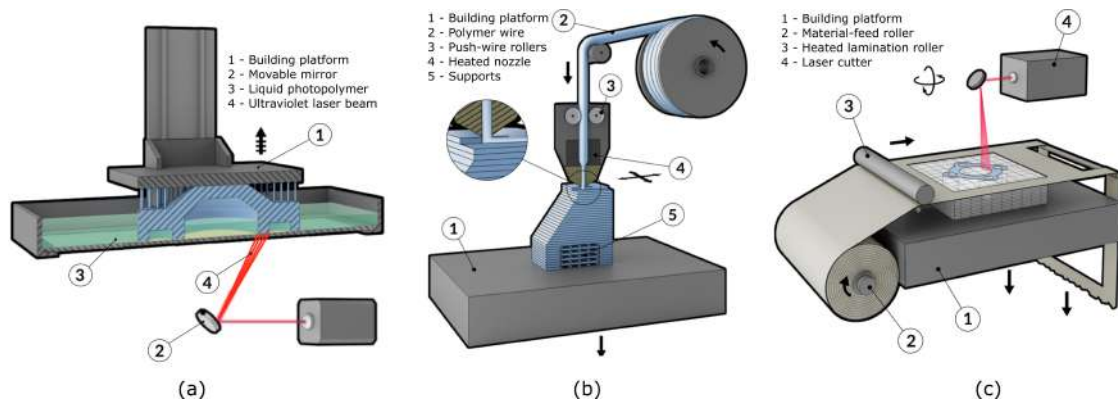


Figure 1.1: Explicative drawings of a) Stereolithography [104], b) FDM technology [105] and c) LOM technology [106].

After the development of machines for the polymeric components realization, various additive techniques for the metal parts production were produced. The technologies that use metal powders as feed, such as the Powder Bed Fusion (PBF) and Direct Energy Deposition (DED) technologies, are the most widespread [131, 78]. The first use of these machines was the creation of prototypes, which helped in the design of the final components, for the following production with traditional technologies; the use of AM as a production technique is a goal not yet reached. The principle that these production techniques have in common is the realization of components layer by layer, following the information included in the 3D reference model [144]. The process begins with the creation of the CAD model of the component to be produced. After this, the model is exported in .stl format and processed in the preparation software (eg Cura, Slicer, Simplify 3D or others for polymers, Netfab or Magics for metals): here it is possible to fix the .stl file (if necessary), the orientation of the component on the build plate, the insertion of the supports (when present) and the slicing. The insertion of the supports is dependent on the orientation chosen for the construction of the piece and is strictly connected to

the additive technology used. In the production of metal components with PBF technology, the supports have different functions, including the heat dissipation of the piece and the fixing of the piece to the building platform. The preparation ends with the saving of the file and by sending it to the machine for the production [76].

1.1.1 Powder Bed Fusion (PBF)

The term PBF refers to AM technologies powered by metal powders, which are deposited, layer by layer, in a powder bed. An energy beam melts, in each layer, the section of the piece indicated by the 3D model. Depending on the type of energetic beam used, a further subdivision can be made: SLM technology if a laser beam is used, EBM technology if an electron beam is used [166]. The common procedure consists of a series of cyclically repeated phases up to the completion of the piece: the spreading of the metal powder by a rake, the melting of the section, the lowering of the building platform and the creation of the next layer, as shown in Figure 1.2 [61]. At the end of the process other operations must be carried out: the extraction of the chamber, the separation of the component from the unmelted powders, the stress-relieving thermal treatment and finally the separation of the piece from the plate and the removal of the supports.

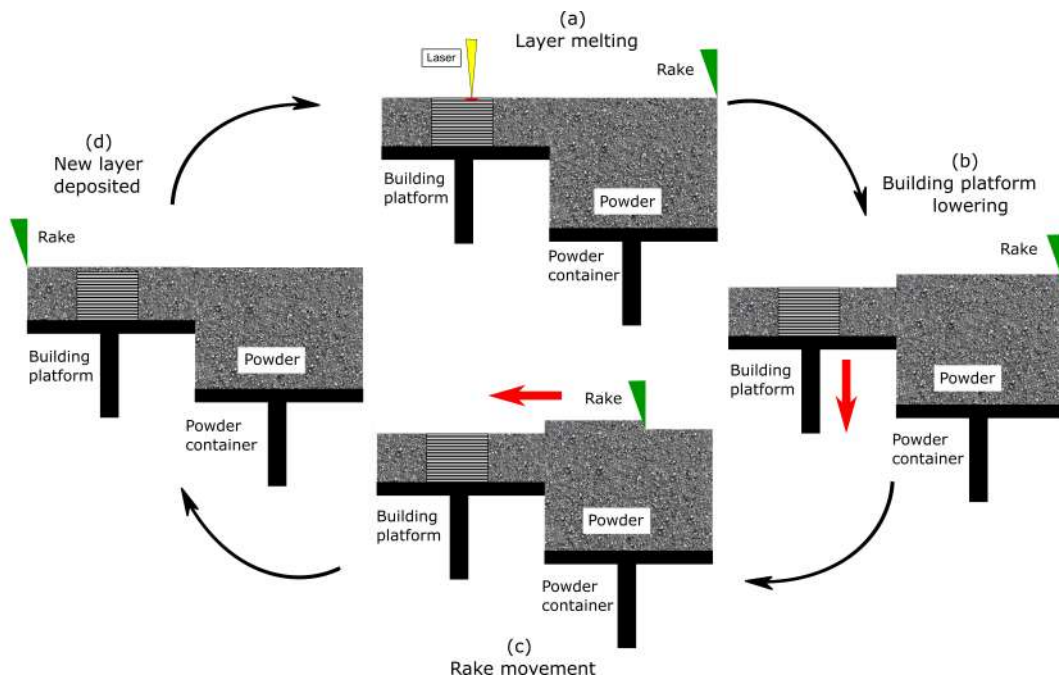


Figure 1.2: Phases for the component creation with PBF technology: a) melting of the layer, b) the lowering of the building platform, c) the movimentation of the rake and d) the creation of the new layer.

The purpose of the supports in the PBF technology is not only to give support to the material, but to fix the whole component to the plate. This prevents the piece from moving during the powder deposition due to contact with the rake. Moreover, the fixing prevents the deformation of the component during its cooling after the fusion of the sections. This causes the formation of internal stresses, which must be eliminated with a stress-relieving thermal treatment, before the piece is separated from the building platform [123]. The supports are waste materials, so it is advisable to choose the piece orientation so as to produce as few supports as possible, without reducing the goodness of the component [76, 120].

Laser Powder Bed Fusion (L-PBF)

The Laser Powder Bed Fusion (L-PBF) (Figure 1.3a) system uses the laser beam to melt the metal powder. The laser used is a fiber type, with a spot size of 50-180 μm , and its operation includes a system of lenses and scanners. The raw material, the powder, is contained in a special case or, in the most innovative systems, in hoppers above the machine. In all cases the powder is used to cover the building platform with layers of variable thickness, between 20 and 100 μm , by a rake [43]. The choice of layer thickness depends on the desired surface finish for the as-built component, on the characteristics of the powder and on the laser power.

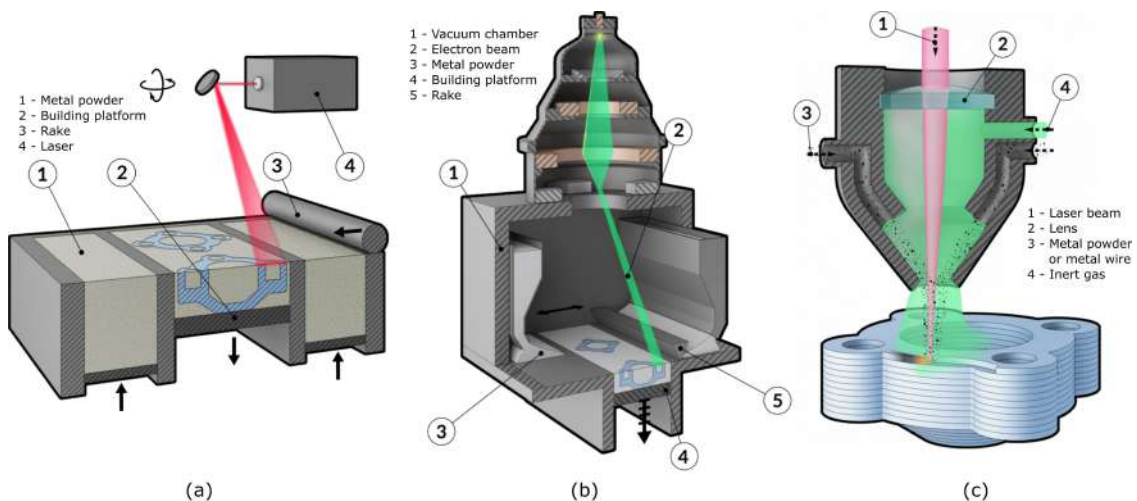


Figure 1.3: Explicative drawings of a) SLM [107], b) EBM [108] and c) DED [109].

The powders to be used in L-PBF technology must be as spherical and regular as possible, with a particle size distribution represented by a Gaussian curve and a particle size between 10 and 100 μm . This allows to spread uniform powder layers, thanks to the good flowability of the powders, and therefore to obtain a final component with optimal density [166]. The success of the subsequent melting process is strictly dependent on the right choice of process parameters; the parameters

that act directly during the process are the laser power, the scanning speed, the layer thickness, the scanning strategy and the pre-heating. However, there are other equally important parameters that must not be overlooked in order to obtain a good result in terms of mechanical properties and microstructure of the component: they are the quality of the powder, the goodness of its conservation and the flushing inside the machine [86, 127, 186, 129]. The building platform provides mechanical support for the growth of the piece and is lowered at each cycle so as to allow the formation of the new layer. It is equipped with heating elements to preheat the powder bed and so to reduce the gradient between melted and unmelted powders. The temperature difference between the part and the unmelted powders affects the solidification process and creates the internal stresses that form in the piece. A lower thermal gradient allows slower cooling and lower internal stresses [68]. It is always important to perform the stress-relieving treatment before separating the piece from the building platform to avoid deformations and cracks, particularly when very large pieces are produced. An example of the effects due to the residual stress is reported in Figure 1.4.

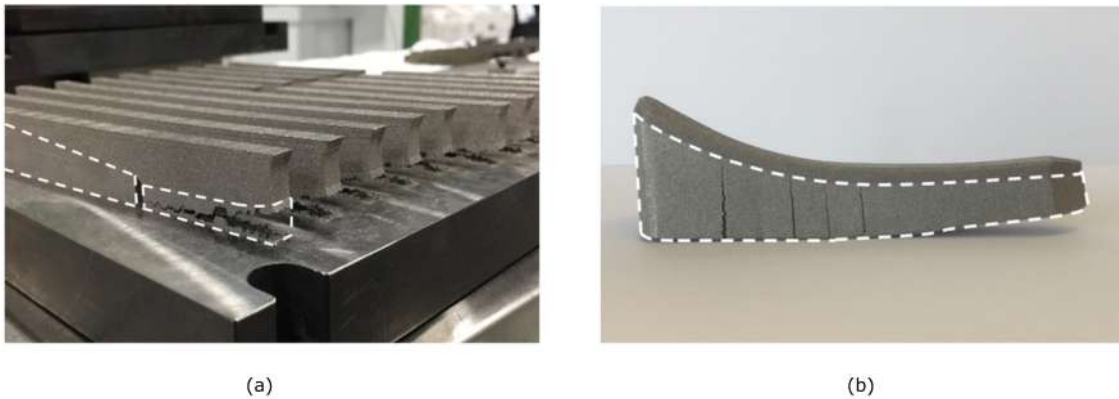


Figure 1.4: Effects of residual stresses in two cases: a) failure of the job during the process and b) deformation and cracking of the component after the separation from the platform [169].

An essential requirement for the success of the components made with L-PBF technology is the maintenance of the inert atmosphere inside the building chamber. The presence of oxygen at high temperatures causes the oxidation of the material in the powder bed, producing impurities in the component and compromising the job. It is necessary that the oxygen content is less than 0.1 % and that the inert gas is compatible with the treated material: the most used gases are Nitrogen and Argon. At the end of the work the post-processing procedures are performed and the unmelted powder is recovered. Before being reused for a new job the powders must be sieved, to eliminate the granules and the large aggregates formed during processing and that would prevent a good laying of the layers. The reuse of the

powder is always good and must be carried out following the regulations on powder management (ASTM Standard [1]): it is recommended to mix the reused powder with the new one and to carry out periodic chemical analyses to check the powder composition.

Electron Beam Melting (EBM)

The Electron Beam Melting (EBM) (Figure 1.3b) system uses the electron beam to melt the powder. The beam is produced by a hot tungsten filament or by a lanthanum hexaboride that emits electrons and these are oriented by a system of electromagnetic lenses [89]. Only one company produces machines with this technology and it is the swedish Arcam, recently acquired by GE. The operating principle is similar to that seen for the L-PBF, only the type of energy beam changes. The powder is contained in a tank or in hoppers and it is distributed on the building platform by a rake. The layers formed are thicker than those made with the previous technology and are about 50-200 μm [43]. The EBM powders are characterized by larger diameters than L-PBF powders, but the same characteristics are desirable: spherical and regular shape, particle size distribution represented by Gaussian distribution and good flowability, as shown in Figure 1.5. The larger size of the powders and of the layers results in a greater surface roughness of the as-built component.

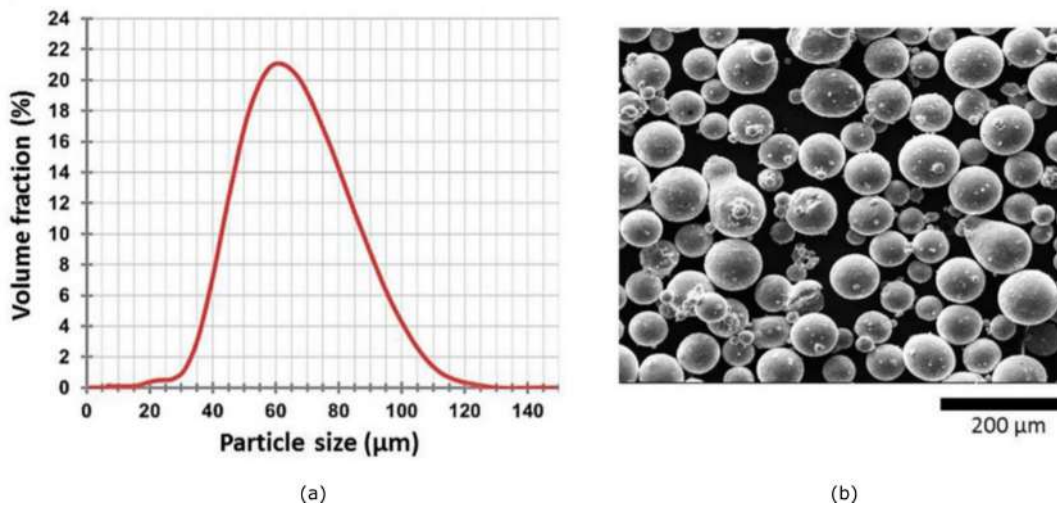


Figure 1.5: a) A particle size distribution for powders designed for EBM technology and b) an example of a SEM image of Ti6Al4V powders [89].

The possibility of making thicker layers depends on the greater power of the electronic beam compared to the laser beam: the electron beam has a power of about 3 kW, against a maximum of 1 kW for the laser, and allows to melt faster

the thicker layers and preheat the powder bed directly with the electron beam. The high pre-heating of the powder bed reduces the thermal gradient between melted and unmelted powders and allows the creation of components with lower internal tensions [89]. The microstructure of the as-built component, however, is coarser than the one obtained with L-PBF, due to the larger particles size and due to the slower cooling of the melted layers. In order to make the electron beam work well, it is necessary that the working chamber is in high vacuum (10^{-3} Pa): if an inert atmosphere was used, as for the laser, the electrons of the beam would collide with the molecules of Nitrogen or Argon and would be partly diverted. This would prevent the powders from melting properly. With the vacuum chamber this phenomenon does not happen, moreover the absence of oxygen protects the powder bed from oxidation phenomena [74]. Once the piece is finished, it is necessary to wait for the working chamber to cool down and returns to atmospheric pressure by entering the inert gas; subsequently the post-processing operations of part and supports separation are performed and the unmelted powder is recovered. Due to the more intense preheating, at the end of the process the powders are compacted into a crumbly block called cake [31]. The state of the powders after EBM pre-heating is highlighted in Figure 1.6. To recover them, it is necessary to detach the cake from the component manually in a glove box with an inert atmosphere and then shake the powder block mechanically to bring it back to its initial state. The materials that can be processed with this technology are metal alloys with a high melting temperature, such as titanium alloys [31].

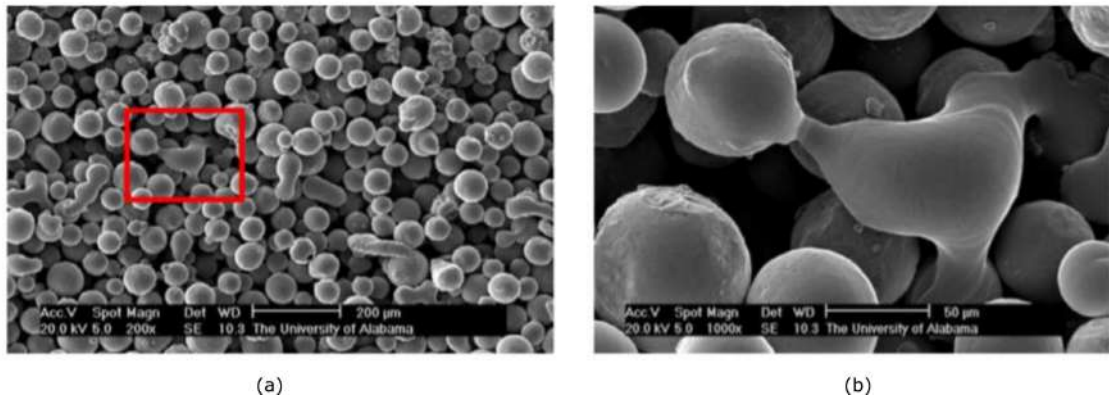


Figure 1.6: SEM images of an example of Ti6Al4V pre-heated powders [31].

1.1.2 Direct Energy Deposition (DED)

The Direct Energy Deposition (DED) (Figure 1.3c) technology uses an energetic beam, typically a laser beam, to melt the powders of metal alloys locally deposited by a deposition head. This technology also allows the feeding of metal in the form

of wire, which is melted by the resistors and deposited by a nozzle. The quality of the components made with wire is of a much lower quality than that obtained with powders. The procedure consists in depositing the powders on a building platform and in the simultaneous fusion by a laser beam. Unlike the PBF, in the DED there is no powder bed and, in order to produce the component, it is necessary that the laser melts the powders and the platform as soon as the powders are deposited. If this operation is not properly calibrated, defects will be present in the final component. Also in this case the piece is made layer by layer, depositing powder and melting it with the laser beam [181, 168]. DED technology allows the use of less powder than PBF, as it is not necessary to completely fill the building platform with powders to complete the piece. In addition, it allows to produce faster and to repair parts already made. However, it is not suitable for making components with too complex shapes, even if some surfaces without supports can be built thanks to the rotating movement of the building platform introduced in some machines. The average powder dimensions for this technology are bigger than those used in the L-PBF and consequently the surface roughness is greater.

1.2 STAMP Project

The current goal of the industry is to achieve a fully automated and interconnected production system, known as Industry 4.0 [60, 12]. This process, extended over several sectors, is carried out by the fourth industrial revolution, which will show the impact of new technologies on four main strands. The first area of influence is the sector of data management, connectivity and computing power that translates into Big data, Internet of Things, open data, cloud computing, and machine to machine interactions [171, 35, 119]. The aim is to obtain centralized information. The second area of interest consists in information and data analysis. From this comes the Machine Learning, which allows the improvement of machine efficiency through the analysis of collected data [119]. The third area of development in the sector that defines the relationship between man and machine and involves the use of augmented reality and touch interfaces [35]. Finally, the fourth area concerns the real components production and includes Additive Manufacturing, 3D printing, robotics and some energy storage technologies [171].

Additive Manufacturing is therefore reported as an emerging industrial technology in Industry 4.0 [171]. In particular, the metal powders AM technology allows the creation of mechanical components through the addition of material layer by layer. This approach allows the creation of components with extremely complex geometric shapes using traditional or innovative materials [63]. The production of components with additive technology does not require additional dedicated equipment such as molds or cutting tools. This is one of the most advantageous economic

aspects of the technology because it cancels the influence of the size of the production lot on the final cost of the component. One of the major obstacles that Additive Manufacturing finds on its market diffusion is the association with prototyping and non-industrial production technologies. Indeed, AM technique was born as a prototyping system and still has some aspects that need to be improved before it can be considered an industrial production system [65]. In order to consider AM technology as an innovative industrial production system, as provided in the context of Industry 4.0, it is necessary to introduce better process control, a higher level of automation, a standard of product repeatability and greater productivity.

The natural affinity of the AM to the production of small lots and geometrically complex pieces, made it a technology particularly suitable for some production sectors, such as aerospace and high-end automotive. These sectors are particularly interesting for many Piedmontese end-users. This economic interest for end-users and the goal of reaching an industrial level for additive technologies led to the realization of the regional project STAMP. The STAMP (Sviluppo Tecnologico dell'Additive Manufacturing in Piemonte) project is a regional project that aims to develop and consolidate AM technologies within the Piedmont industrial landscape and in the framework of the "Intelligent Factory" technological area. The project had a duration of 36 months and ended on 17 October 2019. The partnership, headed by Prima Industrie, involved universities and research centers such as the Politecnico di Torino, the Università di Torino and the Italian Institute of Technology, and a broad partnership of large, medium and small companies including Consoft, Prima Electro, Ge Avio, Thales, Avio Space, FCA Group, APR, BLU Engineering, Iris, Ellena, Itacae, Samec, Cabelectra, Laserlam, Tosca, Power Equipment, SI Engineering, SRS ED, Comutensili, Alfa Meccanica and 3D New Technologies. The project program led to an evolution of the entire AM chain, in particular for the commonly defined PBF and DED technologies, in order to overcome the current process limitations. Indeed, PBF and DED are the two most promising technologies for the additive production of metal components and are currently the most common ones on the market. Thanks to the synergy between research centers and small companies, the effectiveness and convenience of AM production for the Piedmont industrial sector was demonstrated through three main lines of intervention: (i) definition of guidelines for the correct design of AM parts, (ii) improvement of Powder Bed and Direct Deposition deposition techniques with the development of two demonstrators (one for each technology), (iii) analysis, evaluation and possible rewriting of the standards currently present on the AM.

The role of 3D New Technologies within the STAMP project is the realization of the innovative demonstrator for the PBF technology: the machine must fit well into the current market and must propose innovative solutions to the current limitations of the technology.

1.3 PBF technology benchmark

The activities carried out in the STAMP project to realize the L-PBF technology prototype started with analyzing the technological solutions currently present on the market, assessing limits and development trends, in order to identify the area of technological intervention of the machine to be produced. In the current panorama (updated to 2015) the PBF technology occupies about 90% of the market of AM machines for metal, with an exponential growth of the machines sold from 2010 to 2015. This not only implies a rapid updating of the technology, but also the entry of new players in the production sector of AM machines. Therefore it is important to determine the limits of the current machines, but also an estimate of the speed with which they are exceeded by the new technological proposals, to develop a product that is not immediately obsolete.

AM technologies were introduced to the market more than twenty years ago, but the attention of industry has focused on them only in recent years, under the influence of media campaigns on "3D printing" and thanks to the introduction of systems for the production of metal components. Among the various AM technologies, surely the metal systems are those that are arousing the highest expectations, and among these the PBF systems are the most widespread on the market. At the end of 2014, twenty-two manufacturers of additive systems were present in Europe and among these eight companies (Arcam, BeAM, Concept Laser, DMG Mori, EOS, ReaLizer, Renishaw, SLM Solutions, and Trumpf) were manufacturers of metal systems, with a total of 1814 installations in the world (Fig. 1.7) [138]. These are mainly powder bed systems. The energy source is a laser for almost all systems, with the exclusion of ARCAM, which uses an electron beam.

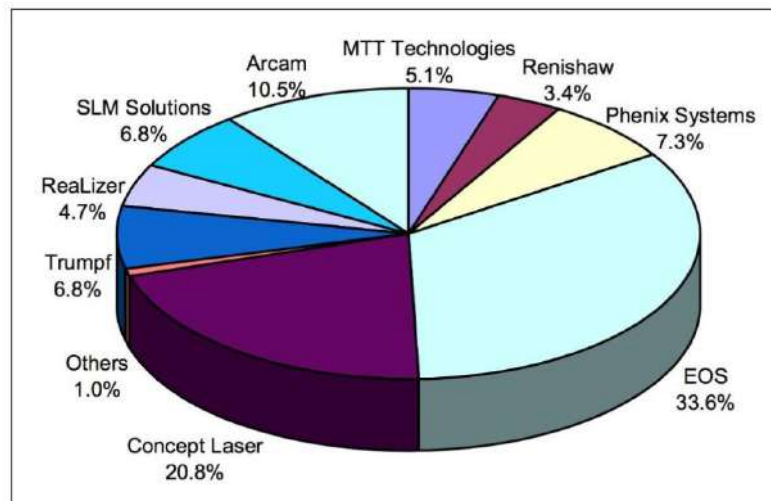


Figure 1.7: Market shares of the main producers of metal systems in Europe (2014) [138].

Table 1.1: Comparison between AM technologies on the market.

Metal AM technology	Laser PBF	Electron Beam PBF	Laser DED
Machine manufacturers	Renishaw, Concept Laser, EOS, ReaLizer, SLM Solution, Sisma-Trumpf, 3D System	Arcam	BeAM, InssTek, Optomec
Forming room dimensions [mm]	50 x 50 x 80, 630 - 400 - 500, typically 250 x 250 x 250	250 x 250 x 400, Φ 350 x 380	100 x 100 x 100 900 x 1500 x 900 typically 650 x 550 x 450
Layer thickness [μm]	10 - 200, typically 50	50 - 200	100 - 1000, typically 400
Build rate [cm^3/h]	1 - 100, typically 20	55 - 80	30 - 180, typically 100
Part accuracy [mm] over 100 mm	± 0.02 - 0.1, typically ± 0.05	± 0.2	± 0.1 - 0.5, typically ± 0.3
Detail capability [mm]	< 0.1 - 0.3, typically 0.1	0.25	0.5 - 1.0, typically 0.6
Maximum part density	99 -100 %, typically 99.5 %	approx. 100 %	99 -100 %, typically 99.5 %
Part surface finish Ra [μm]	3 -20, typically 10	10 - 20	4 - 9, typically 7
Laser/beam power [W]	50 - 1000, typically 400	50 - 3500	300 - 4000, typically 1500
Laser/ beam spot size or deposit width [μm]	10 - 700, typically 100	180 - 1000	600 - 4000, typically 1800
Maximum scan speed [m/s]	2 - 15, typically 7	8	0.06 - 0.17, typically 0.10
Protective gas	Argon or Nitrogen	none (vacuum)	Argon or Nitrogen, typically Argon
Approximate price [$Euro$]	120000 - 1500000, typically 500000	630000	230000 - 1000000, typically 600000

The Table 1.1 compares the additive technologies for the production of metal components on the market. These are the results of a survey on the machines

currently available in the world market. Since only established technologies were considered, the comparison was conducted between the Laser PBF, electron beam PBF, and DED laser techniques. The production systems and their performance were analyzed on the basis of some parameters considered fundamental to outline the state-of-art of AM metal technology. As for the Laser PBF and DED processes, since the machine manufacturers are numerous, the ranges of variation and the typical value of each variable are indicated, deriving from the study of the different devices marketed. It is clear that the working volumes of the AM systems are usually limited; however, many machine manufacturers have more recently introduced larger systems in order to meet market needs. There are also small systems for the production of parts for the dental and goldsmith sectors, which require higher component quality than the one typically obtained for metal AM components. DED laser technology requires energy beams whose power is significantly higher than the one adopted in PBF processes and is characterized by greater productivity. The power of the electron beam that Arcam uses can be adjusted over a wide range; consequently the building speed is variable, with values that are between those of the laser PBF and the DED technologies.

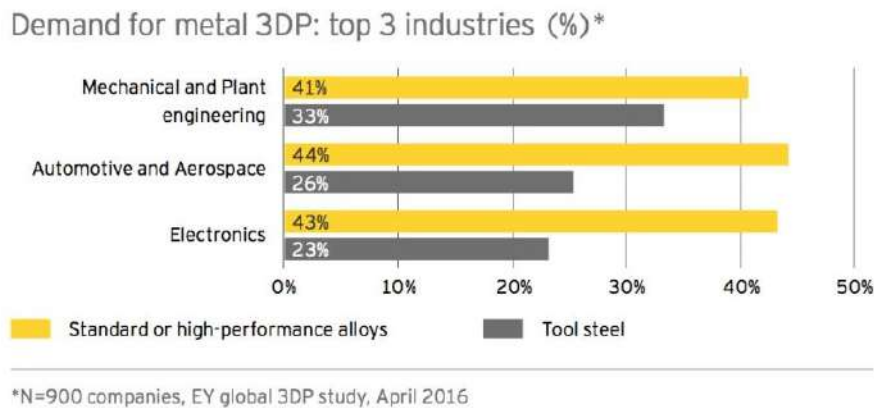


Figure 1.8: Request for components produced for AM divided by each sector [51].

From a study conducted by Ernst & Young in 2016 (Fig. 1.8) [51], the mechanical industry appears to be the most interested in the production of AM metal components. The interest is divided between tool steel and high-performance alloys, due to the different applications within this industrial sector. These include the production of tools, dies, molds, machine parts and vehicle components. In the automotive and aerospace sector and in the electronics sector, the demand for standard and high-performance alloys is even higher, because these materials are used in the production of end components. On the contrary, the interest in tool steels in these sectors is much lower, suggesting that the main objective is the production of final part, rather than the production of related equipment.

1.3.1 PB costs evolution

The analysis conducted on the market landscape of AM starts with an assessment of the number of components produced with this technology starting from 2011 until 2016, and continues with an extended estimate up to 2021, as shown in Figure 1.9. The increase in the number of pieces produced with laser additive technology is very high and is equal to 86 % from 2011 until 2021, with only 24 % for the period 15-21. An increase in this type presupposes a very rapid evolution of technology, an increase in productivity, power and variety of parts that can be produced with machines, including larger components.

Global Production (Unit) of 3D Printing of Metal by Types												CAGR	
	2011	2012	2013	2014	2015	2016E	2017F	2018F	2019F	2020F	2021F	Share	15-21
Selective Laser Melting	84	166	294	426	593	793	1020	1279	1575	1899	2243	85,8%	24,8%
Electronic Beam Melting	14	15	25	35	46	55	73	87	106	126	151	5,8%	21,9%
Other	9	17	29	43	59	76	99	123	148	183	221	8,5%	24,6%
	107	198	348	504	698	924	1192	1489	1829	2208	2.615	100,0%	24,6%

Global Revenue (M USD) of 3D Printing of Metal by Types												CAGR	
	2011	2012	2013	2014	2015	2016E	2017F	2018F	2019F	2020F	2021F	CAGR	15-21
Selective Laser Melting	60,2	120,5	212,9	306,7	418,5	546,7	676,4	825,7	998,0	1183,7	1356,6	36,6%	21,7%
Electronic Beam Melting	12,6	16,3	23,4	39,8	51,2	60,0	77,0	88,8	104,2	121,0	140,2	27,2%	18,3%
Other	5,4	10,0	16,6	23,9	31,9	40,1	50,8	61,6	72,2	86,9	102,4	34,2%	21,4%
	78,2	146,8	252,8	370,3	501,6	646,9	804,2	976,0	1174,4	1391,6	1599,2	35,2%	21,3%
YoY		87,7%	72,2%	46,5%	35,5%	29,0%	24,3%	21,4%	20,3%	18,5%	14,9%		

Figure 1.9: Increase in the number of pieces made with additive technologies from 2011 to 2021 [132].

A forecast of the trend of these factors was made by Roland Berger in 2013 with forecasts up to 2023 [11]. Based on this study it can be said that the costs of AM can be reduced by 50 % within the next 5 years, if the AM system providers will be able to quadruple the speed of construction and improve the stability of the process [11]. The margins for this increase in speed to occur are very wide, as the number of dead times in the process is very high. The time for spreading the powder, e.g., is a dead time from the point of view of productivity, compounded by the fact that many machines provide more than one passage of the recoater for the drafting of each layer. From Figure 1.10 it is possible to see the trend of the AM cost from 2013 to 2023, going from 3.1 €/cm² to 1.1 €/cm²; there can actually be a net reduction in costs.

In general the cost of the machine is destined to rise, but in a much lower way than the productivity does (the speed goes from 10 to 80 cm³/h); consequently a significant lowering of the ratio between machine cost and productivity can be foreseen. The price of the powder (in this analysis stainless steel powder was used) is destined to decrease from a 2013 price of 89 €/kg (it is an average of

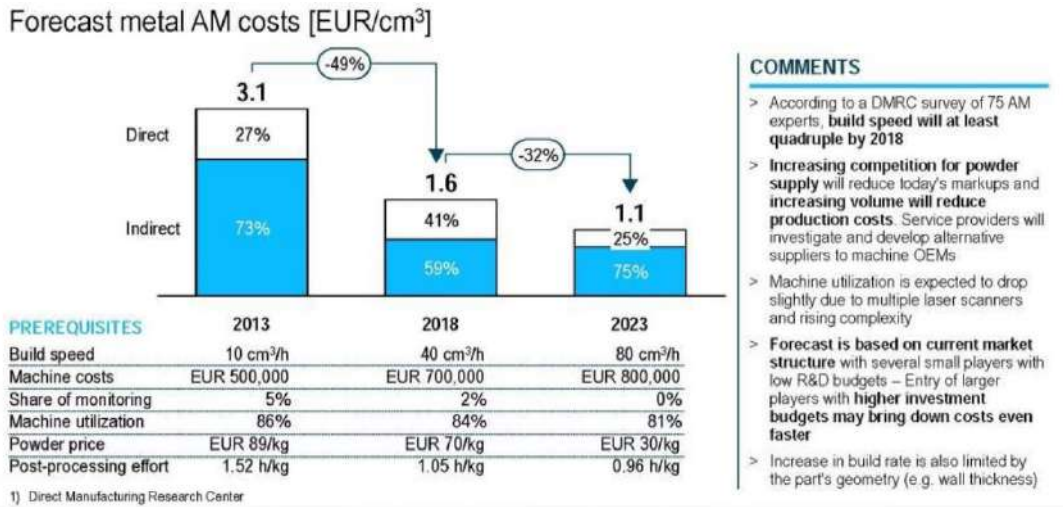


Figure 1.10: Evolution of AM production costs from 2013 to 2023 [11].

Current metal AM costs under series production conditions

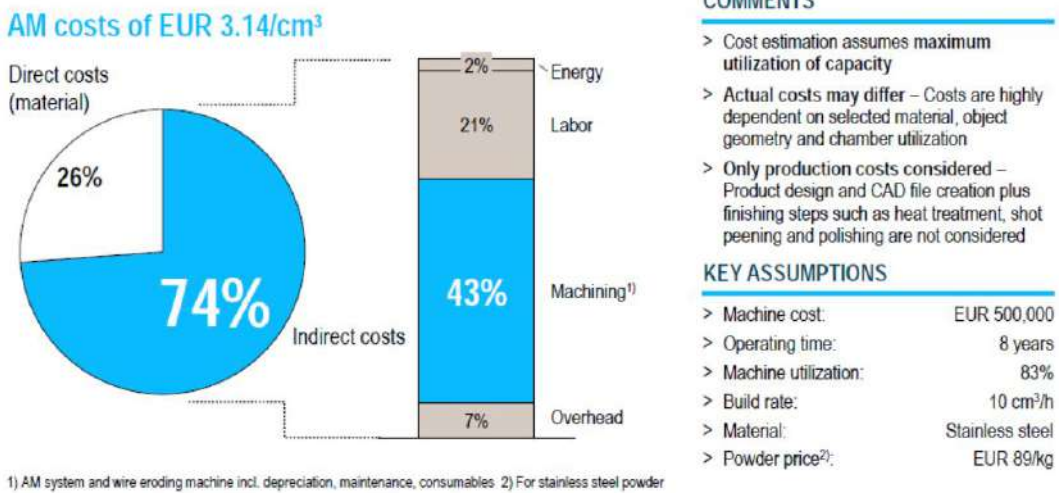


Figure 1.11: Subdivision of additive production costs updated to 2013 [11].

the powder prices obtainable on the market) to 30 €/kg in 2023; this is mainly due to the untying of the machine from the powder supply, also due to the entry of new players among the producers of metal powders. Furthermore, the trend of future machines will be oriented to widen the granulometric and morphological tolerance of the powders, succeeding in guaranteeing optimal drafting performances even with powders with less regular geometries. This will reduce the number of

unsuitable powders to the process with a consequent reduction in the price. Post-processing will see a reduction in the hours of work required due to an increase in the automation of the process.

The cost of production of AM components updated to 2013 is divided as shown in Figure 1.11: 26 % of the total is attributed to direct costs (the material used), while 74 % is due to indirect costs. Indirect costs include the following components: only 2 % due to the energy required for the process, 21 % of labor, 43 % between maintenance, consumables and depreciation of the machine and 7 % of overhead. All the present evaluations have been made on the basis of stainless steel powder and can vary considerably using another material. They also refer to a full load use of the machine, making full use of the capacity of the working chamber.






PARAMETERS	TREND	RATIONALES
Build rates		<ul style="list-style-type: none"> > The application of energy (laser power) per focus point is limited by the process parameters, so the introduction of two and more laser systems (e.g. SLM Solutions) seems the most promising alternative > Optimized layer structure with different layer thicknesses > Process parallelization by simultaneous powder dispensing and laser melting > Optimization of powder dispensing process (e.g. powder dispensing from both directions) > Introduction of two or more chamber systems, continuous production > Increased process stability due to online monitoring systems
Machine prices		<ul style="list-style-type: none"> > Current machine prices seem to be accepted by customers > Increasing addition of process and quality control electronics as well as number of lasers will raise the machine price, partly offset by economies of scales
Powder prices		<ul style="list-style-type: none"> > Powder prices set by AM system providers do not reflect production costs > With increasing market volume, metal powder producers will sell to end customers directly > Furthermore, production costs for high-quality powder will fall with increasing volume > Total AM material consumption is expected to increase from 900 t to 9,000 t by 2023
Labor costs		<ul style="list-style-type: none"> > Reliable systems will reduce effort for monitoring and troubleshooting > Introduction of systems with automated removal of excess powder
Chamber volume		<ul style="list-style-type: none"> > Chamber volumes are currently not perceived as the limiting factor > Problems with process reliability will keep chamber volume increase at a moderate rate

Figure 1.12: Expected developments for the years after 2013 [11].

Figure 1.12 lists the future trends forecast for 2013 for the following years and the advent of some of these developments has already occurred; an example is the multi-beam, made by SLM Solution first with a double-beam and then with a four-beam. Another interesting perspective is the adaptive layer in thickness, because, according to the needs of the piece, thinner and thicker layers can be made. An evolution is foreseen that reduces the dead times of powder deposition, making the melting and deposition processes faster. These developments can lead to better monitoring of the process so as to identify the defect in the piece during its fabrication and then stop the work before the conclusion, avoiding material and time losses. Furthermore, layer-level monitoring must be used appropriately, as poorly fused and defective areas in a layer can be repaired during the remelting to create the next layer. From the point of view of the powder market, there will be a lowering of prices due to: i) the direct relationship between powder producers and users, ii) the reduction of the cost of high quality powder and iii) the increase

in production volumes. Furthermore, automatic systems will be produced for the introduction and extraction of powder in the machine, reducing the manual work and therefore the risks associated with this phase.

1.3.2 Work chamber size and weight

The PBF technology was originated from the need to produce prototypes and still allows the realization of components with limited dimensions. This limit is due to the difficulty in managing the residual stresses that characterize large pieces. This is much more evident for processes that use the laser as a melting beam and that operate a low pre-heating of unmelted powders. By creating the component layer by layer, the sections of the layers are melted as indicated by the model. The melted section begins to cool quickly in the areas in contact with the unmelted powders, while the central area maintains a high temperature for a longer time. Inside the piece the thermal gradients are formed between the central area and the external one. These thermal gradients lead to the deformation of the component that is produced. The supports, that connect the piece to the plate, prevent the deformation of the component, but involve internal stresses of the piece, creating a balance of forces between the base, the supports and the piece. If the size of the object is high, the resulting thermal gradients will be greater and the magnitude of internal stresses will increase. For this reason, components that are too large are difficult to produce with the laser PBF technology, as high internal stresses can lead to the breaking or the distortion of the piece.

The problem of excessive internal stresses is less serious if the PBF technology with electron beam is used. In EBM technology the beam pre-heats much more the unmelted powders and the thermal gradients in the piece are much lower. For the same reason the supports are present, but in smaller quantities than the SLM technology. As shown in Table 1.2, the evolution of the machines experienced the progressive increase in the size of the building chamber both on the X-Y plane and along the Z axis. The further increase in the size of the machine is one of the main objectives of the coming years, as it would bring the additive market to components that are currently produced only with traditional technologies due to the large size. The goal is to produce larger pieces, so the market for larger machines is expanding. Two fundamental aspects for increasing the size of the building chamber, in accordance with the feasibility of the components, are: i) the realization of a hot process with high powder bed pre-heating, which limits the internal stresses of the piece during production, and ii) a preferential development of the chamber along the Z axis. The growth of the pieces with the largest dimension along the Z axis limits the tensions between the external surface and the core of the piece in each layer. So, the thermal gradients are lower and this lead to lower internal stresses. Machines with larger building chambers that produce larger pieces also require equipment suitable for all production-related operations. The

Table 1.2: Building chamber size of the PBF machines currently on the market.

Manufacturer	Model	Year	Building chamber size X * Y * Z [mm^3]
EOS	M100* [47]	2015	100 x 100 x 95
EOS	M290 [48]	2014	250 x 250 x 325
EOS	M400/M400-4 [49]	2016	400 x 400 x 400
SLM Solutions	SLM 125 [154]	x	125 x 125 x 125
SLM Solutions	SLM 280 [155]	x	280 x 280 x 365
SLM Solutions	SLM 500 [156]	2012	500 x 280 x 365
Concept Laser	Mlab Cusing 200R [94]	2012	100 x 100 x 100
Concept Laser	M2 Cusing/Multilaser [93]	2014	250 x 250 x 280
Concept Laser	X LINE 2000R [95]	2015	800 x 400 x 500
3D System	ProX DMP 100 [162]	x	100 x 100 x 100
3D System	ProX DMP 200 [163]	x	140 x 140 x 125
3D System	ProX DMP 300 [164]	x	250 x 250 x 330
3D System	ProX DMP 320 [165]	x	275 x 275 x 420
Sisma - Trumpf	MYSINT100 [150]	2014	Φ 100 x 100
Sisma -Trumpf	MYSINT300 [151]	2016	Φ 300 x 400
Renishaw	RenAM250 [135]	2012	245 x 245 x 300
Renishaw	RenAM400 [136]	2015	245 x 245 x 300
Renishaw	RenAM500 [137]	2015	250 x 250 x 350

extraction of the plate with the unmelted powder and the piece produced is often performed manually by an operator who provides for the following separation of the parts. As the dimensions and the weight of the components produced increase, it is necessary that these operations are no longer carried out manually, but with the use of automatic instrumentation, which, in addition, makes the process safer and faster.

1.3.3 Productivity

The productivity of AM machines is expressed as built rate, that is the ratio between the quantity of material produced by the machine and the time required to produce it (cm^3/h). Today, the PBF machines have an average built rate of 5-20 cm^3/h [\[11\]](#). The built rate values for some PBF machines currently on the market are summarized in [Table 1.3](#). The table indicates the maximum build rate values, but the productivity levels also depend on the type of material and its characteristics, such as the specific heat, the latent heat of fusion, the density and the flowability of the powder.

Table 1.3: Build rate of some PBF machines currently on the market.

Manufacturer	Model	Max build rate [cm^3/h]
EOS	M280/M290	26.6
EOS	M400/M400-4	105
SLM Solutions	SLM 125	25
SLM Solutions	SLM 280	55
SLM Solutions	SLM 500	105
Concept Laser	Mlab Cusing 200R	5
Concept Laser	M2 Cusing / Multilaser	20-35
Concept Laser	X LINE 2000R	120
Sisma - Trumpf	MYSINT100*	5
Sisma - Trumpf	MYSINT300*	25
Renishaw	AM250/AM400	20

*circular building platform

The tendency of the market is clearly to increase the productivity of PBF machines. In order to do this, it is necessary to speed up all the phases that make up the process. The process is made up of three main stages [146]:

1. The time required for the deposition of the powder;
2. The time required for powder fusion;
3. The time required to reset the machine at the end of the process.

The fusion of the powder depends on the amount of energy to be supplied to the material during the process: as the power supplied to the system increases, the material will melt more quickly, making the whole process shorter. The energy density E [J/mm^3] supplied by the laser to the powder bed depends on the laser power P [W], the laser speed v [mm/s], the hatch distance h [mm] and the thickness of the powder layer t [mm], according to the equation 1.1 [158].

$$E = \frac{P}{vht} \quad \left[\frac{J}{mm^3} \right] \quad (1.1)$$

In order to reduce the melting times, the laser power can therefore be increased, passing from the 400 W of the machines already present on the market to the 1 kW power of the new machines. Alternatively, multi-laser systems can be used: in some machines up to four lasers and scanners are already present. For example, systems equipped with two laser systems have a productivity increase of a factor of 1.8 [11].

The melting of the powder layer is followed by the recoating phase of a new powder layer. This must be smooth and regular and must completely cover the

previous layer. The first commercialized systems for creating powder layers included the presence of only one powder container and a blade that distributes the powder on the building platform. This system slowed down the process, because at each cycle the blade had to return to the starting position to collect new powder to distribute the new layer: the return travel of the recoater was a dead time. Subsequently various solutions were proposed to limit this dead time. In Figure 1.13a a system with two containers of powder on the sides of the building platform is schematized: these allow to distribute the powder in both directions and to exploit every passage of the recoater on the building platform, eliminating the dead time of return. In Figure 1.13b another variant is illustrated: the system consists of a hopper above the building chamber that contains the powder. The powder is deposited from the hopper in front of the blade, that creates a new layer. In this way the powder reserve is separated from the working area and this allows the container to be refilled easily.

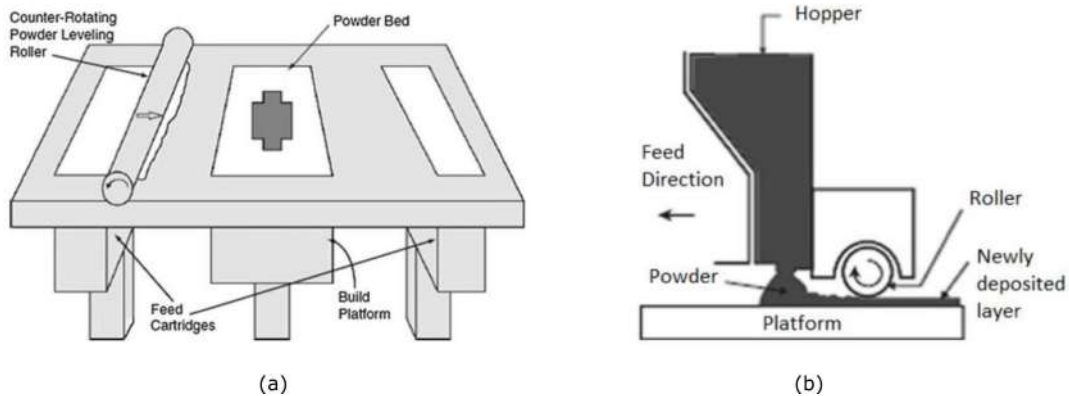


Figure 1.13: Powder distribution systems with a) two containers and b) a hopper [159].

Current market research is therefore aimed at further increasing the overall speed of the production cycle by acting on the recoating time. This can be achieved with innovative powder distribution systems, but also with the choice of good quality powders with good flowability.

Once the process is finished, the working chamber is extracted manually by an operator, who removes the excess powder inside the chamber, obtaining the finished component. At the end of this procedure, the operator prepares the work chamber for the next job. This process carried out for each job takes a remarkable amount of time (about 2 hours) which leads to an increase in costs. Particularly in the case in which large components are produced, the transport and manual management of large volumes is quite complex. The automation of the machine reset phases is certainly a productive choice, which drastically reduces downtime. The operator only carries out the task of starting and monitoring the process, while the room

loading and unloading procedures are automated. In this way it is also possible to guarantee the management of considerable weights, obtain greater freedom in the choice of volumes and materials and guarantee a high level of safety during the process.

1.3.4 Process monitoring

The current level of monitoring and control in L-PBF production systems is not yet such as to meet the stringent requirements for mass production of metal components for AM, especially in the aerospace and biomedical sectors, where a high level of quality of the final product is required. Despite the rapid evolution of technology, robust process monitoring is not currently available, as is closed-loop process control. Those who are already beginning to adopt mass production technologies must rely on knowledge and experience to keep component production at constantly adequate levels. Nowadays, the main manufacturers of AM machines are rapidly developing sensor technologies for process control, already present in their latest prototypes, to maintain the quality and production of components at the levels required by today's market [40]. Process control in L-PBF systems is focused on the two most critical technological aspects [117]:

- the detection of a non-homogeneous deposition of the powder bed (powder bed defects) during the recoating process;
- monitoring of the melting point (melt pool) generated as a result of localized powder melting.

Table 1.4 lists the control systems used by the major AM companies.

Table 1.4: Main control systems for the powder bed defects and the melt pool temperature.

Manufacturer	Control for powder bed defect	Control for melt pool
Concept Laser	QM (Quality Management) coating	QM meltpool
SLM Solution	Layer Control System	Meltpool Monitoring
EOS	EOSTATE PowderBed	EOSTATE MeltPool

PBF defects control

The detection of imperfections in the formation of the powder bed takes place by high-resolution video cameras and software for digital image analysis. The control system compares the images acquired before and after recoating, identifying the presence of areas with a powder content different from the optimal value. If such defects are present, the system automatically corrects itself, repeating the recoating

with the appropriate amount of powder, and proceeds by depositing the next layer. For simple geometry components, the SLM Solutions Layer Control System allows to analyze a single image dividing it into several parts, detecting process errors with greater sensitivity. EOSTATE PowderBed, instead, acquires two images of the entire deposition for each layer, filing them in sequence in a flip-book. Adding the data acquired in each single layer, it is possible to obtain, through a 3D model, a feedback on the quality of the final product and any production defects (e.g. segregations, inclusions, dust agglomerates and porosity) [46].

Melt pool control

The Melt Pool Monitoring (MPM) control process is aimed at localized monitoring of the temperature on the deposition layer after exposure to the laser. Information on the melt pool temperature and any anomalies in the melting process are obtained from thermal maps, which the control software returns at the end of the monitoring process. QM Meltpool by Concept Laser detects thermal radiation in the infrared coming from melt pool by a photodetector diode and a high resolution video camera, coaxial (on-axis) to the optical path of the laser. The system returns extremely precise thermal data on each melt pool by exploiting the narrow field of observation of the video camera used (1 mm^2) [170]. The operating principle of Melt Pool Monitoring by SLM Solutions is completely similar to the previous one. In this case, the detection of infrared radiation emitted by the melt pools occurs through two off-axis sensors [145]. In EOSTATE MeltPool, instead, there are two photodiode sensors allocated in the machine with different configurations. These detect the thermal emissions from the samples in the chamber. The analysis of the data, processed with special software, allows to obtain the thermal mapping of the surfaces [46].

1.3.5 Inert gas management

In the SLM technology, an inert atmosphere in contact with the material is used during the process. This atmosphere prevents the material in the working chamber from oxidizing or reacting at high temperatures. Currently, the most used inert gas is Nitrogen, which is less expensive than Argon. For some materials, e.g. titanium alloys, Nitrogen is reactive, and it is therefore necessary the use of Argon. Generally the machines are set up to use both gases and some ones, like Renishaw machines, have a gas recirculation system.

Table 1.5: Inert gas management for PBF machines currently on the market.

Manufacturer	Model	Nitrogen	Argon	Consumption [L/min]
EOS	M100	External	External	-
EOS	M280/M290	Integrated	External	-
EOS	M400/M400-4	Integrated	External	-
SLM Solutions	SLM 125	External	External	2
SLM Solutions	SLM 280	External	External	2.5
SLM Solutions	SLM 500	External	External	5-7
Concept Laser	Mlab Cusing 200R	External	External	0.8
Concept Laser	M2 Cusing / Multilaser	External	External	17
Concept Laser	X LINE 2000R	External	External	17-34
3D System	ProX DMP 100	External	External	5-10
3D System	ProX DMP 200	External	External	5-10
3D System	ProX DMP 300	External	External	10-15
3D System	ProX DMP 320	External	External	-
Sisma - Trumpf	MYSINT100	External	External	0.3
Sisma - Trumpf	MYSINT300	External	External	-
Renishaw	AM250/AM400	External	External	-
Renishaw	RenAM500M	External	External	0.5

It is possible to choose whether to buy Nitrogen in cylinders, as liquefied gases or to equip the machine with an air-Nitrogen separator on board the machine powered by compressed air from the workshop (6 bar). The use of these inert gases does not entail serious health risks, as they are not toxic, but it is mandatory to follow certain rules to maintain safety. Argon and Nitrogen, if released into a small environment, can excessively lower the oxygen concentration in the room and cause hypoxia. Many machine manufacturers provide external gas management, while others, such as EOS, prefer an integrated supply powered by compressed air (Table 1.5). The choice is often linked to the industrial configuration of the purchaser of the machines. Who intends to install the machines in an industrial infrastructure where compressed air already exists or liquefied technical gas tanks for other processes will prefer a solution with integrated power supply, without adding to the machine cost for unnecessary ancillary equipment.

1.3.6 Powder management

An important aspect of AM machines is the management of powders: most of the machines, as resumed in Table 1.6, proceed with a manual feeding of the material. Instead, the newer models tend to have an automatic feeding system.

Some machines, e.g. SLM Solution SLM500, provide an automatic system in which, at the end of the process, extraction, sieving and feeding of the powders take place all in the same equipment. A system of this type affects the reliability of the overall system since the operation of the machine also depends on the powder management system. The next machines will have an automatic and independent powder feeding system, in order to reduce the contact of the material with a non-inert atmosphere and reduce the dead time for filling the hoppers.

Table 1.6: Powder management for PBF machines currently on the market.

Manufacturer	Model	Powder management
EOS	M100	Manual
EOS	M280/M290	Manual
EOS	M400/M400-4	Manual
SLM Solutions	SLM 125	Manual
SLM Solutions	SLM 280	Manual
SLM Solutions	SLM 500	Automatic
Concept Laser	Mlab Cusing 200R	Manual
Concept Laser	M2 Cusing / Multilaser	Manual
Concept Laser	X LINE 2000R	Automatic
3D System	ProX DMP 100	Manual
3D System	ProX DMP 200	Manual
3D System	ProX DMP 300	Automatic
3D System	ProX DMP 320	Semi-automatic
Sisma - Trumpf	MYSINT100	Manual
Sisma - Trumpf	MYSINT300	Manual
Renishaw	AM250/AM400	Manual
Renishaw	RenAM500M	Automatic

1.3.7 Materials and powder

The metals currently used for L-PBF include fewer alloys than the materials currently used in traditional technologies, and temporarily satisfy the needs of some particular sectors. Cobalt-Chromium and Titanium alloys, for example, are widely used in the biomedical and aerospace fields, while precious metals are used in jewelery. For each alloy used, process parameters were chosen on the machines such as: scanning speed, laser power and spot size. The following materials are the alloys that are currently treated by PBF machines on the market [44].

- Tool steels and maraging steels: this category of materials refers to steels with variable carbon content particularly suitable for tools, due to their high

hardness, resistance to abrasion and deformation and high cutting capacity even at high temperatures. H13 is a chromium tool steel for hot working, workable with PBF technology, often used for making tools and molds [125]. Another steel used for tools is the Maraging 300, a resistant, hard material with high dimensional stability; its high hardness derives from the precipitation of intermetallic complexes rich in nickel, cobalt and molybdenum [134, 9, 176].

- **Stainless steels:** stainless steels have a higher chromium percentage than carbon steels (at least 10.5 %) and present a greater corrosion and oxidation resistance. The most used stainless steel in PBF is 316 L, an austenitic steel used in a wide range of temperatures [59]. Its applications range from the aerospace sector to the biomedical sector and the food sector. 15-5PH is a maraging stainless steel with high corrosion resistance, high hardness and without the ferritic phase inside. Widely exploited in the aerospace, petrochemical and chemical, food and metal processing sectors [14]. Another maraging stainless steel used in AM is the 17-4PH, a material with excellent strength and hardness up to 315 °C [185, 18, 141]. 17-4PH presents different properties depending on the heat treatment carried out [2].
- **Titanium alloys:** the main titanium alloy treated in AM is the Ti6Al4V alloy, which shows an excellent resistance, a high hardness, a great resistance to corrosion, a low specific weight and a good biocompatibility [22, 140]. These features make this alloy suitable for the aerospace and the racing fields and also for the biomedical sector. The Ti6Al4V grade 5 alloy is used for a great variety of applications, while the same alloy, but grade 23 (ELI: extra-low interstitial) has a very low concentration of interstitials and is used for dental and medical implants [116]. The TiAl alloy, mainly used in the aeronautical sector, is made only with EBM technology. It shows excellent mechanical characteristics that make it suitable for the production of parts with critical functionality such as aircraft turbine blades [77].
- **Aluminum alloys:** Al alloys are used in L-PBF technology due to their melting point at a relatively low temperature (about 600 °C). Furthermore the use of these alloys with EBM results in a strong evaporation under vacuum. The two alloys currently processable are AlSi12 and AlSi10Mg; they are the optimal solution for a wide range of applications that require good thermal properties of the material, combined with a low density [101, 19]. Due to the high reflectivity of the Al, the fusion process with the laser of these alloys presents many difficulties, but the optimization of the parameters of the AM machines allows the realization of components with these materials.
- **Nickel-based alloys:** superalloys are widely exploited for their unique characteristics that combine high tensile strength, creep resistance, fatigue corrosion

and thermal fatigue. The first superalloy produced for AM was Inconel 625, good for applications at high temperature up to 815 °C, only up to 595 °C if the exposure is prolonged, while the resistance to corrosion remains excellent up to 980 °C. This material is used in low temperature applications such as chemical processes, in contact with sea water, in corrosive environments, or for high temperature applications such as aerospace and high temperature chemical processes [87, 177]. Other superalloys processed with SLM technology are Inconel 713, with excellent mechanical resistance up to 927 °C, Inconel 718, with high mechanical resistance and corrosion properties up to 650-700 °C and available for cryogenic applications, and the Inconel 738, often used in gas turbines for its good creep resistance up to 920-980 °C, combined with the possibility of exposing it for long periods to corrosive environments [188, 97]. The last superalloy commonly used in AM is Hastelloy X, that presents high mechanical and oxidation resistance up to 1200 °C; it is widely used in the aerospace sector for gas turbine parts and for areas where combustion takes place. Its high resistance to corrosion allows the use of this material in the petrochemical, chemical and industrial furnaces sectors [98, 172].

- Cobalt-Chromium alloys: these alloys are characterized by high mechanical resistance and corrosion, exhibit a non-magnetic behavior and a good biocompatibility [5, 122, 21]. The main alloy processed with AM is the Co28Cr6Mo, used in the surgical and biomedical field due to the biocompatibility and the complete absence of Nickel. This material is also used in the aeronautical field and jewelry industry.
- Gold and platinum: materials used in PBF for the creation of jewels and personalized precious objects.

In the near future, copper alloys, which have high reflectivity and therefore difficulty in their treatment and in the choice of parameters, can be introduced in the list of materials that can be used with SLM technology. The future perspective in the field of materials for AM will certainly be the increase in the number of alloys and treatable materials.

All materials used in PBF technology must be in the form of powders, in order to realize thin layers to form a powder bed. The powders produced for AM must have a controlled chemical composition, a granulometric range with dimensions typically between 10 and 100 μm and a preferably spherical morphology that guarantees a good flowability. The shape and particle size of the particles have a major influence on the density of the powder bed and therefore on the parameters necessary to obtain a component without defects and porosity.

The morphology of the powders is closely linked to the production technique: atomization. The most common and economic technique is water atomization, in

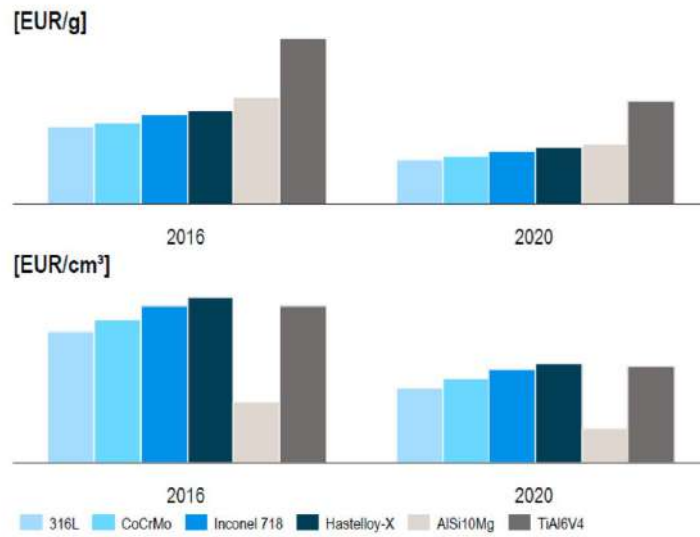


Figure 1.14: Analysis of the evolution of the powder price of the various metals up to 2020 [11].

which a jet of pressurized water impacts the molten metal causing a rapid solidification in irregularly shaped powders. However, this shape is not good for AM, which prefers spherical granules. Indeed, they allow the production of uniform layer of powder. Spherical particles reduce the spreading time of the layer and increase the density of the bed. To obtain such shapes, the gas atomization is preferred: the metal is melted and passed through a nozzle that forms liquid drops. The compressed inert gas meets the metal drops and causes their solidification. Once solid, the powders are collected in the gas atomizer. An important aspect will be the tendency to create machines that can use powders even with the most irregular geometry, lowering the cost of the material. It is also expected that there will be a significant reduction in powder costs for all materials (Figure 1.14).

1.3.8 Design for Additive Manufacturing

One aspect of the technology that will be further expanded by the companies that produce components is the dedicated design. The additive techniques, in particular the PBF ones, offer different advantages to the design, one of the most important is the freedom in the choice of the shape.

The production with layer-by-layer mode allows very complex shapes to be made without increasing the cost of the piece. Furthermore, the absence of additional tools makes possible to create custom-made components at almost the same cost as standard products. This makes possible to produce lightweight components without penalizing mechanical performance and to use structures, such as trabeculars,

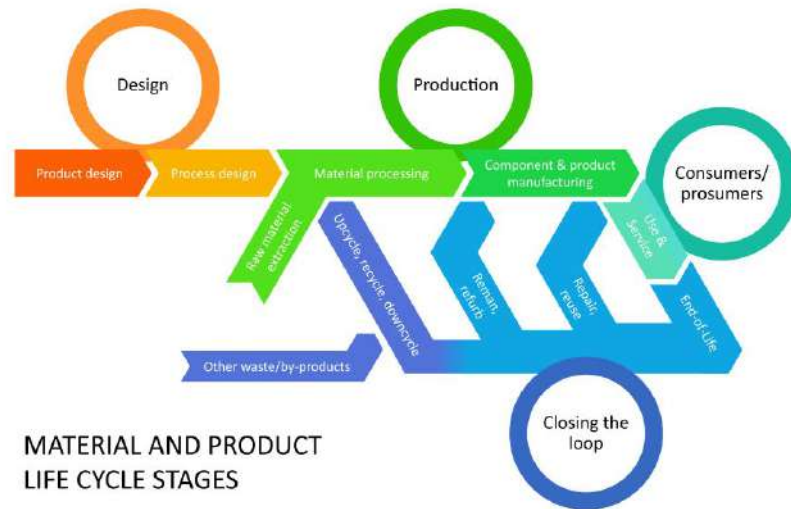


Figure 1.15: Life cycle scheme for a component produced with AM technology [39].

that are impossible to achieve with other technologies. Design freedom is not limited to form, but also to the types of materials to be used. The AM is open to experimentation with new alloys and innovative materials. Moreover, all additive technologies give the possibility to recover the material not used in the production, greatly reducing the quantity of the scraps. This has a positive impact on both the cost of the component and the ecological point of view [30]. To understand and evaluate the real advantage of switching from a traditional technology to an additive one, all the aspects listed must be taken into account and applied to the specific case study. A component produced with traditional technology must be analyzed and redesigned both in its form and in the material chosen. The life cycle that allows the greatest advantages of AM technologies to be exploited is shown in the Figure 1.15.

Designing a component for PBF can have different purposes depending on the case study. A very common situation is one in which a company decides to start producing a component, previously made using conventional technology, with an AM technology. Producing the piece with the same shape would not be completely advantageous, since it should be redesigned. This allows maintaining or improving its mechanical properties, lightening it considerably and sometimes reducing the number of parts from which it is composed. The redesigned component has a different shape and uses less material: this means that it is lighter and faster to produce. The design can be re-started from the beginning by the computer-aided design (CAD), or a topology optimization software can be used, combining CAD and finite element analysis (FEA). The chosen component is loaded into the software and the constraints and loads are applied [96, 114]. They are the stresses which the piece must withstand during its use. A FEM (finite element method)



Figure 1.16: Aerospace bracket produced with SLM technology after topological optimization [52].

analysis is carried out on the component and stressed areas are highlighted. The optimization is aimed at eliminating or reducing the areas of the component that are not subjected to stresses in order to make it lighter. One of the most used topology optimization software is SolidThinking Inspire. The program allows to choose the type of optimization preferred [128]. It is possible to opt for mass reduction if the goal is to minimize the component costs, or to maximize stiffness if the goal is to improve the mechanical characteristics of the piece [113, 42]. Another strategy to lighten the components is to resort to trabecular or lattice structures: they allow maintaining excellent mechanical properties of the component despite the high degree of vacuum, moreover they are excellent as impact absorbers [64]. Figure 1.16 shows an example of a component produced with traditional technology and then re-designed with three different topology optimization strategies.

1.4 Choice of material: aluminum alloys

Aluminum alloys are materials suitable for different applications in various types of industries such as aerospace or automotive [17]. In fact, they have excellent mechanical properties, combined with low density, low cost and excellent thermal conductivity. They allow the creation of cellular fillings capable of absorbing the impact and lightening the structures: these structures are easily achievable with L-PBF technology. Figure 1.17 shows a classification of the Al alloys and the fields in which they are commonly used.

The workability of aluminum alloys in traditional forming technologies can be difficult, and is only allowed by the addition of elements that improve their characteristics. Some of these elements are not necessary to process Al alloys with L-PBF

Form	Designation	Alloy Constituents and heat-treat-ability	Key Properties	Examples for Applications
Cast	Special	Si + Mg, Cu, Zn	HT Low solidification shrinkage, good fluidity, good weldability, & high corrosion & wear resistance	Used in aircrafts and automotive parts, internal combustion engines' pistons and Diesel engines
	1xxx	-	Non-HT Excellent corrosion resistance & workability High thermal & electrical conductivity	Used in general purposes, electrical applications, food packaging, chemical & petrochemical applications, & building components
Wrought	2xxx	Cu + Cu, Fe, Mn, Zn, Zr	HT High strength & toughness Low corrosion resistance - unweildable	Used in the aircraft industry, weapon manufacturing, rivets, & sports equipment
	3xxx	Mn + Cu, Mg, Si, Fe	Non-HT Moderate strength & good workability	Used in general purposes, building sheets, domestic electrical appliances, heat exchangers & cooking utensils
	4xxx	Si + Fe, Cu, Mg, Mn	Non-HT Lower melting point	Used for welding wires & brazing alloys
	5xxx	Mg + Mn, Si, Fe, Zn	Non-HT Moderate to high strength, good weldability and corrosion resistance	Used in building & construction, storage tanks, pressure vessels, electronics, truck bodies, & marine applications
	6xxx	Mg-Si + Zn, Fe, Mn	HT High formability & weldability, excellent corrosion resistance, moderately high strength	Used in architectural, structural, & automotive applications
	7xxx	Zn-Mg + Si, Fe, Cu, Zr, Ag	HT Very high strength, excellent fatigue resistance - highest ageing potential	Used in the aircraft industry, weapons, bolts, transportable bridging, & armour plating.
	8xxx	Otherwise: Sn, Ni, Si, Fe, Li	Non-HT Depending on the alloying element used	Some are used in aircraft wing skins, missile bodies, gas turbine engine components, & pistons & rotating aircraft engine parts

Notes:

- In the alloy designation, the 1st digit denotes the alloy group, the 2nd digit denotes the purity or modifications with the original composition numbered 0 and the modified versions take the numbers 1-9. The 3rd & 4th digits are only meaningful in the case of the 1xxx series as they denote purity but for the rest they only specify a certain alloy.
- Elements greyed out are optional in the alloy's composition.
- Heat treatable alloys can also carry the suffix T followed by a number from 0 to 9 in their designation denoting the heat treatment procedure used.
- There is no widely accepted designation system for cast alloys, therefore they are sometimes given special designations depending on the alloying elements and their contents such as AlSi12 and AlSi10Mg, etc.
- The American system uses different designations for Al alloys in the form of Nxxx where N changes between 1 and 9 denoting the alloy group based on the main alloying element (1:Al, 2:Cu, 3: Si with Cu or Mg, 4: Si, 5: Mg, 6: unmixed, 7: Zn, 8: Sn, 9: other), the following two digits define the minimum Al content in the alloy, and the last digit (after the decimal point) indicates the form, i.e. whether this is a cast or ingot.
- The British system uses different designation in the form of LxMx with no specific sequence for naming the alloys.

Figure 1.17: Aluminum alloys classifications and their common uses in industries [71].

technology and this allows to study a wide range of Al alloys only for AM. The additive production of Al alloys has an excellent effect on the internal microstructure of the components: it is possible to obtain a fine and homogeneous microstructure thanks to the rapid cooling after the fusion, without using chemical modifiers as happens with traditional technologies. However, also the production with L-PBF of components in Al alloys offers various obstacles [4]. One of the main difficulties for processing Al alloys by L-PBF is their high thermal conductivity that causes a difficult management of the fusion, especially in areas where the heat has a limited diffusion due to the shape of the piece. However, the biggest problem is given by the high reflectivity of Al alloys and by the low amount of radiation absorbed in the wavelength emitted by the lasers commonly used for this technology (1.06 μm) [71]. The Al-based powders absorbs only less than 5 % of the laser radiation and reflects 95 %, as shown in the graph in Figure 1.18a: this phenomenon is the cause for the low efficiency of the process.

For now, the only Al alloys that are commonly processed are AlSi10Mg and AlSi12 alloys. The reason is visible from the state diagram of Figure 1.19: their melting point is low and they are very close to the eutectic composition. This allows to have a good behavior during the fusion and to avoid defects like pores and cracks [148].

However, there are many other Al alloys such as 2xxx, 5xxx, 6xxx, and 7xxx series, widely used in aerospace and automotive applications, which are currently very difficult to process with AM [71]. These are materials with excellent mechanical properties, so it would be in high demand. For this reason the L-PBF technology

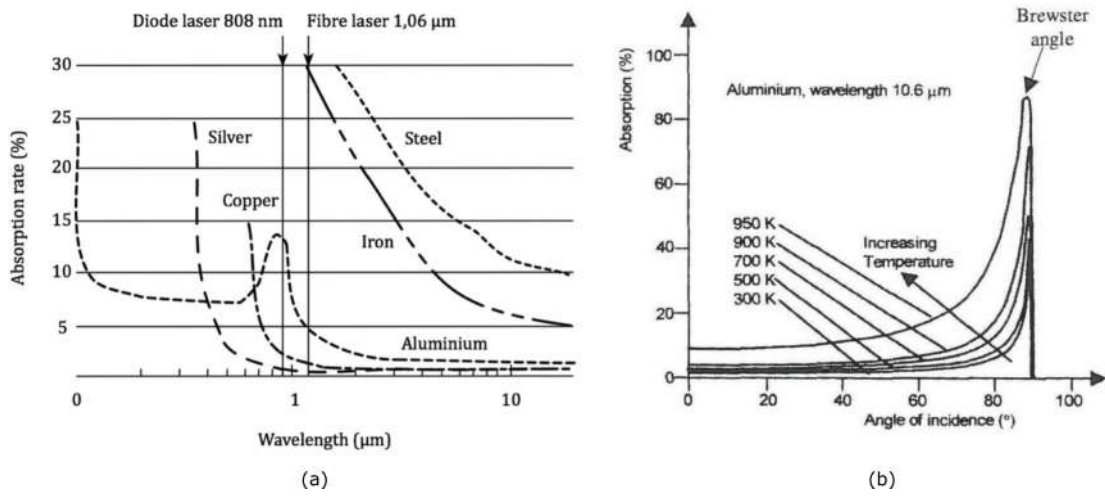


Figure 1.18: a) Absorption rate of different materials varying wavelength [118] and b) absorption of Aluminium by varying the temperature [58].

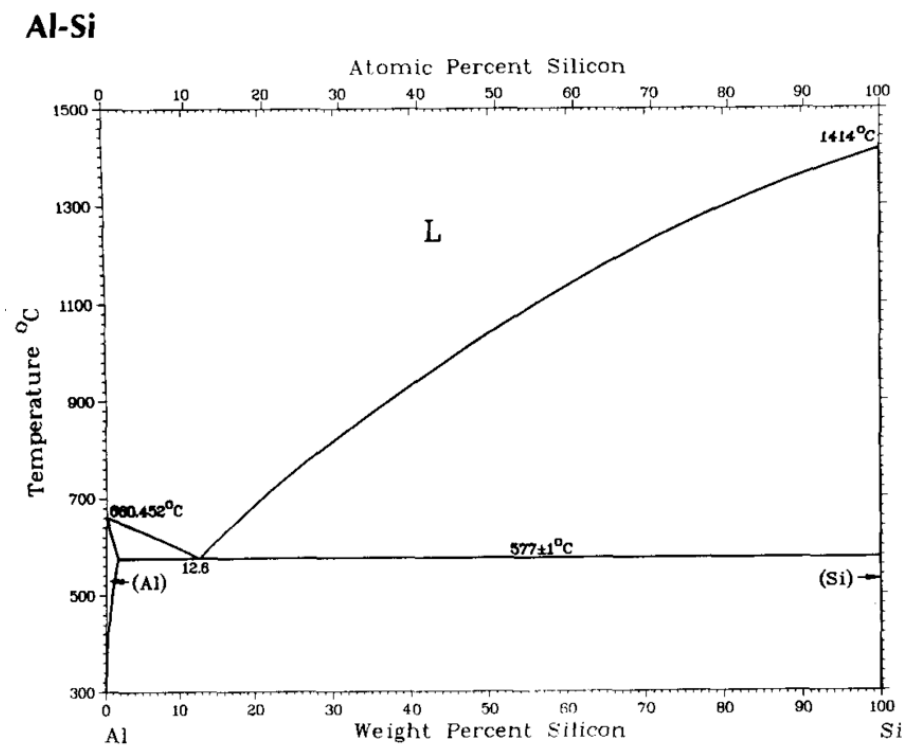


Figure 1.19: Al-Si binary equilibrium diagram [62].

demonstrator produced by 3D New Technologies was studied with particular attention to produce this type of materials. In order to improve the absorption of the laser radiation by Al alloys, an innovative pre-heating system for the powder was

designed. Indeed, from the graph in Figure 1.18b it is possible to see that, with increasing the temperature of the Al alloys, the absorption of the laser radiation is greater. The pre-heating, up to 500 °C, is carried out by the heating resistances in the building platform and by two lamps on the surface of the powder bed.

Chapter 2

LLA400 Machine

2.1 Machine description

To satisfy the need to improve machine productivity, the following areas of intervention were identified:

- Increase the working volume by promoting the growth of the machine dimensions along the Z axis: this allows to contain the deformations and residual stresses of the components;
- Reduce production times by varying the power supplied to the powder, improving the pre-heating and melting functions;
- Improve the thermal conditioning of the piece, in order to reduce the thermal gradient and so the residual tensions;
- Reduce job times by reducing dead-times or non-productive times;
- Reduce the preparation time of the machine between two jobs, adopting architectures compatible with high external automation, in particular for removing and restoring the building chamber and for recovering and recycling powder;
- Integrate the sensor system in the process in order to prevent and reduce the effect of process malfunctions.

After analyzing the solutions of the L-PBF machines currently on the market, the technological areas that could bring the greatest benefits in terms of productivity were defined. This allowed to design an innovative demonstrator that would respond in the best way to the expectations of companies on machines. The innovative L-PBF machine is the LLA400: the abbreviation is explained in the [Figure 2.1](#).

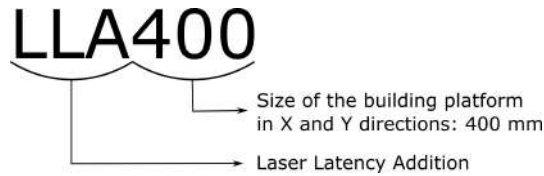


Figure 2.1: Machine name: LLA400.

The name means that the laser only supplies the energy needed to overcome the latent heat of fusion of the metal powder, while the preheating of the powder bed takes place by resistances on the plate and lamps on the upper surface. Figure 2.2 shows the final appearance of the LLA400 machine, explaining how it is composed and where the systems are located.

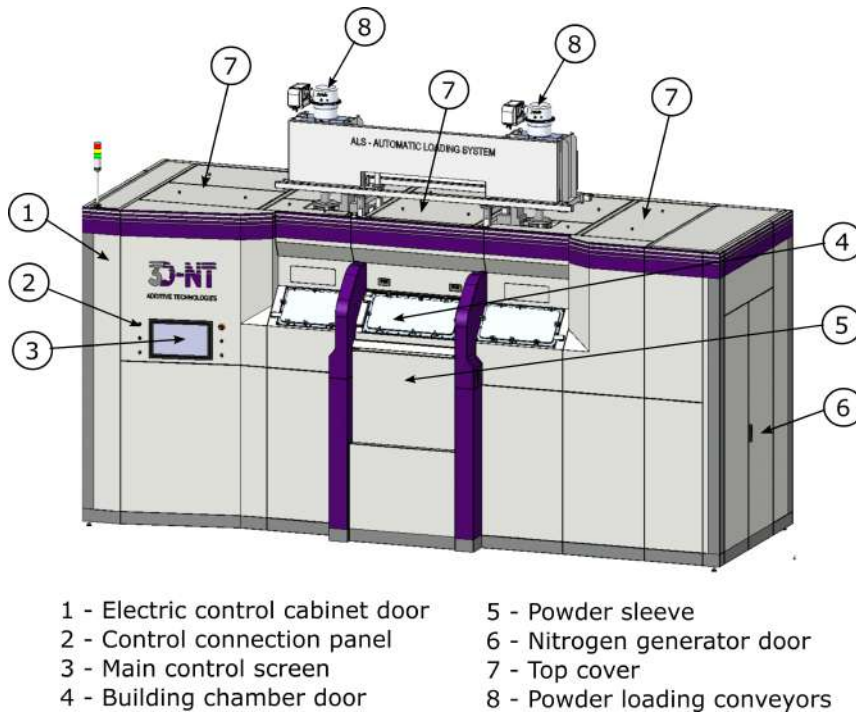


Figure 2.2: Front view of the LLA400 demonstrator.

The electric control cabinet door is the access door to inspect drives, plc, MCP controller, STM 32 card and other electronic devices. STM32 card allows to control all the sensors present in the machine and regulates the operation of the laser. Near the cabinet, there are the control connection panel and the main control screen. The control connection panel is equipped with emergency stop button, start button, and USB connection interface. The main control screen allows the access to machine

functions through the interface. It is possible to use three different operating modes: *manual* mode, to manage the different machine functions separately, such as purging or heating; *semiautomatic* mode, to perform a controlled recoating even with a different layer thickness than the thickness set in the job file, or to perform the scanning of a single layer; and *automatic* mode, to start the job automatically. Near these, the building chamber door is the outside protective cover of the process chamber, while the powder sleeve is the external cover of the sleeve that contains the powder and the job. From this door the sleeve comes out at the end of the process. The Nitrogen generator door is the access door to inspect and do the maintenance of the Nitrogen production system and to change the type of inert gas. Finally, the powder loading conveyors are the inlets used to load the powder into the hoppers, covered by the the panels in the upper part of the machine.

2.1.1 Building chamber and powder management

The working volume of the LLA400 machine has the dimensions of 400x400 mm² on the X-Y plane and 600 mm along the Z axis; this value can be rapidly extended to 1000 mm in the following version of the machine. The building chamber is saturated with inert gas before the start of the job and remains in the same state even during operation; the gas can be Nitrogen or Argon. In the case of the N₂ it is possible to choose to feed it from cylinders or use a generator integrated in the machine. The monitoring of the oxygen level inside the chamber is obtained by sensors. The inert gas is also blown and aspirated locally near the melting area to remove the fusion fumes and guarantee the good quality of the material. The gas is finally sent to a reconditionable filter to collect the powders before being introduced into the room. The filter is easily removable: it is isolated from the rest of the machine through a valve system. The powder is loaded into the hoppers above the machine via a pneumatic system. From the hoppers the powder is then discharged into the tanks above the recoater. This avoids contact between the material and air during all the process phases. In order to guarantee completely repeatable pieces with a high standard, a complete control of the production process is required at every stage. In this regard, various types of monitoring have been provided immediately, using sensors present throughout the machine. There is a stereoscopic monitoring system using cameras. Furthermore, different types of sensors were introduced, such as oxygen, humidity, pressure and temperature sensors, capacitive for monitoring the amount of powder, inductive distance, limit switches and inductive anti-collision distributed in the various areas of interest.

2.1.2 Powder distribution system, preheating and melting

One of the ways to make process dead times as small as possible is to make the powder distribution and melting phases contemporary. To achieve this, a fusion

system consisting of several strips was devised. There are three different carriages that move on the building plate, as illustrate in Figure 2.3: two for recoating, each of which is equipped with a rake and a powder container, and one for the heating lamps and the blowing and fumes and lapilli removal system. The carriage with lamps and fumes removal is in the middle of the two rakes, which move independently. Between the two pre-heating lamps mounted on the central carriage there is a window in which the laser acts to melt the powder.

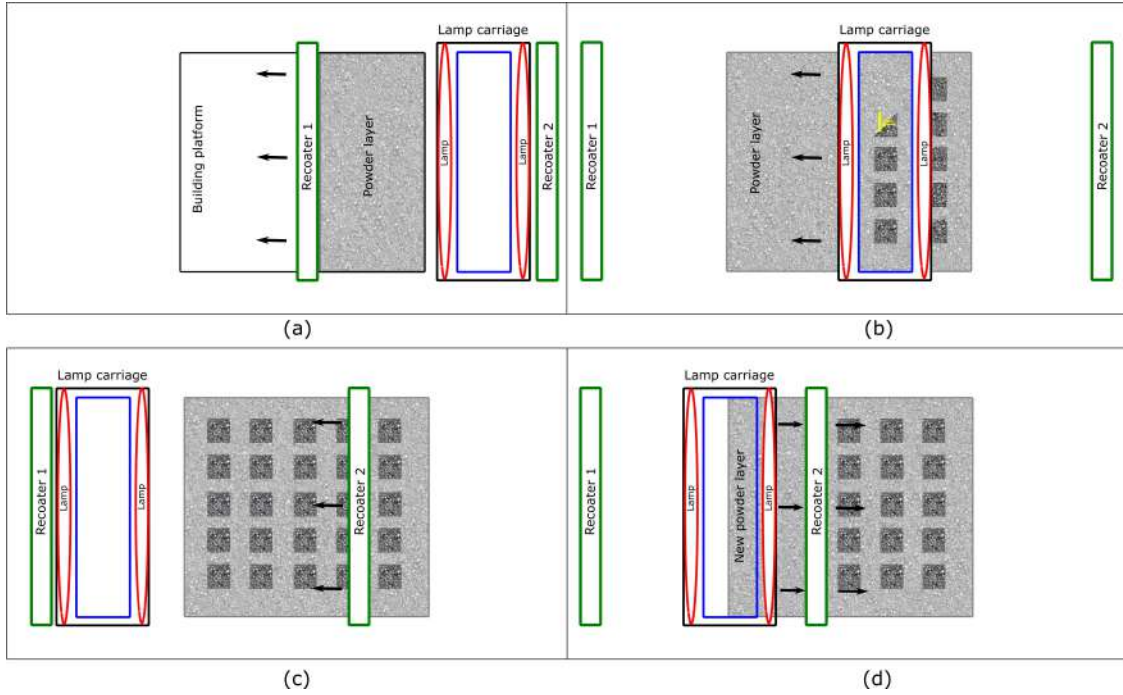


Figure 2.3: Phases for components creation with LLA400 demonstrator: a) creation of the layer with recoater 1, b) movement of lamp carriage and melting of the powder, c) movement of recoater 2 without recoating, d) creation of the new layer with recoater 2.

The phases necessary to the process for making metal components are illustrated in the Figure 2.3. The first phase is the realization of the first layer by the recoater 1. The second phase is the movement of the lamp carriage, which takes place while the recoater 1 is still distributing the powder. The lamp carriage moves in steps, working with a method stripe-by-stripe: when the carriage is stopped, the lamps heat the surface of the powder bed in the central window (highlighted in blue) and the laser melts the layer in the same area. Once the strip is finished, the carriage moves to the next one and repeats the process until it reaches the opposite end of the building platform. The third phase is the movement of the recoater 2, which tracks the lamp carriage while it is moving without distributing new powder. This

phase has the purpose of bringing the recoater 2 to the left, in a proper position to be able to spread the new layer from left to right. The third phase takes place after lowering the building platform and consists of the formation of the new layer by the recoater 2. The process is repeated with the same phases, changing only the direction of the movements.

The large size of the work volume makes the powder bed preheating operations essential. The preheating of the powder bed takes place both through the lamps that heat the surface of the bed, and through the resistances that warm the building platform. To allow the realization of large pieces without distortions it is possible to achieve preheating up to 500 °C. The demonstrator is currently equipped with a 450 kW single mode laser, but for the future a dual laser version is designed.

2.1.3 Z axis

The building platforms are anchored to the piston that controls the growth on the Z axis. In the piston there are also the heating system of the plate through electric resistances and two thermocouples in contact with the plate for the temperature control.

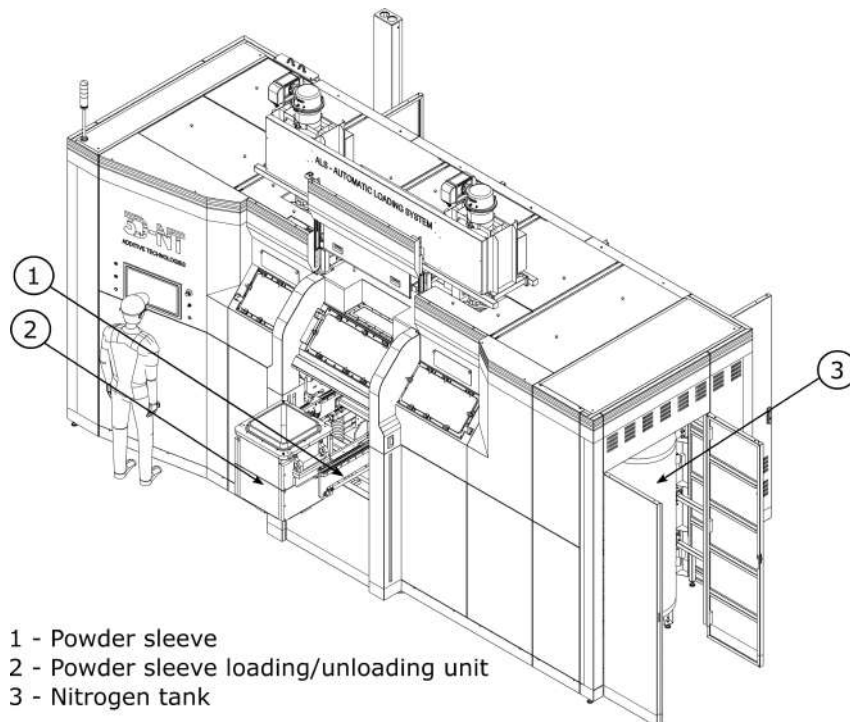


Figure 2.4: Front view of the LLA400 demonstrator open.

The piston must descend inside a sleeve that houses all the powder that is not

melted. At the end of the process it is necessary to extract the sleeve containing the entire work block. Due to the large size of the building envelope, this phase is completely automated. As illustrated in the Figure 2.4, the sleeve, suitably isolated from the environment, is expelled horizontally. The part is then moved in a glove box and subjected to powder removal in inert atmosphere.

2.2 Fume blowing and suction system

One of the problems that affects the production of metal components is the atmosphere in the building chamber. All L-PBF machines operate in an inert atmosphere, generally using Nitrogen gas or, more rarely, Argon. This allows the protection of the material from the reaction with oxygen on any newly melted surface. This would lead to the introduction of impurities in the finished piece and alteration of the parameters necessary to adequately melt the powders used [161, 147]. However, even with an adequately low oxygen content ($> 0.2\%$), problems can be noted on components made with L-PBF. The impurities detected on the surfaces are due to the presence of fumes produced by the melt pool after the passage of the laser. Some elements present in the powders evaporate from the melt pool and remain near the surface, depositing on it. The effect is a dark halo that indicates the presence of impurities in the metal.

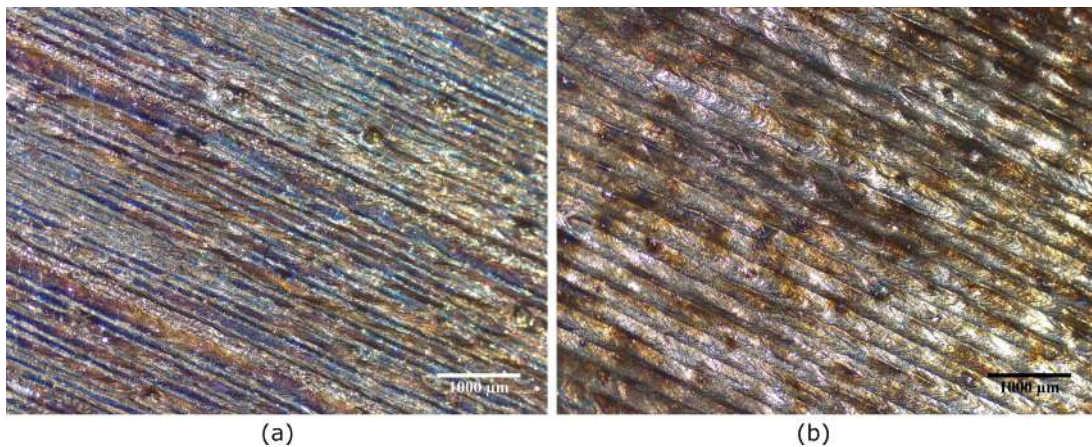


Figure 2.5: Two OM images (16X) of single layers of 316L SS with dimensions of 20 mm x 20 mm x 40 μm produced with a laser power of 300 W and a scanning speed of a) 400 mm/s and b) 200 mm/s with two different problems: a) oxidation and b) fume deposition.

An example of oxidation and one of fumes deposition are shown in Figure 2.5 for single layers of 20 mm x 20 mm x 40 μm in 316L Stainless Steel. The first sample was made with an oxygen content in the building chamber $> 2\%$, while

the second sample was produced with an oxygen content in the building chamber $< 0.2\%$, but without activating the fumes removal system.

To prevent the deposition of fumes, they must be removed from the melting area as soon as they are produced. It is therefore necessary that the machine has a blowing and suction system: the blowing serves to remove the fumes produced by the passage of the laser and bring them closer to the suction outlet, which sends them to the filters. This system also serves to eliminate the lapilli that can form during the melting of the powder and that can jeopardize the piece and the laying of the subsequent layers. In order to have a fumes and lapilli removal homogeneous throughout the chamber, a system which creates a homogeneous flow along the entire length of the plate is required; however, this flow must be laminar in order to avoid turbulence which would ruin the newly spread powder layer.

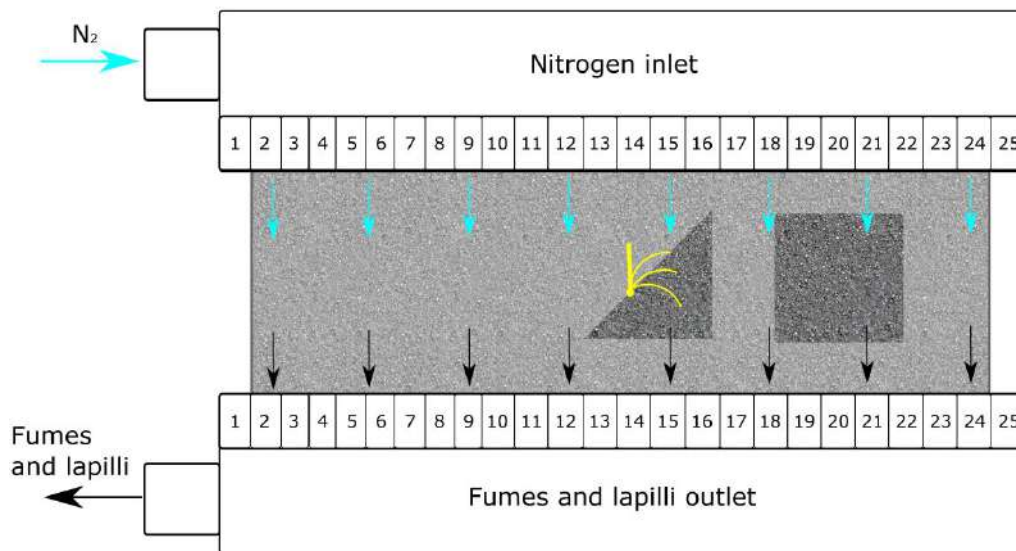


Figure 2.6: Fumes and lapilli removal system.

In the LLA400 machine the fumes and lapilli removal system, schematized in Figure 2.6, is mounted on the lamp carriage and acts locally in proximity of the zone melted by the laser: this area is the strip in the center of the carriage. In this way the blowing and suction system is always close to the area to be melted in any point of the plate. The flow is always laminar and since the gas inlet and outlet are very close to the melting area, the speed of the gas can be lower. To have a homogeneous flow along the entire plate, two air knife technology vents were installed. The shape of the nozzle has a gas tank and a small outlet slot. The Nitrogen is fed in laterally, the tank reaches a slight over-pressure and the gas flows homogeneously along the slot. Experimental tests were carried out on a prototype of the vents to verify the uniformity of the flow. The speed of the inert gas at

the outlet of the blowing inlet was measured when the pump power varied. The values were collected at 25 points equidistant in the length of the inlet, as shown in Figure 2.6, and at 4 different distances from the flow exit point. The size of the openings from which the gas exits were also varied, to evaluate the effect. The results are reported in the Figures 2.7, 2.8, 2.9, 2.10 and 2.11, for the size of the slots of 0.5 mm, 0.75 mm, 1 mm, 1.25 mm and 1.5 mm, respectively. It can be seen that at high pump power values, the output gas speed is high and irregular due to turbulence. At low pump power the outgoing flow is fairly homogeneous, especially for measurements taken further from the exit area. The best situation is the vent with the slot of 1.5 mm for powers of 2000 mV or 3000 mV, that was chosen and mounted in the machine. The suction outlet has the same shape as the blowing inlet. The suction tests were good for all the slot dimensions (Figure 2.12), but, also in this case, the 1.5 mm slot was chosen to facilitate the aspiration of the lapilli.

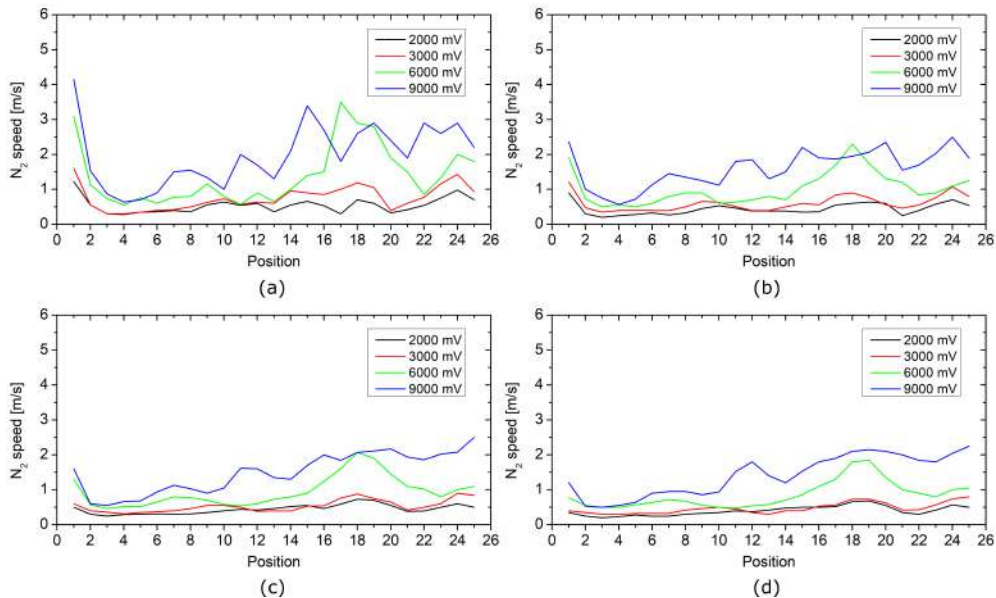


Figure 2.7: N_2 speed values of the blowing nozzle with a slot of 0.5 mm. The measurements are taken at a) 2 cm, b) 5 cm, c) 7.5 cm and d) 10 cm from the nozzle.

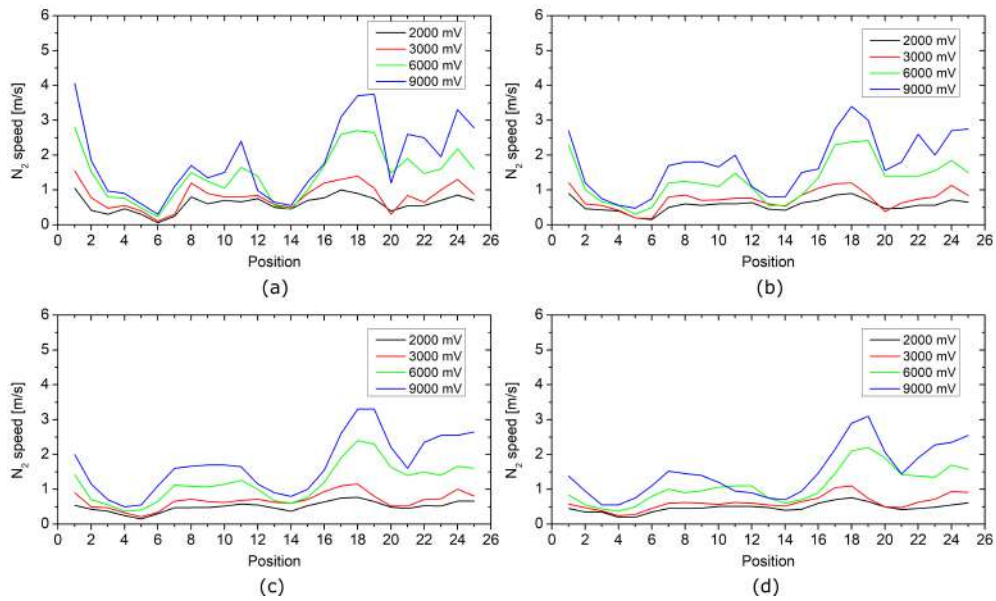


Figure 2.8: N_2 speed values of the blowing nozzle with a slot of 0.75 mm. The measurements are taken at a) 2 cm, b) 5 cm, c) 7.5 cm and d) 10 cm from the nozzle.

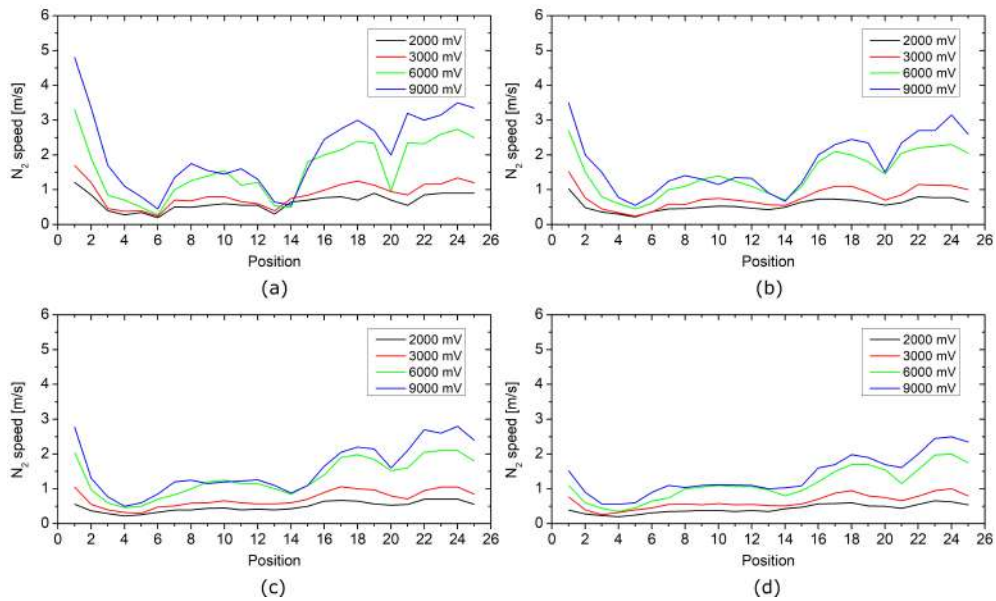


Figure 2.9: N_2 speed values of the blowing nozzle with a slot of 1 mm. The measurements are taken at a) 2 cm, b) 5 cm, c) 7.5 cm and d) 10 cm from the nozzle.

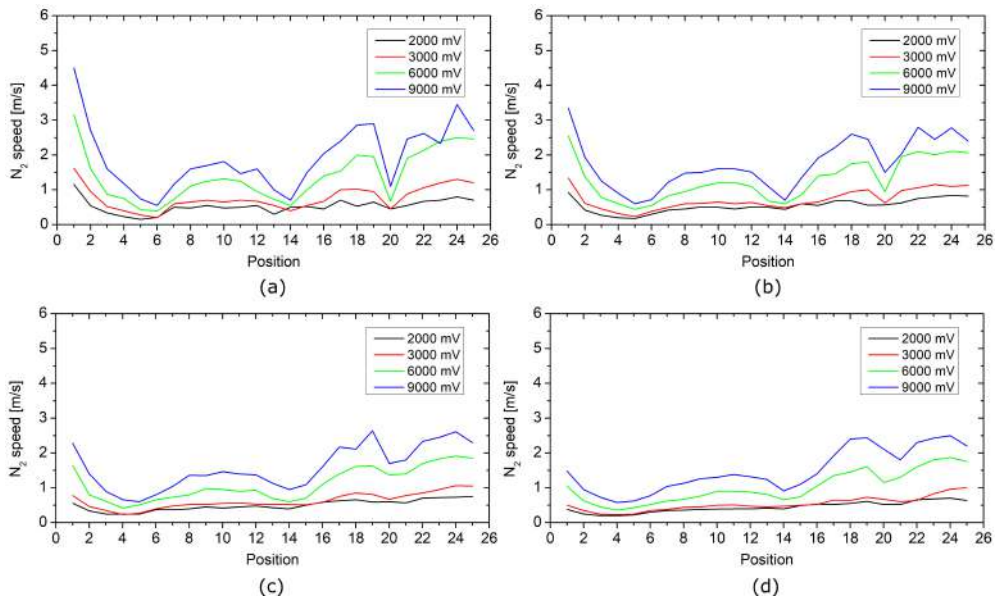


Figure 2.10: N_2 speed values of the blowing nozzle with a slot of 1.25 mm. The measurements are taken at a) 2 cm, b) 5 cm, c) 7.5 cm and d) 10 cm from the nozzle.

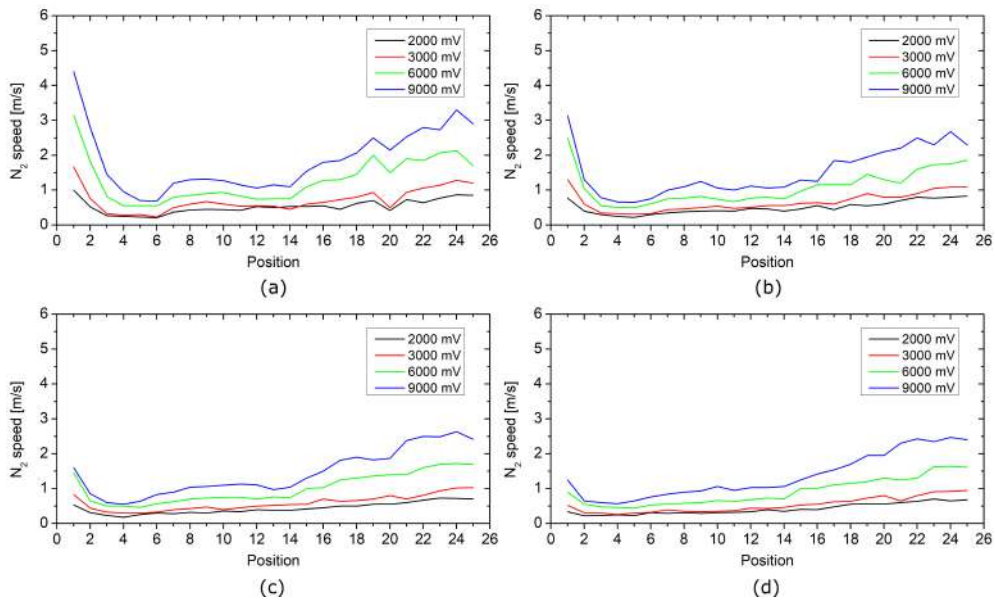


Figure 2.11: N_2 speed values of the blowing nozzle with a slot of 1.5 mm. The measurements are taken at a) 2 cm, b) 5 cm, c) 7.5 cm and d) 10 cm from the nozzle.

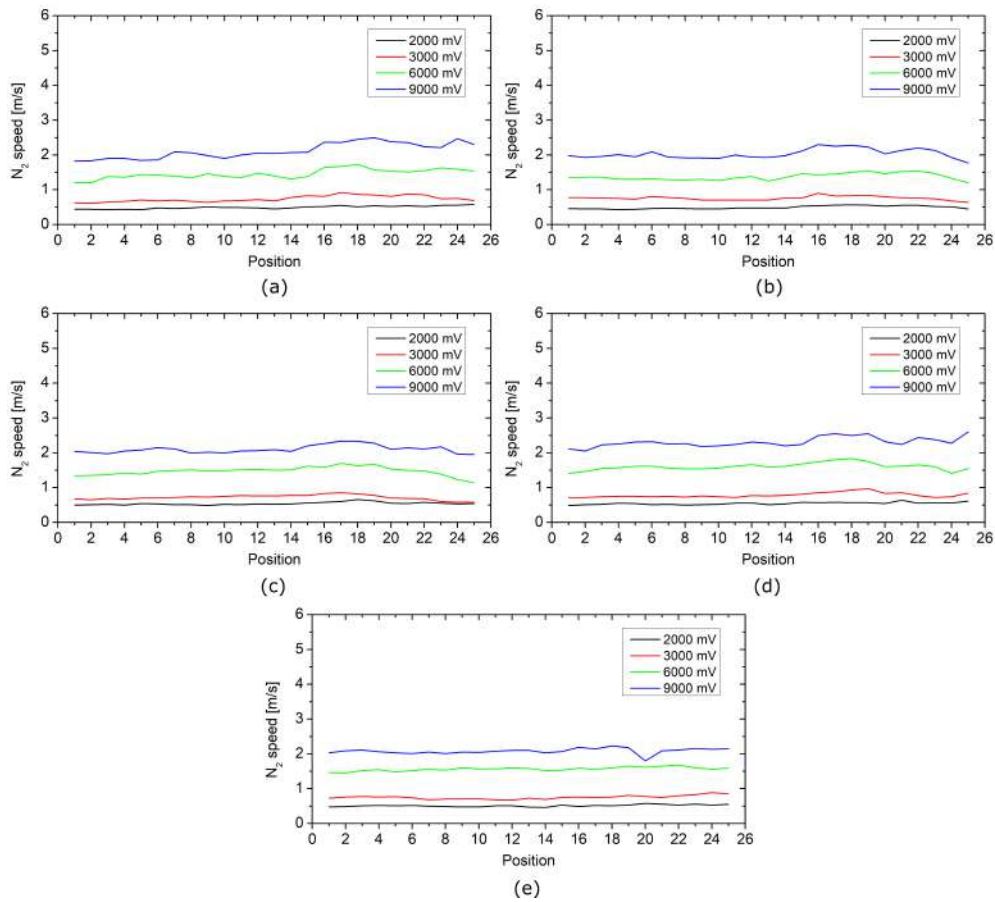


Figure 2.12: Suction speed values of the suction nozzle with a slot of a) 0.5 mm, b) 0.75 mm, c) 1 mm, d) 1.25 mm and e) 1.5 mm.

2.3 AlSi10Mg powder characterization

In this section some powders produced with different atomization methods are analyzed, in order to evaluate those are good for the technology. Some atomization techniques are the following [157]:

- Gas atomization: mostly used for Fe, Ni, Co, Al and Ti alloys.
- Water atomization: used for unreactive materials and produces irregular shaped particles.
- Plasma atomization: produces high-quality spherical powder, limited to alloys that can be formed into a wire feedstock.

- Electrode induction melting gas atomization: suitable for all alloys and most economic with reactive alloys like Ti. A bar feedstock is rotated and melted by an induction coil before it flows downward into a gas stream for atomization.
- Centrifugal atomization: is a good trade-off between gas atomization and plasma atomization, best suited to larger batch size of less reactive and low-melting temperature alloys. It can also produce Ni-based superalloy powders.

Four types of AlSi10Mg powder were provided by Poudres Hermillon, with different size distributions and production methods (Table 2.1).

Table 2.1: Powder types and description.

Powder Number	Material	Quality/grade
1	AlSi10Mg	Coarse grains
2	AlSi10Mg	Brut Atomization
3	AlSi10Mg	20 - 63 μm
4	AlSi10Mg	Fine grains

Is a useful practice to evaluate which powders are suitable for use in AM, based on the particle size distribution and the morphology of the granules. The best AM powder shows a particle size distribution represented by a Gaussian curve, a spherical shape, and a smooth surface with fewer satellites. Moreover, the size of the granules should be small enough to allow the formation of a thin layer and large enough to not form irregular aggregates and not to stick to the rake. These features describe a powder with good flowability, good processability and a predictable bed density [126]. For each of the powders listed in the table, the apparent density, the apparent density after powder bed compacting, the morphology and the particle size distribution (where it was possible) were evaluated. The density of the powder bed was carried out by evaluating the volume and mass of the powder deposited. Subsequently, the volume was measured after compacting the same amount of powder through vibration. All calculation were carried out considering the density of AlSi10Mg equal to 2.67 g/cm^3 . Morphological and granulometric evaluations were carried out through Scanning Electron Microscope (SEM) and image analysis. In particular, the particle size distribution graphs were obtained by measuring the granules diameters in SEM images of a representative amount of powders. These tests were performed by 3D-NT with the collaboration of the Politecnico di Torino, which provided the instrumentation.

2.3.1 Powder 1

Powder 1 presents an apparent density of 1.6 g/cm^3 with a volume fraction of 60 %, both before and after the compaction of the powder bed, as listed in Table 2.2.

Table 2.2: Powder bed density analysis for AlSi10Mg Powder 1.

Powder Number	Apparent Density [g/cm^3]	Apparent Density after Compaction [g/cm^3]	Powder Volume Fraction [%]	Compacted Powder Volume Fraction [%]
1	1.6	1.6	60	60

So the initial configuration is already optimized by the presence of very large particle sizes: smaller particles immediately fill empty spaces left and the subsequent vibration does not lead to a measurable density change. This assertion is proved by the particle size distribution based on particles number, illustrated in Figure 2.13. The amount of granules with size smaller than $20 \mu\text{m}$ is very high, up to 150 repetition. Furthermore, the large particles causes large cavities, where the smaller powder granules can stay.

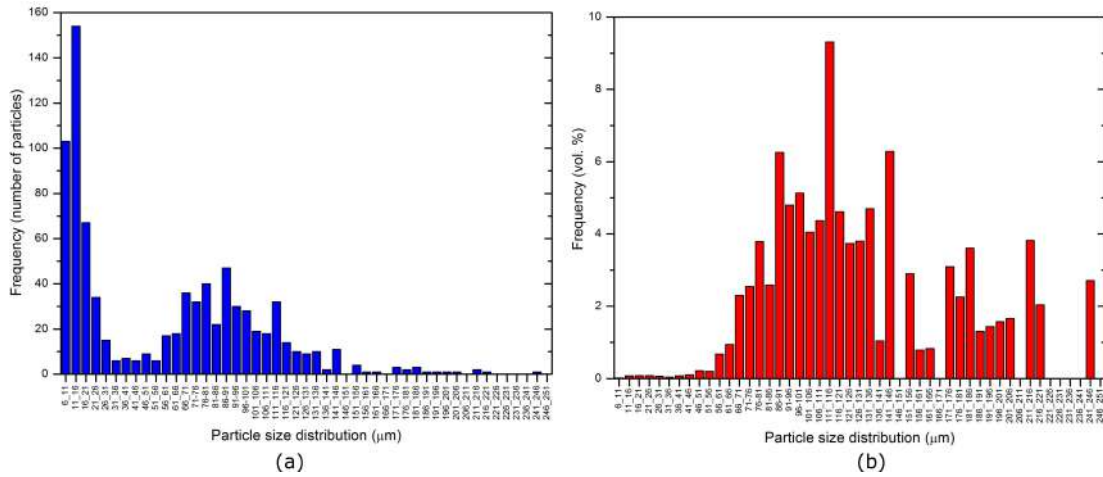


Figure 2.13: Particle size distribution in a) number of particles and in b) volume for Powder 1.

The complete information is provided by the graph in Figure 2.13b, that reports the same information of Figure 2.13a, but the frequency is given in volume percentage. This is the best way to show whose classes of particles fill the larger parts of

powder bed and so are most influent in the process. The graph shows the distribution of the powders as produced and so there is a large curve: it is hence advisable to sift in order to eliminate too fine and too coarse powder particles (extremes of the curve).

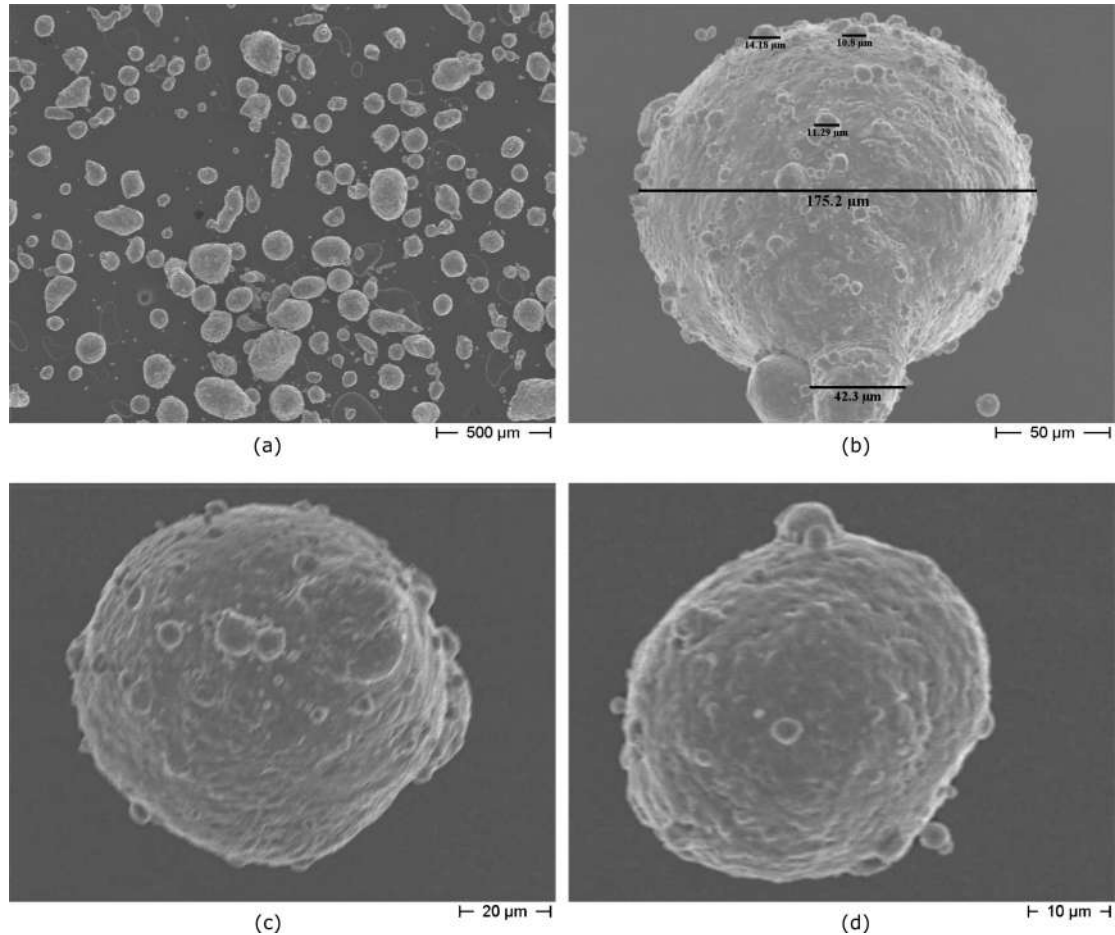


Figure 2.14: SEM images for Powder 1 at magnification of a) 50X, b) 500X, c) 1000X and d) 1800X.

The morphology of powders is directly observed from SEM images reported in Figure 2.14. From Figure 2.14a it is possible to observe that there are some spherical particles and some ones with very irregular and elongated shapes. Coarse and irregular particles, not suitable for use in AM, can be eliminated by sieving, in particular when the size is high. The large amount of very small particles is also visible, around 15 μm , causing the first peak in the chart in Figure 2.13a. Figures 2.14b, 2.14c and 2.14d show single particles with spherical shapes suitable for AM. On each granule a great number of spherulites are present: for example the particle in Figure 2.14b present a diameter of 175 μm and on the surfaces there are

satellites with various size (from 10 μm to 42 μm). The presence of this imperfection jeopardizes a little the flowability of the powder bed, even though the shape is spherical.

2.3.2 Powder 2

In this case the apparent density is 1.4 g/cm^3 before the compaction and rises up to 1.7 g/cm^3 after the compaction (Table 2.3). This fact indicates that the initial configuration is not optimized, as for the Powder 1, due to the irregular morphology of the granules.

Table 2.3: Powder bed density analysis for AlSi10Mg Powder 2.

Powder Number	Apparent Density [g/cm^3]	Apparent Density after Compaction [g/cm^3]	Powder Volume Fraction [%]	Compacted Powder Volume Fraction [%]
2	1.4	1.7	53	64

Indeed, this powder is produced with a different production method: brut atomization, that has a great influence on powder size and morphology. Already from the handling of the sample, there is a greater tendency to aggregation and a low flowability. From Figures 2.15a and 2.15b it is possible to state that particles present various shapes and sizes: a lot of particles have irregular shapes and, although some are spherical, these are small and bonded to form irregular shape aggregates. The powder bed consists in a series of aggregates of particles, ranging from 5 μm to 60 μm , with very irregular shapes, that make impossible and useless the identification of a particle size distribution. Figure 2.15a shows that the larger particles, about 60 μm , have a great amount of satellites on the surface. This can also be seen from Figure 2.15b where the smaller particles, from 5 μm to 12 μm , form large irregular aggregates that penalize fluability. The set of characteristics observed for this powder define it not suitable for the use in Additive Manufacturing.

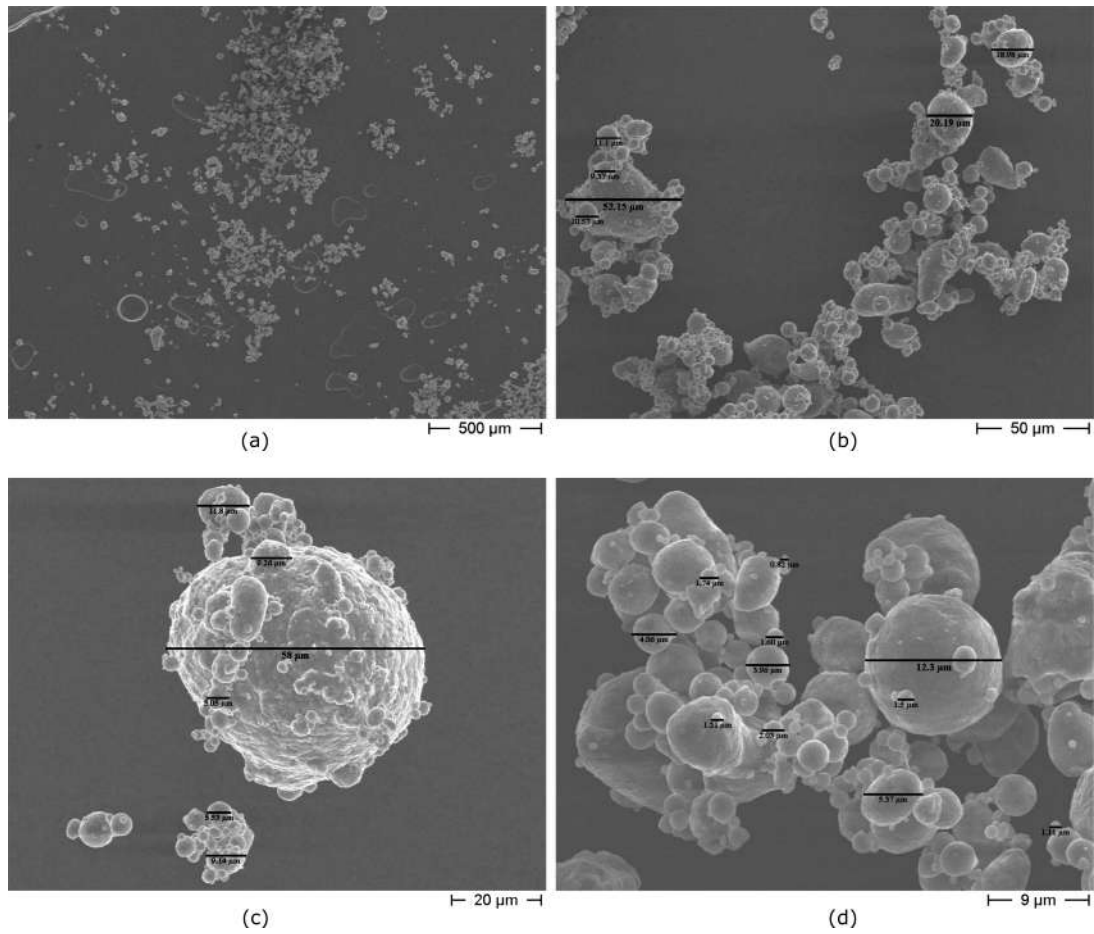


Figure 2.15: SEM images for Powder 2 at magnification of a) 50X, b) 500X, c) 1000X and d) 2500X. .

2.3.3 Powder 3

Powder marked with number 3 shows an apparent density of 1.4 g/cm^3 before the powder bed compaction and of 1.6 g/cm^3 after compaction (Table 2.4).

Table 2.4: Powder bed density analysis for AlSi10Mg Powder 3.

Powder Number	Apparent Density [g/cm^3]	Apparent Density after Compaction [g/cm^3]	Powder Volume Fraction [%]	Compacted Powder Volume Fraction [%]
3	1.4	1.6	53	59

As in the previous case, this is due to the better arrangement of powders of different size due to the use of a vibrating medium. The apparent density of this powder is lower than apparent density of powder number 2. This is due to the narrower granulometric distribution of Powder 3, as shown in Figure 2.16a, which indicates more granules of the same size and thus smaller amounts of smaller particles. Small granules, in fact, can slip into empty spaces and optimize space, as is the case of the Powder 2.

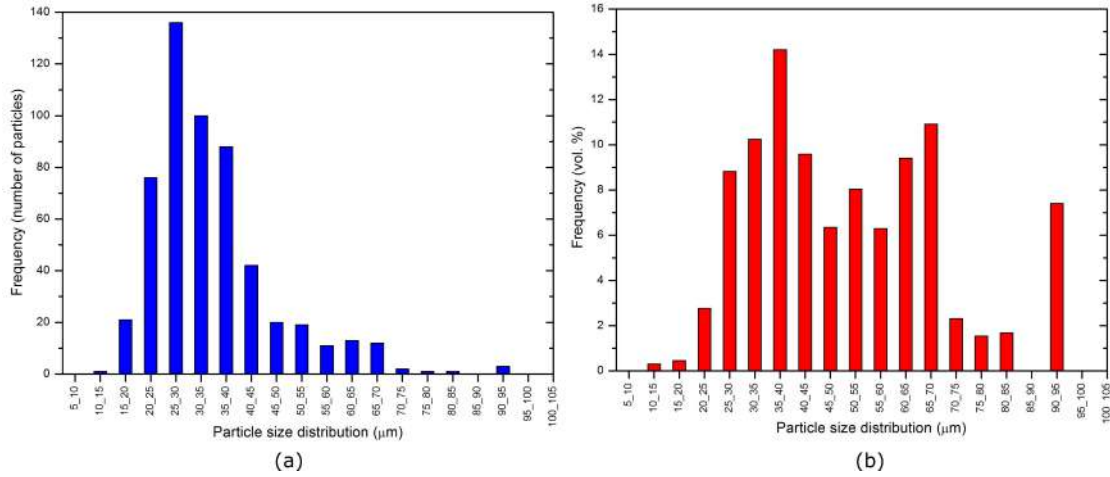


Figure 2.16: Particle size distribution in a) number of particles and in b) volume for Powder 3.

The complete information is provided by the graph in Figure 2.16b, that reports the same information of Figure 2.16a, but the frequency is given in volume percentage. The second graph better highlights the presence of excessively large granules that must be eliminated by powder sieving before the use in AM.

Figure 2.17 reports the SEM images of the powder at different magnifications. In Figures 2.17a and 2.17b it is shown how the powders have a uniform distribution and a low tendency to form aggregates, that deteriorate flowability of the powder bed. Moreover, the almost total absence of very small particles can be noticed. Smaller granules can aggregate to the larger ones creating irregular shapes. The images at greater magnification in Figures 2.17c, 2.17d and 2.17e highlight the regular shape, although not perfectly spherical, of the particles and their good dimensional uniformity. Moreover, the granules present a few satellites. The set of these observed characteristics makes this type of powder suitable for AM.

2.3.4 Powder 4

The apparent density is 1.3 g/cm^3 before the compaction and rises to 1.6 g/cm^3 after the compaction (Table 2.5). This fact indicates that the initial configuration

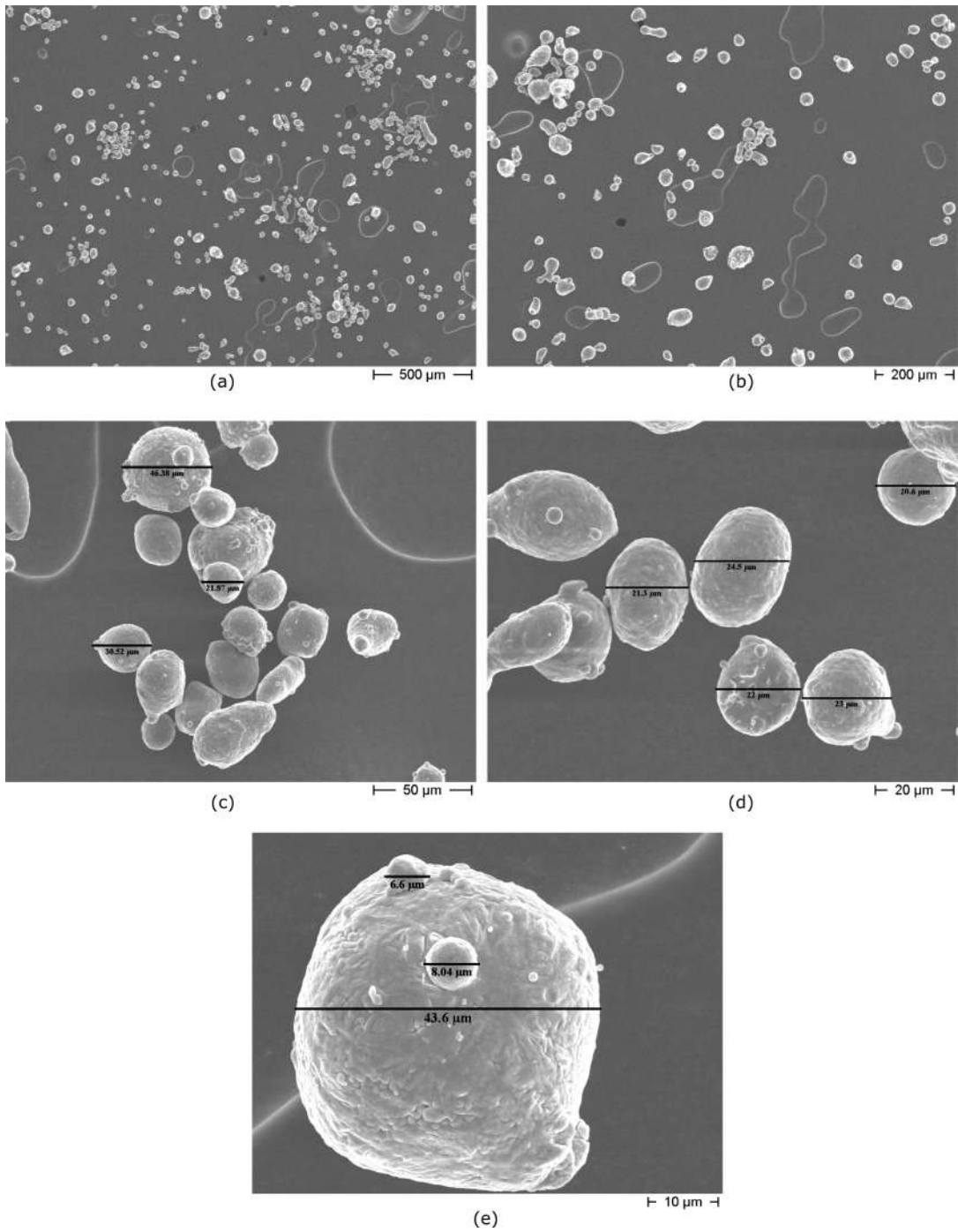


Figure 2.17: SEM images for Powder 3 at magnification of a) 50X, b) 100X, c) 500X, d) 1000X and e) 1800X.

is not optimized.

The granulometric distribution of the powder in Figure 2.18a is quite narrow,

Table 2.5: Powder bed density analysis for AlSi10Mg Powder 4.

Powder Number	Apparent Density [g/cm^3]	Apparent Density after Compaction [g/cm^3]	Powder Volume Fraction [%]	Compacted Powder Volume Fraction [%]
4	1.3	1.6	48	58

but the maximum is centered on very small dimensions, 6-8 μm . The so small size of the particles makes them subject to the formation of aggregates, forming structures that make difficult to lay down the powder bed, as visible from a low density value such as 1.3 g/cm^3 . The increase in density after compacting results from a better arrangement of the particles of different sizes, which have a proportional importance as seen in the Figure 2.18b.

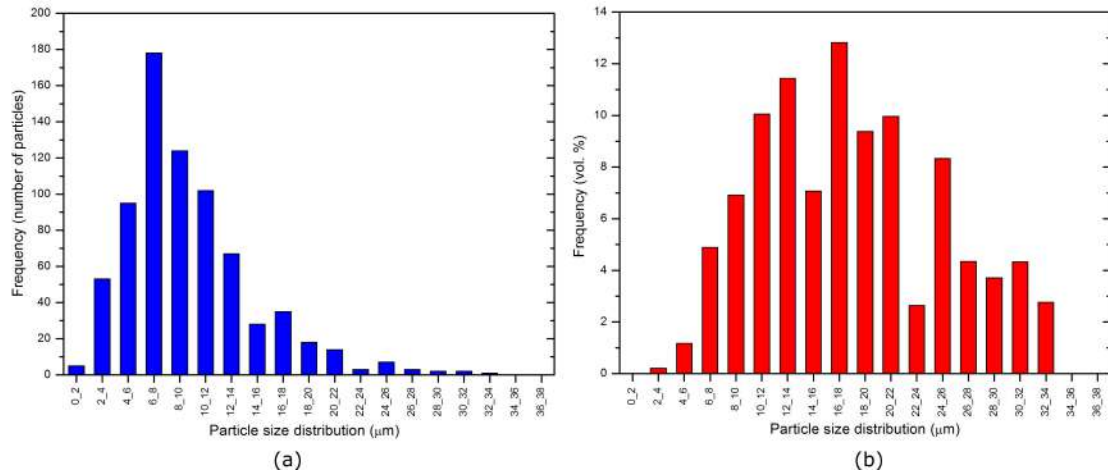


Figure 2.18: Particle size distribution in a) number of particles and in b) volume for Powder 4.

Figure 2.19 reports the SEM images of the powder at different magnifications. In Figures 2.19a and 2.19b the powder at low magnifications is shown: there are only a few large granules, up to about 30 μm , and lots of very small particles that tend to stick to the bigger as satellites or aggregate. The formation of the aggregates and the morphology of the powder granules are highlighted in Figures 2.19c and 2.19d. The particles are all almost spherical, for all sizes, but the irregularity is due to the presence of satellites on larger granules. For example, on 25 μm particles, satellites 1 to 10 μm can be present. As shown also in the Figure 2.19e, Powder 4 has an ideal morphology for AM, but the dimensions are too small and cause

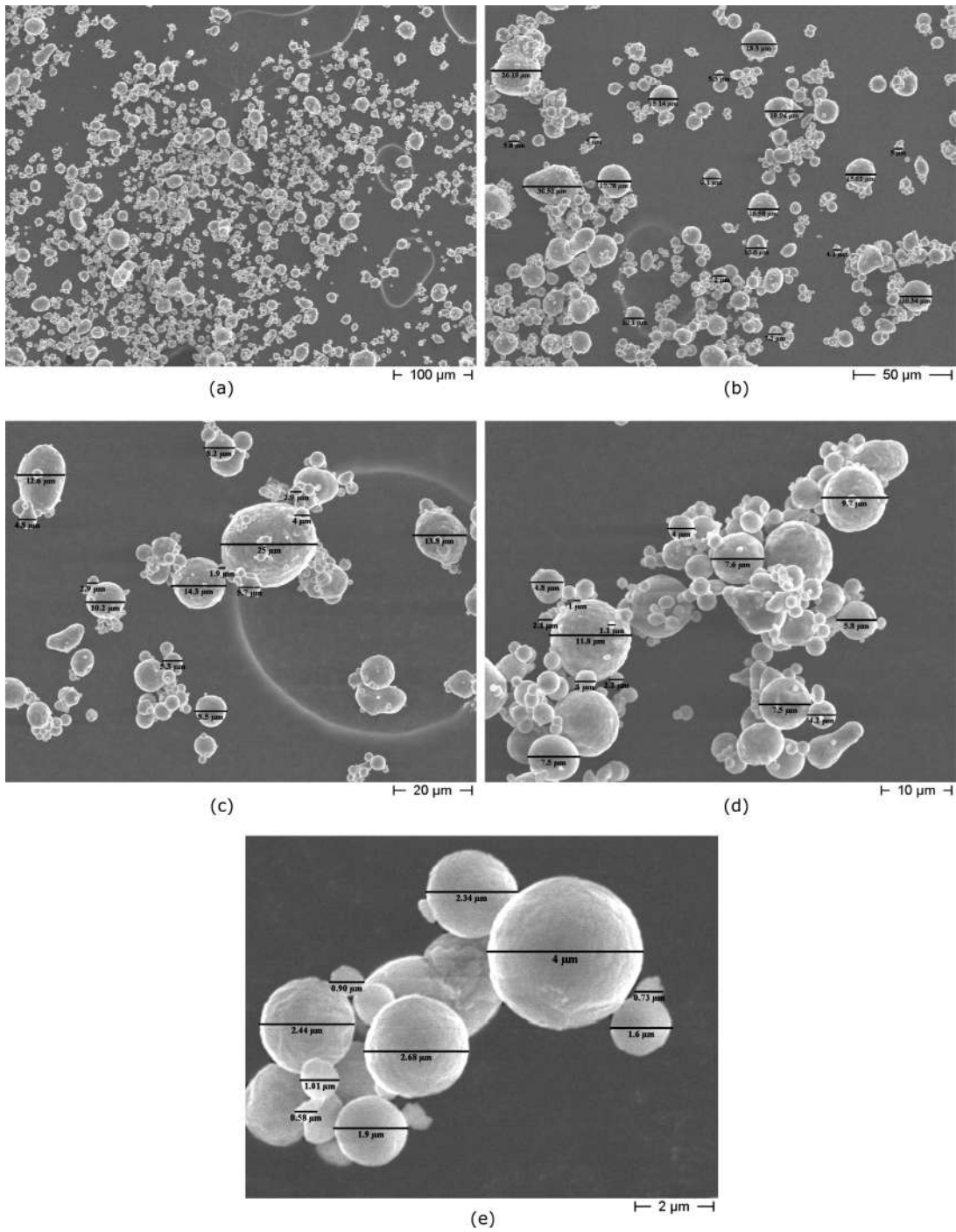


Figure 2.19: SEM images for Powder 4 at magnification of a) 200X, b) 500X, c) 1000X, d) 1800X and e) 10000X.

irregular structures.

2.3.5 Final comparison between powders

The four types of powders provided have been analyzed and characterized in order to identify the granulometric distribution and the morphological characteristics. These features allow to evaluate which of these powders can be used in AM and which are not suitable. Powder 1 shows a morphology suitable for use in AM, but the granulometric distribution is adequate only after sifting the powder to eliminate the fraction of too small and too large particles. Powder 2 has an irregular granules structure and large aggregates, that make it impossible to use it in AM, due to the low flowability and tendency to aggregate. Powder 3 demonstrates the best set of features: good particle size distribution and regular morphology. These make it the best among the four powders provided for use in AM. Powder 4 presents an optimal morphology of the particles, that are quite spherical, but the granules size is too small and causes formation of irregular aggregates. For this reason the last powder is not suitable for AM.

In Table 2.6 are listed the values of D10, D50 and D90 for the powders 1, 3 and 4. These values provide a statistical indication on the Particle Size Distribution and allow a comparison between the different powders.

Table 2.6: Values of D10, D50, D90 and SPAN for all the AlSi10Mg powders.

Powder Number	D10 [μm]	D50 [μm]	D90 [μm]	SPAN
1	11	58	116	1.81
3	22	31	51	0.91
4	5	9	17	1.31

In particular, D10 is value below which there is 10 % of the powder population, D50 is value below which there is 50 % of the powder population and D90 is value below which there is 90 % of the powder population. These values allow us to immediately identify the type of powder distribution. Powder 1 has a very wide distribution because it has a very low D10 and a very high D90. The powder 3 has a more narrow distribution with the three values very close to each other. Finally the powder 4 has a very shifted distribution towards small grain sizes. The last column of the Table 2.6 shows the SPAN value, obtained from the equation 2.1. SPAN is a value, normalized on D50, of how wide the distribution of powders is, that is how D10 is far from D90. Larger is the SPAN value, larger is the powder distribution curve.

$$SPAN = \frac{D90 - D10}{D50} \quad (2.1)$$

2.4 316L Stainless Steel powder characterization

The LLA400 demonstrator within the STAMP project is aimed production of complex shape components with different types of metals, in particular with Al alloys. Some materials, as Al alloys, present different problems during the process and their use requires greater care. The commissioning of a prototype leads to various problems and inconveniences that can make the process very complex. For this reason, in the first phase of the use of the LLA400 machine it was decided to exploit a simple material to process. The most suitable material for this purpose is stainless steel: 316L was chosen because it was already widely used in literature and has a known behavior in L-PBF.

This section shows the characterization of a gas-atomized stainless steel 316L powders supplied by LPW for L-PBF technology. This powder was used to produce first specimens with the LLA400 machine. From the graphs in Figure 2.20 the particle size distribution of the 316L powder can be observed. The distribution is represented by a Gaussian curve and has a range of 10-55 μm . As the Table 2.7 also shows, the distribution is quite narrow, as the SPAN is low.

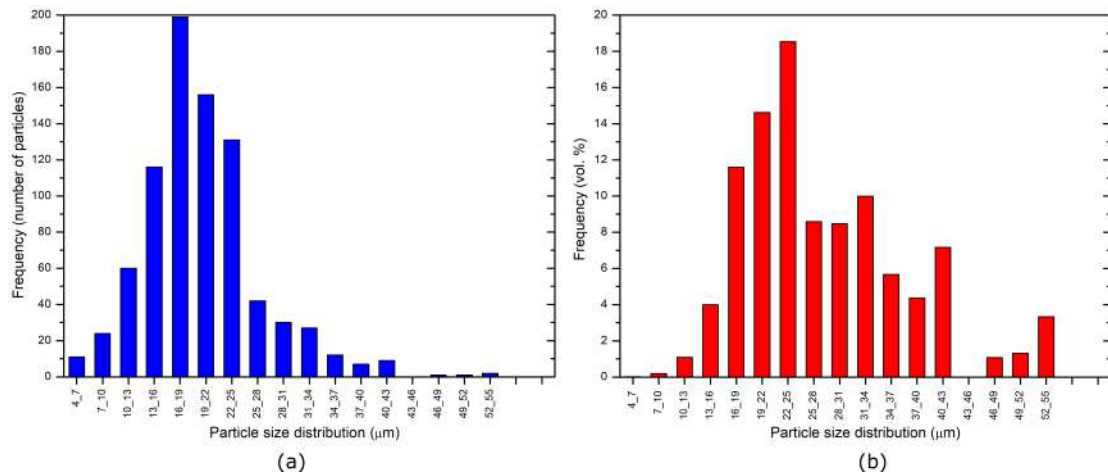


Figure 2.20: Particle size distribution in a) number of particles and in b) volume for 316L powder.

Table 2.7: Values of D10, D50, D90 and SPAN for all the 316L powder.

Powder type	D10 [μm]	D50 [μm]	D90 [μm]	SPAN
316L	13	19	29	0.83

The SEM images of the 316L powder at two different magnifications (500X and 1000X) reported in Figure 2.21 allow to analyze the morphology of the particles.

Powder particles are mainly spherical and regular, a very positive feature for their use in L-PBF technology because it allows good flowability. However, some particles of more irregular shape and the presence of some satellites (the small particles attached to the larger ones) can be noted. A percentage of particles with a more irregular shape is always present in all the powders, but if the quantity is low they do not penalize the properties of the powder in use.

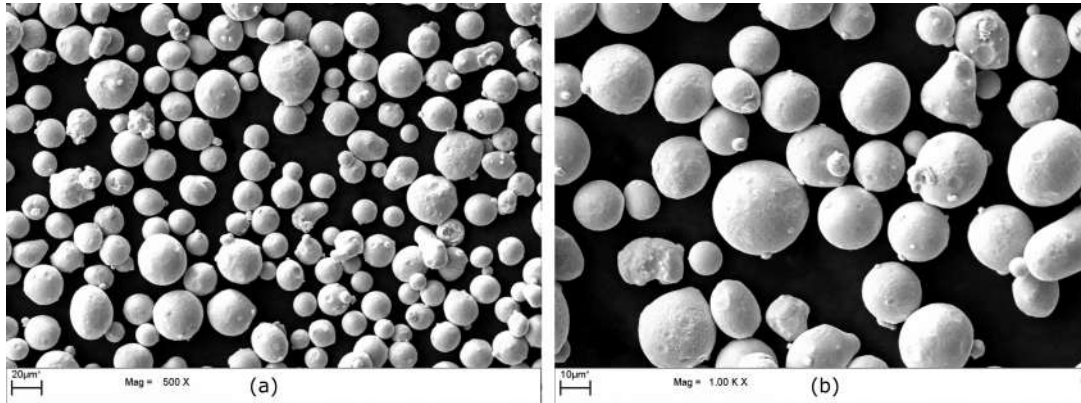


Figure 2.21: SEM images for 316L powder at magnification of a) 500X and b) 1000X.

2.5 Experimental tests: single layer

Once the LLA400 machine was completed it was possible to activate it and produce the first samples to check the operations. The laser mounted on the machine, CS1000 from Prima Industrie, is not the definitive laser. This laser in fact is a dual mode and has a spot not suitable for L-PBF: about $150\ \mu\text{m}$. The first tests conducted with this laser, however, served to identify some of the problems present in the prototype and to evaluate their effects on the material as the energy density varied. The material used for the tests is SS 316L, in particular the lot of powder analyzed in the previous section.

Based on the information found in the literature for L-PBF on 316L [149, 173, 56, 99, 178] it was decided to carry out the first test campaign with a power of 300 W, a hatch distance of 0.12 mm, a layer thickness of $40\ \mu\text{m}$ and different scanning speeds. The scanning speeds chosen are: 100 mm/s, 200 mm/s, 300 mm/s, 400 mm/s, 500 mm/s, 600 mm/s, 700 mm/s, 800 mm/s, 900 mm/s and 1000 mm/s. The energy densities range from $625\ \text{J}/\text{mm}^3$ to $63\ \text{J}/\text{mm}^3$ and were calculated with the Equation 2.2 and listed in the Table 2.8. In the equation E is the energy density [J/mm^3], v is the scanning speed [mm/s], h_d is the hatch distance between the laser tracks [mm] and t is the layer thickness [mm].

$$E = \frac{P}{vh_d t} \quad (2.2)$$

The first set of samples are single layers with a total area of 20x20 mm², produced with the blowing system active, but without the heating of the platform, in order to avoid introducing too many variables in this first phase (e.g. the powder pre-heating temperature for best results). All tests were conducted with an oxygen quantity reported by the sensor of less than 0.2 %.

Table 2.8: Energy density for all the samples of the first set.

Power [W]	Scanning speed [mm/s]	h_d [mm]	Layer thickness [mm]	Energy density [J/mm ³]
300	100	0.12	0.04	625
300	200	0.12	0.04	313
300	300	0.12	0.04	208
300	400	0.12	0.04	156
300	500	0.12	0.04	125
300	600	0.12	0.04	104
300	700	0.12	0.04	89
300	800	0.12	0.04	78
300	900	0.12	0.04	69
300	1000	0.12	0.04	63

Since the building platform is 400x400 mm² and the initial specimens are very small, it was decided to produce a second plate with removable disks, fixed to the plate with screws (Figure 2.22) [124]. In this way the specimens can be analyzed by extracting the disk of interest, without having to cut the entire platform. To avoid having differences in the results depending on the position of the disks on the plate, only the central disk was used for these first tests.

In the Figure 2.23 are listed some OM images of the produced samples for all scanning speeds. From a first look it is possible to notice a problem of removal of the fumes, which are deposited on the already melted areas, making the surfaces dark. The inefficiency of the fumes removal system was solved by improving the piping that brings the Nitrogen to the vents. Moreover, the coloring also indicates a presence of oxygen greater than that indicated by the sensor.

At low scanning speed the fusion pattern is quite regular, but the layer is overmelted and is very low: the energy density for 100 mm/s, 200 mm/s and 300 mm/s is in fact very high (650-208 J/mm³). Increasing the scanning speed from 400 mm/s to 800 mm/s the energy densities are in the range considered the most suitable in literature (156 J/mm³ - 78 J/mm³), many unstable fusion phenomena can be noticed, with holes forming on the surface. The instability of the molten

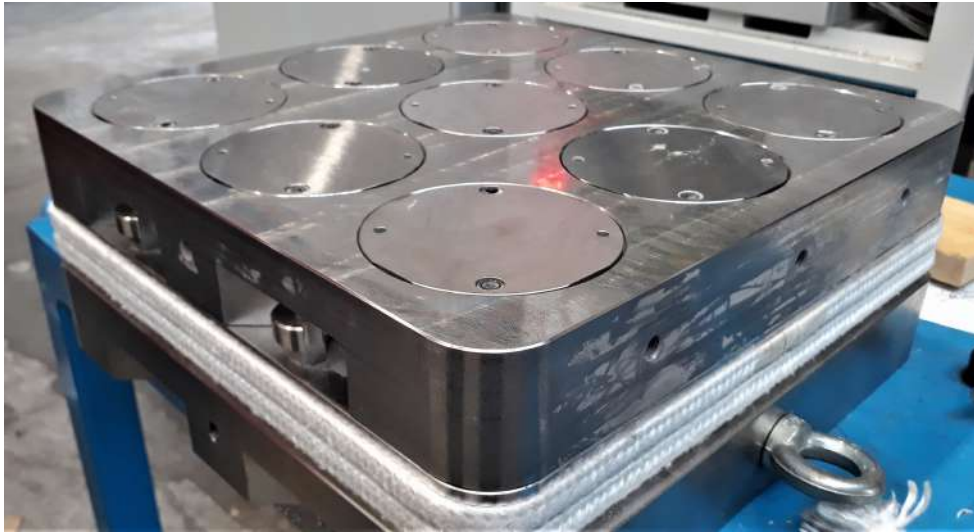


Figure 2.22: Building platform with removable discs.

area may be due to the presence of oxygen [175], but also caused by too high laser power [182]. The result can be a combination of the two cases. The pattern of fusion, however, is not homogeneous in all the samples: as the Figures 2.23h and 2.23i present, at 800 mm/s, there are areas with more stable fusion and some areas very rich of holes. Finally the samples at speeds of 900 mm/s and 1000 mm/s have only areas of unstable fusion and a large balling effect [175, 55], due to low energy density (69 J/mm^3 and 63 J/mm^3 , respectively) and high laser power, and aggravated by the local presence of oxygen.

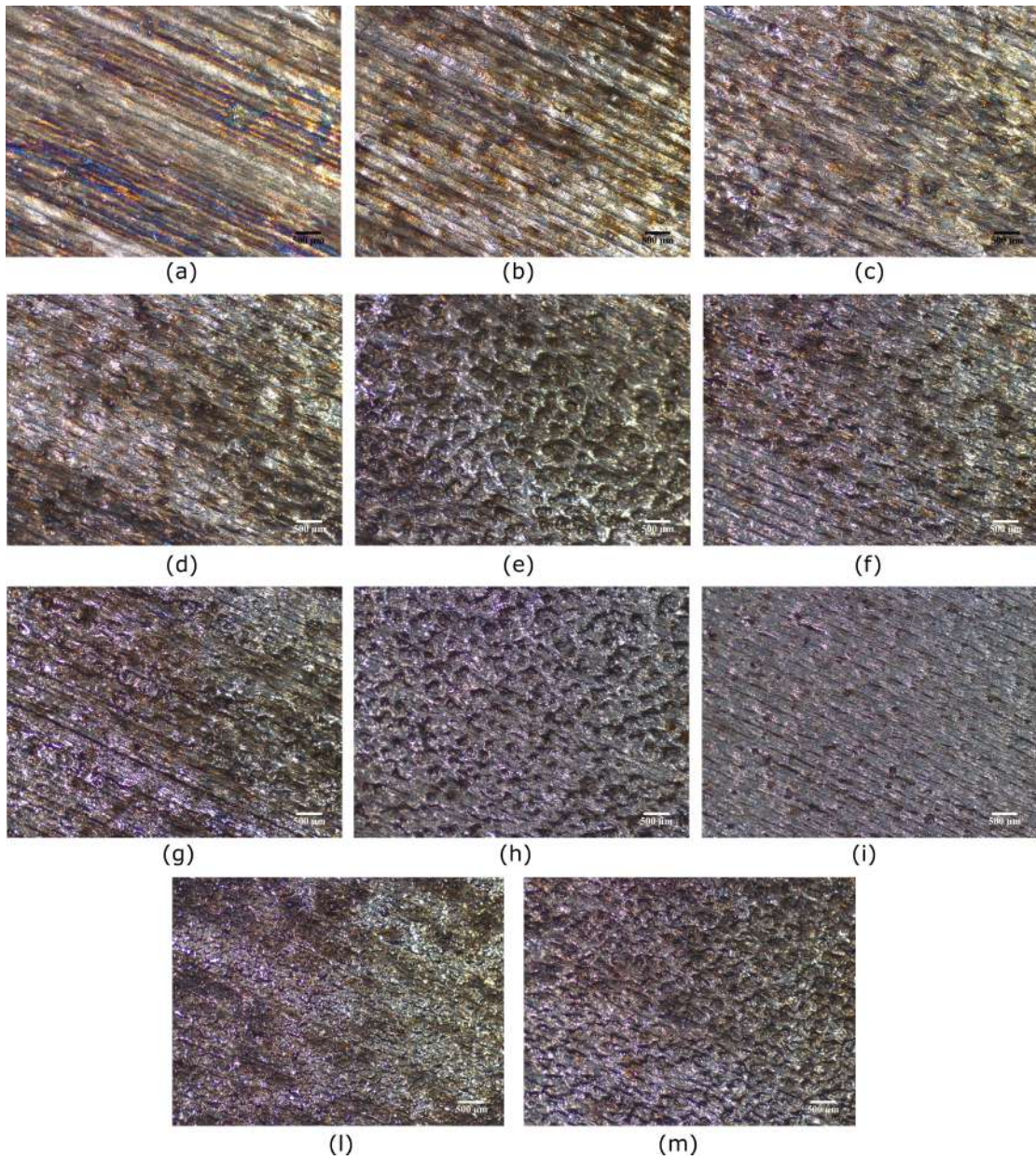


Figure 2.23: OM (stereomicroscope) images at 16X magnification of 316L single layers produced with a laser CF1000 and a power of 300 W and a scanning speed of a) 100 mm/s, b) 200 mm/s, c) 300 mm/s, d) 400 mm/s, e) 500 mm/s, f) 600 mm/s, g) 700 mm/s, h), i) 800 mm/s, l) 900 mm/s and m) 1000 mm/s.

On the basis of these first results it was decided to make a second test set with a lower laser power, 195 W, and with the scanning speeds of 300 mm/s, 400 mm/s, 500 mm/s, 600 mm/s, 700 mm/s, 800 mm/s, 900 mm/s, 1000 mm/s, 1100 mm/s, 1200 mm/s, 1300 mm/s, 1400 mm/s and 1500 mm/s. The new tests were also

Table 2.9: Energy density for all the samples of the second set.

Power [W]	Scanning speed [mm/s]	h_d [mm]	Layer thickness [mm]	Energy density [J/mm ³]
195	300	0.12	0.04	135
195	400	0.12	0.04	102
195	500	0.12	0.04	81
195	600	0.12	0.04	67
195	700	0.12	0.04	58
195	800	0.12	0.04	51
195	900	0.12	0.04	45
195	1000	0.12	0.04	41
195	1100	0.12	0.04	37
195	1200	0.12	0.04	34
195	1300	0.12	0.04	31
195	1400	0.12	0.04	29
195	1500	0.12	0.04	27

performed with the new laser, CS450 from Prima Industrie, that is a single mode with a minimum spot of $80 \mu\text{m}$. The values of layer thickness and h_d remained unchanged ($40 \mu\text{m}$ and 0.12 mm , respectively). The energy densities for the new samples are listed in the Table 2.9. To avoid effects due to the position of the disk in the platform, also for this test set, only the central disk was used in these jobs. However, on each disk four identical samples were produced, with the same parameters, in order to verify the repeatability of the process within the working area. The problems highlighted by the first tests, such as the presence of oxygen and fumes, were solved through modifications to the machine set up.

The second set of samples is presented in Figures 2.24, 2.25 and 2.26. From a first look it is possible to see that the oxidation phenomena are not present, but a little quantity of fumes are already present in some areas. The most serious thing is that, even if all parameters are equal, the four samples in each disc are different from each other. This phenomenon is more accentuated at low scanning speeds. For all the scanning speeds, the samples are melted in this order: 3, 1, 4 and 2, and always starting from the lower triangle (the darkest one). The first area melted in all the samples is the one with a greater deposition of fumes. Furthermore, the second sample produced (number 1 in the figure), for all the scanning speeds, is always the one with the most unstable melting zones (with holes and balling phenomena). The images also show that the deposition of fumes on the samples is reduced as scanning speed increases. This happens because, when the laser stops less on one point, it produces less melting fumes from the powder; more the laser insists on an area, more fumes are produced from the metal powder. Another problem that can immediately be seen is the absence of melting in some places, like missing laser

tracks. This is due to the operation of the laser and can be easily solved by the laser settings.

Also for this set of tests the samples were observed at the OM. The images obtained are reported in the Figures 2.27, 2.28, 2.29, 2.30, 2.31, 2.32, 2.33, 2.34, 2.35, 2.36, 2.37, 2.38 and 2.39 highlighting the areas of the layer from which they were taken. The samples produced with 300 mm/s (Figure 2.27) of laser speed have a fairly regular pattern, with some irregularities and balling phenomena concentrated in the samples number 1 and 3. In the samples number 2 and 4 the balling is almost absent, but there is an extensive problem of fume deposition. This difference between the specimens is particularly evident at low scanning speeds and may depend on the fusion strategy. As explained, in fact, in the previous section about the machine description, the jobs are printed strip by strip, with the movement of the carriage with the lamps and the fumes removal system. The specimens 1 and 3 are printed in the first stripes, while the specimens 2 and 4 in the second one. The differences may be due to a different efficiency of the fumes removal system based on the carriage position.

At 400 mm/s of scanning speed (Figure 2.28) the fumes problem is partly reduced compared to 300 mm/s specimens, but not entirely absent, especially for the layers number 2 and 4. Furthermore, the specimen number 1 shows a greater quantity of surface irregularities. The phenomena are even more widespread in the specimens with scanning speed of 500 mm/s (Figure 2.29) and are present in all the specimens. There are both holes on the surface and balling effect. At the scanning speeds of 600 mm/s and 700 mm/s (Figures 2.30 and 2.31, respectively), however, the irregularities of the fusion seem less marked (and all concentrated in the sample number 1), as well as the problem of the deposit of fumes, which is almost absent. The energy densities of these specimens are 67 and 58 J/mm³, very low values, so many surface defects were seen.

The specimens produced with scanning speeds in the range of 800-1500 mm/s present all the effects of the low energy density: thin laser tracks, track breaks and balling effect. At these speeds, however, the effect of the position on the specimens is less influential. In order to improve the productivity of the process and use high scanning speeds, it is necessary to increase the energy density. About this, another set of tests was planned with a laser power of 250 W and a h_d of 0.08 mm.

Furthermore, it is necessary to carry out many analyzes to verify the operation of the fumes removal system in the different positions of the carriage and to evaluate its influences on the final result.

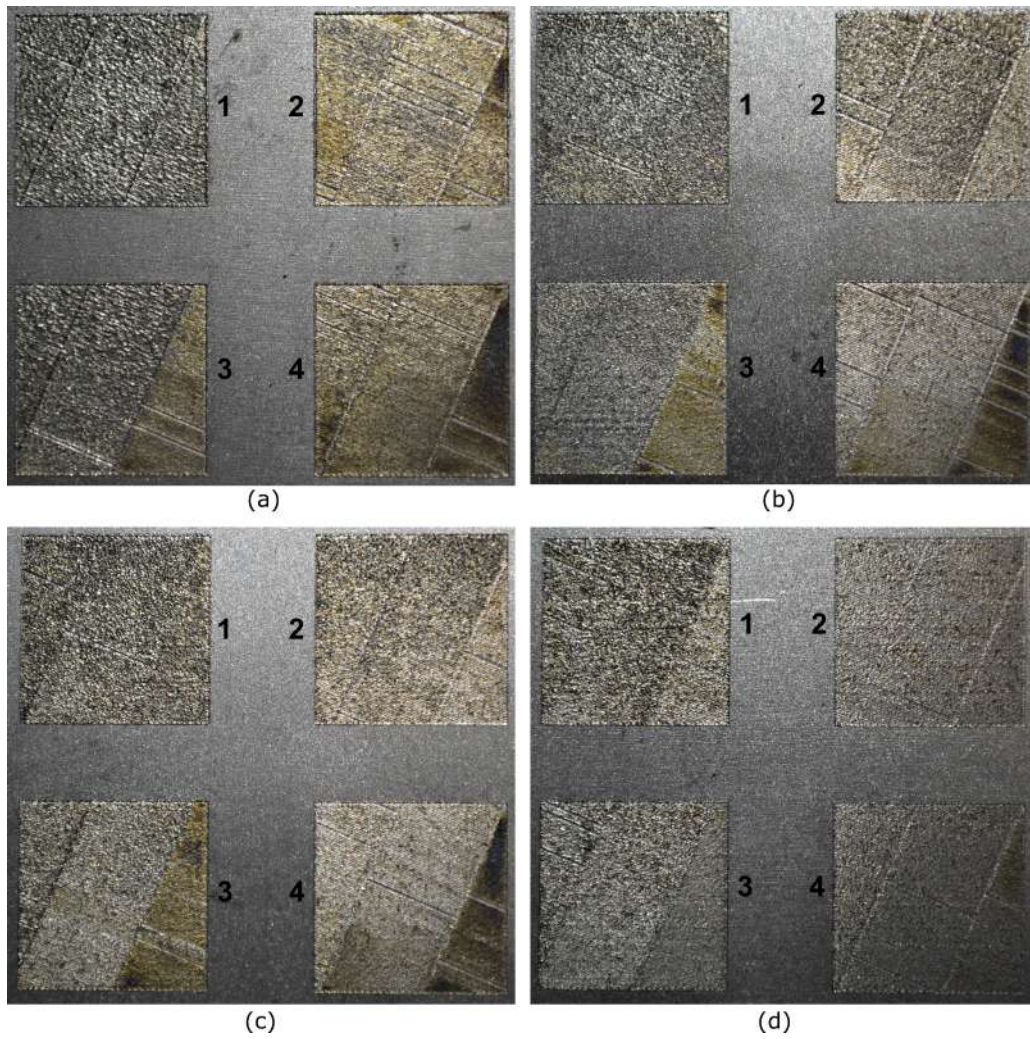


Figure 2.24: 316L single layer produced with a laser produced with a laser CS450 and a power of 195 W and a scanning speed of a) 300 mm/s, b) 400 mm/s, c) 500 mm/s and d) 600 mm/s.

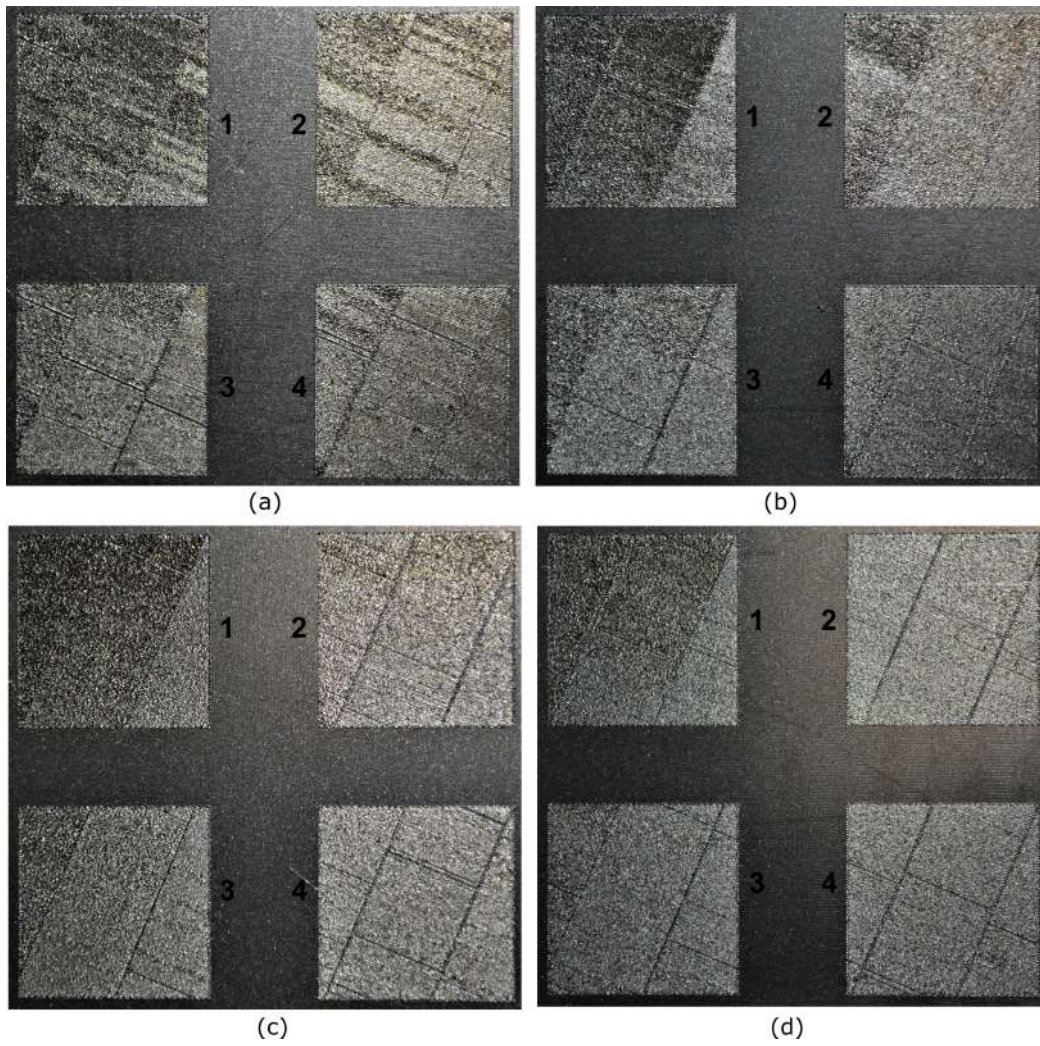


Figure 2.25: 316L single layer produced with a laser produced with a laser CS450 and a power of 195 W and a scanning speed of a) 700 mm/s, b) 800 mm/s, c) 900 mm/s and d) 1000 mm/s.

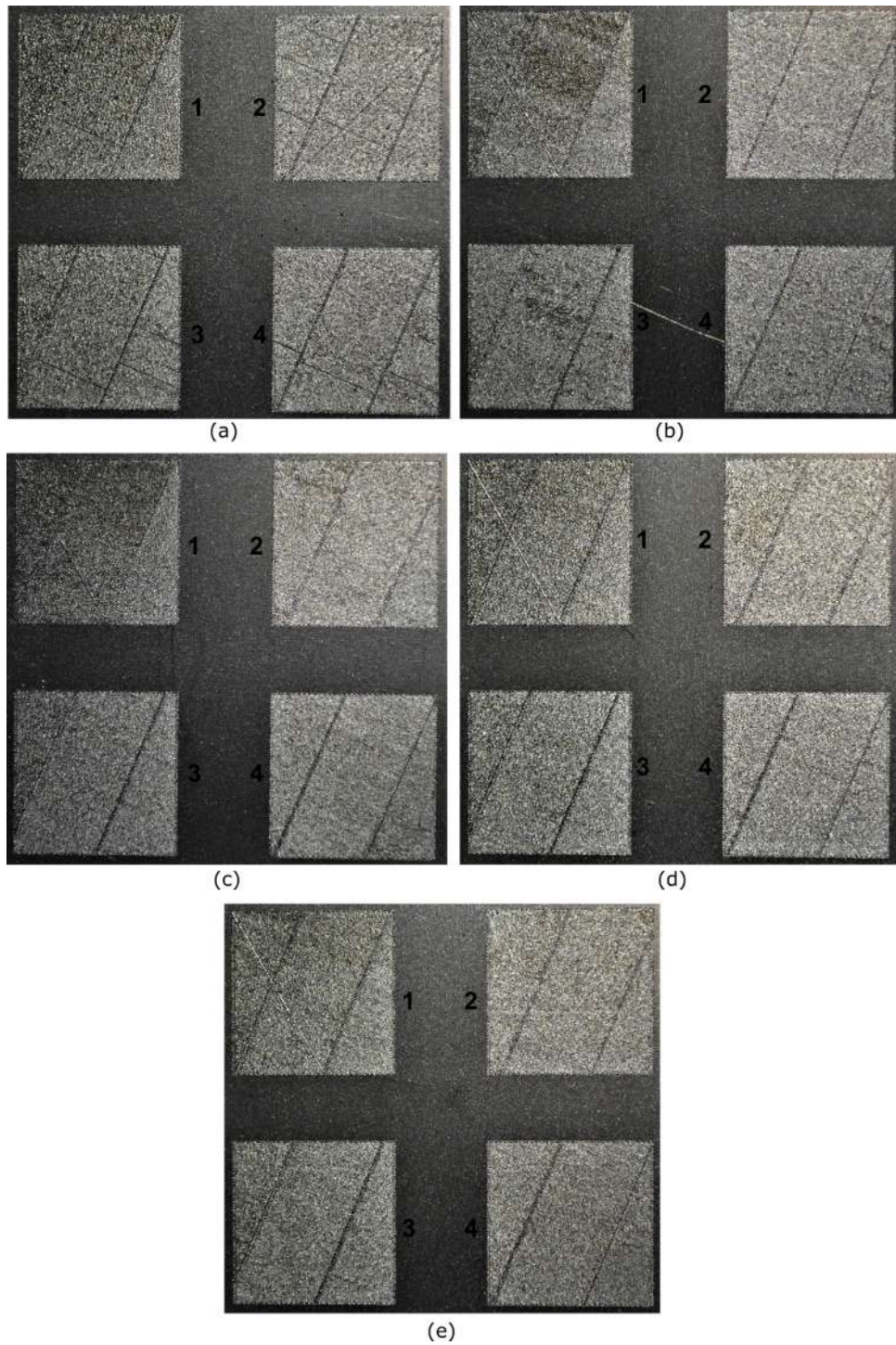


Figure 2.26: 316L single layer produced with a laser produced with a laser CS450 and a power of 195 W and a scanning speed of a) 1100 mm/s, b) 1200 mm/s, c) 1300 mm/s, d) 1400 mm/s and e) 1500 mm/s.

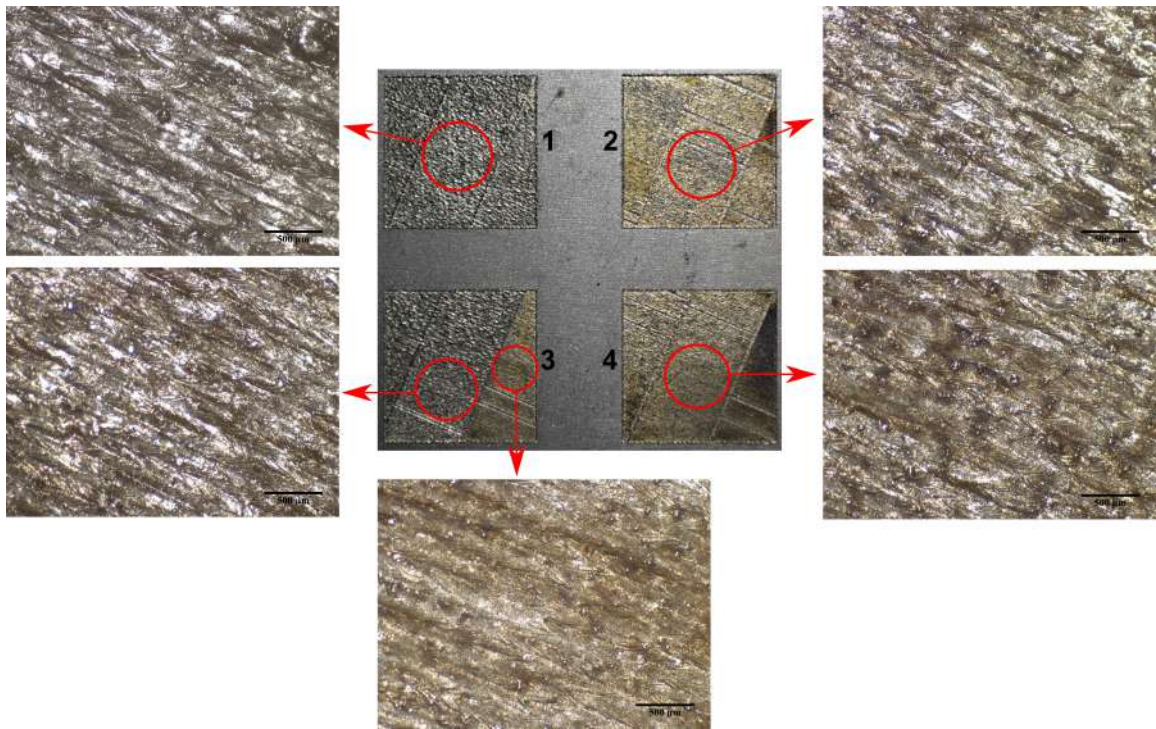


Figure 2.27: OM (stereomicroscope) images at 35X magnification of 316L single layers produced with a laser CS450 and a power of 195 W and a scanning speed of 300 mm/s.

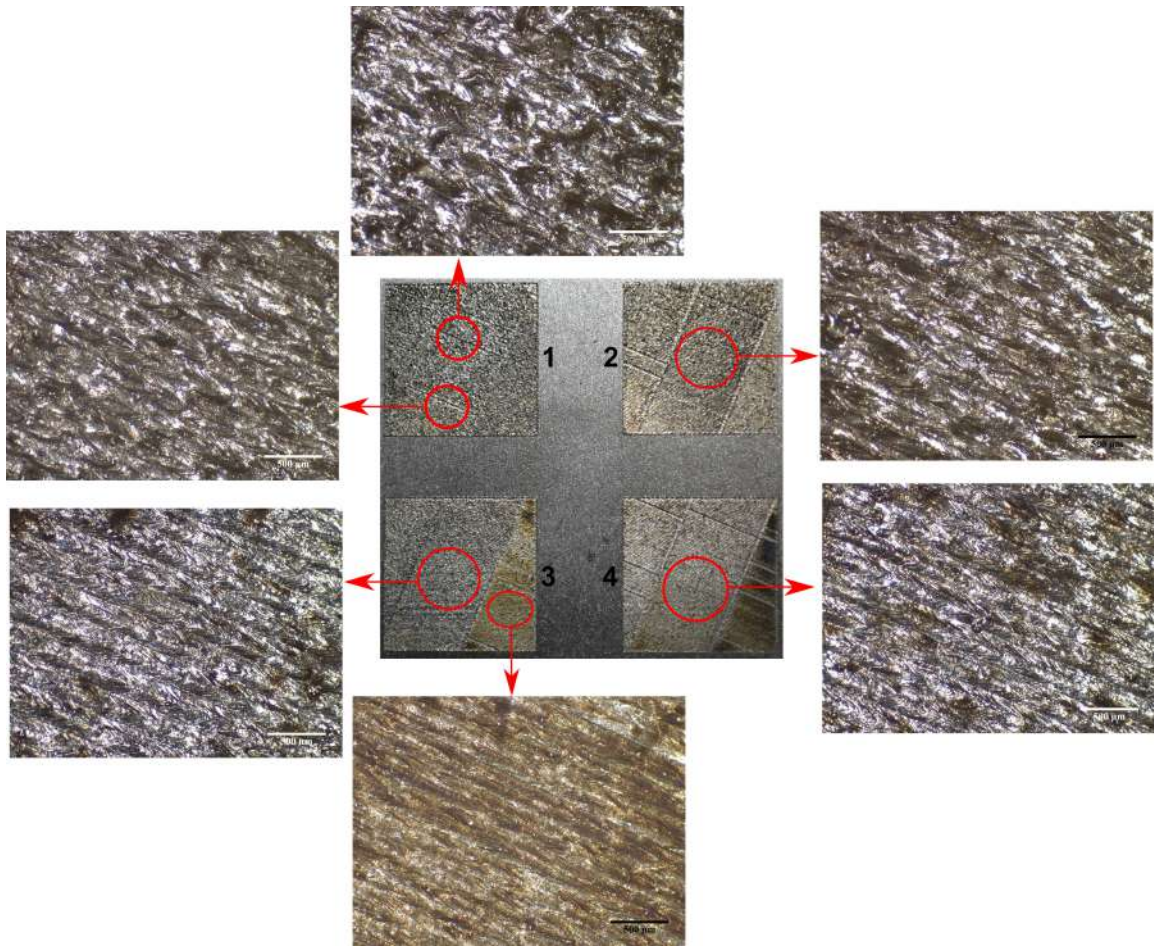


Figure 2.28: OM (stereomicroscope) images at 35X magnification of 316L single layers produced with a laser CS450 and a power of 195 W and a scanning speed of 400 mm/s.

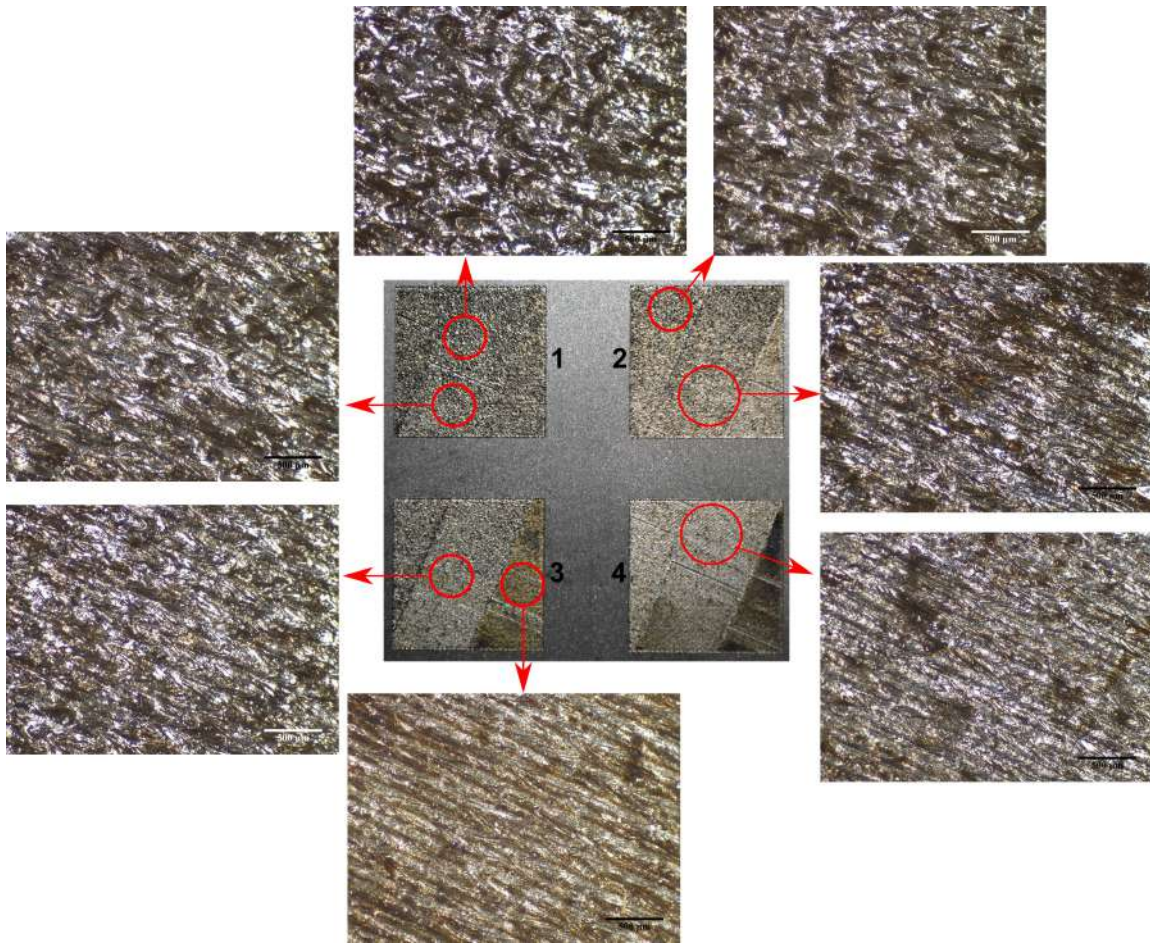


Figure 2.29: OM (stereomicroscope) images at 35X magnification of 316L single layers produced with a laser CS450 and a power of 195 W and a scanning speed of 500 mm/s.

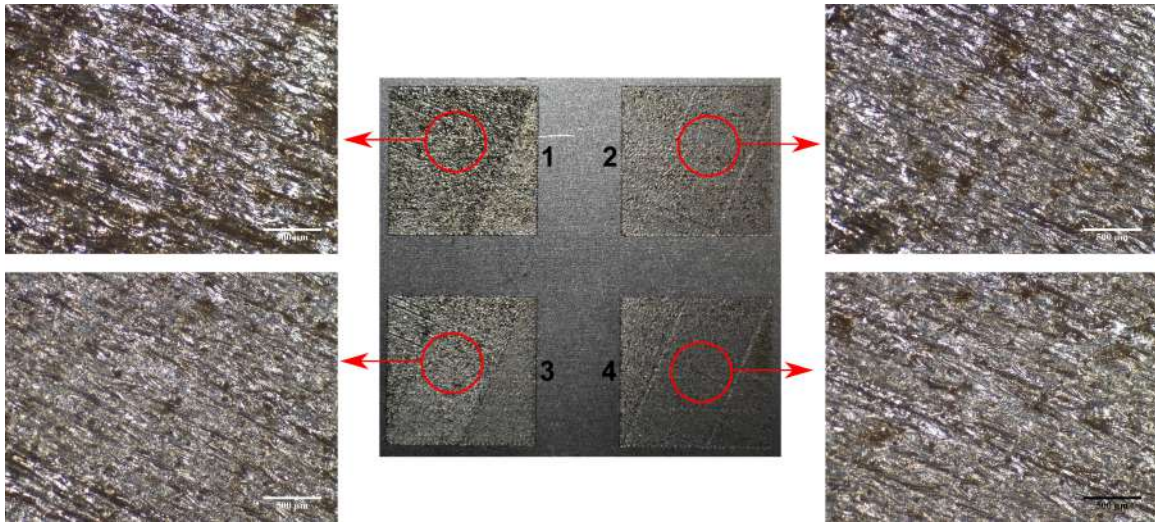


Figure 2.30: OM (stereomicroscope) images at 35X magnification of 316L single layers produced with a laser CS450 and a power of 195 W and a scanning speed of 600 mm/s.

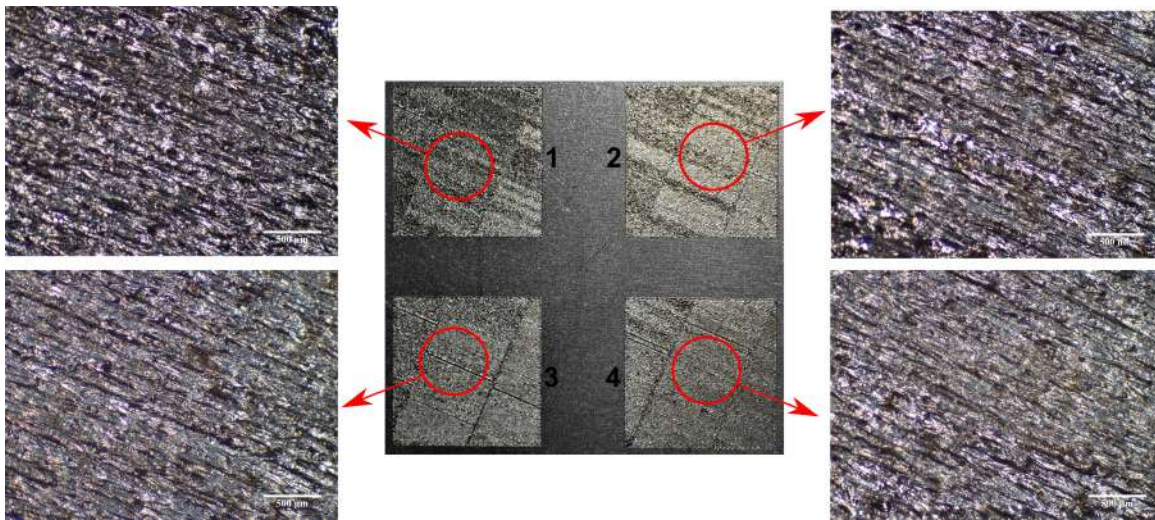


Figure 2.31: OM (stereomicroscope) images at 35X magnification of 316L single layers produced with a laser CS450 and a power of 195 W and a scanning speed of 700 mm/s.

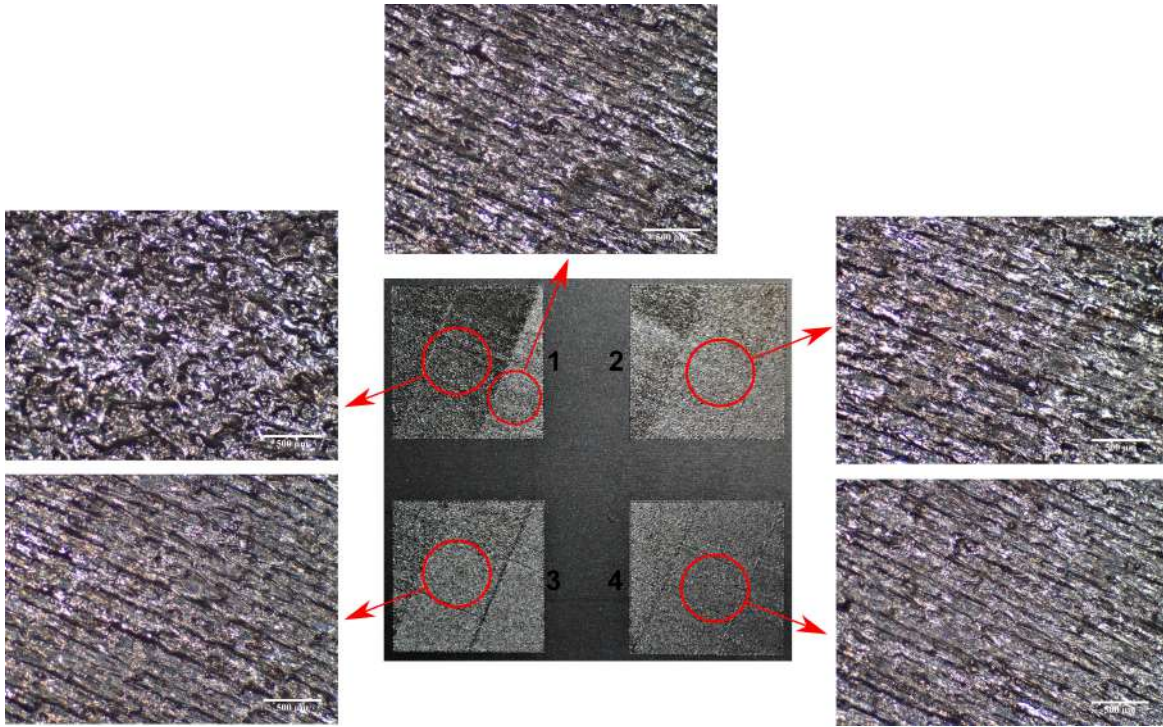


Figure 2.32: OM (stereomicroscope) images at 35X magnification of 316L single layers produced with a laser CS450 and a power of 195 W and a scanning speed of 800 mm/s.

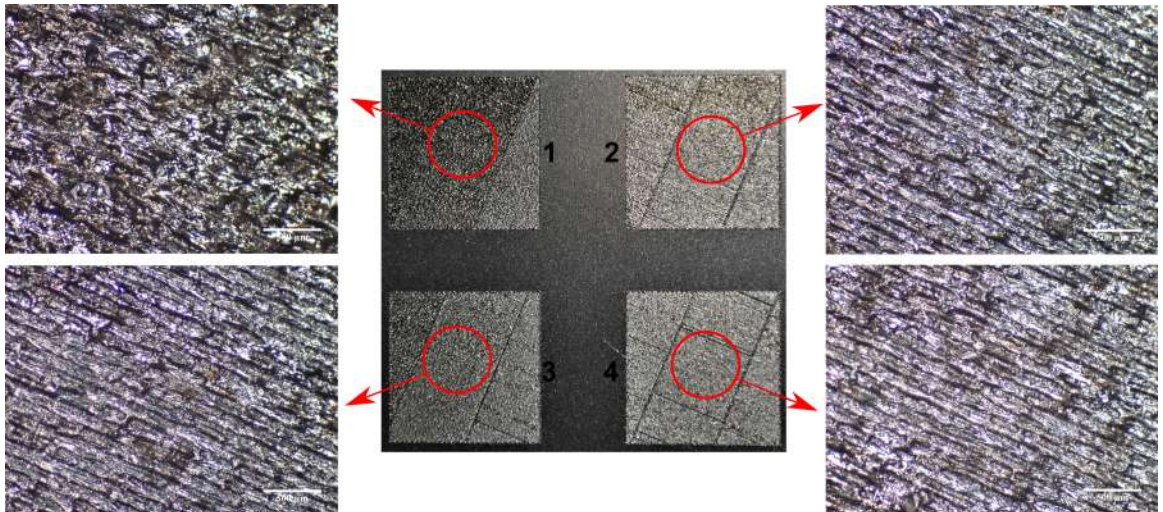


Figure 2.33: OM (stereomicroscope) images at 35X magnification of 316L single layers produced with a laser CS450 and a power of 195 W and a scanning speed of 900 mm/s.

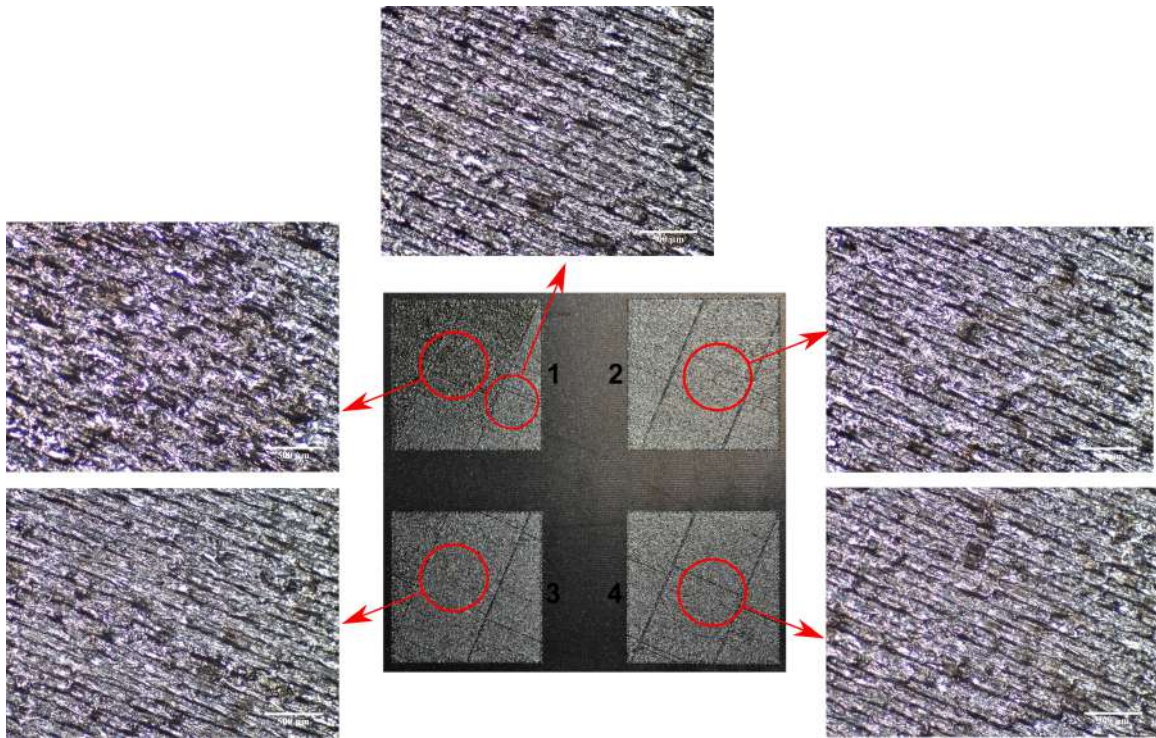


Figure 2.34: OM (stereomicroscope) images at 35X magnification of 316L single layers produced with a laser CS450 and a power of 195 W and a scanning speed of 1000 mm/s.

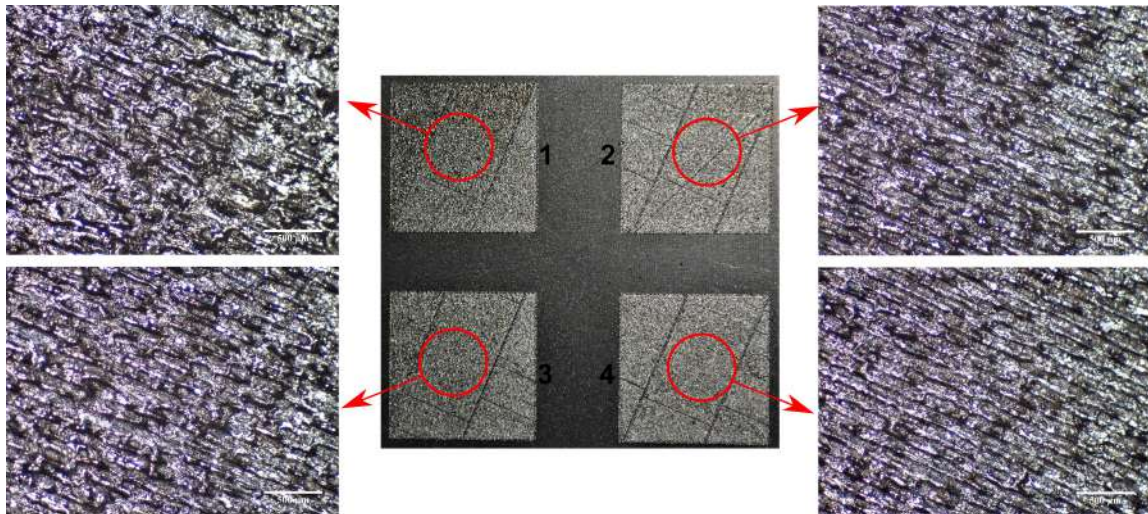


Figure 2.35: OM (stereomicroscope) images at 35X magnification of 316L single layers produced with a laser CS450 and a power of 195 W and a scanning speed of 1100 mm/s.

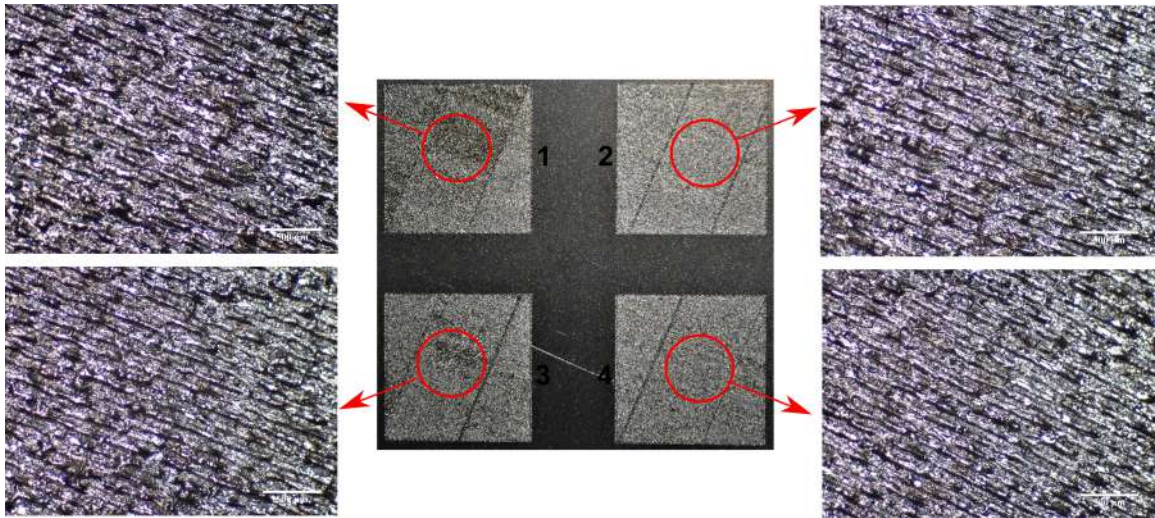


Figure 2.36: OM (stereomicroscope) images at 35X magnification of 316L single layers produced with a laser CS450 and a power of 195 W and a scanning speed of 1200 mm/s.

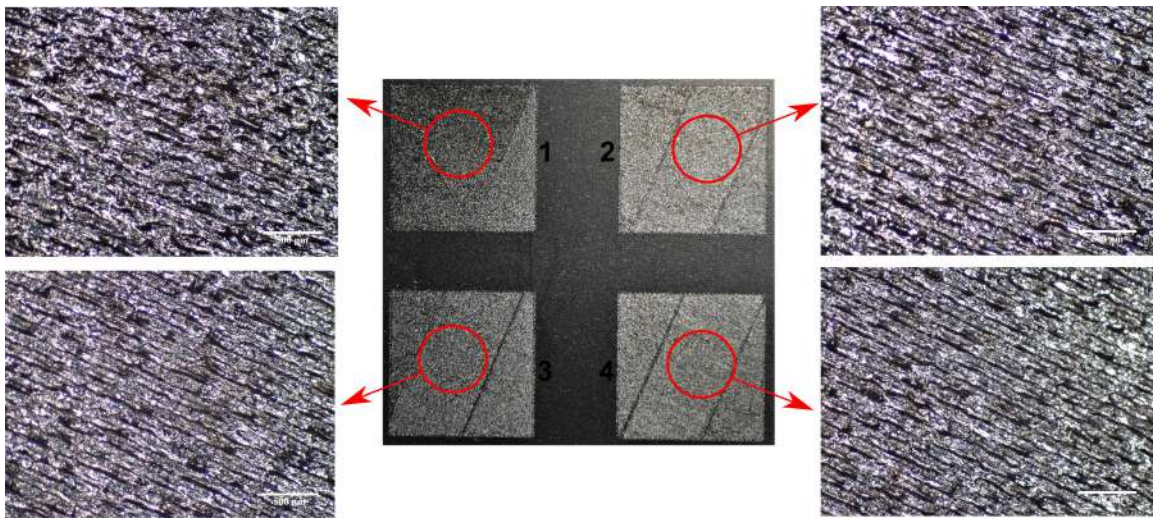


Figure 2.37: OM (stereomicroscope) images at 35X magnification of 316L single layers produced with a laser CS450 and a power of 195 W and a scanning speed of 1300 mm/s.

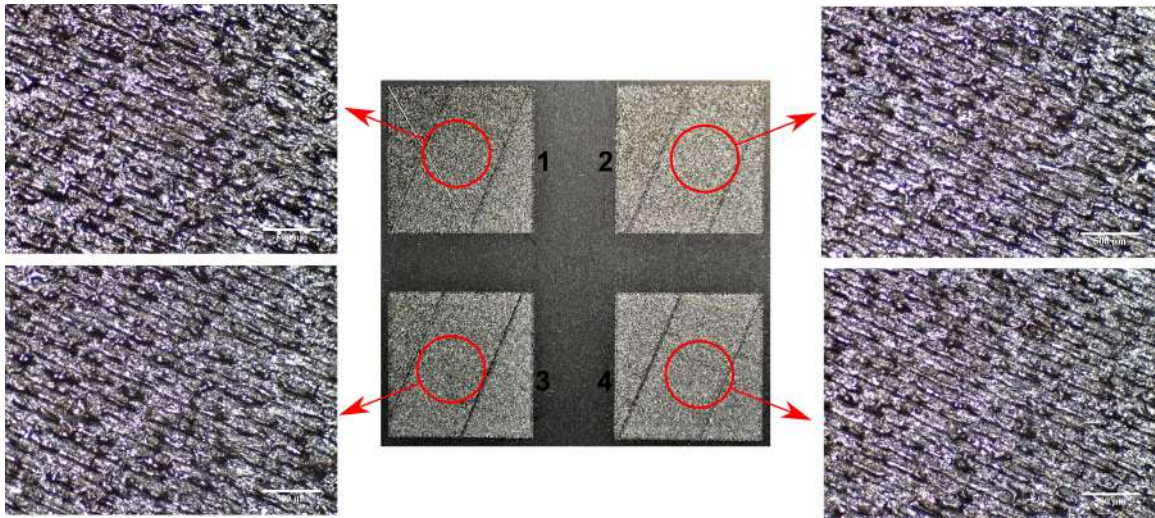


Figure 2.38: OM (stereomicroscope) images at 35X magnification of 316L single layers produced with a laser CS450 and a power of 195 W and a scanning speed of 1400 mm/s.

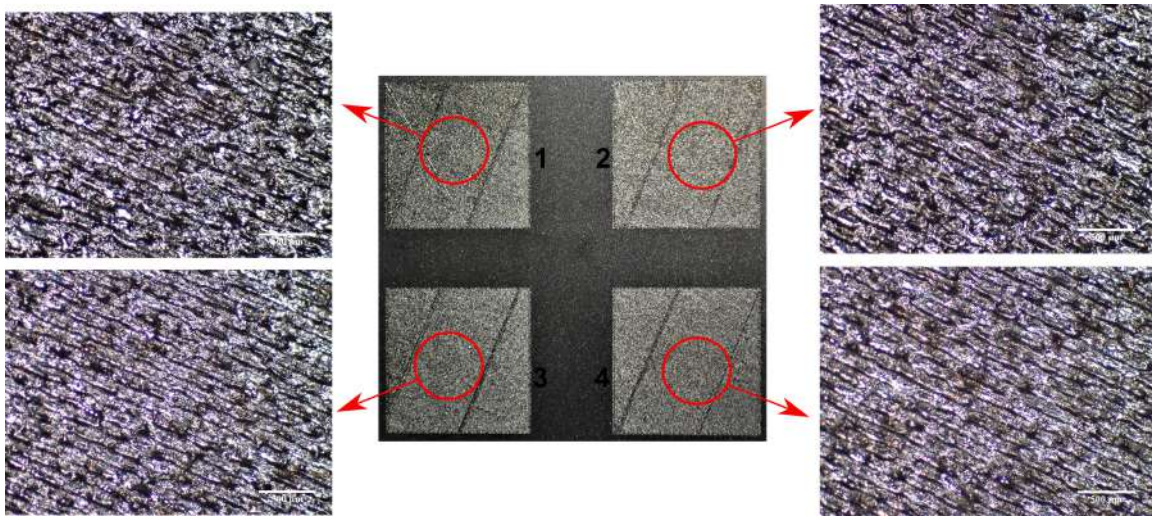


Figure 2.39: OM (stereomicroscope) images at 35X magnification of 316L single layers produced with a laser CS450 and a power of 195 W and a scanning speed of 1500 mm/s.

Chapter 3

Trabecular structures

3.1 Trabecular structures: state-of-art

One of the most important aspects in the design of a component is to evaluate the material. The material must have a mechanical and thermal resistance suitable for use with a good safety margin. The compromise that is always sought and difficult to obtain is to have the best mechanical performance with the lowest possible density. As can be seen from the Ashby diagram in the Figure 3.1a, the density increases with increasing mechanical strength for all materials. Another constraint is the temperature of use of the component: as shown in Figure 3.1b, materials with low density and resistance also have a limited use temperature. In general, metallic materials have good mechanical performance and have a good temperature resistance based on the type of alloy selected.

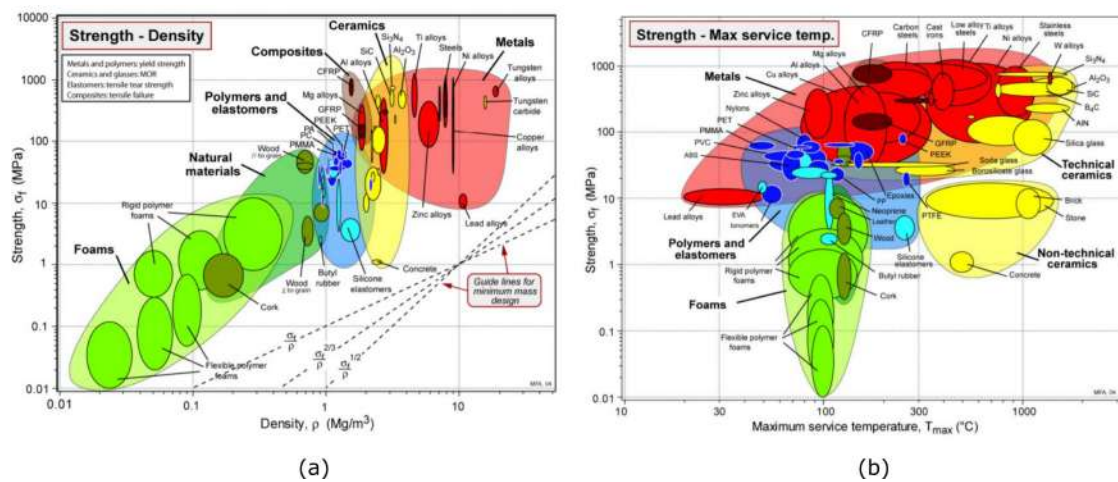


Figure 3.1: Ashby diagrams a) strength vs. density and b) strength vs. maximum service temperature [6].

One of the ways often used to exploit the good characteristics of materials, limiting the density of the pieces is the use of cellular structures. Structures of this type were always present in nature: wood and bones are among the most characteristic examples.

The use of foam is due to the particular characteristics that this structure has compared to the dense material. Foams of polymeric materials and glass are often used for thermal insulation due to their low thermal conductivity. They are also excellent in construction, where they are used inside the walls of buildings to improve their insulation. The good impact absorption and the good compressive strength of the foam also make them suitable for packaging, as they protect the contents from external shocks and pressures. Moreover, the low density of the package does not make it heavier and does not aggravate transport costs. The compressive strength makes cellular structures also good structural materials, especially if the load is properly oriented to the shape of the cells. A typical example of this use is the sandwich panels, widely exploited in the aerospace field due to the low density, which allow to obtain the mechanical strength with a limited weight. Sandwich panels consist of two surfaces between which there is a cellular core, as schematized in Figure 3.2. Generally the shape of the cells in the core is honeycomb: it is a structure obtained from the bending of sheets of different materials that recalls the shape of bee hives. The core and the two surfaces are held together by the glue. The foam of ceramic and metallic materials are also suitable as catalytic supports due to the high specific surface area, while the cellular structures of metals with high thermal conductivity can be used as heat exchangers.

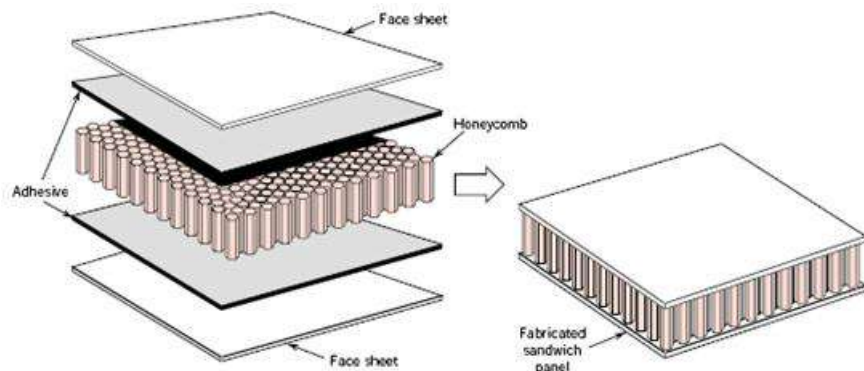


Figure 3.2: Sandwich panel composition.

Honeycomb cellular structures are regular two-dimensional geometries with a generally hexagonal section and are obtained by bending the sheets and gluing them together. Foams are three-dimensional structures with irregularly shaped cells and sizes indicated by a range of values. They can in fact be made in different ways: for metal foam the most used method is the introduction of a gas or a blowing

agent that produces bubbles in the liquid metal. Depending on the type of blowing agent, temperature and many other factors to be controlled, the size and final shape of the cells can be adjusted. Another technique used is investment casting: a foam in polymeric material is coated with metal, the polymer is then eliminated, leaving only the metal foam. An example of metallic foam made with this technique is Duocel. The foam cells are divided into open cells, when they are connected by struts, and in closed cells, when they are bounded by thin walls. The connection angles between the faces and the struts greatly influence the mechanical behavior of the cell. According to the Gibson-Ashby model, the mechanical characteristics of the foam are reported as relative values with respect to the quantities of the equivalent full solid (with the same dimensions and material). The relative density, the compressive modulus and the compressive strength are calculated respectively using the equations 3.1, 3.2 and 3.3.

$$\rho = \frac{\rho_f}{\rho_s} \quad (3.1)$$

$$\frac{E_f}{E_s} = C_1 \left(\frac{\rho_f}{\rho_s} \right)^2 \quad (3.2)$$

$$\frac{\sigma_f}{\sigma_s} = C_2 \left(\frac{\rho_f}{\rho_s} \right)^{1.5} \quad (3.3)$$

where ρ is the relative density, ρ_f is the density of the foam, ρ_s of the solid, E_f is the Young modulus of the foam, E_s is the Young modulus of the solid, σ_f is the compressive strength of the foam, σ_s is the compressive strength of the solid, C_1 and C_2 are specific constants that include all the geometric features of proportionality.

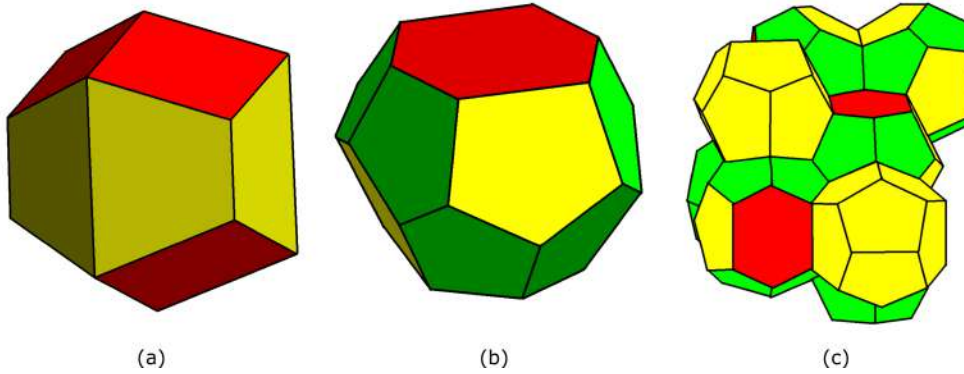


Figure 3.3: a) Rhombic dodecahedron [139], b) Tetrakaidecahedron [167] and c) Waire and Phelan structure [174].

Three-dimensional cells have been studied for many years in their regular version and different geometries have been evaluated based on their ability to fill the space.

In 1873 Plateau spoke of rhombic dodecahedron (Figure 3.3a), while in 1887 Kelvin proposed geometry called tetrakaidecahedron (Figure 3.3b). More recently, in 1994, Waire and Phelan presented, through the use of software, a structure that filled all the space formed by a cell with 14 faces (12 pentagonal and 2 hexagonal) similar to that of Kelvin, and by a cell called pyritohedron (Figure 3.3c).

Currently cellular structures with regular cells have been extensively studied for structural, medical and heat exchange uses [88, 27]. Thanks to PBF technologies, in fact, it is possible to create trabecular structures with a controlled porosity. The complexity of the structure, the size of the struts and the shape of the cells are parameters compatible with the production technology, which allows to obtain a custom product according to the needs. The interest in these structures is proved by the large number of studies on the subject, in particular on feasibility, on fluid-dynamic and structural simulations and on mechanical tests [20]. The trabecular structures analyzed were produced with EBM and SLM technologies in different materials including Ti6Al4V alloy [115], 316L stainless steel [153], 18Ni maraging 300 steel [92] and AlSi10Mg alloy [133]. The characteristic of trabecular structures that is generally varied is the shape of the cell. Some examples are the body-centered cubic (bcc) cells, body-centered cubic with vertical struts along the Z axis (bccz), face-centered cubic (fcc) and face and body-centered cubic with vertical struts along the Z axis (fccz), which are geometries formed by struts and intersection. Other types of cells are obtained from three-dimensional surfaces such as the Schoen Gyroid [153, 15] and the Schwartz Diamond [133]. In addition to the shape of the cell, the other parameters that are most often varied to evaluate the behavior of the structures are the size of the cell and the fraction in volume of solid. For aluminum alloys such as AlSi12Mg the paper [16] analyzed various forms of cells such as bcc, bccz, fcc and fccz. The results showed that the bcc and fcc cells have a high concentration of compression stresses at the intersection nodes of the struts that causes a failure of the structure due to low loads. The bccz and fccz cells, on the other hand, have better mechanical performances thanks to the presence of vertical struts in the cell. The paper [10] analyzed the effects of the process parameters necessary for cell construction, such as the laser power and the scanning speed, on mechanical performance. The specimens were produced with SLM technology in AlSi10Mg with bcc geometry and were tested in compression. The mechanical tests revealed that with low scanning speed and high laser power the performances are better because the high power of the laser causes thicker struts and a low speed reduces the porosity of the structure. In the work [70] the mechanical compression behavior of trabecular structures with bcc cell with a density gradient along the Z axis was evaluated. The fracture mode of the specimens with uniform density is a failure of the plane at 45° with respect to the Z axis and then a densification of the structure, while the specimens with graded density have a collapse of the layers parallel to the X-Y plane starting from the less dense one. In addition to the structures formed by struts, in the literature [133, 187] Schwartz Diamond and Schoen

Gyroid geometries in AlSi10Mg have been also evaluated. Compression tests have shown that, as required by the Gibson-Ashby model, increasing the solid volume fraction of the specimens increases the mechanical performance of the structures. In this thesis work different shapes of trabecular cells were analyzed, also varying cell size and solid volume fraction, to evaluate which solution is more suitable for the realization of a sandwich panel with trabecular core by SLM technology.

3.2 Anti-ice systems

One of the most dangerous phenomena during the flight of an airplane is the formation of ice on surfaces. There are some parts of the plane that, if covered with a layer of ice, can stop performing their functions [180, 82, 13]. The ice acts mainly with a decrease in lift and with an increase in weight, factors that could cause a loss in altitude; moreover a decreasing in thrust and drag also occurs, with a consequent loss in lift and speed. This factors are schematized by the comic image in Figure 3.4a.

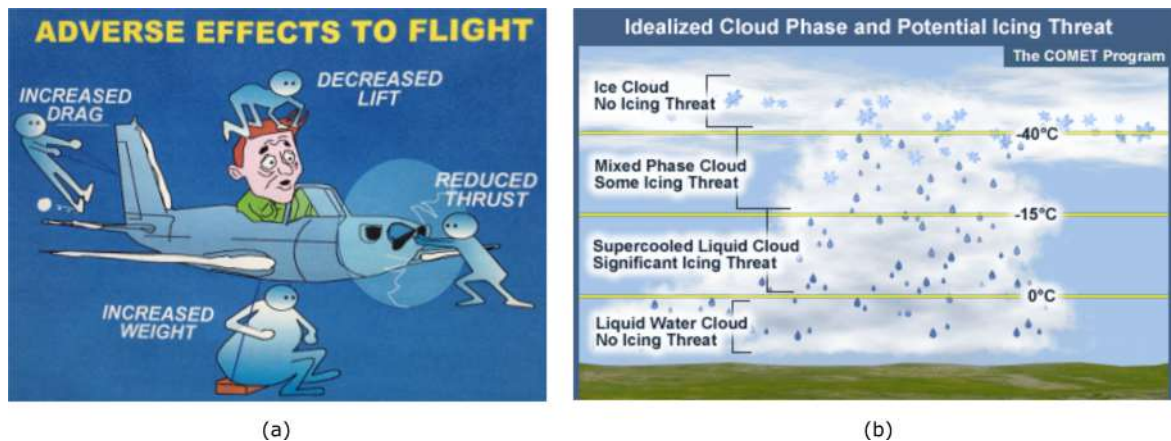


Figure 3.4: a) Schematic image of the four main effects of ice: lift, thrust and drag decreasing and weight increasing. b) Effect of temperature on the amount of SLD in the clouds [80].

This always happens for the wings, which due to the formation of ice lose their aerodynamics and weigh down the structure. Another part that must never be blocked by ice is the static Pitot system, which allows to assess the altitude and the speed of an aircraft. The speed is evaluated through a dynamic pressure detected by the anemometer: this dynamic pressure is the difference between the pressure obtained from the Pitot tube and the static pressure. The higher the dynamic pressure, the higher the aircraft's speed. During the flight Airbus A330-203 Air France 447 Rio de Janeiro - Paris 2009 some ice formed on the Pitot tube,

distorting the detection of pressure. The wrong value of the dynamic pressure led to a wrong assessment of the plane's speed. This caused the stall of the aircraft, which finally crashed [32]. The formation of ice occurs in the presence of humidity in the atmosphere during the flight in a temperature range from $-40\text{ }^{\circ}\text{C}$ to $0\text{ }^{\circ}\text{C}$ [28]. The humidity in the clouds is in the form of drops of water in the liquid state below $0\text{ }^{\circ}\text{C}$, defined as Supercooled Large Droplets (SLD) and with a minimum diameter of $50\text{ }\mu\text{m}$ [152]. These drops are still in liquid form because the nucleation process has not been activated. They are responsible for the formation of ice on aircraft surfaces. In fact, when they encounter the surfaces of the planes, the surface tension breaks down and the subcooled water contained in the drop forms the ice. The humidity of the clouds that are found with a temperature between $0\text{ }^{\circ}\text{C}$ and $-15\text{ }^{\circ}\text{C}$ is almost completely in the form of SLD. The clouds between $-15\text{ }^{\circ}\text{C}$ and $-40\text{ }^{\circ}\text{C}$ are mixed, and contain both SLD and ice crystals, formed by the vapor. Finally, clouds with temperatures lower than $-40\text{ }^{\circ}\text{C}$ contain almost exclusively ice crystals, which do not stop on the aircraft surfaces and are not a problem for flight [160].

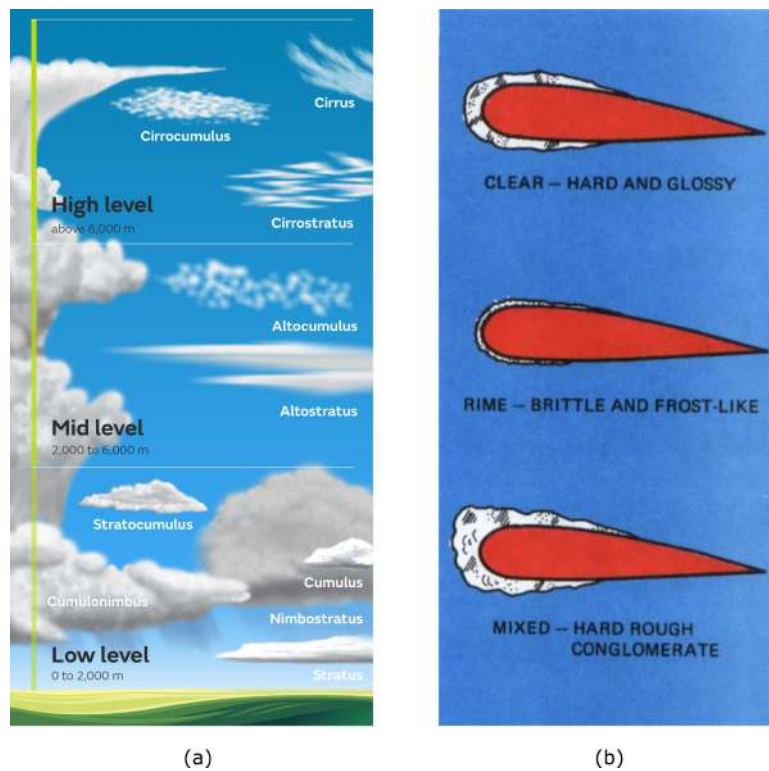


Figure 3.5: a) The classification of the clouds varying the altitude [33] and b) the classification of ice formed on aircraft surfaces [79].

The temperature, the level of humidity and the size of the water droplets in the

air are the three factors that most influence the type of ice that forms on the aircrafts surfaces. Furthermore, the size of the water drops depends on temperature (when the temperature is high, close to 0 °C, the water drops are larger) and on the type of cloud that is crossed. The classification of the types of clouds at different altitudes that can be encountered during the flight is shown in Figure 3.5a. The largest drops, from 100 µm, are found crossing the clouds defined *cumulonimbus*: they are clouds that develop vertically and are responsible for atmospheric instability. The types of clouds called *cumulus* and *stratocumulus* are found at low altitude and contain moisture in form of drops of about 50 µm in diameter. Finally, high-altitude clouds, such as *cirrostratus*, have smaller droplets, around 40 µm.

There are mainly two types of ice: *clear ice* and *rime ice*. To these is added a third type which is a mixture of the first two: the *mixed ice*. A graphic representation of the three types of ice is shown in the Figure 3.5b. The *clear ice* is formed between -10 °C and 0 °C; in this temperature range the worst conditions occur because the SLD in the clouds are large and very numerous. The water drops meet the surface of the plane and start the solidification process, which takes place quite slowly due to the size of the SLD and the not too low temperatures. The drops, before becoming completely solid, have time to expand on the surfaces, until form a homogeneous film. The result is a layer of hard, shiny and transparent ice that is difficult to identify: from this the name clear ice. This type of ice is the most difficult to remove. Between -40 °C and -15 °C the *rime ice* is formed. In this temperature range there are small droplets of water mixed with ice crystals. The drops solidify rapidly once in contact with the aircraft due to its smaller size and low atmospheric temperature. The result is a very porous and friable layer of ice called rime ice. This type, unlike the previous one, can be easily eliminated from the critical areas by a suitable de-ice system. Finally, from -15 °C to -10 °C there is an intermediate situation between the previous two cases which forms a typology called *mixed ice* [53, 183, 84, 81].

Given the criticality of the problem of ice for flight safety, studies in the aerospace field on anti-ice systems have always been a fundamental aspect. On the one hand, methods have been devised to make the sensors able to detect the presence of ice more precise and reliable [73]; on the other hand, the ice removal systems on the aircraft are improved to make them more efficient [75, 143, 142].

Ice removal systems are present on all critical surfaces [83]. In this thesis particular attention will be given to the systems installed on the wings leading edge. These systems work mainly in two ways [3]:

- the *de-ice* systems allow the formation of an ice layer and when it reaches a certain thickness they intervene to remove it;
- the *anti-ice* systems work continuously, keeping the conditions that prevent the formation of ice constantly.

Among the systems that work as anti-ice there is the category defined *chemical anti-ice* and it works by lowering the freezing point of water on the wing surface. This goal can be achieved by using a freezing point depressant liquid, such as glycol. The glycol is sprayed onto the surface of interest and works both in ice prevention and as a rain repellent [54]. The systems called *Electromagnetic Impulse De Icing (EIDI)* are de-ice. Some generators create eddy currents, which form movements on the surface and cause the separation and breaking of the newly formed ice [184, 91]. Another system is the *pneumatic de-ice* one, which works by mechanically breaking the ice layer on the surface. The structure, as shown in the Figure 3.6a, consists of rubber chambers attached to the surface of the leading edge. When the ice layer reaches a certain thickness, the chambers are filled with air, swell and break the layer, removing the ice. One of the main problems of this system is the damage that the newly removed pieces of ice can cause to the aircraft colliding with some parts [91].

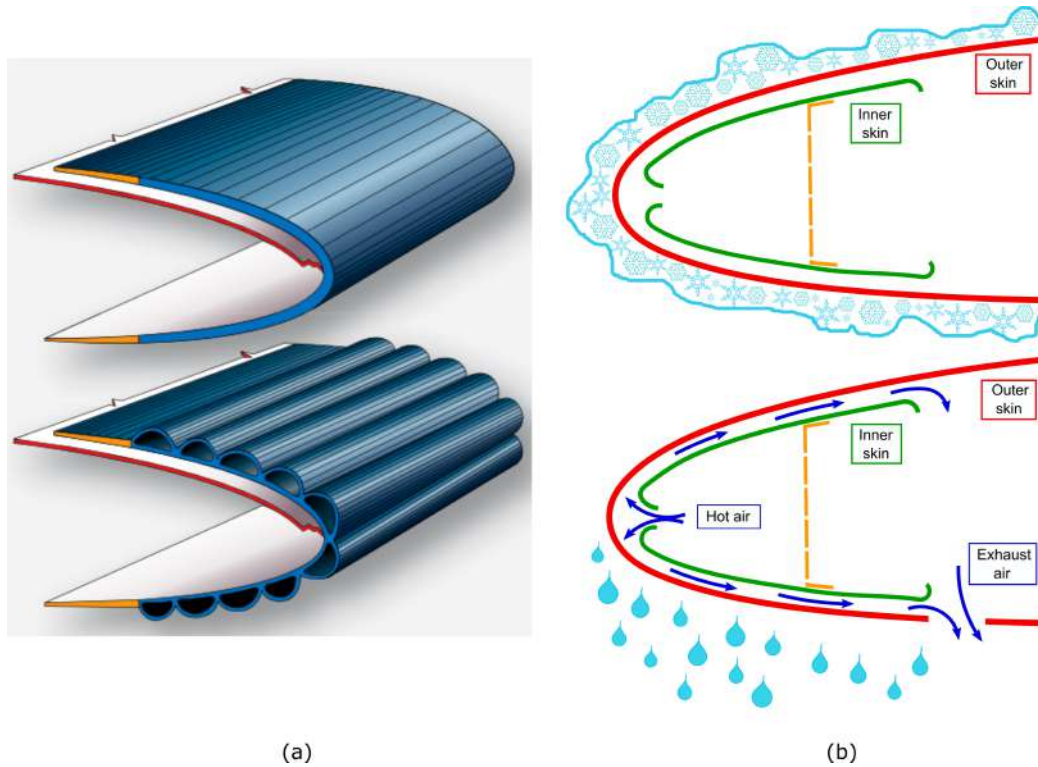


Figure 3.6: a) Pneumatic de-ice system [130] and b) hot-air anti-ice system.

A very common category of anti-ice is thermal anti-ice systems. The basic principle that accumulates them is to supply heat to the outer surface of the wing leading edge. The heat must be sufficient to reach a temperature high enough to prevent the formation of the ice layer. The thermal systems differ according to the

way in which heat is supplied. A widely used typology is the *electric anti-ice*. Heat is supplied to the leading edge through resistors, which heat the surface by Joule Effect. The resistors are integrated in the structure of the leading edge and work continuously to keep the external surface temperature. This system is very often used also for small parts of the aircraft and for helicopter blades, also affected by the possible formation of ice [184, 69]. The most widespread thermal solution for wings leading edges is the *hot-air* anti-ice system. In this case the heat is transferred to the external surface by a flow of compressed hot air taken from the motor. The air passes through two surfaces, one internal and one external, and at the end of the path it is discharged into the environment. The overall system consists of two sheets with the shape of the leading edge, gluing and welding between the parts, air inlet tubes and drain holes [53, 121, 85]. The operation is schematized in the Figure 3.6b. The anti-ice hot-air can work in two ways, one with a lower power with a temperature on the surface such as to keep the SLD in liquid state and one with a higher power level with a temperature such as to vaporize the droplets.

The innovative anti-ice system that will be discussed in this thesis belongs to the hot-air type.

3.3 Proof Of Concept

An innovative anti-ice hot-air system, which uses trabecular structures as heat exchangers, was patented [102, 25, 112, 26, 100]. The structure consists of a sandwich panel with the shape of the leading edge of the aircraft wing of the aircraft. The panel is formed by an external skin, an inner skin and a trabecular core. The trabecular core with open cell works as heat exchanger and performs structural functions such as mechanical resistance to bird strike. The panel becomes itself the leading edge of the wing. The PBF technology makes possible to produce all the parts that compose the system in a single component, including the hot air supply tubes. This allows to eliminate the bonding and welding of traditional systems, which lower the reliability of the structure. A scheme of a section of the innovative hot-air system is shown in the Figure 3.7.

As all hot-air de-icing systems, the compressed hot air is drawn directly from the engine. It is introduced into the panel by pipes which, in the Figure 3.7, are called *multiple hot air inlets*. Inside the panel the hot air is in contact with the trabecular structures with high specific surface area to which it supplies heat. This heat allows the external skin to reach a temperature high enough to prevent the formation of a layer of ice on the wing leading edge during the flight. The advantage of using trabecular structures inside the panel is not only the lightening of the structure, but also the optimization of the heat exchange: a more efficient heat exchange allows to reach the temperature with a small amount of hot air. This means using less compressed hot air and limiting aircraft consumption. The hot air, once the

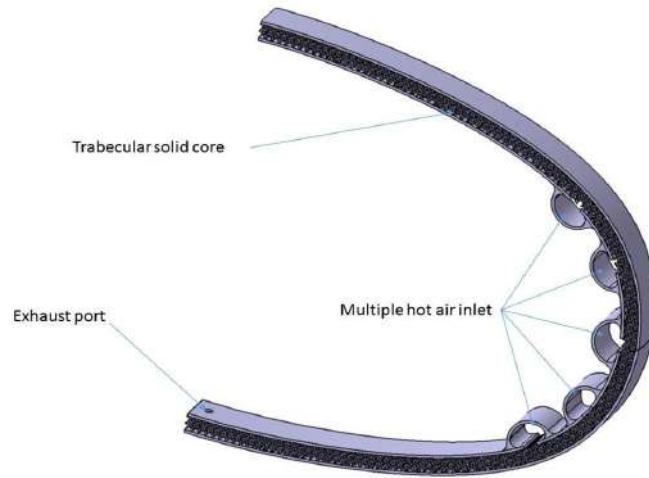


Figure 3.7: A scheme of the innovative hot-air anti-ice system.

path inside the panel is finished, is discharged outside the plane through openings, which in the Figure 3.7 are called *exhaust ports*. To further improve this operation, an aluminum alloy, AlSi10Mg, was chosen as the material. Like all aluminum alloys it has a good thermal conductivity that optimizes heat exchange and a low density that lightens the structure. Furthermore the alloy is compatible with the temperature range in which the anti-ice system operates, which vary from 130 °C to 150 °C depending on the type of aircraft and the size of the wing. AlSi10Mg is also a material widely used in L-PBF technology and allows to obtain components with excellent mechanical and thermal properties. For some aircraft that proceed at supersonic speeds, the mechanical stresses suffered are excessive for materials such as Al alloys. For these types of aircraft, a titanium alloy, Ti6Al4V, has been proposed as a material for the construction of the anti-icing panel. Titanium does not have all the advantages of aluminum in terms of thermal conductivity and low density, but has a greater mechanical resistance, which makes it suitable for this application.

The patent of the innovative anti-ice system was funded by the Proof Of Concept of Politecnico di Torino. The research activities carried out had the objective of developing a functional prototype, taking the project from an initial state of TRL 0 to a state of TRL 5. The first phase of the tests was the mechanical tests.

Uniaxial compression tests were carried out on trabecular specimens to evaluate the behavior of six cell types, varying three cell size values and three solid volume fraction of the specimens. This first set of tests allowed to restrict the number of geometries and to make the subsequent phases more specific. Subsequent mechanical tests were uniaxial compression tests on sandwich panels, bending and shear

tests and fatigue tests. Finally, a test bench was also used to verify the effective operation of the panels. A sandwich panels was mounted on the bench, hot air was injected and the external surface temperature was measured with thermocouples. These operations allowed to identify the most suitable trabecular structure for the realization of the final prototype of the project. The prototype is a part of the wing leading edge of the Piaggio P180 aircraft, complete with trabecular structures core, outer and inner surfaces of the sandwich, and hot air inlet tubes.

Chapter 4

Trabecular structures characterization

4.1 Design of the specimens

Principles on which is based the patented solution of anti-icing panel were verified through mechanical and thermal characterizations. The mechanical tests described in this chapter allowed to check the good structural resistance of the panel according to the stresses present during its use. The most common stresses for this type of system are certainly the compression: in fact, the first group of specimens were produced for compression tests with different materials (Ti6Al4V or AlSi10Mg), geometries, densities and cell size. The largest test campaign was carried out only on AlSi10Mg specimens, due to the affinity of this type of alloy with heat exchanger applications. In the second phase, only a smaller group of analyzed specimens was made with Ti6Al4V. This alloy is less efficient as material for heat exchanger, but has a higher mechanical strength and temperature resistance than aluminum alloys. It is necessary for the leading edges of ultrasonic aircraft, such as fighters, due to the high temperatures reached. The high number of types of compression samples allowed to evaluate the feasibility of some structures with L-PBF technology, while the compression tests allowed to select the best cells and parameters for the application. The subsequent tests, such as compression tests on the sandwich panels, bending tests and fatigue tests were conducted only on the structures with the best compressive behavior in terms of strength and elastic modulus and only on samples produced in AlSi10Mg. This section describes how the specimens are produced, with an SLM 500 machine, for each type of mechanical and thermal test. Finally, the realization of large panels used for thermal tests in the test bench and the realization of the bench itself is described. The informations and the pictures of each type of specimens produced are collected in [Appendix A](#) and [Appendix B](#).

4.1.1 Trabecular specimens for uniaxial compression tests

The first group of specimens produced are for compression tests. They are square-based parallelepipeds with a double height compared to the side of the base. The reference size is $20 \times 20 \times 40 \text{ mm}^3$, but the real dimensions vary with the size of the cell to maintain a whole number of cells within the structure.

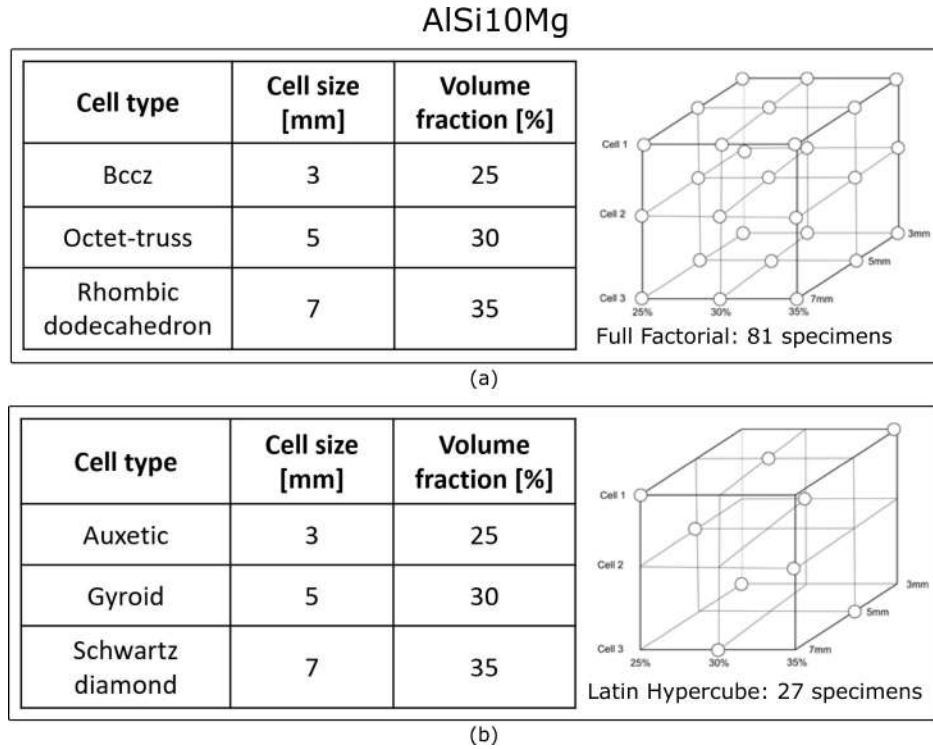


Figure 4.1: DoE for AlSi10Mg compression specimens with a) Bccz, Octet-truss and Rhombic dodecahedron cells and for b) Auxetic, Gyroid and Schwartz diamond cells.

The form of the specimens chosen allows to analyze the fracture mechanism of the different trabecular structures that will constitute the core of the sandwich panel. Six types of cells have been chosen: Bccz (Body Centered Cubic with vertical struts along Z axis), Octet-truss, Rhombic dodecahedron, Auxetic, Gyroid and Schwartz diamond. The first four samples are structures formed by struts that intersect in knots forming the elementary cell that is repeated throughout the piece. The Gyroid and Schwartz diamond are structures obtained from three-dimensional surfaces, which form tortuous paths within the component. For the AlSi10Mg specimens two different Design of Experiment (DoE) were used. For the Bccz, Octet-truss and Rhombic dodecahedron cells a 3^3 DoE Full Factorial was used, while for the Auxetic, Gyroid and Schwartz diamond the same DoE was

used, but in Fractional Factorial mode. The factors considered were the shape of the cell, the size of the cell (3, 5 and 7 mm) and the volume fractions of the solid (25, 30 and 35 %). A scheme of the parameters that varies in the DoE is resumed in Figure 4.1. The figure also shows the total number of different types of produced specimen. For each of specimen types, compressive tests were recorded for three different samples.

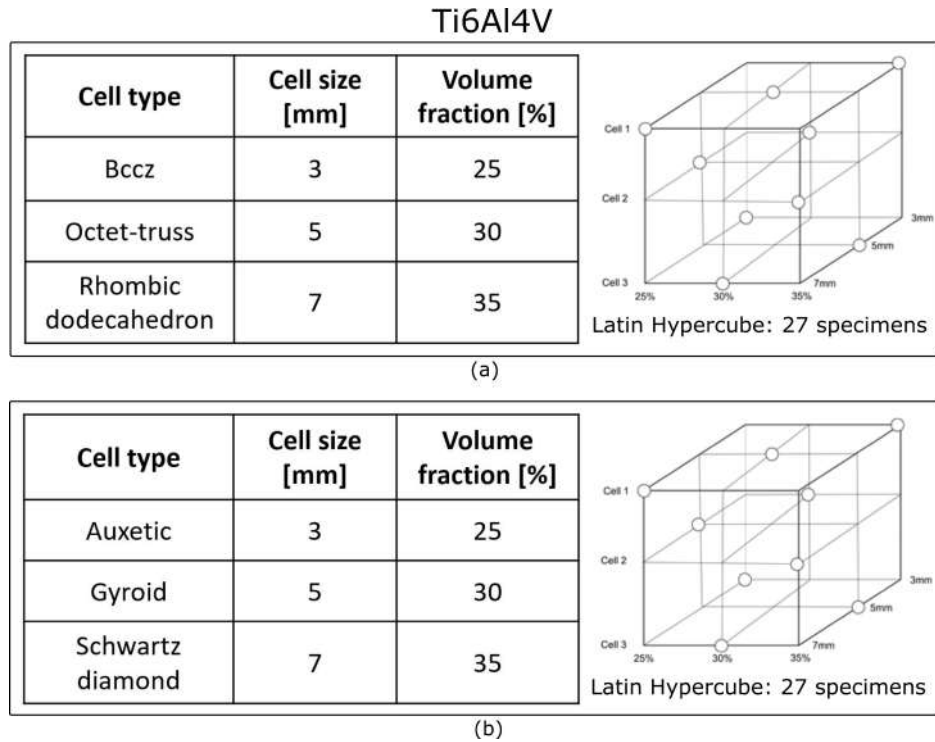


Figure 4.2: DoE for Ti6Al4V compression specimens with a) Bccz, Octet-truss and Rhombic dodecahedron cells and for b) Auxetic, Gyroid and Schwartz diamond cells.

For the Ti6Al4V specimens only one DoE was used for both the groups: a 3^3 DOE Fractional Factorial for Bccz, Octet-truss, Rhombic dodecahedron, Auxetic, Gyroid and Schwartz diamond cells. Also for these samples, the factors considered were the shape of the cell, the size of the cell (3, 5 and 7 mm) and the volume fractions of the solid (25, 30 and 35 %). The parameters that varies in the DoE is schematized in Figure 4.2. The figure also shows the total number of different types of specimen produced. All compression tests were performed with a Zwick Roell machine with a load cell of 50 kN and with an Instron machine with a load cell of 100 kN. The tests were conducted at 1 mm/min and with a pre-load of 1 kN. The set up of the machine for uniaxial compression test is shown in Figure 4.3.

Each specimen is labeled by a name that resumes the shape of the cell, the size

of the cell and finally the percentage fraction. For instance, the specimen Rhom-5-25-2 presents a Rhombic dodecahedron geometry, a cell size of 5 mm and a solid volume fraction of 25 %. The last number in the specimen name is the number of repetition, in this case the samples is the second repetition.

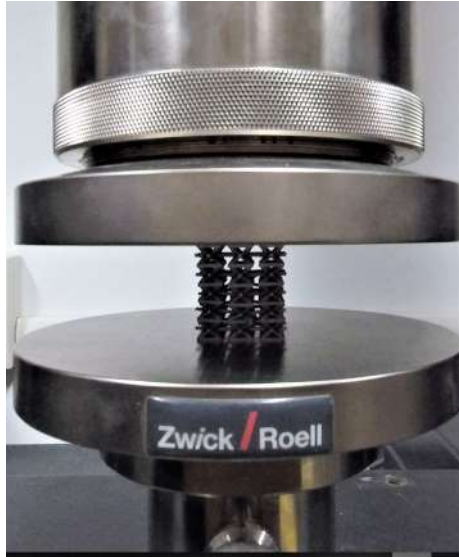


Figure 4.3: Setup of the Instron machine for uniaxial compression test on trabecular specimens.

The compression tests were characterized and compared using three variables obtained from stress strain curves:

- Young modulus (E), is obtained by the slope of the stress-strain curve in the linear elastic range;
- Maximum stress (σ_{\max}), that corresponds to the peak of the curve;
- $\sigma_{0.2}$, that is the stress corresponding to a permanent deformation of 0.2 %. This value identifies the beginning of the plastic section. A line parallel to the linear elastic range and intersecting the deformation of 0.2 % is drawn: $\sigma_{0.2}$ is the value at the intersection between this line and the stress strain curve.

Being the dimensions of the specimens different, values measured for the main compressive properties are also presented referring to the relative density ρ , in order to compare them. All the results of uniaxial compression tests tests are listed in Appendix C.

4.1.2 Sandwich panels with trabecular core for uniaxial compression tests

Based on the results obtained from the compression tests on the specimens, the parameters of sandwich panels used for compression tests were chosen. For this reason, the sandwich panels for the compression tests were defined with a smaller DoE, summarized in the Table 4.1.

Table 4.1: Factors used to produce sandwich panels for uniaxial compression tests

Cell type	Cell size [mm]	Volume fraction [%]
Bccz	5	25
Octet-truss	7	30
Schwartz diamond	-	-

Sandwich panels were built according to the ASTM C365/C365M-16 standard [23] by varying the three types of cell (the Bccz, the Schwartz diamond and the Octet-truss ones), two cell sizes (5 and 7 mm) and two volume fractions of solid (25 and 30 %). The value of 35 % in solid volume fraction and the value of 3 mm for the cell size were not used for the sandwich panels due to the excessive filling of the structure, which prevents the proper passage of the heating air and causes an excessive weighting. Each panel has 10 cells on each side: the sandwich panels with a 5 mm cell measure 50x50x7 mm³, while the 7 mm panels measure 70x70x9 mm³ (panel skins are 1 mm thick). For each type one panel was compressed with a Zwick Roell machine with load cell of 500 kN, a speed of 1 mm/min and a preload of 60 kN. The setup of the machine for the tests is shown in Figure 4.4. The values of Young modulus (E), σ_{\max} and $\sigma_{0.2}$ were obtained in the same way described for the trabecular specimens. All the results of uniaxial compression tests tests are listed in Appendix C.



Figure 4.4: Zwick Roell machine setup for uniaxial compression test on a Octet-truss sandwich panel.

4.1.3 Sandwich panels with trabecular core for 3-point bending tests

The selected samples for the bending tests have the following cells: Schwartz diamond, Bccz and Octet-truss. Sandwich panels for bending tests were designed according to ASTM C393/C393M-16 [24], ASTM D7250/D7250M-16 [37] and ASTM D7249/D7249M-18 [36] standards, varying these three types of cell cell (Schwartz diamond, Bccz and Octet-truss ones), two cell sizes (5 and 7 mm) and two solid volume fractions (25 and 30 %), as shown in Table 4.2.

Table 4.2: Factors used to produce sandwich panels for for 3-point bending tests

Cell type	Cell size [mm]	Volume fraction [%]
Bccz	5	25
Octet-truss	7	30
Schwartz diamond	-	-

Two types of sandwich panels for bending test were realized, with two different designs. The longer specimen type, used to highlight the bending behavior, has dimensions of 85x21x9 mm³ for the 7 mm cell size and of 80x15x7 mm³ for the 5 mm cell size. The shorter specimen type, used to highlight the shear behavior and the delamination, has dimensions of 42x21x9 mm³ for the 7 mm cell size and 40x15x7 mm³ for the 5 mm cell size. All panel skins are 1 mm thick. The panels, two for each type, were tested with a Zwick Roell bending test machine with a 50 kN load cell and a speed of 6 mm/min (according to the standard). The setup of the machine for the bending tests on long and short panels is shown in Figure 4.5.

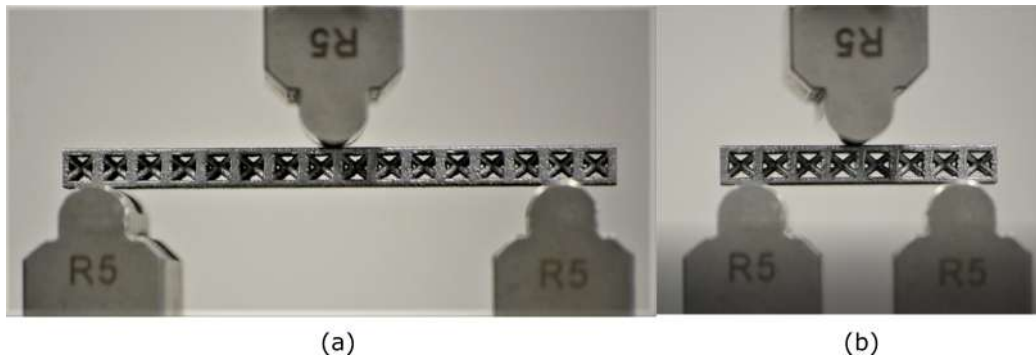


Figure 4.5: Zwick Roell machine setup for 3-point bending tests on a) a Bccz long panel and b) a Bccz short panel.

The mechanical properties, shearing and bending, of the trabecular sandwich panels were analyzed based on the observation of the specimen fracture mechanics

and on some parameters indicated obtained by the ASTM C393/C393M-16 [24]. The *facing stress* [MPa] is a value necessary to evaluate the stresses on the lower face of the sandwich panel; it was calculated using equation 4.1, where σ is the *facing stress* [MPa], P is the load [N], S is the span length [mm], t is the facing thickness [mm], d is the sandwich thickness [mm], c is the core thickness [mm] and b is the sandwich width [mm]. The span length S and the sandwich width b are shown in Figure 4.6.

$$\sigma = \frac{PS}{2t(d+c)b} \quad (4.1)$$

The facing stress obtained from the load corresponding to the breaking of the specimens is calculated by the equation 4.2, where P_{\max} [N] is the load in correspondence to the failure.

$$\sigma_{\max} = \frac{P_{\max}S}{2t(d+c)b} \quad (4.2)$$

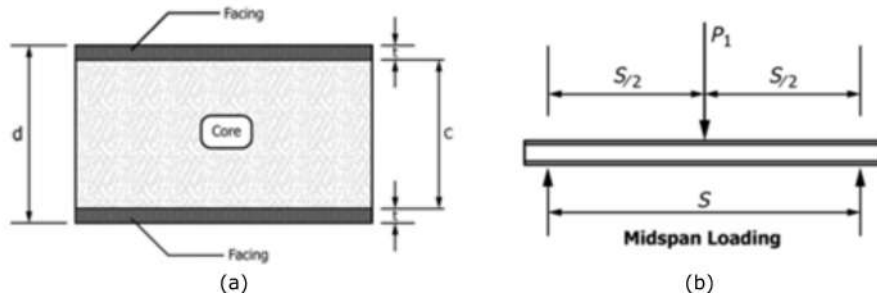


Figure 4.6: Images from ASTM C393/C393M-16 [24] about a) the dimensions of the panels and b) the 3-point load position.

Other two values allows to evaluate the mechanical properties of the core in the sandwich panels during the bending tests. The first one is the *core shear ultimate stress* [MPa], that indicates the stress of the trabecular core at the moment of the specimens failure. It is obtained from the equation 4.3, where F_s^{ult} is the core shear ultimate stress [MPa].

$$F_s^{\text{ult}} = \frac{P_{\max}}{(d+c)b} \quad (4.3)$$

The second one is the *core shear yield stress* [MPa], that indicates the stress value where begins the permanent deformation of the trabecular core. It was obtained from the equation 4.4, where F_s^{yield} is the core shear ultimate stress and P_{yield} is the load at 2% offset shear strain [N]. P_{yield} is calculated according to the method in ASTM D7250/D7250M-16 [37], explained in Figure 4.7.

$$F_s^{\text{yield}} = \frac{P_{\text{yield}}}{(d + c)b} \quad (4.4)$$

All the results of bending tests on long and short panels are listed in Appendix C.

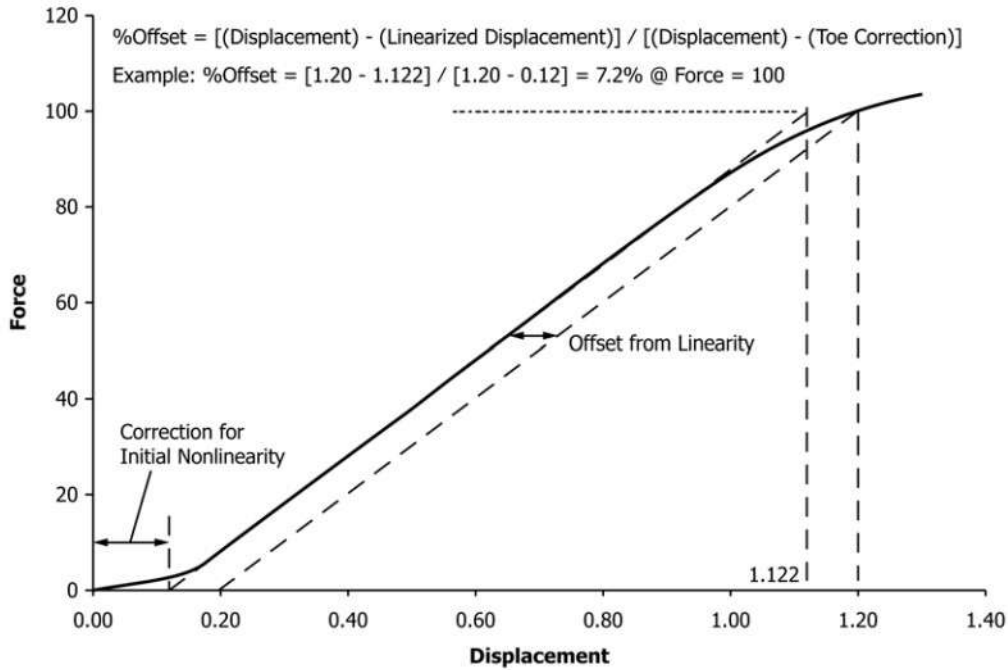


Figure 4.7: Calculation method of the offset according to ASTM D7250/D7250M-16 [37].

4.1.4 Trabecular specimens for compressive fatigue tests

The trabecular specimens for the fatigue tests present a different criterion for choosing cells and a different setup of the samples. Three types of cell were selected, all consisting of struts: Bccz, Octet-truss and Rhombic dodecahedron. These cells were chosen to observe the fatigue failure mechanisms that occur at the nodes of the struts. Two cell sizes (5 and 7 mm) and two volume fractions of solid (25 and 30 %) were used. In particular, the sample for each cell type are: 5 mm cell size with 25 % of solid volume fraction, 5 mm cell size with 30 % of solid volume fraction and 7 mm cell size with 30 % of solid volume fraction, as shown in Table 4.3. These specimens presented a double height compared to the base sides with dimensions of about 20x20x40 mm³. All specimens present two skins of 1 mm thick at the square

bases. The compression-compression fatigue tests were carried out according to scientific literature [7, 115, 38, 90].

Table 4.3: Factors used to produce specimens for fatigue tests.

Cell type	5-25	5-30	7-25	7-30
Bccz	yes	yes	no	yes
Rhombic dodecahedron	yes	yes	no	yes
Octet-truss	yes	yes	no	yes

The working parameters are: R 0.1, 50 Hz frequency and a variable maximum load of 80, 60, 40 and 20 % of the static yield load in order to obtain the Wohler curves. The ratio of R=0.1 means that the compressive load on the specimens oscillates sinusoidally from 10 % to 100 % of the imposed load, with a frequency of 50 Hz. The maximum value of the oscillation is σ_M , obtained from the Equation 4.5, where x corresponds to the values of 80 %, 60 %, 40 % and 20 % and σ_{02} is the average result of the uniaxial compression tests on the corresponding trabecular specimens. The minimum value of the oscillation is σ_m , obtained from the equation 4.6, where R is always 0.1. The average value between σ_M and σ_m is σ_a , calculated with the equation 4.7. To construct the Wohler curve it is necessary to know for each specimen the σ_a value and the number of cycles (N) corresponding to the specimen failure. In order to reach a large number of tests, a value of N equal to $1.5 \cdot 10^7$ was set as the fatigue limit for our application.

$$\sigma_M = x\sigma_{02} \quad (4.5)$$

$$\sigma_m = R\sigma_M \quad (4.6)$$

$$\sigma_a = \frac{\sigma_M + \sigma_m}{2} \quad (4.7)$$

The values of σ_M , σ_m , σ_a and N are listed in Appendix C. All specimens were processed with an Instron machine, with three repetitions for each type.

4.1.5 Sandwich panels for thermal tests

The experimental campaign on the panels had the objective of evaluating the heat transfer within a trabecular panel. Various parameters were compared, such as temperature drop between input and output and static pressure. The static pressure is useful to evaluate the dynamic pressure drop between input and output. In the experimental analysis four different panels were considered. Two cell type were chosen, Bccz and Rhombic dodecahedron, and two relative density values were set for each cell, 12.5 % and 25 %. In this manner it was possible to evaluate both

the effect of density on different cells and that of cellular topology on different relative densities. The panels structure for the test is represented by a cell size for the core of 7 mm and the skins of 1 mm. The general dimensions are represented by a square having a edge of 350 mm. At the ends of the panel flanges were prepared, made during the additive process, so as to allow a simple and easy installation on the test bench. The material used is AlSi10Mg of the same batch as that used for the realization of the specimens for mechanical tests. Also, the manufacturing machine, SLM 500, is the same as previously described. The photos in Figure 4.8 represent one of the realized panel, the Rhombic cell with a solid volume fraction of 25 %.

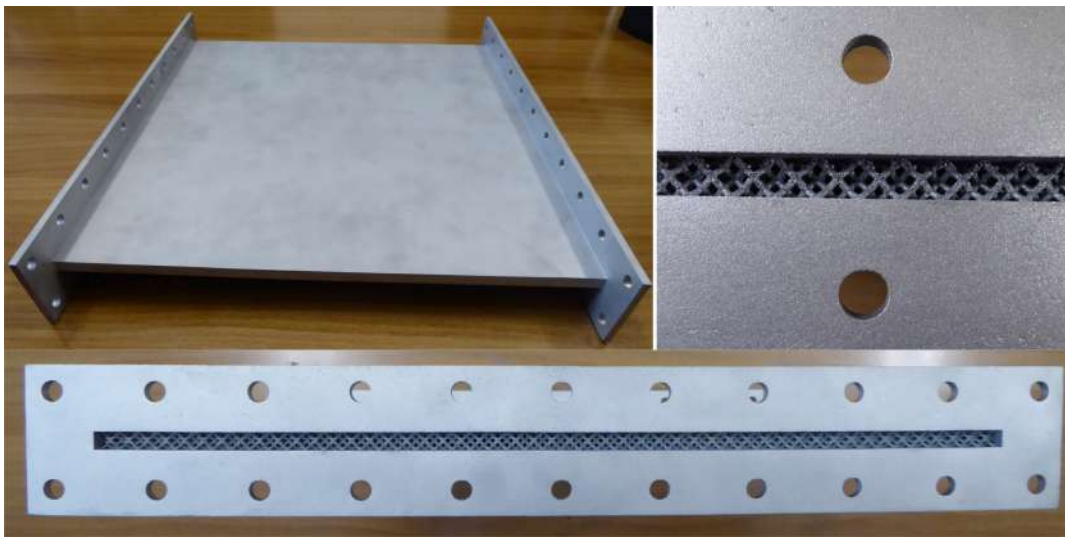


Figure 4.8: Example of Rhombic panel with cell size of 7 mm and with a solid volume fraction of 25 %.

The test bench set up has three main purposes: evaluate the pressure drop, the temperature drop of the air flow passing through and finally providing reliable information regard to the heat field on the external surface of the panel. To carry out these three measurements, various design strategies were developed. The first task is performed by four static pressure intakes positioned upstream (A) and downstream (C) of the test article, as shown in Figure 4.9. These sockets are connected in parallel with two measuring instruments: pressure transducers for each and differential pressure gauges for the two upstream-downstream pairs. This choice was the result of the request to provide reliable data using two different measurement systems connected in parallel to the same source. For what concerns the second task, four thermocouples were inserted in the incoming airflow and in the outgoing flow after the panel. The thermocouples are positioned symmetrically in the middle

position in the channel to avoid boundary layer influences. The upstream thermocouples are indicated as TA1 and TA2 while the downstream ones are named TA3 and TA4. The last measure concerns the surface temperature field on the panel to evaluate the uniformity of the distributed heat. This evaluation was carried out with six thermocouples arranged longitudinally in two rows of three thermocouples each. Each row collects punctual information on the temperatures of the skin adjacent to the inlet flange, median and to the outlet flange. One array is positioned in correspondence of the axis of symmetry while the second is adjacent to the edge of the panel to evaluate the effect of the boundary layer. This measurement was integrated with the help of an infrared camera (FLIR) in order to have field information and not timely information.

In Figure 4.10 it is possible to evaluate extensively the layout of the positioned sensors. All data are collected in a single data-bus and sent digitally via a LAN dedicated to the acquisition PC. These acquisitions were made with the LabView Signal Express software.

The structural design of the bench involved the reuse of a pre-existing turbine test bench. The air ducts were designed towards the test article and from the test article towards the chimney. The details of test bench designed and produced are shown in Figure 4.11. The material selected for the construction of the bench is AISI 416 in bent and welded sheets. The joints between the different components are flanged and a special sealant for high temperatures was placed between the flanges (Figures 4.11f and 4.11h). To minimize aerodynamic losses, the structure was covered with insulating ceramic wool at high temperatures (Figure 4.11i).

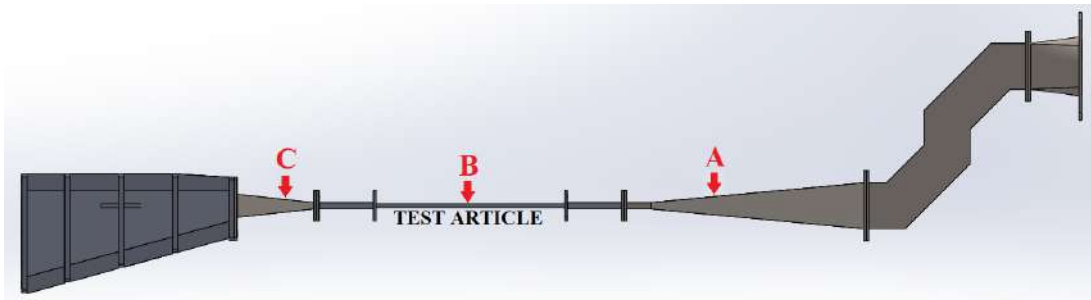


Figure 4.9: Section view of the test bench.

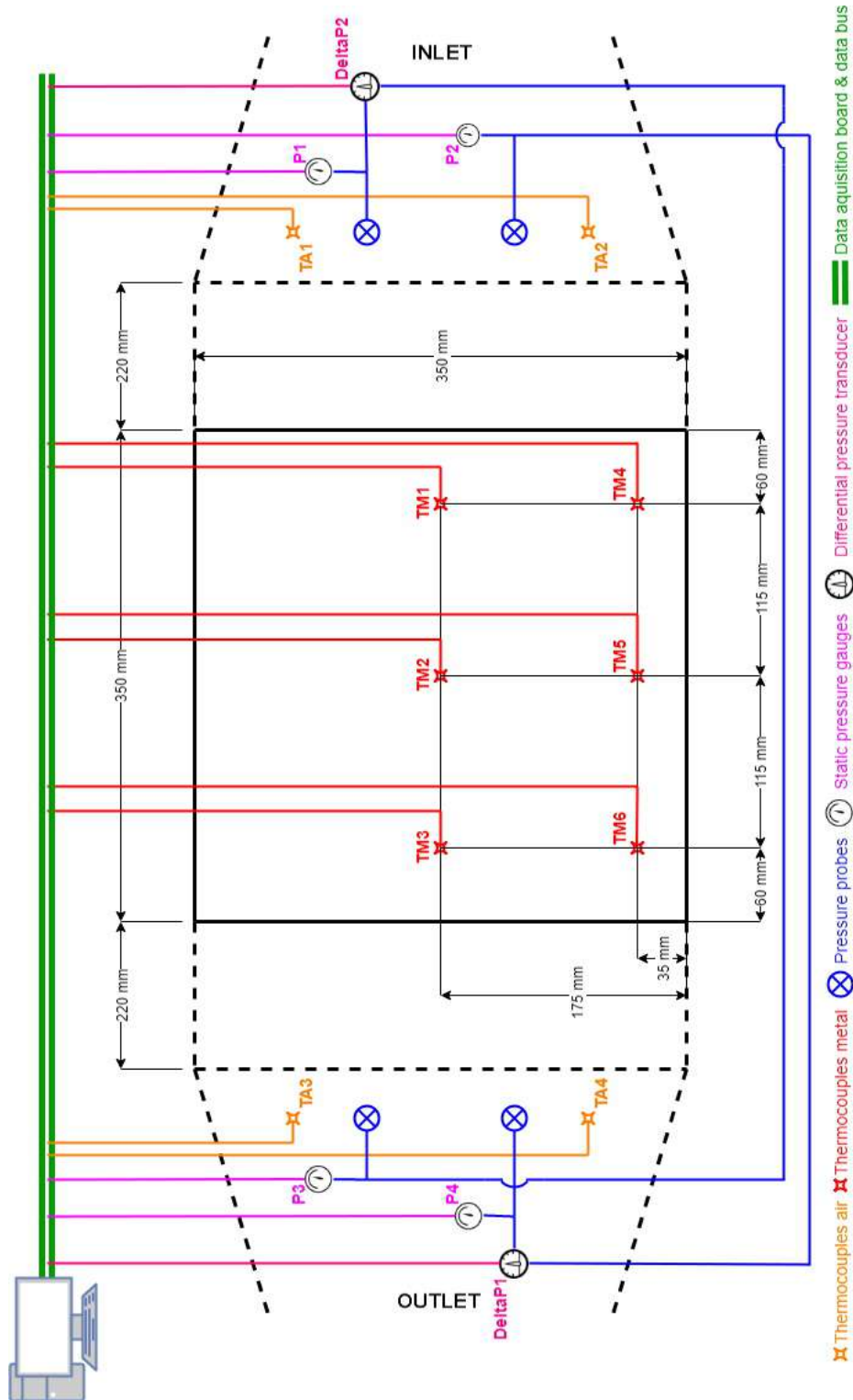


Figure 4.10: Synoptic scheme of the test bench.

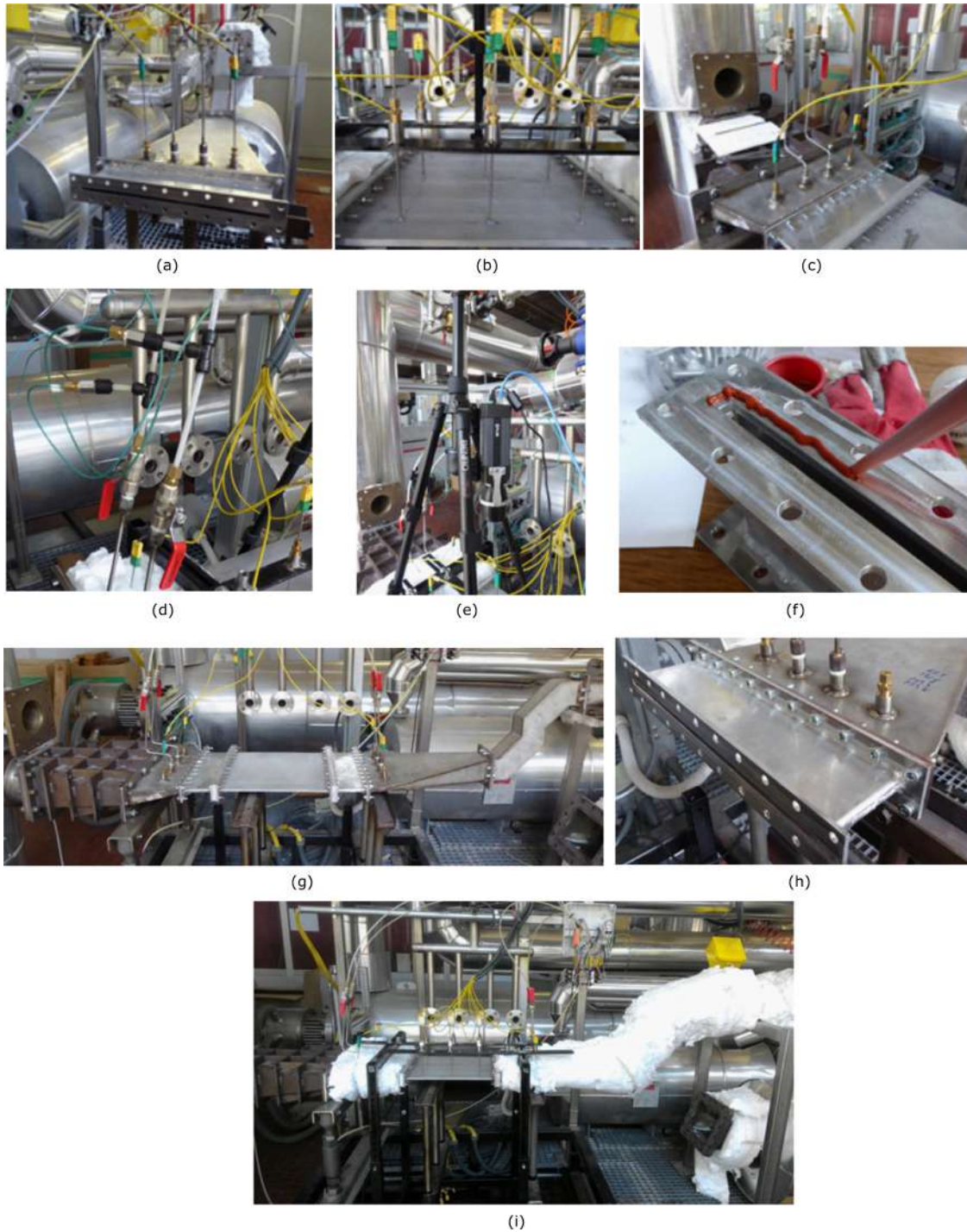


Figure 4.11: Detail view of the measuring equipment: a) convergent duct, b) external skin of the test article, c) divergent duct, d) static outport of the test article and e) infrared thermal camera FLIR. Detail view f) and h) of the junctioning process with high temp silicone and of the test bench g) pre and i) post insulating blanket installation.

The experimental tests carried out on the panels were set at a constant heat quantity of 1450 J/s. This value is comparable with the heat supplied per square meter in aeronautical anti-ice applications, as calculated in the thesis in reference [29]. Three different experiments were designed varying the inlet mass flow rate and the inlet temperature, maintaining the heat flow constant. The values were chosen by the equation 4.8, where \dot{q} is heat flow rate setted at 1450 J/s, \dot{m} is the mass flow rate, c_p of the air (1003 J/kg°C), T_{amb} is the temperature of the laboratory (20 °C) and T_{in} is the air inlet temperature [°C].

$$\dot{q} = \dot{m}c_p(T_{in} - T_{amb}) \quad (4.8)$$

Three experiment sets up are illustrated in the Table 4.4. Data acquisitions began after 15 minutes of flushing to ensure airflow complete stabilization and continued for 15 minutes each. This allowed a wide sampling and a statistically reliable database. The results obtained are:

- The pressure drop calculated as the weighted average of the difference between the inlet pressure (P_{in} - P_{out}) and outlet pressure;
- The temperature drop calculated as the weighted average of the of the difference between the inlet temperature (T_{in} - T_{out}) and outlet temperature.
- The heat transfer (from air to the panels).

Table 4.4: Thermal tests setup.

Input parameters	Test 1	Test 2	Test 3
Air inlet temperature [°C]	93.5	75	66.8
Air inlet pressure [bar]	1.23	1.42	1.44
Mass flow fate [kg/s]	0.0194	0.0259	0.0306

4.2 Optical Microscope and CT-scan analysis

Before subjecting the compression specimens to the mechanical tests for which they were produced, they were observed at the Optical Microscope and subjected to tomography. This allowed to identify some characteristics related to the shape of the cell, its size and the production process. These features are useful to explain some of the behaviors observed during mechanical tests.

4.2.1 Optical Microscope (OM) analysis

The images of the trabecular structures were obtained from an optical stereomicroscope: an optical microscope with lateral illumination that allows a greater depth of field. An example of the images obtained for each type of cell is shown in the Figure 4.14: the specimens with a 5 mm cell were taken as an example. From the images it is possible to see a high roughness on the struts of the specimens, in particular on the specimens with Octet and Rhombic cells. The high roughness is due to the amount of powder near the molten area that attaches to the struts or surfaces, during the production process. The high thermal conductivity of Al alloys makes the bed of unmelted powder near the laser pass warm up a lot, bringing many powder grains to melt with the surface of the piece.

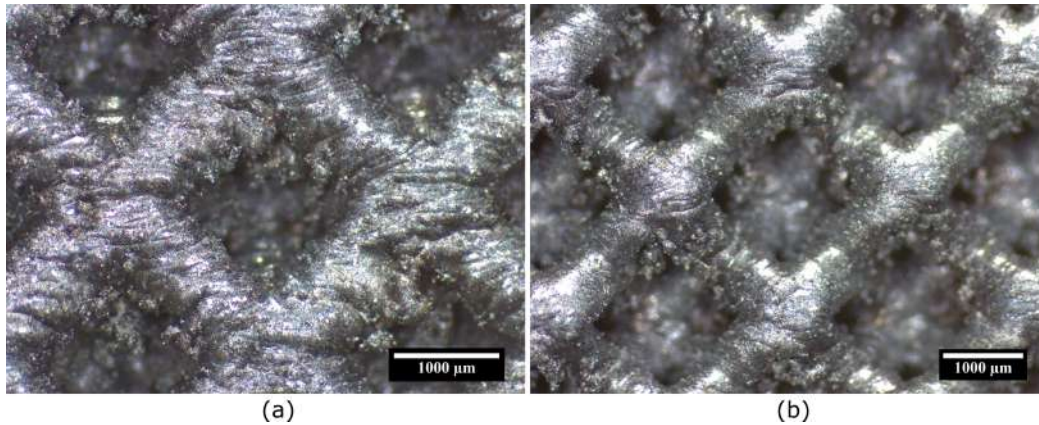


Figure 4.12: OM images of AlSi10Mg compression specimens: a) Oct-3-30 at magnification of 20X and b) Rhom-3-25 at magnification of 16X.

The adhesion of unmelted powders to the surface is particularly visible in the part of the struts or surfaces facing downwards, as highlighted in Figure 4.12 for some specimen types at higher magnifications. This phenomenon is due to the mechanics of the production technology. When the laser melts a layer of powder the heat passes to the previous layer that is below, increasing the temperature. If the previous layer is composed only of unfused powders, the particles stick to the just melted layer forming a rough surface. The upper surface of the struts, when melted, is never in direct contact with unmelted powders: the new layer is spread when the temperature of the molten pool is already lower. For this reason the upper surface of the temples has a much lower roughness. This phenomenon can cause, for some specimens, not only an increase in surface roughness, but also a significant enlargement of the struts and an excessive increase in the density of the component. The problem involves the densest structures, such as 3 mm cells, in particular for the geometries Bccz, Octet and Rhombic. The denser structures

penalize the diffusion of heat supplied by the laser during the production process. The heat also melts the areas around the melt pool and causes an increase in density compared to the nominal one. The abnormal increase in the density of some specimens causes a heavier of the structure, making it more difficult the removal of the powders from the specimen and alters the mechanical performance during the tests. The mechanical tests, in fact, are performed on a specimen that is denser than expected and the mechanical performances are not reliable.

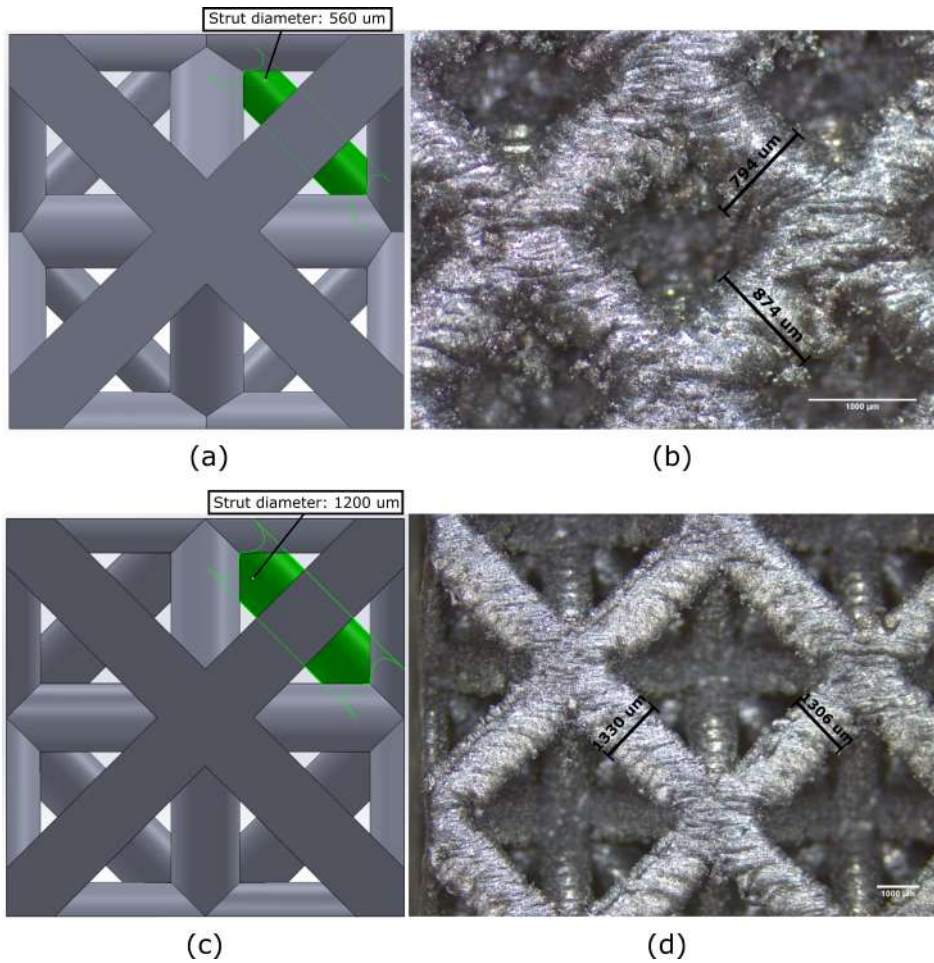


Figure 4.13: Strut diameter of AlSi10Mg Oct-3-30 from a) CAD model and b) from OM image 20X and of Oct-7-30 from c) CAD model and d) from OM image 8X.

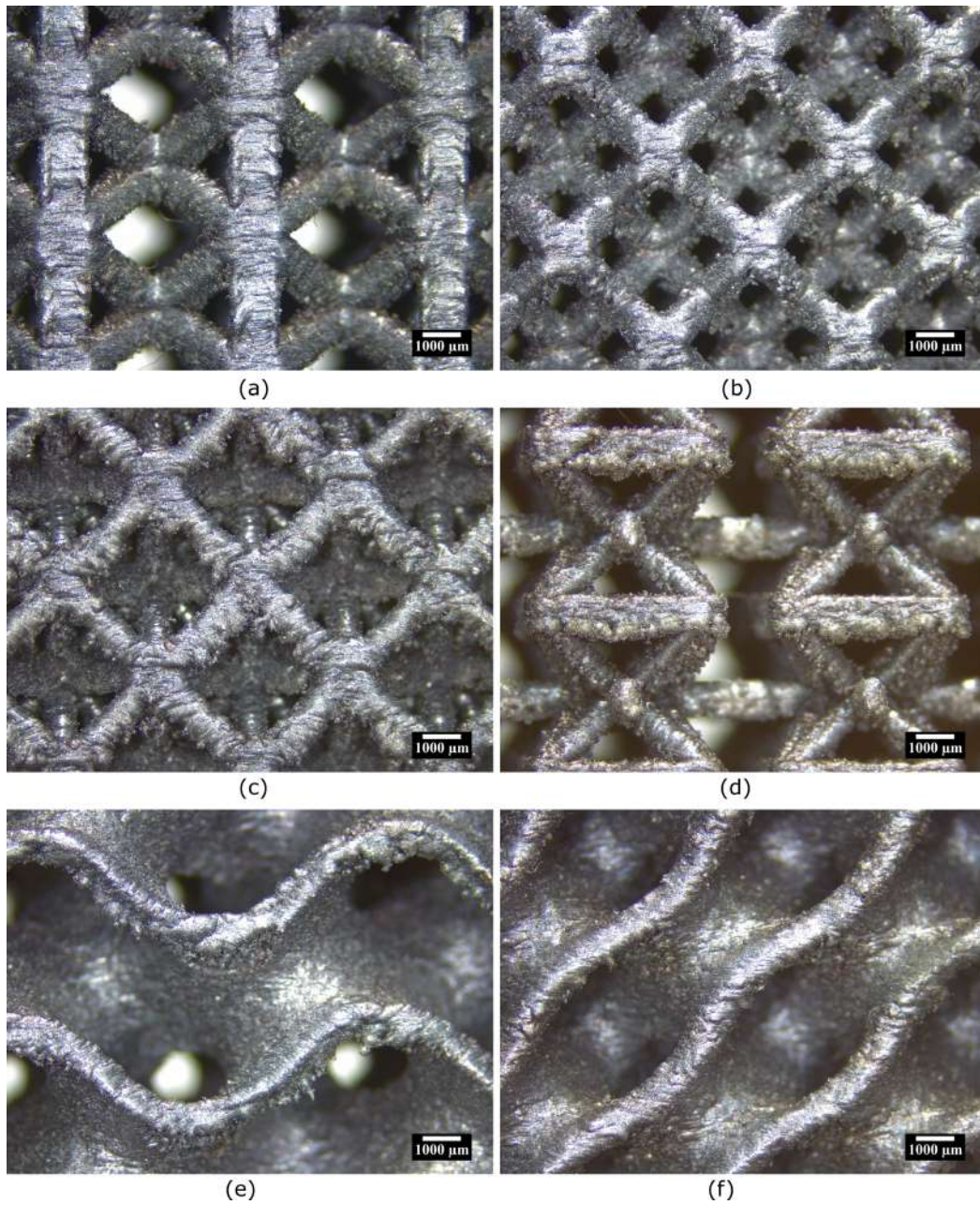


Figure 4.14: OM images of AlSi10Mg compression specimens at magnification of 8X: a) Bccz-5-30, b) Rhom-5-30, c) Oct-5-30, d) Aux-5-30, e) Gyr-5-25 and f) Sch-5-35.

This phenomenon is more evident for Octet specimens with a 3 mm cell. The Octet geometry, in fact, due to its very tortuous conformation, makes heat dissipation very difficult and this causes a considerable thickening of the struts. The

Figure 4.13 shows the comparison between the measurements of the struts obtained from the CAD model and the measurements of the struts measured experimentally by the OM images. For the 3 mm cell the struts from the CAD have a diameter of $560\ \mu\text{m}$, while the struts measured have diameters of $794\ \mu\text{m}$ and $874\ \mu\text{m}$. For the 7 mm cell, the CAD struts are only slightly smaller than those measured experimentally.

The Table 4.5 lists the specimens with the cells Bccz, Octet and Rhombic and their average relative densities. The second column lists the measured values for the specimens in AlSi10Mg. For Octet cells the model foresees solid volume fractions of 25, 30 and 35 %, but the experimental values obtained for the 3 mm cells are respectively 41, 47 and 52 %. On the contrary, samples with 5 and 7 mm cells presented an experimentally calculated solid volume fraction similar to values of the model and the enlargement of the struts is limited. Immediately after the density increase of the 3 mm Octet cells, there is that of the Rhombic cells and finally that of the Bccz cells. The Auxetic, Gyroid and Schwartz cells are not reported in the table because, thanks to the conformation of the larger cell, they never exhibit this behavior. The third column shows the average relative density values obtained for the Ti6Al4V specimens. The Ti-alloy specimens do not exhibit this behavior, even in the densest cells. The reason is the lower thermal conductivity of the Titanium, which does not cause the heating of too much unmelted powder near the melt pool. The only exception is the Oct-3-35 specimens, with a solid fraction volume of 51 % instead of 35 %. In this case the high density of the structure and the shape of the Octet cell influenced the enlargement of the struts also for Titanium. The Figure 4.15 illustrates an example that compares the same cell produced in Ti6Al4V and in AlSi10Mg: the 3 mm Rhombic cell and with solid volume fraction of 25 %. From the image it is possible to see that the struts of the Titanium specimen are much thinner than the Aluminum one.

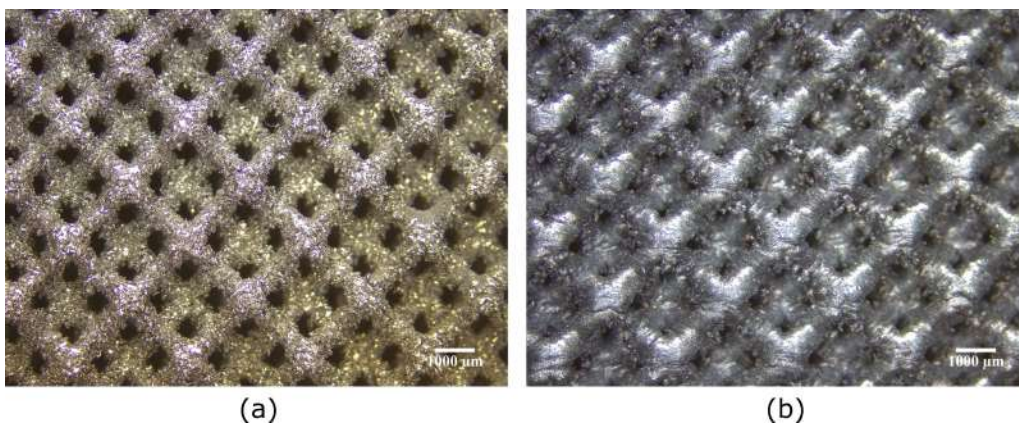


Figure 4.15: Rhom-3-25 produced in a) Ti6Al4V and b) AlSi10Mg.

Table 4.5: Average relative density experimentally measured for Bccz, Rhombic and Octet specimens for AlSi10Mg and Ti6Al4V.

	AlSi10Mg	Ti6Al4V
Specimen	$\rho_f/\rho_s * 100$ [%]	$\rho_f/\rho_s * 100$ [%]
Bccz-3-25	41	-
Bccz-3-30	47	29
Bccz-3-35	52	-
Bccz-5-25	22	24
Bccz-5-30	29	-
Bccz-5-35	33	-
Bccz-7-25	25	-
Bccz-7-30	28	-
Bccz-7-35	33	35
Rhom-3-25	47	25
Rhom-3-30	52	-
Rhom-3-35	60	-
Rhom-5-25	24	-
Rhom-5-30	29	-
Rhom-5-35	34	36
Rhom-7-25	24	-
Rhom-7-30	29	35
Rhom-7-35	34	-
Oct-3-25	54	-
Oct-3-30	62	-
Oct-3-35	64	51
Oct-5-25	28	-
Oct-5-30	32	31
Oct-5-35	37	-
Oct-7-25	26	25
Oct-7-30	30	-
Oct-7-35	36	-

4.2.2 CT-scan analysis

X-ray tomography or CT-scan is a non-destructive imaging technique that allows the production of high-resolution three-dimensional images composed of two-dimensional projections of a sample bombarded by an X-ray beam. The reconstruction of a 3D image is obtained by rotating the sample in order to generate a series of 2D projections, which will be transformed into a 3D image using a digital process, called back-projection. The principle of CT-scan is the attenuation of X-rays passing through the analyzed sample, and it is described by the Equation 4.9, where I_x is the intensity of the ray at a distance x from the source, I_0 intensity of the incident ray, x is the distance from the source and μ is the linear attenuation coefficient.

$$I_x = I_0 e^{-\mu x} \quad (4.9)$$

The attenuation of the radius, therefore, depends on the nature of the material and, knowing the intensity of the emitted radiation, it is possible to reconstruct the sample from the analysis of the outgoing rays.

X-ray tomography was performed on trabecular specimens for the uniaxial compression test before tested in order to see the inner part of the struts [8]. In the Figure 4.16 there is a comparison between different sections on XY planes of the Bccz specimens in AlSi10Mg. From the comparison, diffuse porosity can be seen especially in the specimens with 3 mm and 5 mm cells, with solid volum fraction of 30 % and 25 %, respectively. Porosities are present in particular along the perimeters of the struts, but also in the central area. The pores are present both on the vertical struts and on the oblique struts.

The specimens with 7 mm cell and solid volume fraction of 35 % (presented in the Figures 4.16c and 4.16d in two XY planes) have limited porosity and the pores are concentrated only in the perimeters. The fact that the struts are thicker due to the greater density can facilitate the better production of the specimens.

The Figures 4.18 and 4.17 represent the X-ray tomography for the 5 mm cells with Rhombic dodecahedron and Octet-truss geometry in AlSi10Mg and Ti6Al4V. The images of the specimens in AlSi10Mg show that the porosities present for the Bccz are also present for the other cell geometries formed by struts. In fact the pores are present in both cells, in particular in the Octet-trusses. The titanium specimens, on the other hand, do not show porosity in the structure. This indicates that the defects in the construction of the struts, or more generally of the components, are particularly common for Al alloys. The few pores visible in Ti alloy structures are concentrated in the perimeter of the struts.

Finally in the Figure 4.19 two sections of the same cell geometry (Sch-5-35) are represented, but made with different materials: AlSi10Mg and Ti6Al4V. Also in this case the Al alloy presents more porosity than the Ti one, but the quantity of pores is much lower than the geometries formed by struts. This geometry is

in fact formed by surfaces, less critical than the struts to be produced by L-PBF technology.

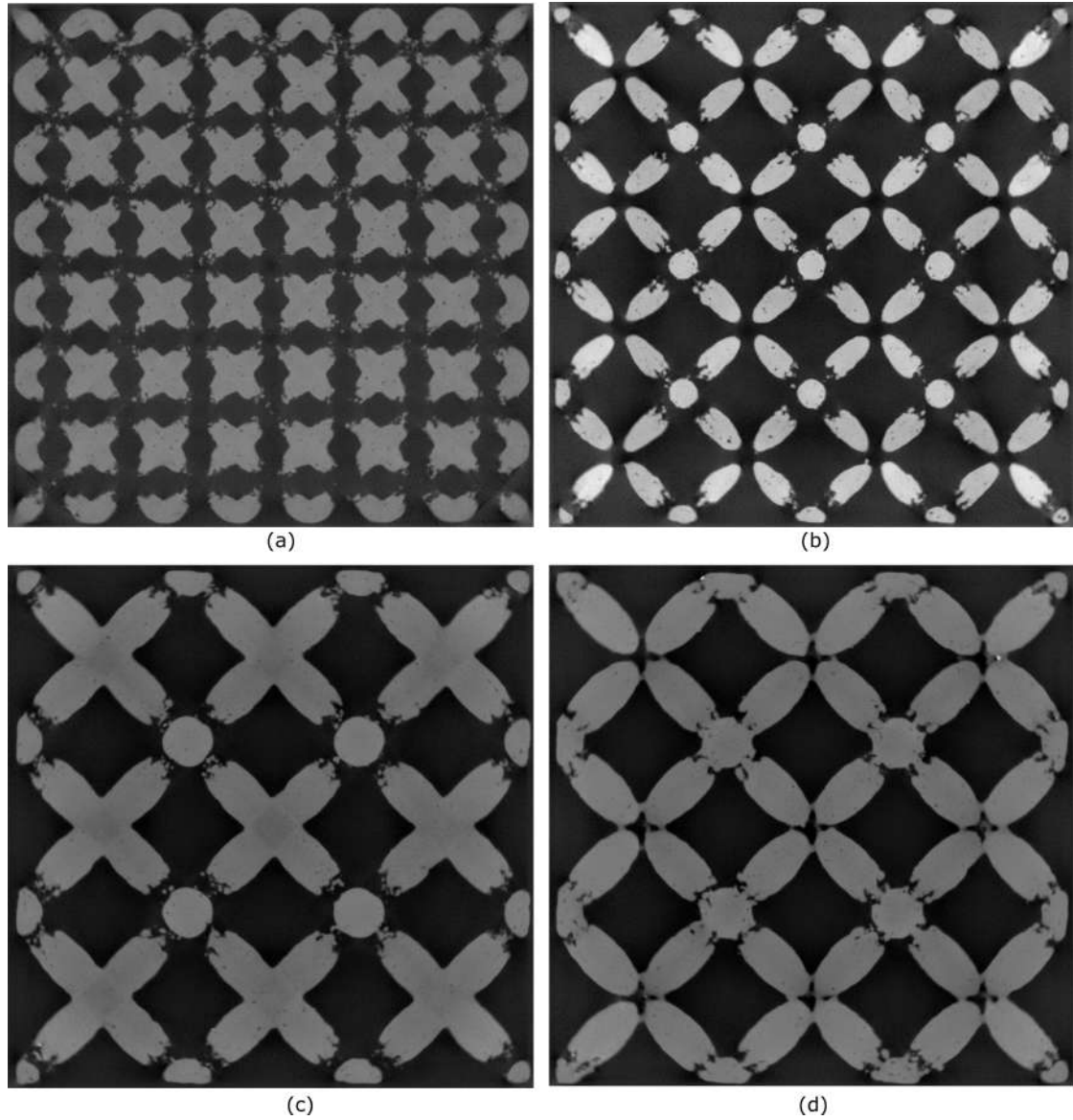


Figure 4.16: Tomography of AlSi10Mg Bccz specimens in XY plane: a) Bccz-3-30, b) Bccz-5-25, c) and d) Bccz-7-35.

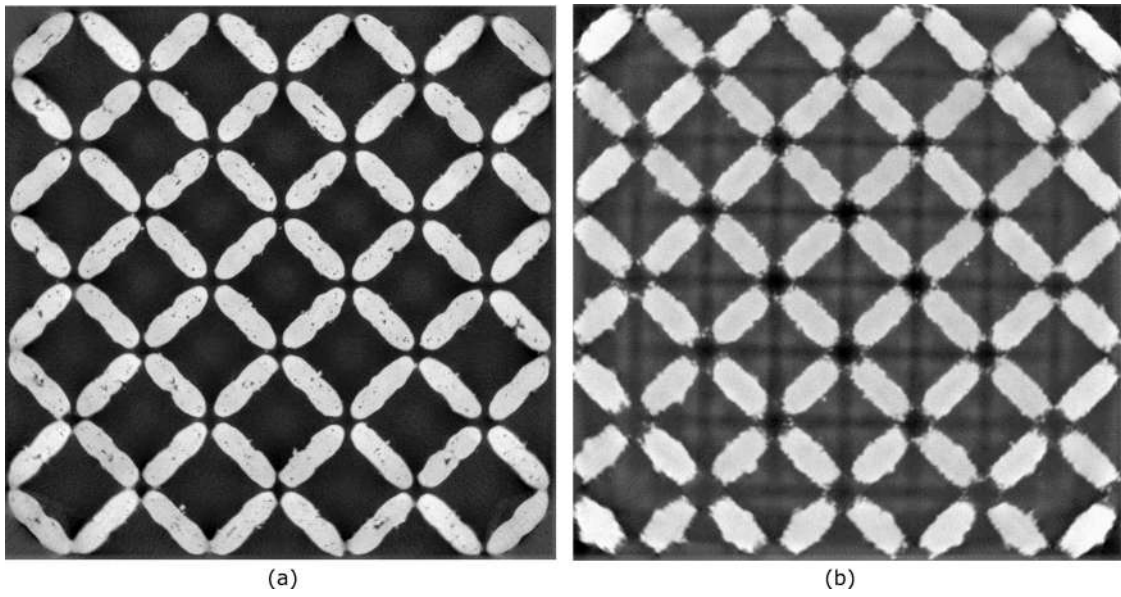


Figure 4.17: Tomography of Rhombic dodecahedron specimens in XY plane: a) Rhom-5-35 in AlSi10Mg and b) Rhom-5-35 in Ti6Al4V.

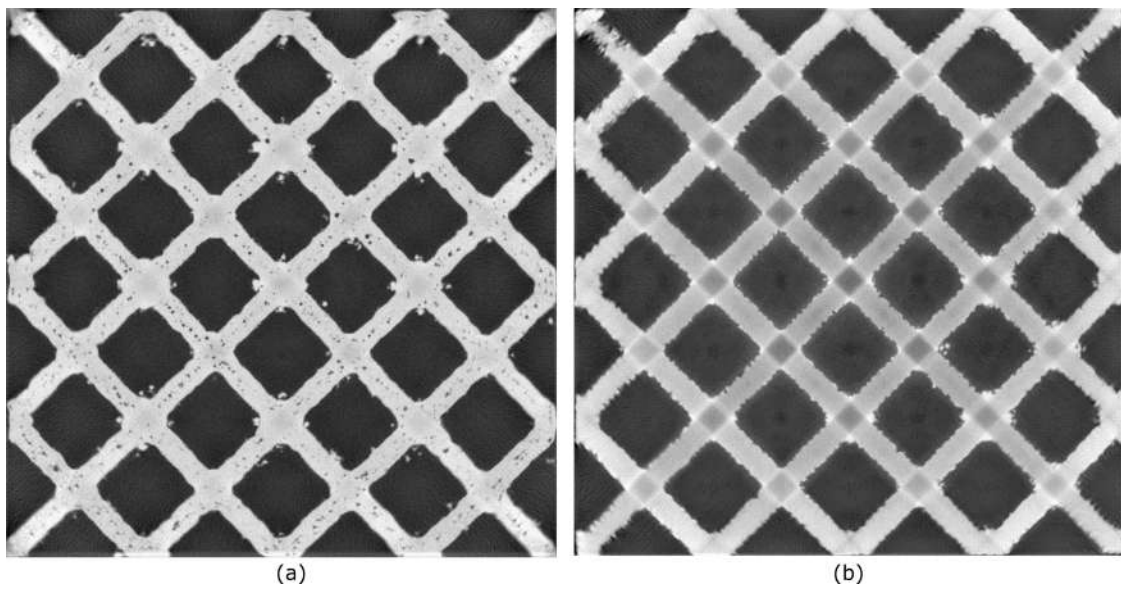


Figure 4.18: Tomography of Octet-truss specimens in XY plane: a) Oct-5-30 in AlSi10Mg and b) Oct-5-30 in Ti6Al4V.

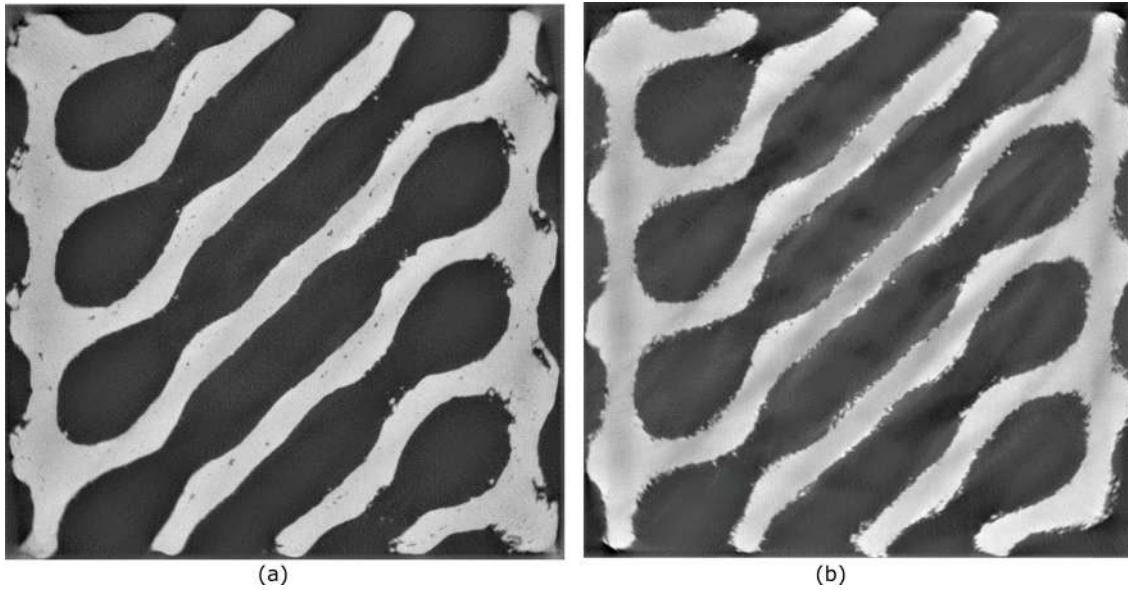


Figure 4.19: Tomography of Schwartz diamond specimens in XY plane: a) Sch-5-35 in AlSi10Mg and b) Sch-5-35 in Ti6Al4V.

4.3 Uniaxial compression tests on AlSi10Mg trabecular specimens

In this section the results of the uniaxial compression tests on AlSi10Mg trabecular specimens were presented. The observations were carried out based on stress-strain curves, the calculated values of σ_{\max} , σ_{02} and E , and the specimen fracture modes. The methods of failure of the different types of cells were analyzed through videos performed on all the tests. The videos were made with a Nikon D7100 and a Nikkor 18-25 mm f3.5 lens. The description of the results can be helped by the stress-strain curves in Appendix D.

4.3.1 Bccz specimens

The specimens with Bccz cell have a good mechanical resistance thanks to the work of the vertical struts. As observed the video of the mechanical tests, the origin of the failure is always due to the buckling of the vertical struts; this phenomenon always starts from one of the sides of the sample and at about half the height of the specimen. After this initial episode, the collapse of an entire plane of trabecular cells follows, where the collapsing plane is inclined by 45° with respect to the Z axis [103, 179]. In stress-strain curves, the failure of the plane corresponds to a sharp reduction in resistance. When the compression test proceeds after the failure

of the first plane at 45° , there is a new increase in the resistance of the specimen. This is due to the stability reached by the planes of cells adjacent to the collapsed one, which are crushed between themselves and resist the load. The second failure generally occurs for loads lower than those at which the first plane collapses. The second phase of the failure differs depending on the size of the cell, while it does not seem to be influenced by the solid volume fraction.

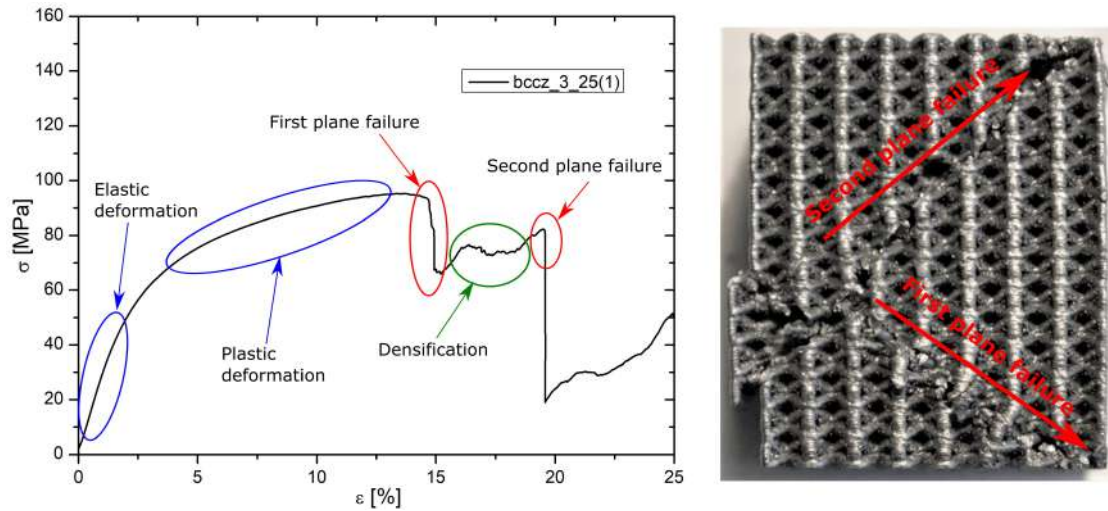


Figure 4.20: Phases of the compression test on Bccz-3-25-1 specimen.

For specimens with a 3 mm cell, the failure of a second plane at 45° with respect to the Z axis occurs, but perpendicular to the first one, as shown in the Figure 4.21a, with the mechanism illustrated in the right side of the Figure 4.20. In stress-strain curves this corresponds to the second lowering of resistance. Compaction also occurs of the second collapsed plane and the resistance of the specimen can start to rise again if the test is continued. The plane by plane compaction that is observed for 3 mm cell specimens is similar to the phenomenon observed for metallic foam and called densification [70]. All the phases of increase and decrease in mechanical resistance during the compression test are shown in the graph in Figure 4.20.

For specimens with a 5 mm cell, the first plane collapses as described (Figure 4.21b). If the test continues, there is a new increase in resistance, but the second failure occurs with the separation of the sample into several fragments that do not compact each other, as shown in the Figure 4.21c. In stress-strain curves this corresponds to the second decrease in resistance. If the test is continued the specimen continues to crumble.

Even for the specimens with a 7 mm cell, the failure of the first plane at 45° with respect to the Z axis occurs. Unlike the other cells, however, the breaking of the first plane already causes the separation in two parts of the specimen, as visible in

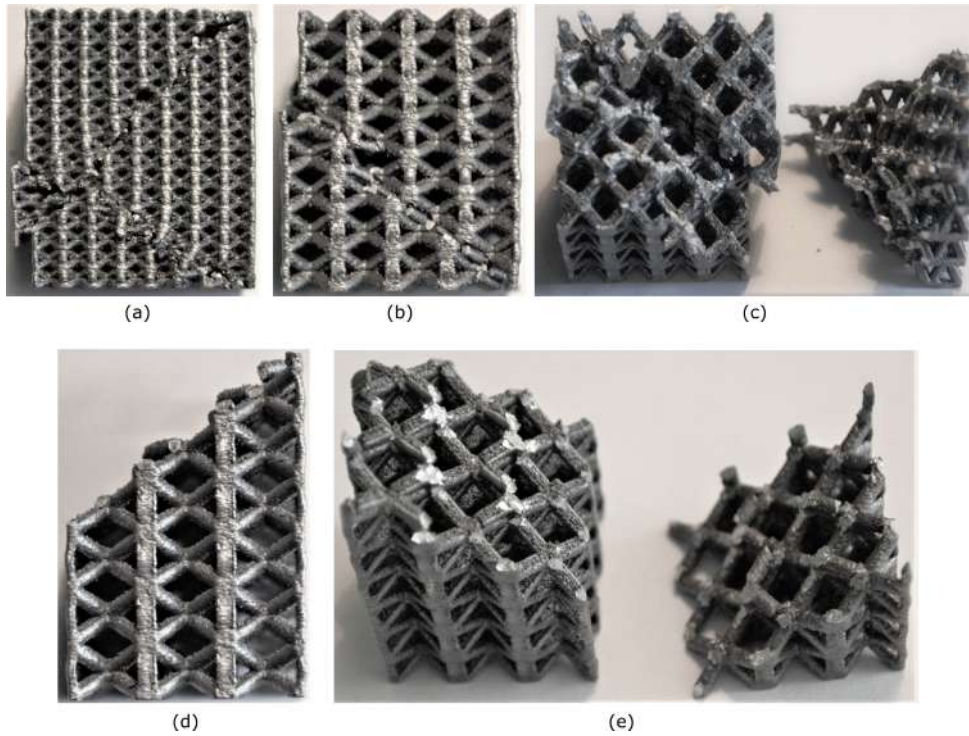


Figure 4.21: Tested specimens in different condition: a) Bccz-3-25-1 after the failure of the second plane, b) Bccz-5-30-2 after the failure of the first plane, c) Bccz-5-35-1 continuing the test after the failure of the first plane, d) Bccz-7-25-1 after the failure of the first plane and e) Bccz-7-30-2 after the failure of the first plane.

the Figures 4.21c and 4.21e . This makes it impossible to continue the test further beyond the first break. The dependence of the breaking mechanism on the size of the cell is caused by the phenomenon giving rise to the failure of the specimen: the buckling of the vertical struts. For 3 mm cells the struts are short and failure occurs by combination of yielding and buckling. So the buckling deflection is small and the deformation that intervenes allows a less abrupt collapse of the specimen. As the cell size increases up to 7 mm, the struts become longer. By imposing a compression load, the struts break for elastic buckling. The critical load is reached before the yielding of the material, and the failure of the specimen occurs abruptly with separation of the pieces. The critical load P_{cr} is calculated according to the equation 4.10 [67], where L is the length of the struts, E is the Young modulus and I is the moment of inertia.

$$P_{cr} = \frac{\pi^2}{L^2} EI \quad (4.10)$$

As can be seen from the equation, if the strut is very long the critical load

for which there is a break due to buckling lowers a lot. The strut breaks due to buckling before reaching the yield strength. For shorter struts the critical load becomes greater. If it exceeds the yield strength of the strut, it deforms before breaking. For Bccz 7 mm cells the yield strength is very close to P_{cr} , so the struts present a little deformation before buckling. For 3 mm ones the critical load is higher than for 7 mm cells, so the 3 mm cell struts deform more before collapsing due to buckling. Cells with size of 5 mm present an intermediate situation.

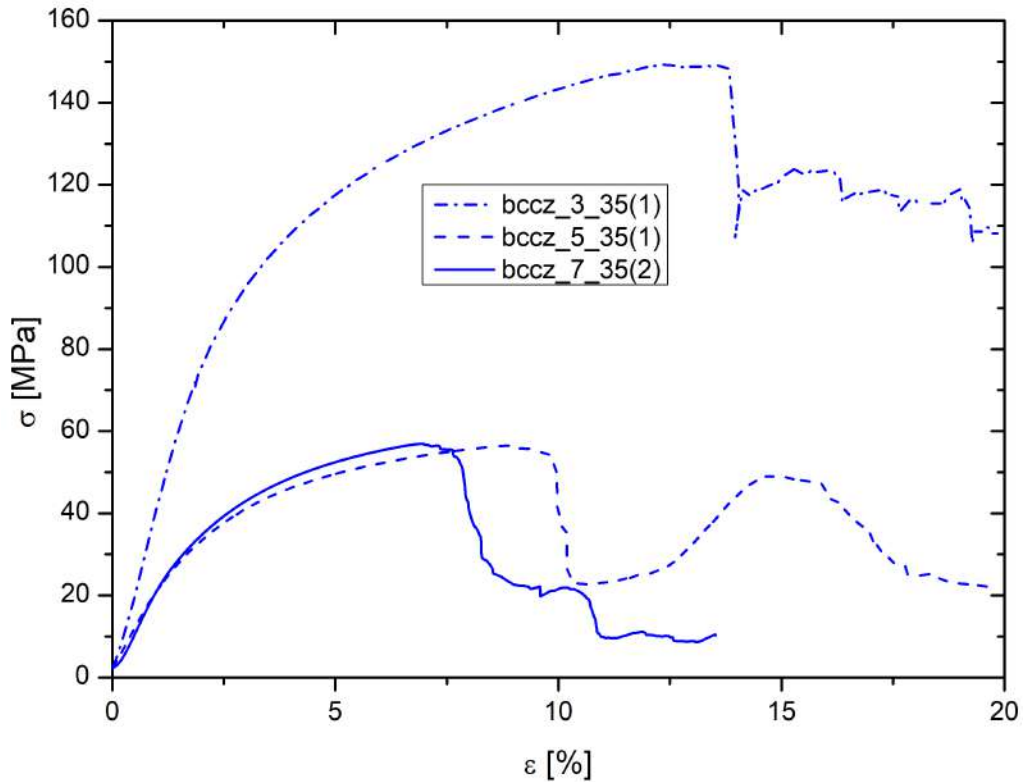


Figure 4.22: Stress-strain curves for specimens with Bccz cell and 35 % of solid volume fraction.

In the Figure 4.22 it is possible to observe some stress-strain curves of the compression tests on the Bccz specimens with different cell size and a constant volume fraction of 35 %. From all the curves it is possible to see a considerable deformation of the specimens before reaching the breaking point. The widest deformation is recorded for the 3 mm cells, while the less wide for the 7 mm cells. This is due to the buckling phenomenon explained. From the graph it is possible to notice how, from the point of view of the mechanical performances, there is a big difference between the 3 mm cells and the 5 mm and 7 mm cells. On the other hand, there is not much difference between 5 mm cells and 7 mm cells.

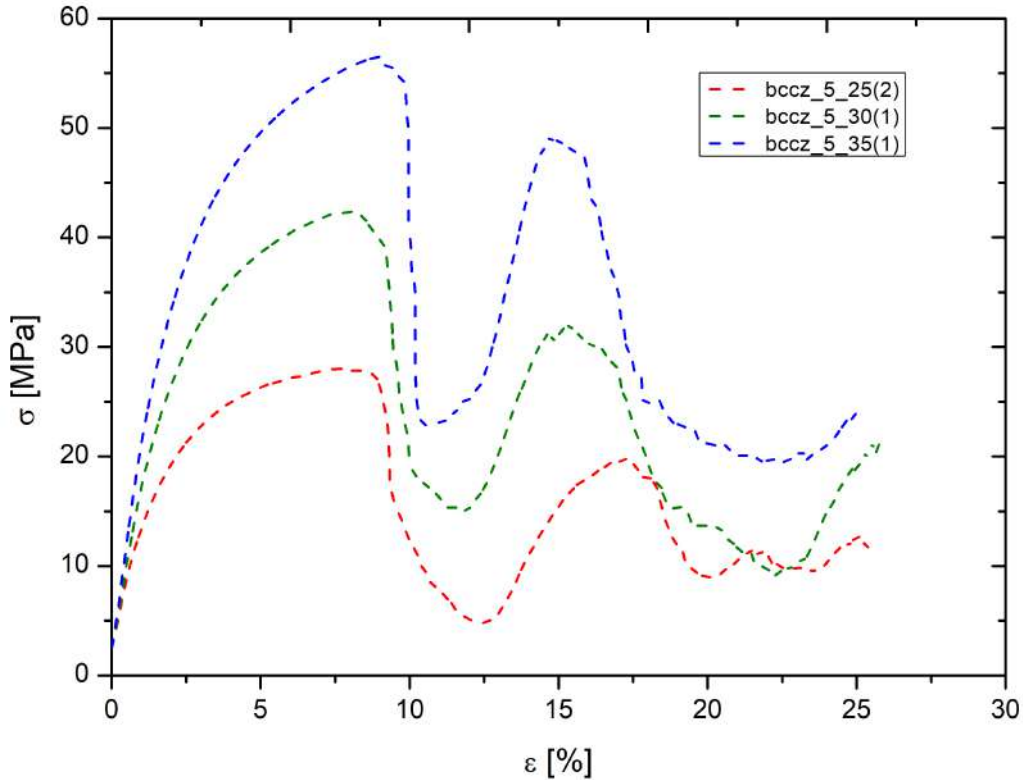


Figure 4.23: Stress-strain curves for specimens with Bccz cell and 5 mm cell size.

There are two reasons for this great mechanical superiority of the 3 mm cells. The first is the different 3 mm cell rupture mechanism, explained above, which allows a high deformation of the 3 mm specimens before the break occurs. The second reason is due to the manufacturing problems of the 3 mm cell specimens explained in the previous paragraph. Due to the dense structure of the 3 mm cells, a difficult diffusion of heat occurs during the powder fusion production process. This causes an excessive thickening of the structure and an undesired increase in the solid volume fraction. The solid fraction volume of 35 % is not a respected value for 3 mm cells, so the compression test cannot be adequately compared with those performed on the 5 mm and 7 mm specimens.

The Figure 4.23 allows to appreciate the influence of the solid volume fraction on the mechanical performances of the specimens. The graph shows the stress-strain curves for specimens with Bccz cell and 5 mm cell size, as the volume fractions vary. The increase in the solid volume fraction of the specimens leads to an increase in mechanical performances, as expected from the Gibson-Ashby model. The increment is regular and occurs for all the cell sizes analyzed.

4.3.2 Rhombic dodecahedron specimens

The specimens made with Rhombic dodecahedron cell geometry they have a different breaking mechanism than the Bccz specimens. All the Rhombic specimens failure occurs due to the breaking of the struts at the nodes. In fact, due to the compression solicitation, the stresses are concentrated at the nodes where the struts are connected. The oblique struts approach each other progressively until they break in correspondence with the node. The failure occurs by collapse of a plane at 45° with respect to the Z axis, but it starts from a corner of the specimens, and not from a side as for the Bccz specimens. This phenomenon is visible in Figure 4.24, which shows some broken specimens during the compression test, as the size of the cell varies.

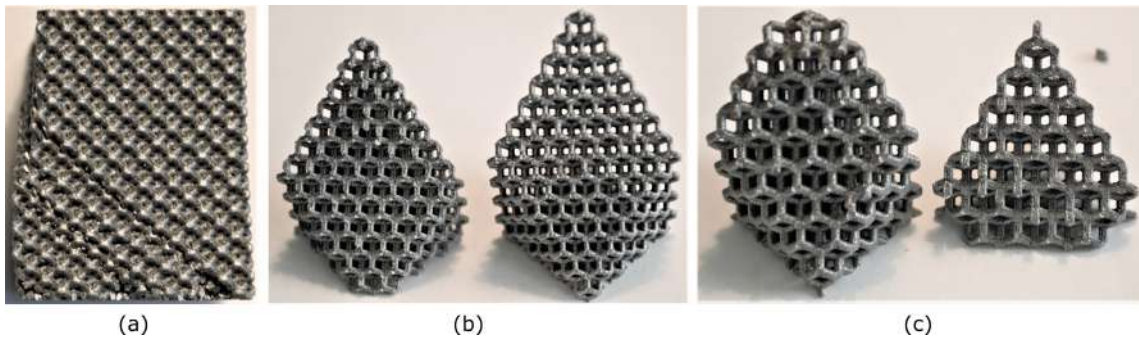


Figure 4.24: Tested specimens in different conditions: a) Rhom-3-25-1 after the failure of the second plane, b) Rhom-5-25-1 after the failure of the first plane and c) Rhom-7-30-2 after the failure of the first plane.

Also in this case the fracture mechanism presents differences depending on the size of the cell considered. The 3 mm cell specimens show a first failure of the 45° plane which corresponds to a decrease in the resistance in the stress-strain curves. This failure does not cause a separation of the parts of the specimen; the collapsed surface is deformed and finds the necessary stability to undergo the mechanical strength increase again. If the compression test continues, the failure of a new plane at 45° with respect to the Z axis occurs, but always parallel and adjacent to the collapsed first floor. This behavior is visible in the Figure 4.24a. The test can continue in this way further increasing the densification of the specimen. This behavior is attributable to the high density of Rhombic specimens with a 3 mm cell, which exhibit behaviors more similar to a solid than to a structure composed of struts and knots. The high deformation of the nodes and of the struts close together allows a continuous settlement of the breaking planes without ever having a violent separation in several parts.

For 5 mm and 7 mm specimens the deformation before the collapse of the plane at 45° is low and once the first plane collapses it is impossible to continue the test

due to the violent separation in two parts of the specimen in two parts. For these specimens the rods crack at the nodes and collapse, sometimes causing a noise and a violent removal of part of the specimen. The specimens with a 5 mm and 7 mm cell after the compression tests are in the Figures 4.24b and 4.24c. This behavior makes it impossible to continue the compression test after breaking the first plane.

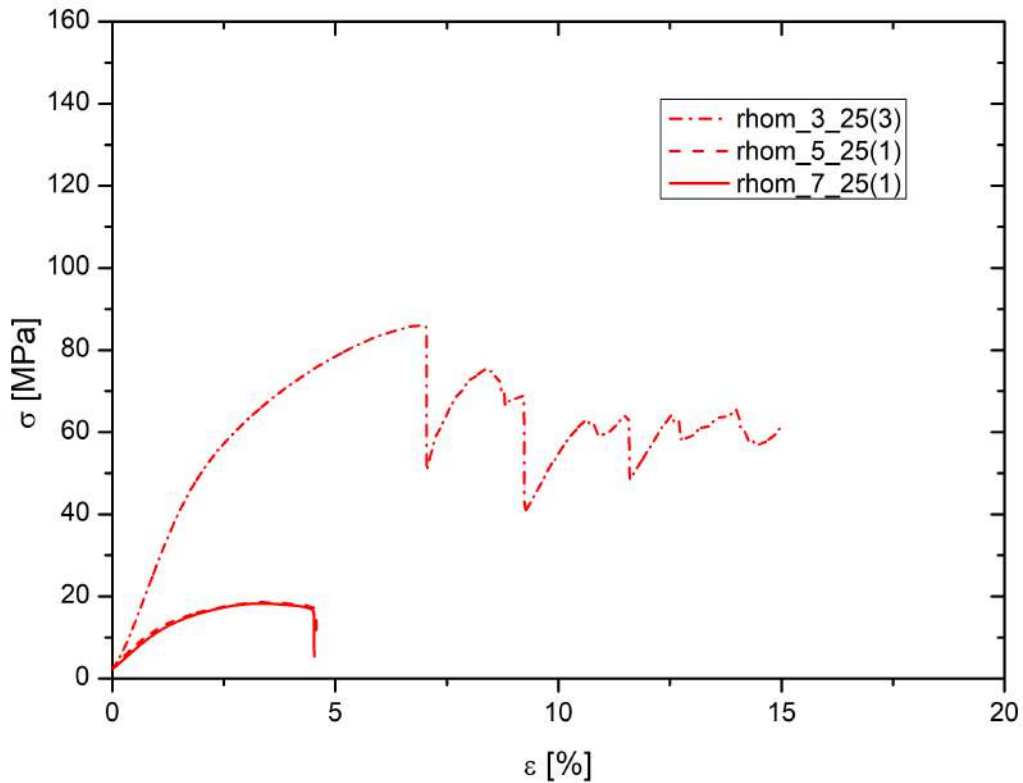


Figure 4.25: Stress-strain curves for specimens with Rhombic dodecahedron cell and 25% of solid volume fraction.

The Figure 4.25 reports the stress-strain curves of the Rhombic dodecahedron specimens with different cell size and a constant volume fraction of 25 %. The curves show a less deformation before breaking compared to what was seen for the Bccz specimens. Furthermore, overall mechanical properties are worse. To confirm what was explained before, the curve for the specimen with 3 mm cell is characterized by an extended densification section. The tests of the specimens with 7 mm and 5 mm cells, instead, end abruptly after the first peak of the curve.

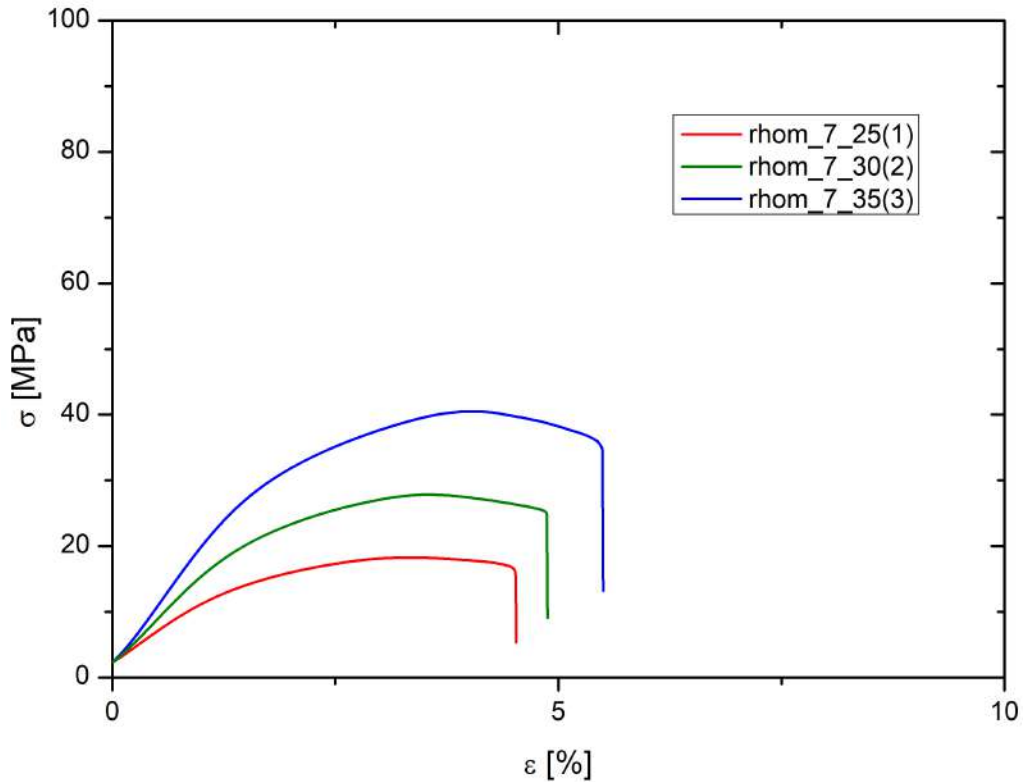


Figure 4.26: Stress-strain curves for specimens with Rhombic dodecahedron cell and 7 mm cell size.

From the graph it is possible to see, also for this cell shape, that there is a big difference in mechanical performances among the 3 mm cells and the 5 mm and 7 mm cells. On the other hand, there is not much difference between 5 mm cells and 7 mm cells. The reasons why this happens are the same as for the Bccz cell. The 3 mm specimens are very dense and have a much larger solid fraction than the nominal one. This distorts the mechanical tests for the specimens with a 3 mm cell and also affects the mechanics of the fracture, which is more similar to that of a solid.

The Figure 4.26 allows to observe the influence of the solid volume fraction on the mechanical performances of the specimens. The graph shows the stress-strain curves for specimens with Rhombic dodecahedron cell and 7 mm cell size, as the volume fractions vary. The increase in the solid volume fraction of the specimens leads to an increase in mechanical performances, as expected from the Gibson-Ashby model. The increment is regular and occurs for all the cell sizes analyzed. Moreover, it can be noticed that, for higher volume fraction, the deformation before the break seems to be greater. This may be due to the greater thickness of the struts for larger volume fraction; the thicker struts deform more before breaking at the

nodes.

4.3.3 Octet-truss specimens

The mechanical behavior at breaking of the structures with Octet-truss cell is very similar to that of the Rhombic dodecahedron cells, but occurs at higher loads. All the Octet-truss failure occurs due to the breaking of the struts at the nodes [189]. In fact, due to the compression solicitation, the stresses are concentrated at the nodes where the struts are connected. The oblique struts approach each other progressively until they break in correspondence with the node.

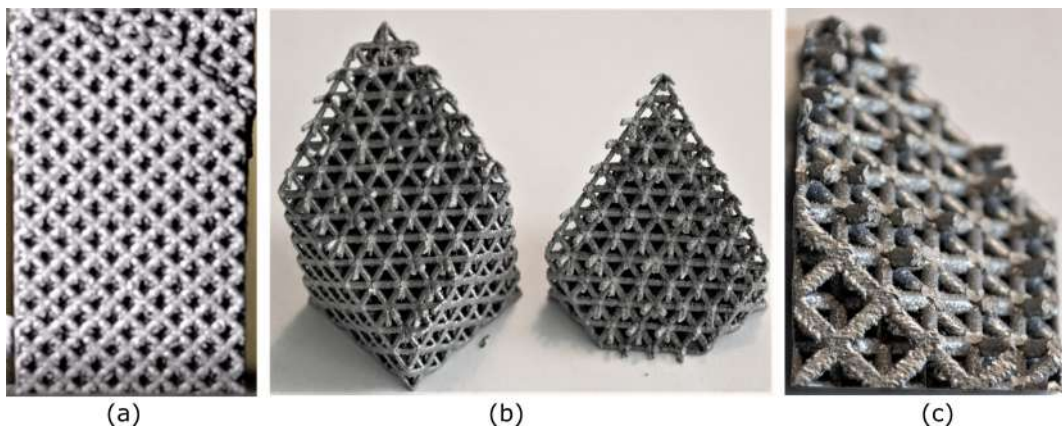


Figure 4.27: Tested specimens in different condition: a) Oct-3-25-2 after the failure of the second plane, b) Oct-5-25-1 after the failure of the first plane and c) Oct-7-35-1 after the failure of the first plane.

The failure occurs by collapse of a plane at 45° with respect to the Z axis. It starts from a corner of the specimens, as for the Rhombic cells. This phenomenon is visible in Figure 4.27, which shows some broken specimens during the compression test, as the size of the cell varies. As has been seen for the Rhombic, the 3 mm octet cells also have a different behavior compared to the 5 mm and 7 mm cells. After the failure of the first plane, the adjacent ones begin to give way, with densification of the specimen. Unlike the Rhombic however, the densification for the Octets is less regular and already after the first broken plane, the specimen begins to crumble. For 5 mm and 7 mm cell size, the deformation before breaking is very low and once the first plane collapses it is impossible to continue the test due to the separation of the specimen in two parts. The failure of the specimen is presents a noisy collapse of the plane and sometimes a violent separation of the parts occurs.

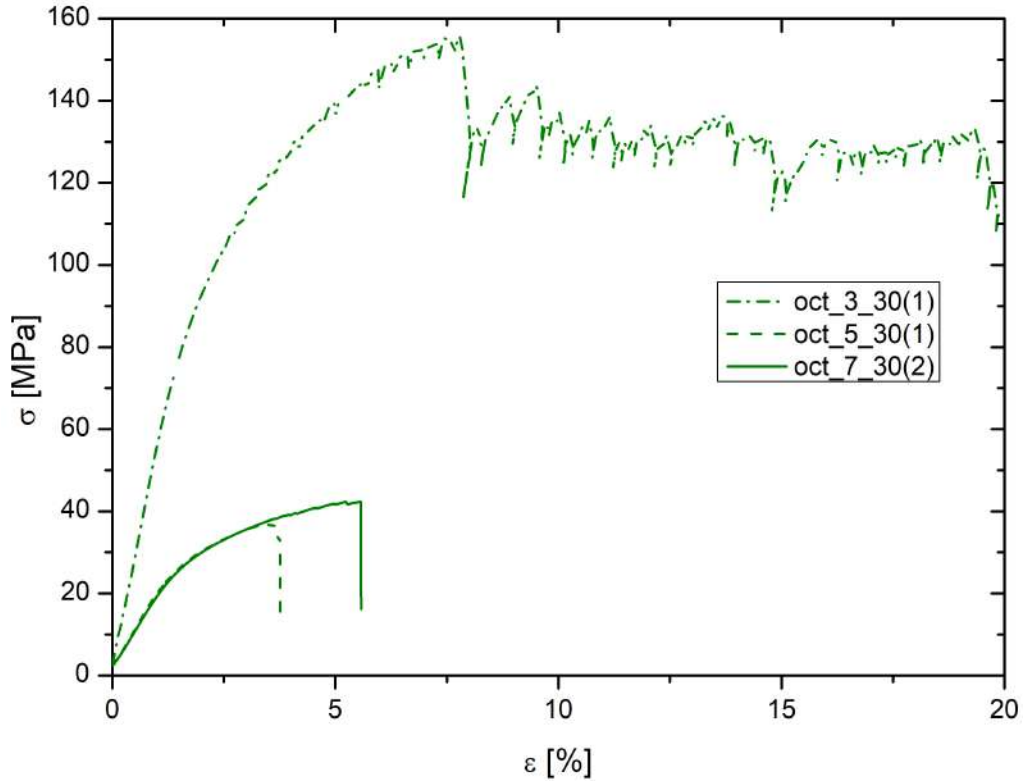


Figure 4.28: Stress-strain curves for specimens with Octet-truss cell and 30% of solid volume fraction.

The Figure 4.28 reports the stress-strain curves of the compression tests on the octet-truss specimens with different cell size and a constant volume fraction of 30 %. The curves show a short deformation range before breaking. The behavior is similar to the Rhombic one, but with a higher mechanical results in terms of σ_{\max} , σ_{02} and E.

As seen for the other cell type, the specimen with 3 mm cell shows a different behavior and higher mechanical results compared to 5 mm and 7 mm cell sizes. The tests of the specimens with 7 mm and 5 mm cells, instead, end abruptly after the first peak of the curve. Also in this case there is a densification section for the 3 mm cell, which is more irregular than that of the Rhombic cell. In the Rhombic cell it is possible to recognize different peaks of the curve that correspond to the failure of the planes. In the Octet cell, instead, the densification section does not show peaks, but a jagged area, compatible with the crumbling phenomena after the first plane collapse, observed during the test. The curves for the 5 mm and 7 mm cells are similar and the specimens have the same failure behavior. Observing the curves, however, it is possible to notice a greater deformation before the break for the 7 mm cell compared to the 5 mm cell and the failure occurs for greater loads.

This behavior suggests that larger Octet cells better withstand stress at the nodes.

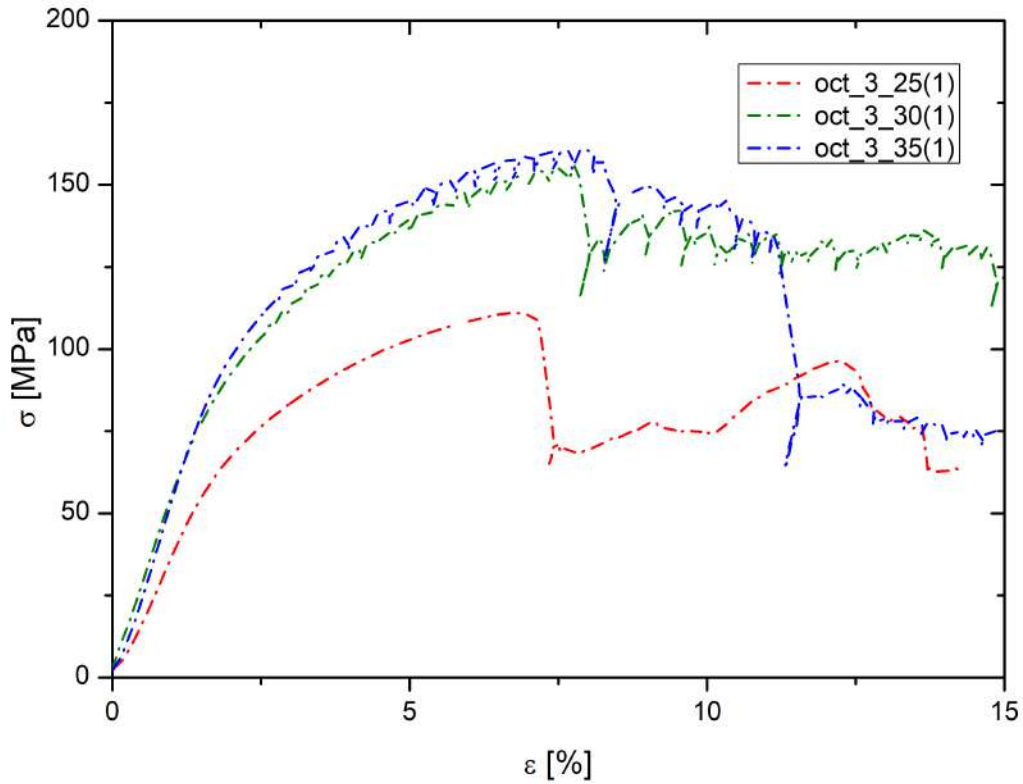


Figure 4.29: Stress-strain curves for specimens with Octet-truss cell and 3 mm cell size.

The Figure 4.29 allows to observe the influence of the solid volume fraction on the mechanical performances of the specimens. The graph reports the stress-strain curves for specimens with Octet-truss cell and 3 mm cell size, as the volume fractions vary. It was chosen to illustrate the behavior of the 3mm cell because it shows anomalies with respect to the 5 mm and 7 mm cells. For cells of 5 mm and 7 mm the behavior with increasing density is similar to that seen for the other cell forms. Indeed, the increase in the solid volume fraction of the specimens leads to an increase in mechanical performances, as expected from the Gibson-Ashby model.

The 3 mm Octet cells present an exception, that emerges from the comparison between the curves at 30 % and 35 % of solid volume fraction. The graph shows that the shape of the curves and the values reached as σ_{\max} are very similar. Also in this case, the explanation of this behavior is due to the production process. As for the Bccz and Rhombic cells, the great density of the specimens with a 3mm cell bring to a great enlargement of the struts during the production process. So the dense structure of the 3 mm cells impedes a good dissipation of heat during

the process. This phenomenon causes an excessive adhesion of the powder to the structure and this leads to a large increase in density. The nominal solid volume fractions are 25 %, 30 % and 35 %, but the values obtained experimentally for the octet 3 mm cells are respectively 54 %, 62 % and 64 % (as shown in Table 4.5). This does not occur for 5 mm and 7 mm cells, and their solid volume fractions correspond to the nominal one. This problem was detected for all 3 mm cells with Bccz, Rhombic dodecahedron and Octet-truss geometry. However, for the first two cells, this anomaly affected only the difference in performance between the 3 mm cell and the larger cells. For Octet cells this phenomenon is particularly pronounced due to the Octet cell structural conformation of the elementary cell. The result is that this problem also influences the behavior as the solid volume fraction changes. In fact the 3 mm Octet cells are the only cell for which the solid volume fraction for 30 % and 35 % has almost the same experimental value.

4.3.4 Auxetic specimens

Auxetic cells are part of a Fractional Factorial DoE aimed at testing their functioning. The Auxetic structures should compact during the uniaxial compression test and offer a greater resistance due to a negative Poisson's coefficient [57].

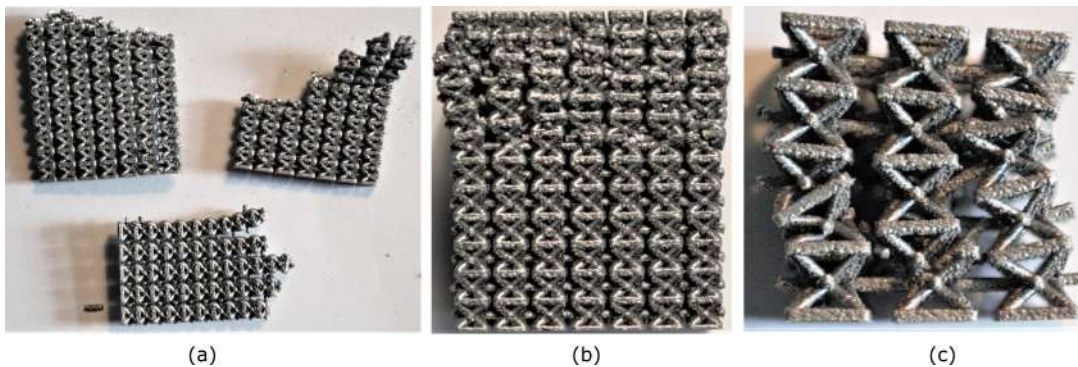


Figure 4.30: Tested specimens: a) Aux-3-35-1, b) Aux-3-35-5 and c) Oct-7-25-2.

Some of the tested Auxetic cells works in this way and compact during the test by increasing the density of the resistant section. This happens when the break starts from the cell nodes, but despite this, good mechanical performance is not achieved. Furthermore, many others specimens broke due to failure of the horizontal struts, with a consequent separation in layers of the specimen, as shown in Figure 4.30. Due to the unexpected and variable behavior and the low strengths obtained in all cases, specimens with this cell design were then excluded from the subsequent tests. The use of these cells requires an improvement in the original model.

Figure 4.31 shows the stress-strain curves for Auxetic specimens.

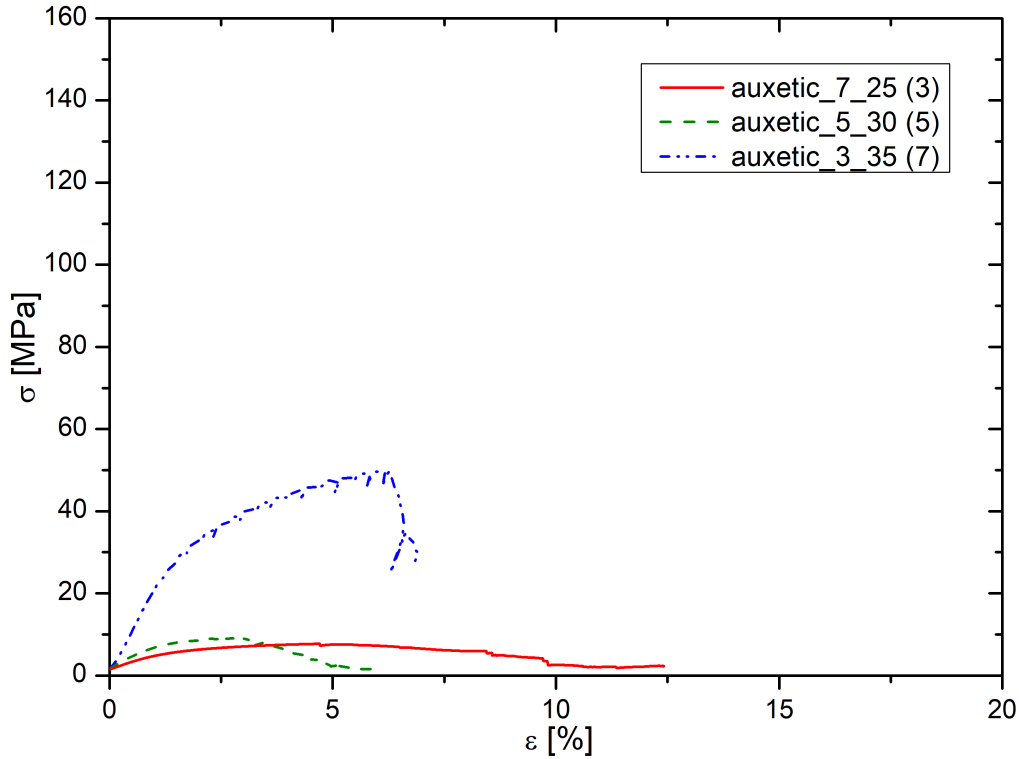


Figure 4.31: Stress-strain curves for specimens with Auxetic cell.

The irregular areas of the curve correspond to the breaking of the struts one by one. For Auxetic cells a particular phenomenon happens, similar to that seen for Octet, Bccz and Rhombic geometry related to the realization of 3 mm cells. For Octet, Bccz and Rhombic cells the density of the specimens produced is higher than that imposed by the model, but for Auxetic cells the opposite phenomenon occurs. The solid volume fraction of the 5 mm and 7 mm cells is lower than that imposed by the model. This is why there is a big difference between the mechanical performance of 3 mm cells and the performances of 5 mm and 7 mm cells. In any case all the mechanical performances in terms of σ_{\max} , σ_{02} and E are very low in respect to the results of the other cell shapes.

4.3.5 Gyroid specimens

The Gyroid structures are part of a Fractional Factorial DoE aimed at testing their functioning. The Gyroid models were generated by an elaboration of three-dimensional surfaces and have not struts as the other geometries.

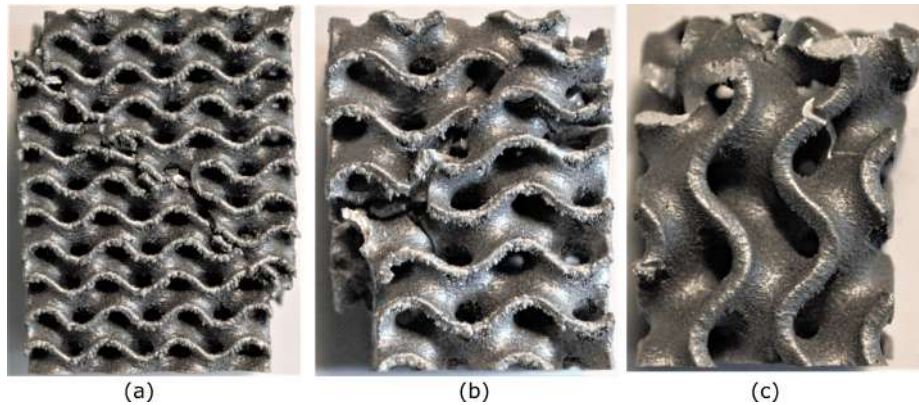


Figure 4.32: Tested specimens: a) Gyr-3-30-1, b) Gyr-5-25-2 and c) Gyr-7-35-2.

All the Gyroid specimens break by collapse of the plane at 45° with respect to Z axis, starting from a side of the specimen as for the Bccz specimens. The fracture proceeds with to the crumbling of the specimen and subsequent collapse of the cells. For the 5 mm and 7 mm cells, the fracture can proceed more irregularly, following the angles of the three-dimensional surface. An example of fractures occurred in each cell size is shown in Figure 4.32.

Figure 4.33 shows the stress-strain curves for Gyroid specimens. All the Gyroid specimens present a good correspondence between experimental solid volume fraction and the solid volume fraction of the model, also in the case of the 3 mm cells. The three-dimensional surfaces that make up the Gyroid cell do not create obstacles to heat dissipation during the production process. This allows to produce always specimens with good consistency with respect to the model. In fact, the anomalies on the 3 mm cells found for the other geometries are not visible from the graphs. As seen from the comparison of the curves, the increase in solid volume fraction leads to an increase in mechanical performance, in accordance with the Gibson-Ashby model.

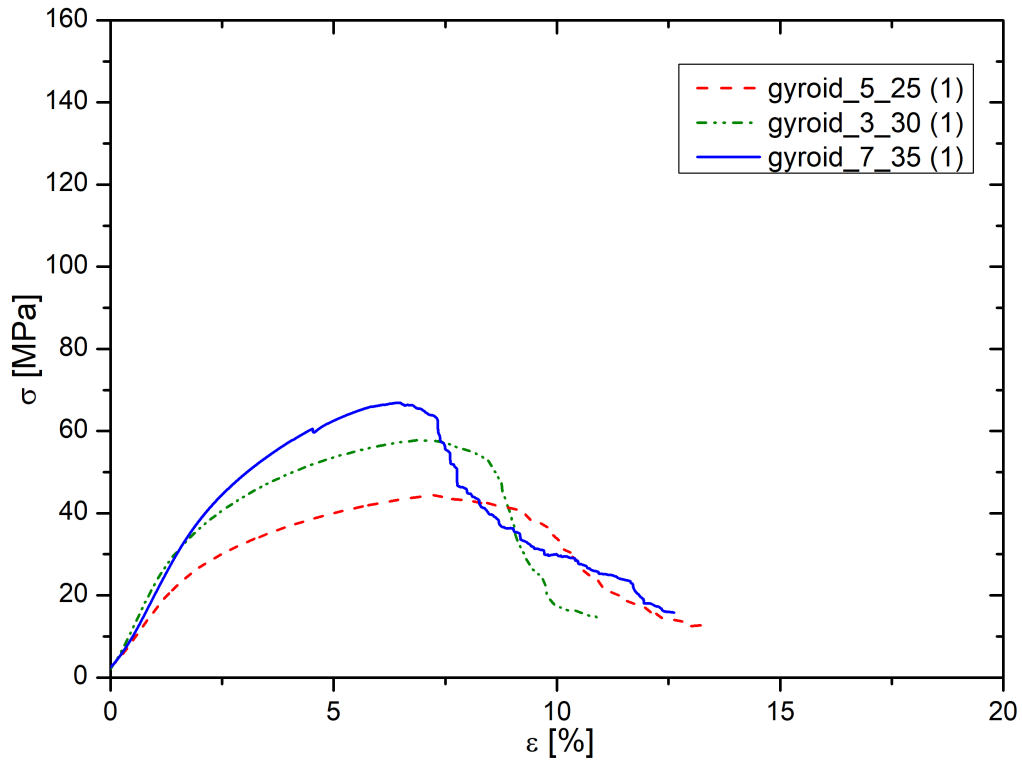


Figure 4.33: Stress-strain curves for specimens with Gyroid cell.

4.3.6 Schwartz diamond specimens

The Schwartz diamond structures are part of a Fractional Factorial DoE aimed at testing their functioning. The Schwartz models were generated by an elaboration of three-dimensional surfaces and have not struts as the other geometries.

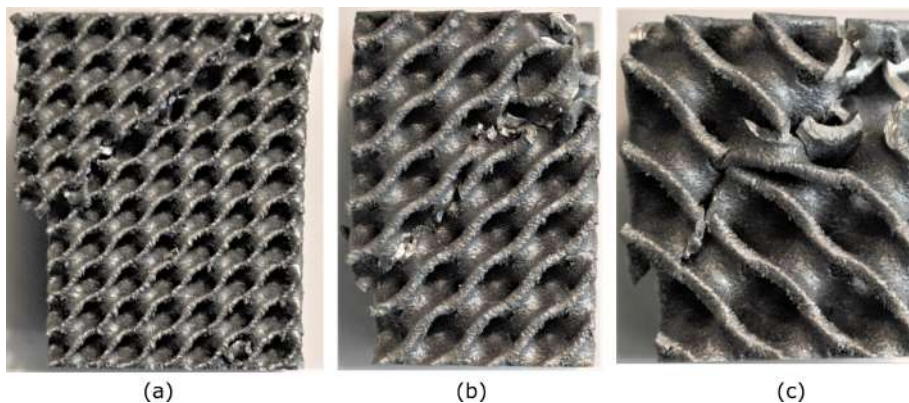


Figure 4.34: Tested specimens: a) Sch-3-25-1, b) Sch-5-35-2 and c) Sch-7-30-1.

All the Schwartz specimens break by collapse of the plane at 45° with respect to Z axis, starting from a side of the specimen as for the Bccz specimens. The fracture proceeds with to the crumbling of the specimen and subsequent collapse of the cells. For the 5 mm and 7 mm the fracture can proceed more irregularly, following the angles of the three-dimensional surface. An example of fractures occurred in each cell size is shown in Figure 4.34.

Figure 4.35 reports the stress-strain curves for Schwartz specimens. All the Schwartz specimens present a good correspondence between experimental solid volume fraction and the solid volume fraction of the model, also the 3 mm cells. The three-dimensional surfaces that make up the Schwartz cell do not create obstacles to heat dissipation during the production process. This allows to always produce specimens with good consistency with respect to the model. In fact, also in this case, the anomalies on the 3 mm cells found for the other geometries are not visible from the graphs. As seen from the comparison of the curves, the increase in solid volume fraction leads to an increase in mechanical performance, in accordance with the Gibson-Ashby model. The mechanical properties, in terms of σ_{\max} , σ_{02} and E, of the Schwartz cells are a little better than those seen for Gyroid cells.

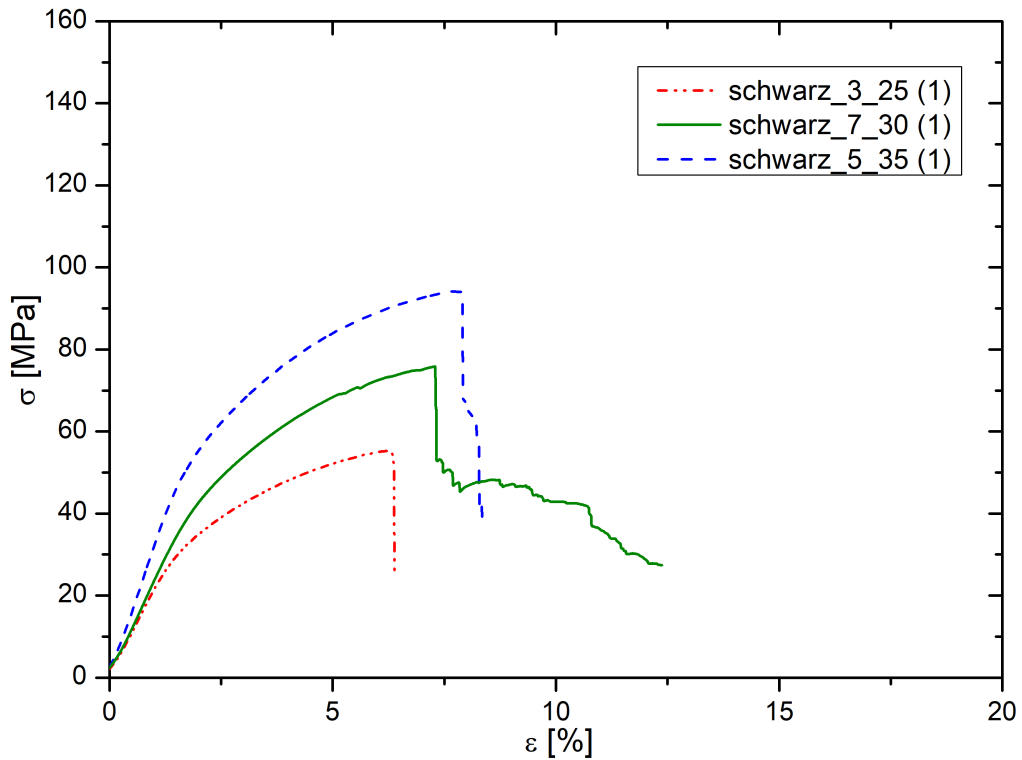


Figure 4.35: Stress-strain curves for specimens with Schwartz diamond cell.

4.3.7 Comparison between stress-strain curves

After the analysis carried out on the different types of cells based on the mechanical behavior and the fracture modes, it is necessary to make a comparison between the results obtained to choose which geometries are most suitable for the final use. On the basis of this comparison, the cells and the cell sizes to be used in other mechanical tests were chosen, in order to optimize the final result and the times for obtaining it. Figure 4.36 reports a comparison among the stress-strain curves of the cell size with 5 mm and 7 mm of the three cells of the Full Factorial DoE: Bccz, Octet-truss and Rhombic dodecahedron.

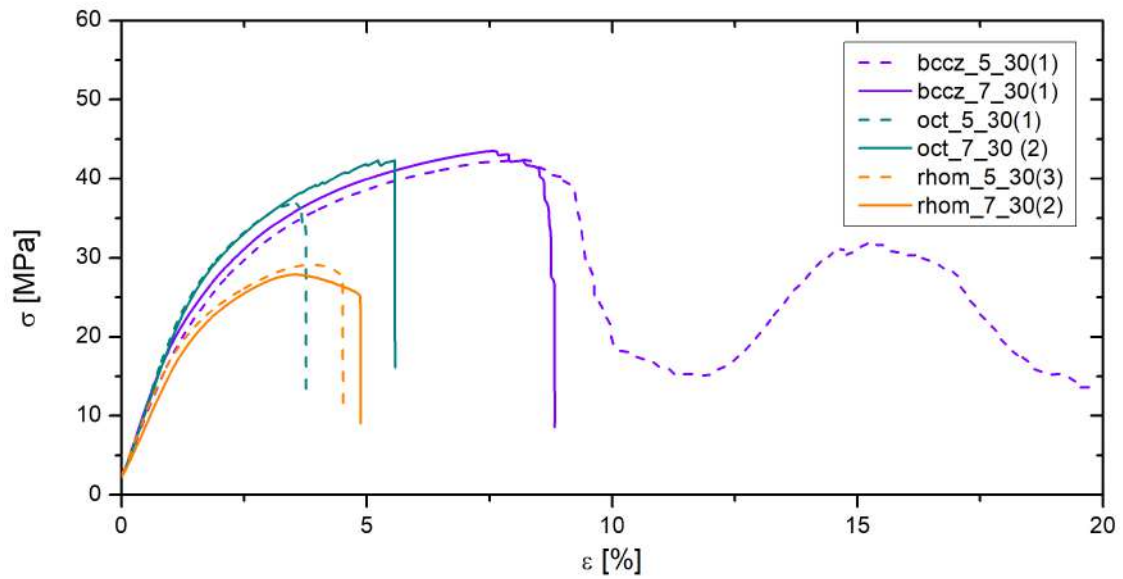


Figure 4.36: Stress-strain curves for Bccz, Octet-truss and Rhombic dodecahedron specimens with 5 mm and 7 mm cells.

All 3 mm cells are excluded from this evaluation because, based on what was observed previously, they are not suitable for the final purpose. The 3 mm cell structure is too dense and cannot be properly produced. Furthermore, such a dense structure does not allow an adequate passage of air through the cells, which would cause too many pressure drops. Comparing the stress-strain curves of 5 mm cell size and 7 mm cell size is possible to see some differences in terms of mechanical performances. The graphs show that the Rhombic and Octet cells have a similar mechanical behavior with a low deformation before breaking. Bccz cells, instead, have a great deformation before the collapse of the first plane. The best mechanical performances in terms of σ_{\max} , σ_{02} and E were obtained for Bccz and Octet specimens, as shown in Table C.3, but the good results of Octet cell are combined with a catastrophic failure mode.

The DoE analysis allows to have the main effect plots. The main effect plots show the influence of the factor (cell type, cell size and solid volume fraction) on the mechanical results expressed by σ_{\max} , σ_{02} and E. Greater is the slope of the line connecting the points, greater is the influence of the factor in the results. In the Figures 4.37, 4.38 and 4.39 the main effect plots for σ_{\max} , σ_{02} and E are reported. As observed, the average values of σ_{\max} are closely related to the shape in the cell: the higher results are for Bccz and Octet, while the Rhombic performance are lower. The influence of the cell size on σ_{\max} is connected to the abnormal behavior of 3 mm cell, while the influence of 5 mm cell size is the same of 7 mm cell size. In the last section of the main effect in Figure 4.37 is shown that σ_{\max} increases almost linearly with the increasing in the solid volume fraction from 25 % to 35 %. Figure 4.38 shows that also the cell type have a big influence on σ_{02} . In this case the results are much higher for Octet cells, followed by Rhombic cells and finally by Bccz cells. This means that for Bccz cells the plastic deformation starts much earlier than the other two cells. Octet and Rhombic have σ_{02} values very similar to σ_{\max} : this suggests a more fragile breaking behavior with a low deformation range. Also for this parameter, the influence of the cell size on σ_{\max} is connected to the abnormal behavior of 3 mm cell, while the influence of 5 mm cell size is the same of 7 mm cell size. As seen for σ_{\max} , the last section shows that σ_{02} increases almost linearly with the increasing in the solid volume fraction from 25 % to 35 %. Finally, as illustrated in Figure 4.39, all the factors influence the Young modulus E in the same way of σ_{02} . The only difference is that the average Young modulus of Bccz structure is higher than the modulus of Rhombic specimens. After analyzing all the aspects of the compression tests on the Bccz, Rhombic and Octet specimens it was decided to continue the tests with the Bccz and Octet cells. The cell sizes that have been chosen are 5 mm and 7 mm, because the 3 mm ones have many production and use problems. Finally, it was decided to use the solid volume fraction of 25 % and 30 % for the specimens for further mechanical tests, to avoid the excessive thickening and weighting of the cell structure with a solid volume of 35 %.

The cells of the Fractional Factorial DoE have to be analyzed in different way. The Auxetic cells did not show mechanical performances comparable with those of the other cells. Furthermore, the breaking method is not repeatable between specimens of the same type and is therefore difficult to evaluate. For this reason they were not chosen to make the specimens for the other tests. The Gyroid and Schwartz diamond cells have both have good and very similar mechanical performances, but those of the Schwartz cells are slightly higher. Therefore, the Schwartz geometry was chosen for the subsequent mechanical tests on sandwich panels. In order not to have too many different cells in the subsequent tests it was decided to choose only a geometry formed by three-dimensional surfaces. Since the mechanical results of the Schwartz cell are slightly better, it was decided to make sandwich panels for the other tests with that one.

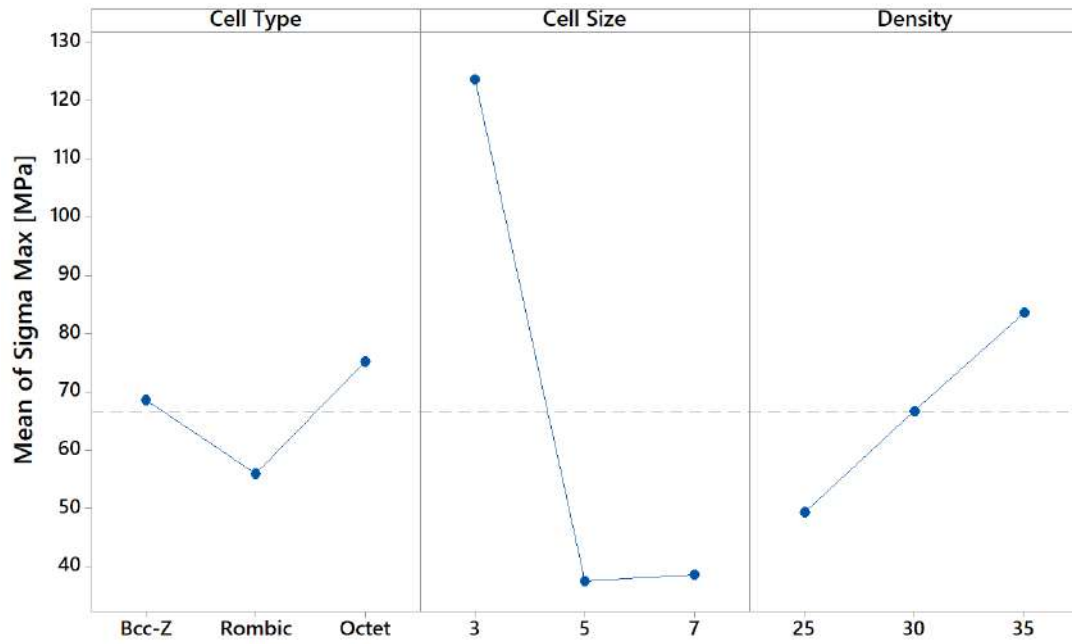


Figure 4.37: Main effect plot for σ_{max} .

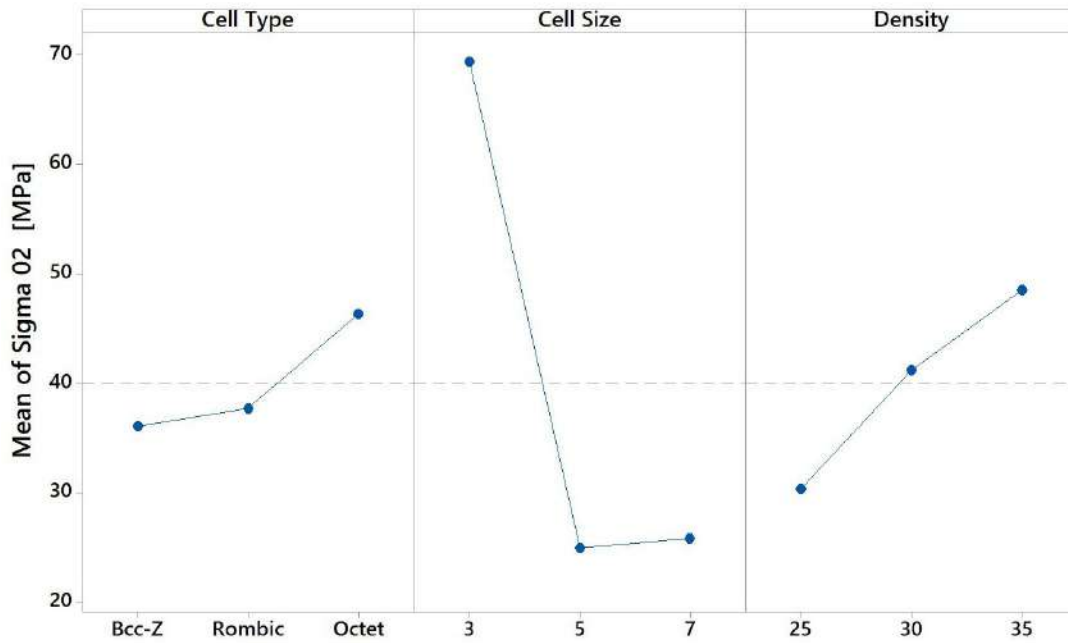


Figure 4.38: Main effect plot for σ_{02} .

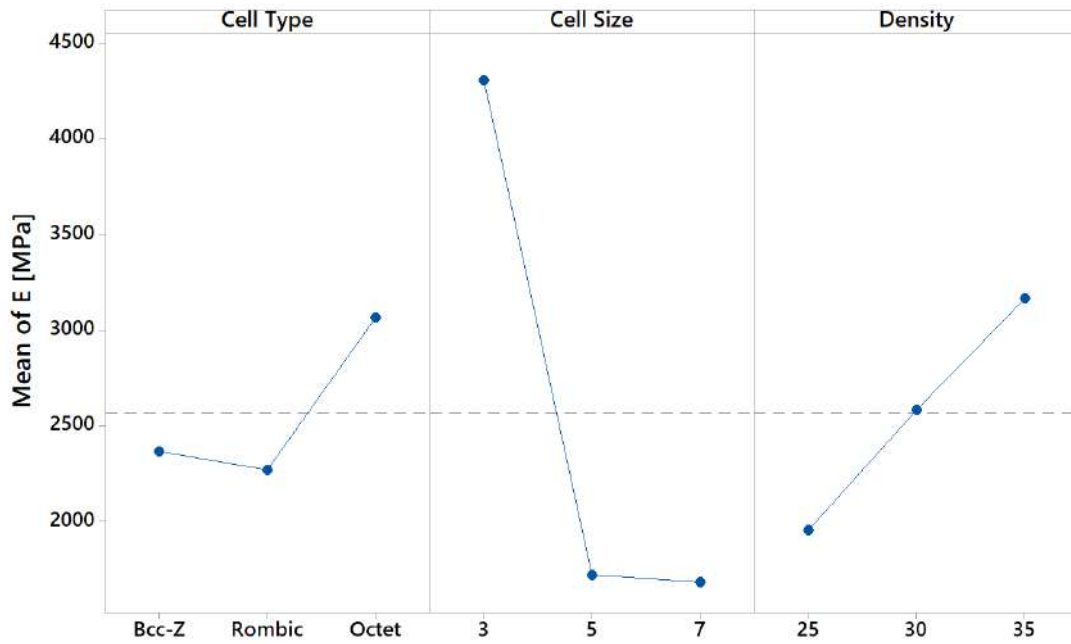


Figure 4.39: Main effect plot for E.

All the mechanical results for uniaxial compression tests on AlSi10Mg specimens are listed in Appendix C in the Tables C.1, C.2, C.3 and C.4. The average values of σ_{\max} , σ_{02} and E are summarized in Figures 4.40 and 4.41.

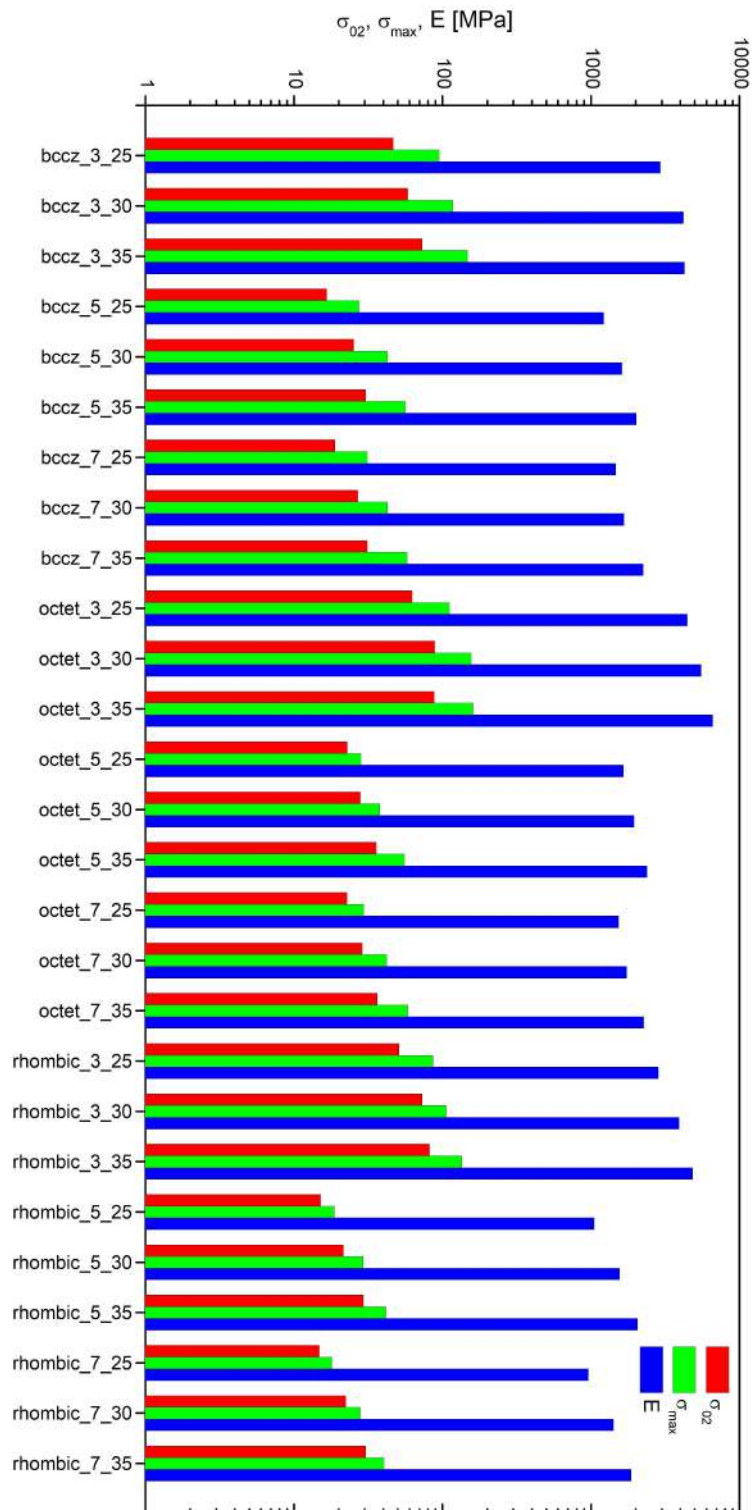


Figure 4.40: Bar chart of the mechanical results for Bccz, Octet-truss and Rhombic dodecahedron cells.

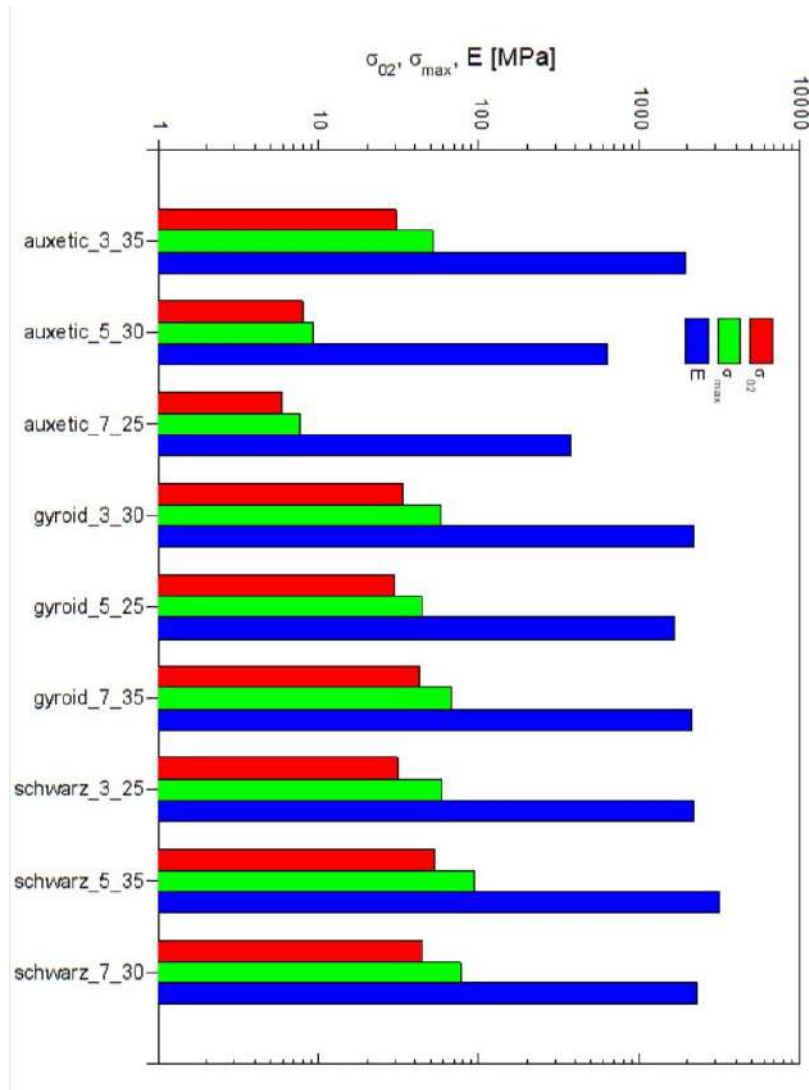


Figure 4.41: Bar chart of the mechanical results for Auxetic, Gyroid and Schwarz diamond cells.

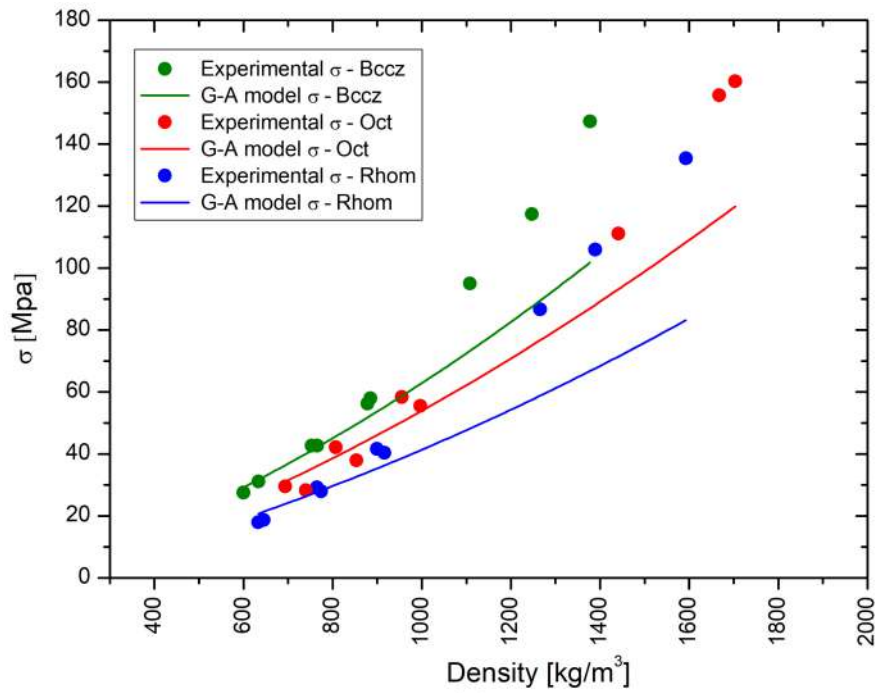
4.3.8 Comparison with Gibson - Ashby model

In this section, the experimental data obtained for all the six cell geometries were compared with the Gibson-Ashby model for the foam with open cells described by the Equations 3.2 and 3.3, reported in the Chapter 3. The model allows to calculate maximum strengths and the Young modulus of the trabecular specimens, using the density and the mechanical values of the foam and of the correspondent dense material. The mechanical values and properties of the fully dense AlSi10Mg alloy components were taken from EOS Datasheet [45]: the value of compressive

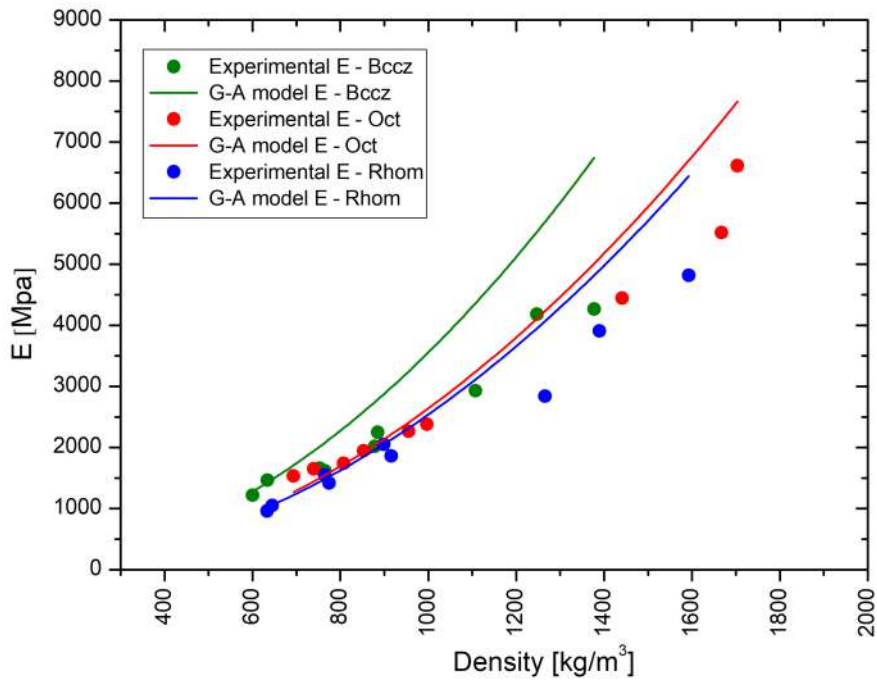
σ_{\max} is equal to 392 MPa, E is 72.4 GPa and ρ is 2.67 kg/dm³.

The Figure 4.42 presents the comparison between the experimental data and the values obtained from the Gibson-Ashby model for the first set of specimens subjected to uniaxial compression tests: Bccz, Octet and Rhombic. The Graph 4.42a shows the results in terms of σ_{\max} , where the lines represent the model, while the points represent the experimental data. It is noted that for low density values the model fits well with the experimental data, while it differs from these for high values. This behavior is due to two causes. The first cause derives from the fact that the Gibson-Ashby model is used for foam, which has very low densities, so it makes difficult to predict the behavior of trabecular structures with higher density. The second reason is the problems related to the 3 mm cells for the geometries of this experimental set (Bccz, Octet and Rhombic). The densities obtained for these specimens are very high due to the problems of the production process and the samples are closer to a fully dense solid respect to a foam. In fact, at high densities it is possible to see how the model provides lower mechanical results than experimental data. The Graph 4.42b illustrates the results in terms of E, where the lines represent the model, while the points represent the experimental data. For the elastic modulus there is less correspondence between the experimental data and the model: they fit well dense for low density values, but separate almost immediately. This shows how the fracture behaviors for the trabecular structures differ from those of the foam. The separation between model and experimental data is, in fact, very evident for the Bccz cells, which, due to the failure of the vertical struts, present a large deformation before the break and an elastic modulus lower than the one foreseen by the model. For the Octet and Rhombic cells this behavior is present for high density but less marked: their fracture mechanism is in fact more similar to that of the foam, with fragile collapse of the cells.

The Figure 4.43 presents the comparison between the experimental data and the values obtained from the Gibson-Ashby model for the second set of specimens subjected to uniaxial compression tests: Auxetic, Gyroid and Schwartz. The Graph 4.43a shows the results in terms of σ_{\max} , where the lines represent the model, while the points represent the experimental data. The model fits well with the experimental data, except for the Auxetic cell, which presents a separation from the model for high density (specimen of 3 mm cell size). The Gyroid and Schwartz cells, on the other hand, have a very similar pattern between the model and experimental data. In the Graph 4.43b the situation is the opposite: the model has difficulty in predicting the elastic modulus of the Gyroid and Schwartz cells, because they are designed by tridimensional surfaces and their behavior is very far from that of the foam. The theoretical and experimental elastic modulus for Auxetic cells, on the other hand, have the same trends.

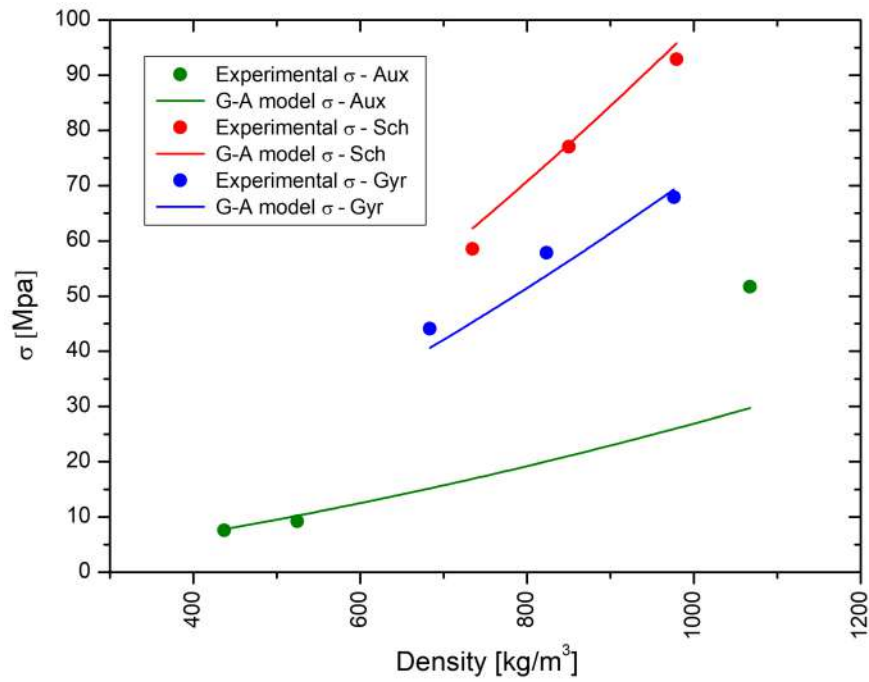


(a)

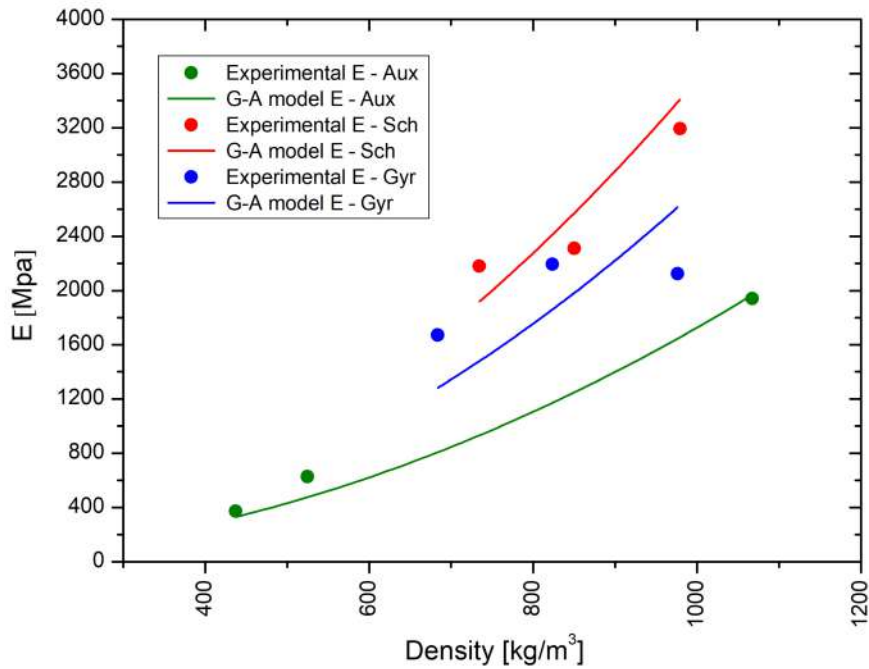


(b)

Figure 4.42: Comparison between experimental data for Bccz, Octet and Rhombic cells in AlSi10Mg with the values obtained from Gibson-Ashby model for the same cells in terms of a) σ_{\max} and b) E .



(a)



(b)

Figure 4.43: Comparison between experimental data for Auxetic, Gyroid and Schwartz cells in AlSi10Mg with the values obtained from Gibson-Ashby model for the same cells in terms of a) σ_{\max} and b) E .

4.4 Uniaxial compression tests on Ti6Al4V trabecular specimens

The second part of the uniaxial compression tests on trabecular specimens is on Ti6Al4V samples. This alloy is widely used in AM and, thanks to its high mechanical resistance, it is suitable for the production of anti-ice systems for supersonic aircraft. This set of tests on Ti6Al4V did not aim to select cells for subsequent tests, but to compare mechanical behaviors with those observed for AlSi10Mg specimens. Two Fractional Factorial DoE were carried out with the same cells used for AlSi10Mg specimens produced for compressive tests.

4.4.1 Bccz specimens

As for AlSi10Mg, all the Bccz Ti6Al4V specimens underwent a fracture mode due to the buckling of the vertical struts and the subsequent failure of the plane at 45° with respect to Z axis, that always starts from one of the sides of the sample. Tested specimens are shown in Figure 4.44.

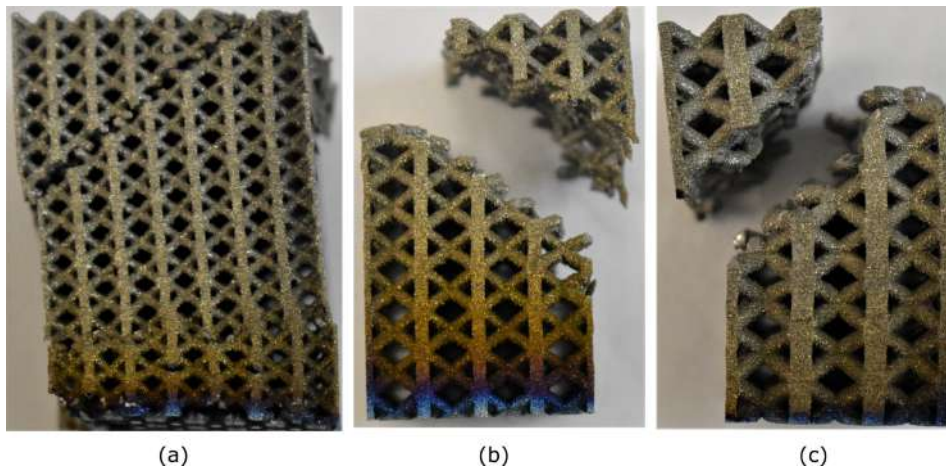


Figure 4.44: Tested specimens: a) Bccz-3-30-3, b) Bccz-5-25-2 and c) Bccz-7-35-1.

In Figure 4.45 the stress-strain curves for Bccz specimens are reported. The mechanical behavior of the Bccz specimens in Ti6Al4V is very similar to the same specimens in AlSi10Mg: in fact the curves present a wide range of deformation before reaching the failure point of the first plane. Unlike the Bccz specimens in AlSi10Mg, all the Ti6Al4V samples present the same failure mode: the failure of the first layer due to buckling and then fragmentation around the broken area. After the collapse of the first layer it is impossible to continue the test due to the separation of the specimens into two parts. The failure of the second layer for specimens with a 3 mm cell does not occur. The behavior of the 3 mm cells is therefore

similar to that of the 5 mm and 7 mm cells. This is due to the fact that Ti alloys have a tendency to deform much lower than Al alloys. Moreover, for the Ti6Al4V alloy there are no problems in the production process seen for the AlSi10Mg alloy. The solid volume fraction of the 3 mm cells has a good correspondence with the nominal one and there are no anomalies that can influence the test result (Table A.5). This happens because the Al alloys have a higher thermal conductivity and a lower melting point. The heat due to the pass of the laser widens more easily to the adjacent areas, thickening the structure. Ti alloys do not present this problem and are able to guarantee heat dispersion even for very dense structures without compromising the production of specimens. The comparison between the stress-strain curves confirms that the increase in solid volume fraction leads to an increase in mechanical results, as predicted by the Gibson-Ashby model. The graphs are very similar to the curves obtained for the same cell in AlSi10Mg, but with the breaking point at higher loads.

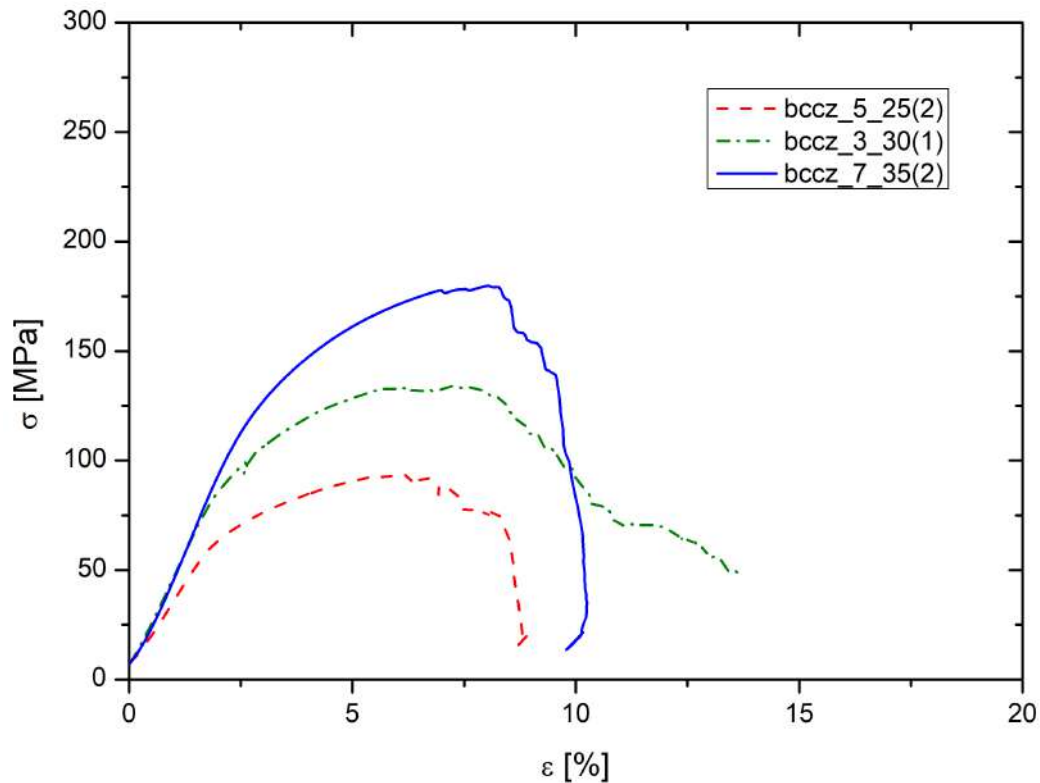


Figure 4.45: Stress-strain curves for Ti6Al4V Bccz specimens.

4.4.2 Rhombic dodecahedron specimens

For all the Ti6Al4V Rhombic dodecahedron specimens the failure occurs with a small deformation range due to the breaking of the struts at the nodes, as described for Rhombic AlSi10Mg cells. The failure occurs by collapse of a plane at 45° with respect to Z axis, starting from a corner of the specimen. The failure of the structure is followed by a violent separation of the parts of the specimen and by the noise generated by the fracture of the cells. Tested specimens are shown in Figure 4.46.

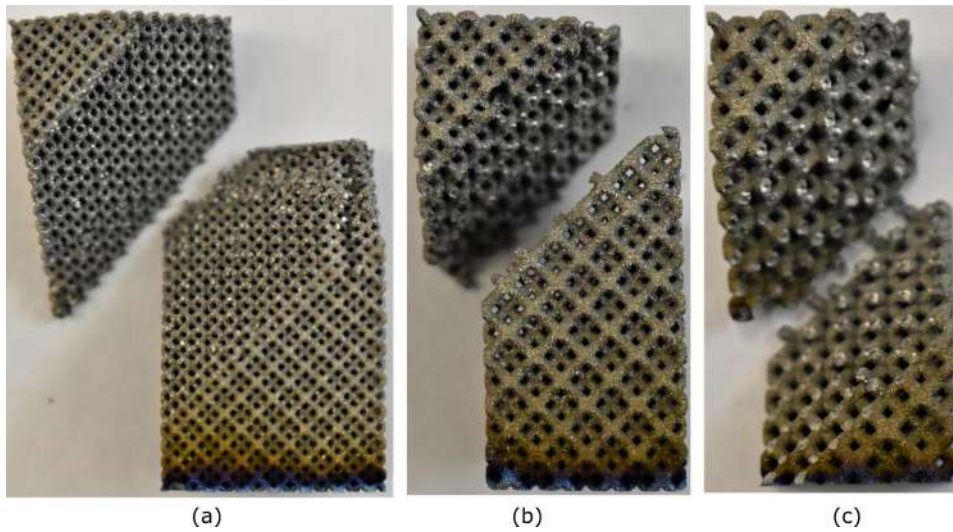


Figure 4.46: Tested specimens: a) Rhom-3-25-1, b) Rhom-5-35-3 and c) Rhom-7-30-3.

In the Figure 4.47 the stress-strain curves for Rhombic dodecahedron specimens are reported. As described for AlSi10Mg, the Ti6Al4V specimens with Rhombic cell present a low deformation before reaching the failure point for all the cell sizes. Also in this case the experimental solid fraction volume of the 3 mm cell fits well with the nominal one. The comparison of the curves proves that the increase in solid volume fraction leads to an increase in mechanical performance, in accordance with the Gibson-Ashby model. For the specimens in AlSi10Mg the Rhombic cells had lower mechanical performances than those of Bccz and Octet-truss. For specimens in Ti6Al4V, on the other hand, the results in terms of σ_{\max} , σ_{02} and E are comparable between the three geometries of the first DoE. This may be due to the mechanical properties of Ti6Al4V, which has a higher mechanical strength than Al alloys, but a lower ability to deform. In fact, all the cells of this material have a more fragile type of break.

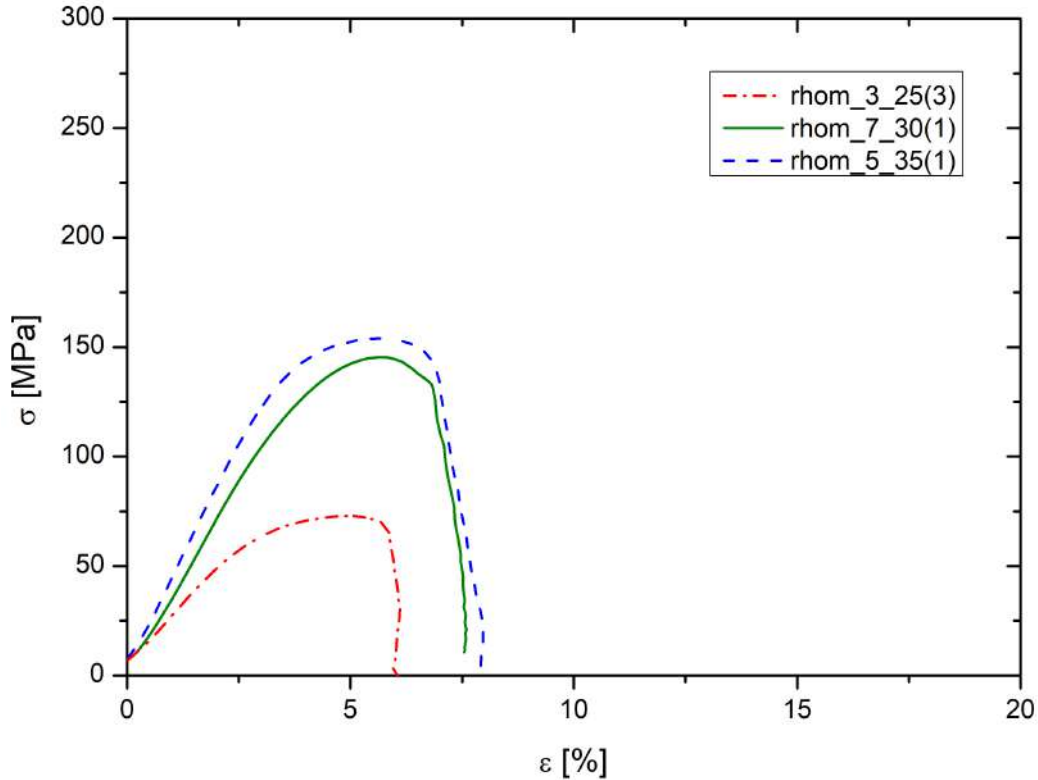


Figure 4.47: Stress-strain curves for Ti6Al4V Rhombic dodecahedron specimens.

4.4.3 Octet-truss specimens

For all the Ti6Al4V Octet-truss specimens the failure occurs with a small deformation range due to the breaking of the struts at the nodes, as described for Octet AlSi10Mg cells. The failure occurs by collapse of a plane at 45° with respect to Z axis, starting from a corner of the specimen. The failure of the structure is followed by a violent separation of the parts of the specimen and by the noise generated by the fracture of the cells. For Octet cells only, the 3 mm cell behaves abnormally even with the Ti6Al4V material. Tested specimens are shown in Figure 4.48.

As it is possible to see from the stress-strain curves in Figure 4.49, the specimens with Octet-truss geometry and 5 mm and 7 mm of cell sizes present a low deformation before the failure of the first plane. For the 3 mm cells specimens a different behavior is recorded: the deformation range is bigger and there are some irregular ranges due to the breaking of the struts.

This behavior is the same observed for the 3 mm Bccz, Octet-truss and Rhombic dodecahedron cells made of AlSi10Mg, so the measured solid fraction volume was greater than the nominal one. For specimens in Ti6Al4V it happens only in the case of the Octet cell, due to the particular conformation of the elementary cell

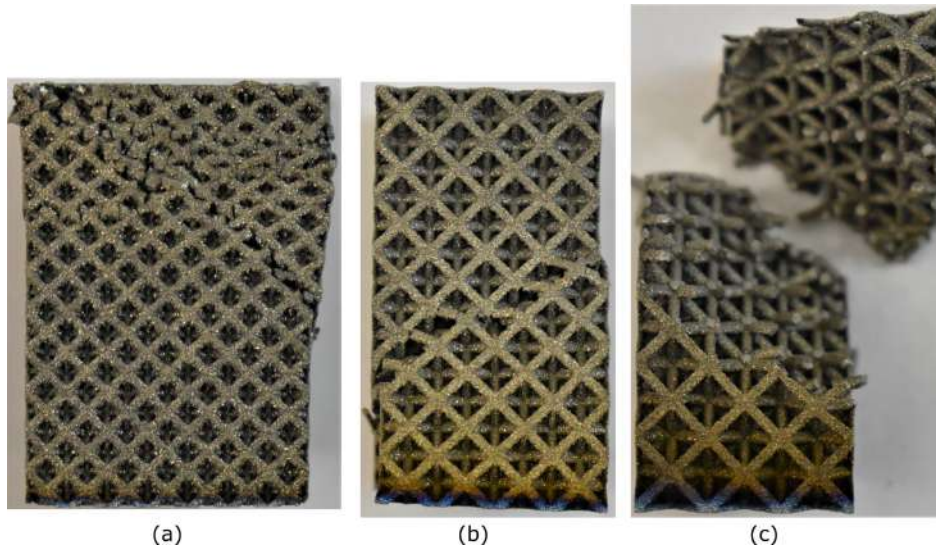


Figure 4.48: Tested specimens: a) Oct-3-35-1, b) Oct-5-30-2 and c) oct-7-25-3.

structure that hinders the diffusion of heat during the production process, causing the adhesion of the unmelted powders. The model present a solid volume fractions of 35 %, but the experimental value measured for the 3 mm cell is 51 %, as shown in Table 4.5.

The comparison among the stress-strain curves confirmed that the increase in solid volume fraction leads to an increase in mechanical results, as predicted by the Gibson-Ashby model.

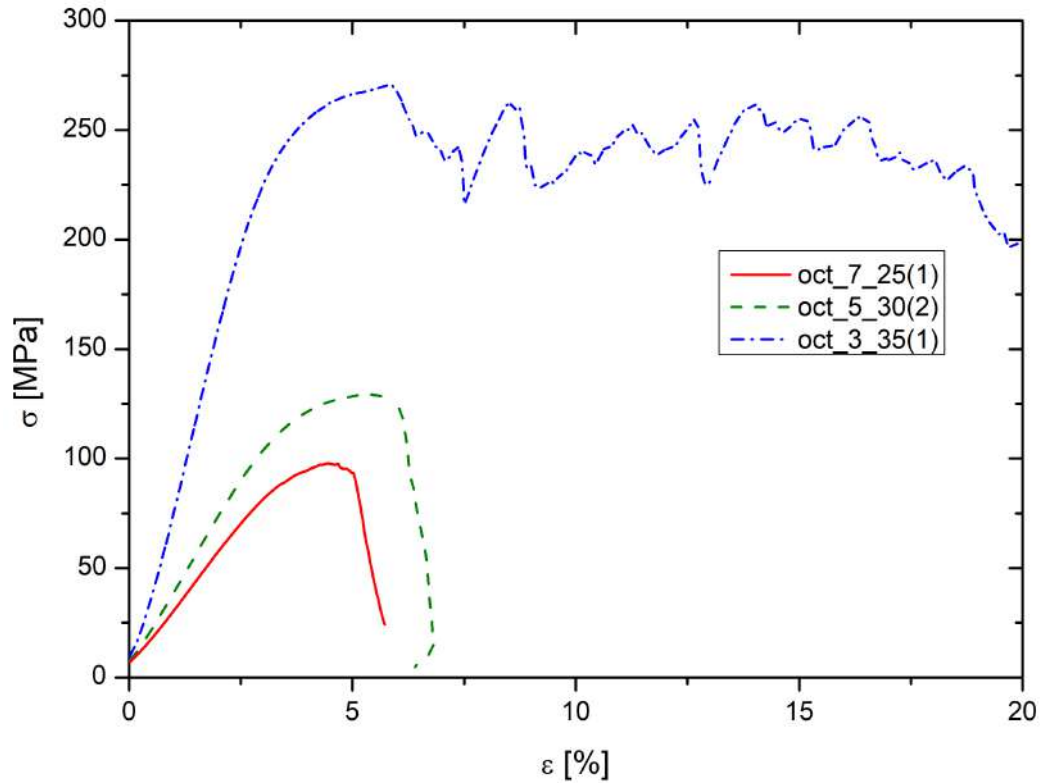


Figure 4.49: Stress-strain curves for Ti6Al4V Octet-truss specimens.

4.4.4 Auxetic specimens

Auxetic cells are part of the second Fractional Factorial DoE for Ti6Al4V specimens. The Auxetic structures should compact during the uniaxial compression test and offer a greater resistance due to a negative Poisson's coefficient.

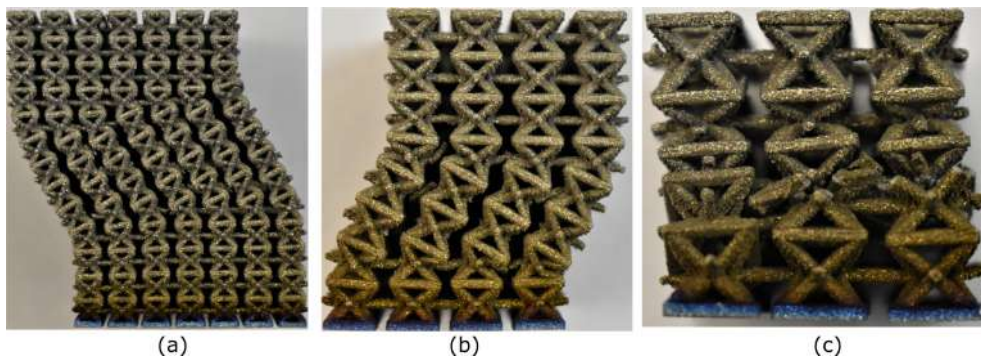


Figure 4.50: Tested specimens: a) Aux-3-35-1, b) Aux-5-30-2 and c) Aux-7-25-5.

Some of the tested auxetic cells works in this way and compact during the test by increasing the density of the resistant section. This happens when the break starts from the cell nodes, but despite this, good mechanical performance is not achieved. Furthermore, many others specimens broke due to failure of the horizontal struts, with consequent separation in layers of the specimen. Still other samples, as shown in the Figures 4.50a and 4.50b, underwent the collapse of a lateral cell which caused a wrinkling of the whole specimen. Also for Ti6Al4V the use of these cells requires an improvement in the original model.

The Figure 4.51 reports the stress-strain curves for Auxetic specimens, where is possible to see in the curves some irregular areas, corresponding to the breaking of the struts. All the mechanical results, σ_{\max} , σ_{02} and E, are lower compared to the results of all the other cell shapes.

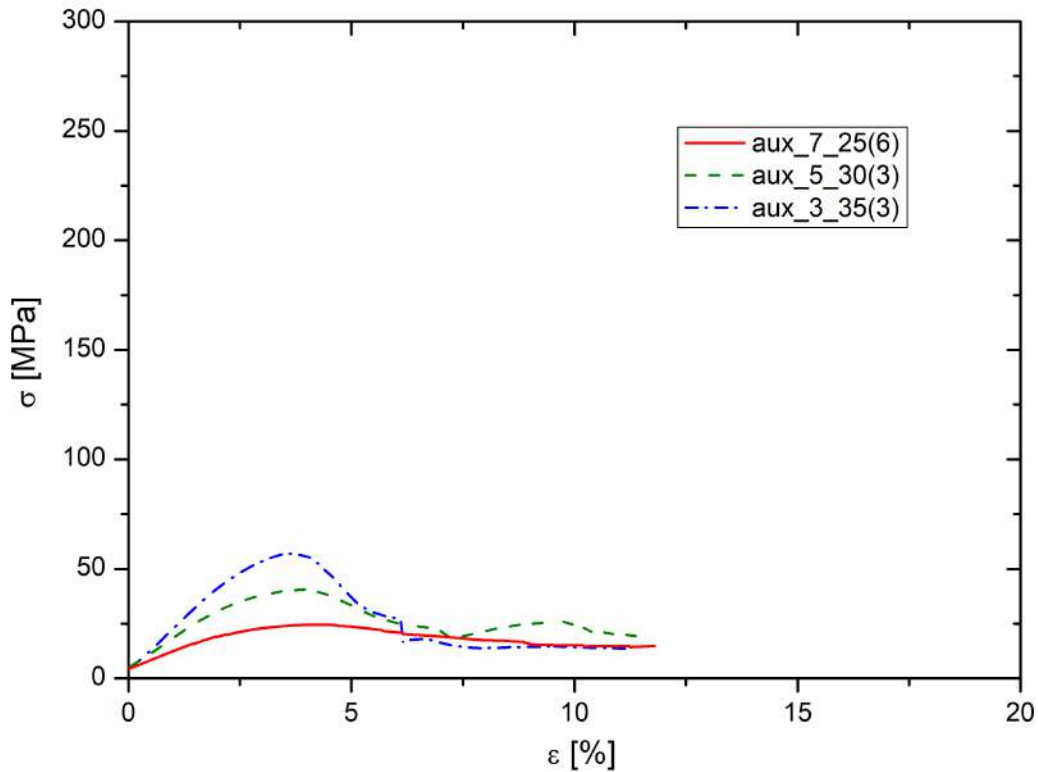


Figure 4.51: Stress-strain curves for Ti6Al4V Auxetic specimens.

4.4.5 Gyroid specimens

The Gyroid structures are part of the second Fractional Factorial DoE for Ti6Al4V specimens. The Gyroid models were generated by an elaboration of three-dimensional surfaces and have not struts as the other geometries. All the Gyroid

specimens break by collapse of the plane at 45° with respect to Z axis, starting from a side of the specimen as for the Bccz specimens. The fracture proceeds with to the crumbling of the specimen and subsequent collapse of the cells. For the 5 mm and 7 mm the fracture can proceed more irregularly, following the angles of the three-dimensional surface. Tested specimens are shown in Figure 4.52.

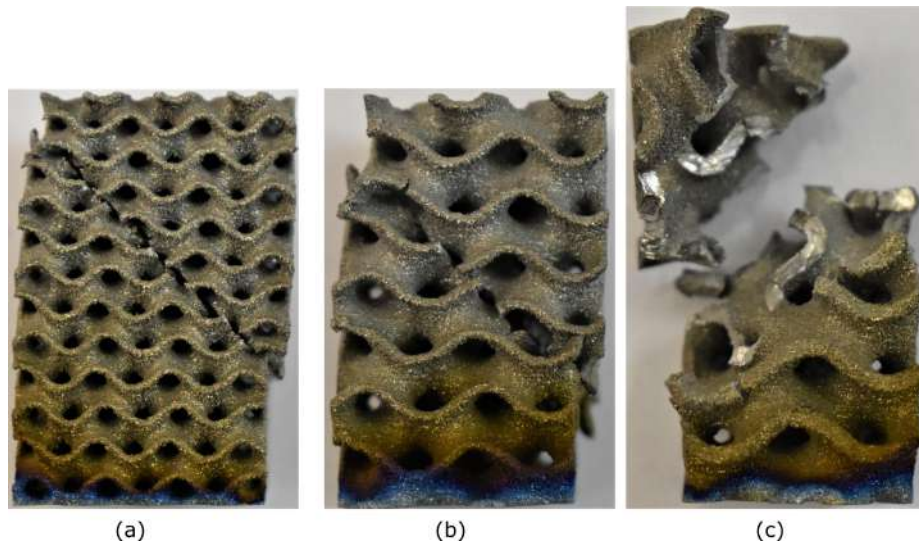


Figure 4.52: Tested specimens: a) Gyr-3-30-2, b) Gyr-25-2 and c) Gyr-7-35-1.

Figure 4.53 reports the stress-strain curves for Gyroid specimens. As seen from the comparison of the curves, the increase in solid volume fraction leads to an increase in mechanical performance, in accordance with the Gibson-Ashby model.

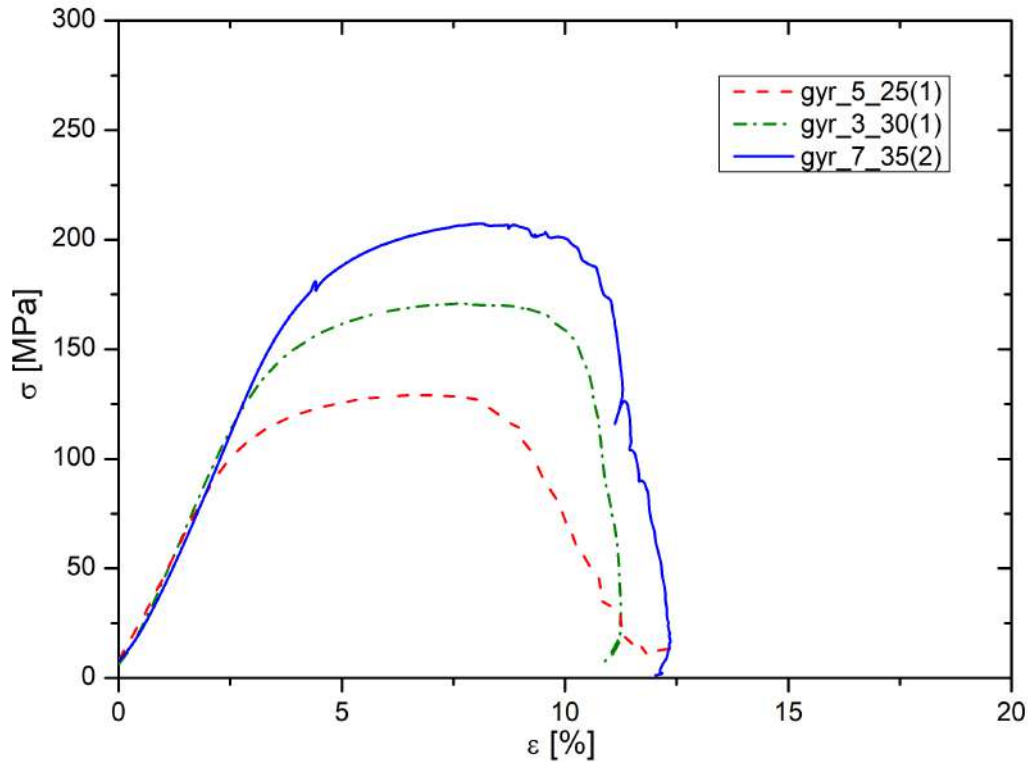


Figure 4.53: Stress-strain curves for Ti6Al4V Gyroid specimens.

4.4.6 Schwartz diamond specimens

The Schwartz diamond structures are part of the second Fractional Factorial DoE for Ti6Al4V specimens. The Schwartz models were generated by an elaboration of three-dimensional surfaces and have not struts as the other geometries. All the Schwartz specimens break by collapse of the plane at 45° with respect to Z axis, starting from a side of the specimen as for the Bccz specimens. The fracture proceeds with to the crumbling of the specimen and subsequent collapse of the cells. For the 5 mm and 7 mm the fracture can proceed more irregularly, following the angles of the three-dimensional surface. Tested specimens are shown in Figure 4.54.

Figure 4.55 reports the stress-strain curves for Schwartz specimens. As seen from the comparison of the curves, the increase in solid volume fraction leads to an increase in mechanical performance, in accordance with the Gibson-Ashby model. The mechanical properties, in terms of σ_{\max} , $\sigma_{0.2}$ and E, of the Schwartz cells are a little better than those seen for Gyroid cells, as seen for AlSi10Mg specimens.

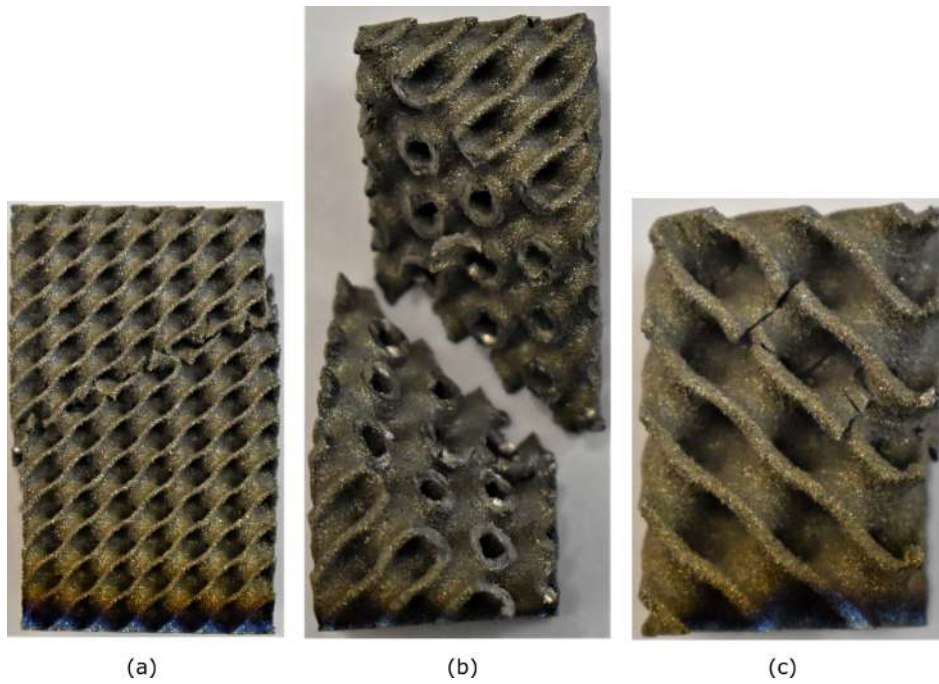


Figure 4.54: Tested specimens: a) Sch-3-25-2, b) Sch-5-35-2 and c) Sch-7-30-2.

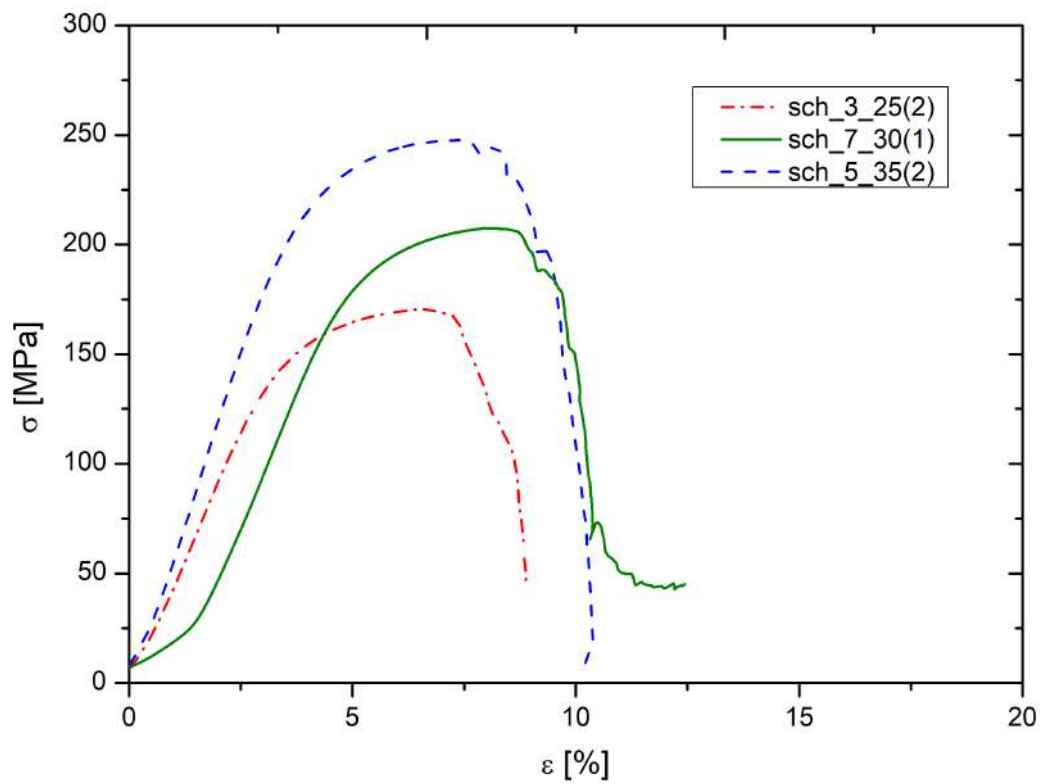


Figure 4.55: Stress-strain curves for Ti6Al4V Schwartz diamond specimens.

4.4.7 Comparison between stress-strain curves

As seen also for the specimens in AlSi10Mg, the cell that shows the most deformation before the breaking of the first plane is the Bccz. Octet and Rhombic cells have a much narrower range of deformation. However, compared to Al specimens, the deformation of all Ti structures is much lower. Thanks to the greater mechanical resistance of Ti alloys, all the sample breaks take place at much higher loads than the Al alloy specimens. The only exception is given by the auxetic specimens, which have failure due to brittle fracture of the horizontal struts: in this case the excellent mechanical performances of Ti alloys do not bring benefits. The mechanical results of the Gyroid and Schwartz cells are in line with what seen for AlSi10Mg specimens: very good for both cells, but better for Schwartz cells. For Ti specimens, due to the lower thermal conductivity and the high melting point, the phenomenon of thickening of the structure for 3 mm cells almost never occurs, with the sole exception of Octet cells.

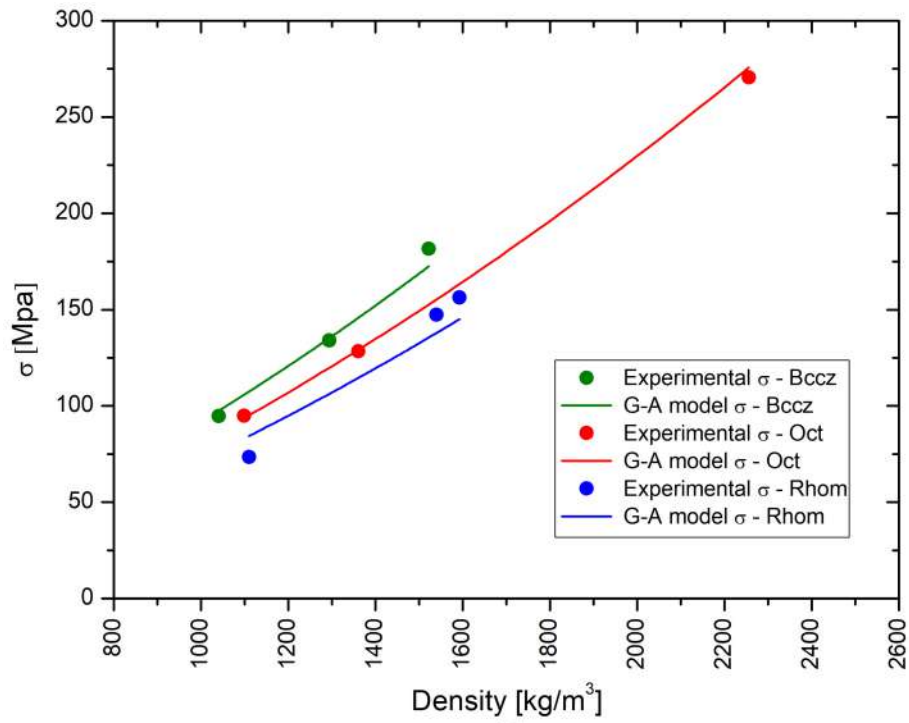
4.4.8 Comparison with Gibson-Ashby model

In this section, the experimental data obtained for all the six cell geometries have been compared with the Gibson-Ashby model for the foam with open cells described by the Equations 3.2 and 3.3, reported in the Chapter 3. The model allows to calculate maximum strengths and the Young modulus of the trabecular specimens, using the density and the mechanical values of the foam and of the correspondent dense material. The mechanical values and properties of the fully dense Ti6Al4V alloy components were taken from EOS Datasheet [50]: the value of compressive σ_{\max} is equal to 1215 MPa, E is 110 GPa and ρ is 4.41 kg/dm³.

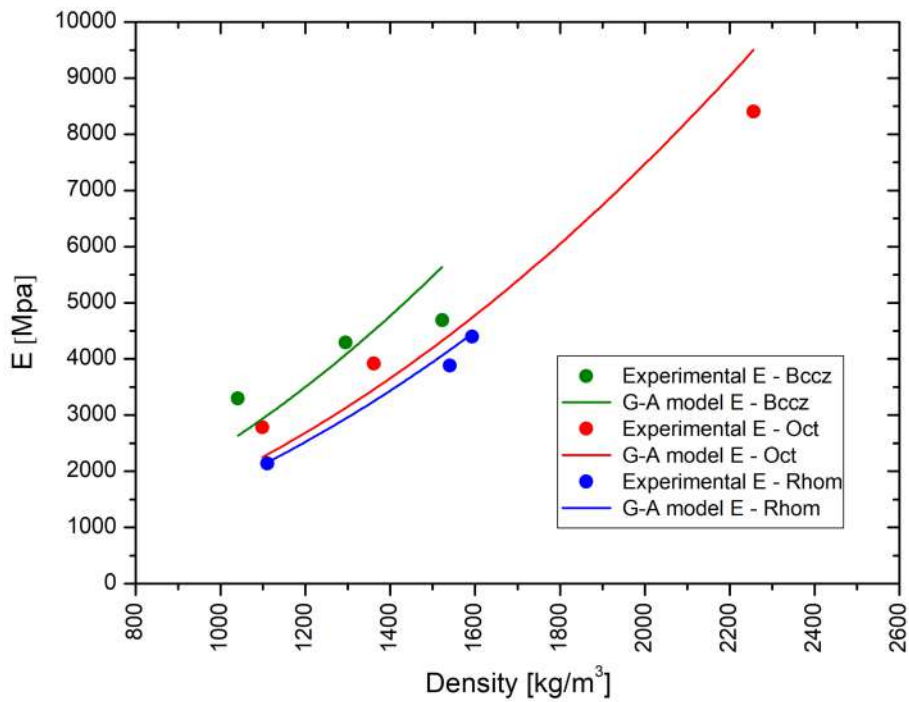
The Figure 4.56 presents the comparison between the experimental data and the values obtained from the Gibson-Ashby model for the first set of specimens subjected to uniaxial compression tests: Bccz, Octet and Rhombic. The Graph 4.56a shows the results in terms of σ_{\max} , where the lines represent the model, while the points represent the experimental data. The model and the experimental data fit well for all densities, because, as seen in the previous sections, for Ti6Al4V the problem of density increase in 3 mm cells is almost absent. The Graph 4.42b illustrates the results in terms of E, where the lines represent the model, while the points represent the experimental data. For the elastic modulus there is less correspondence between the experimental data and the model. This shows how the fracture behaviors of the trabecular structures differ from those of the foam. The separation between model and experimental data is, in fact, very evident for the Bccz cells, but less than what was seen for the same cells in AlSi10Mg. This is because, as seen from the stress-strain curves, even the Bccz cell produced in Ti alloy deforms less before The breaking. For the Octet and Rhombic cells this behavior si less marked: their fracture mechanism is in fact more similar to that of

the foam, with fragile collapse of the cells.

The Figure 4.57 presents the comparison between the experimental data and the values obtained from the Gibson-Ashby model for the second set of specimens subjected to uniaxial compression tests: Auxetic, Gyroid and Schwartz. The Graph 4.57a shows the results in terms of σ_{\max} , where the lines represent the model, while the points represent the experimental data. The model fits well with the experimental data for all the cells geometry. In the Graph 4.57b the situation is the opposite: the model has difficulty in predicting the elastic modulus, in particular for the Gyroid and Schwartz cells, because they are designed by tridimensional surfaces and their behavior is very far from that of the foam. The theoretical and experimental elastic modulus for Auxetic cells, on the other hand, have the same trends, because Auxetic cells have similar fracture and densification characteristics of the foam structures.



(a)



(b)

Figure 4.56: Comparison between experimental data for Bccz, Octet and Rhombic cells in Ti6Al4V with the values obtained from Gibson-Ashby model for the same cells in terms of a) σ_{max} and b) E .

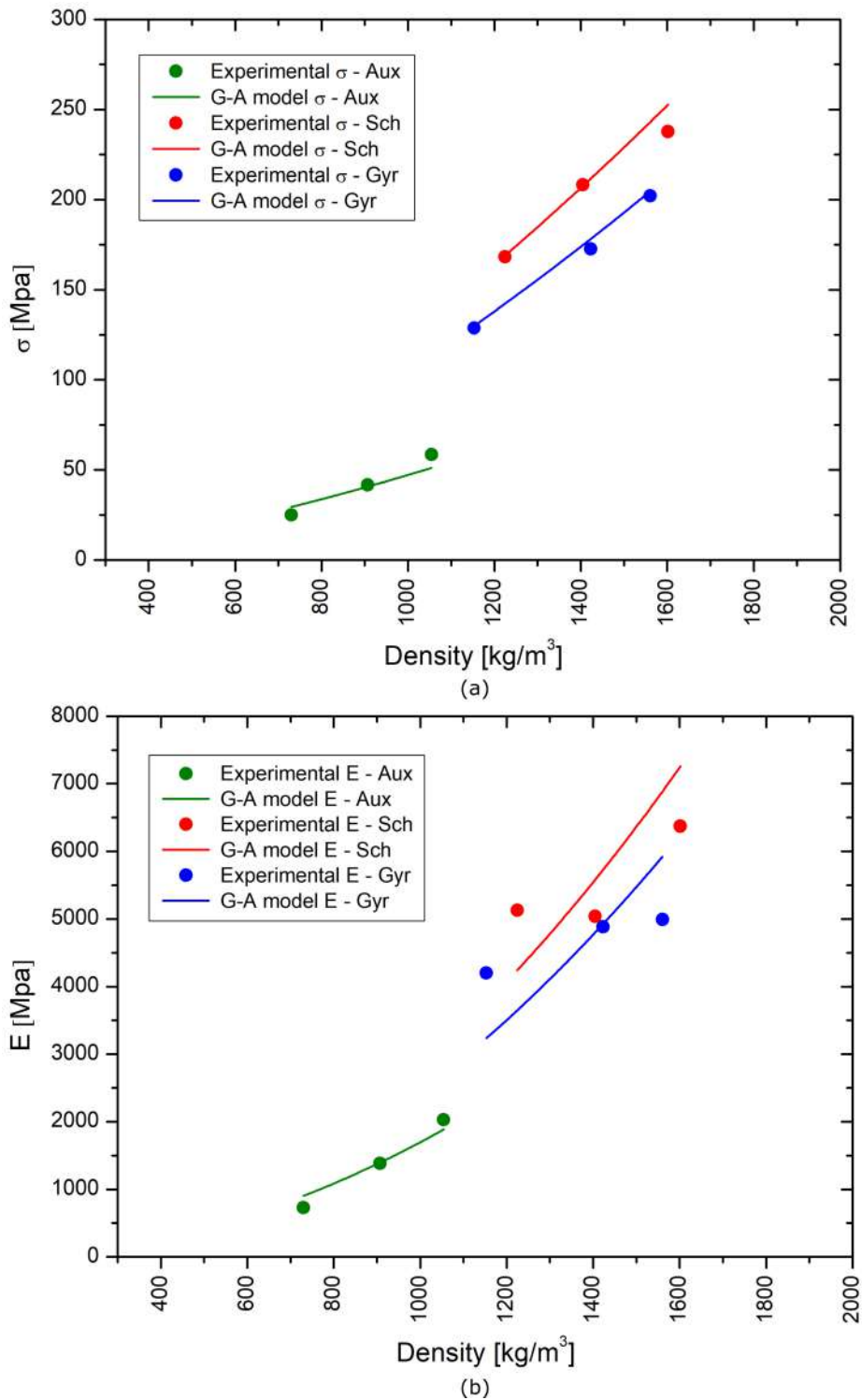


Figure 4.57: Comparison between experimental data for Auxetic, Gyroid and Schwartz cells in Ti6Al4V with the values obtained from Gibson-Ashby model for the same cells in terms of a) σ_{\max} and b) E .

4.5 Uniaxial compression tests on sandwich panels

Only AlSi10Mg panels were tested by compression with the structures defined at the end of the compression tests on the specimens. In this section the failure modes for compression panels were evaluated and compared with those seen for the specimens. In general, the observed fracture modes confirm those seen during the compression of the specimens. In Figure 4.58 the panels after compression are shown.

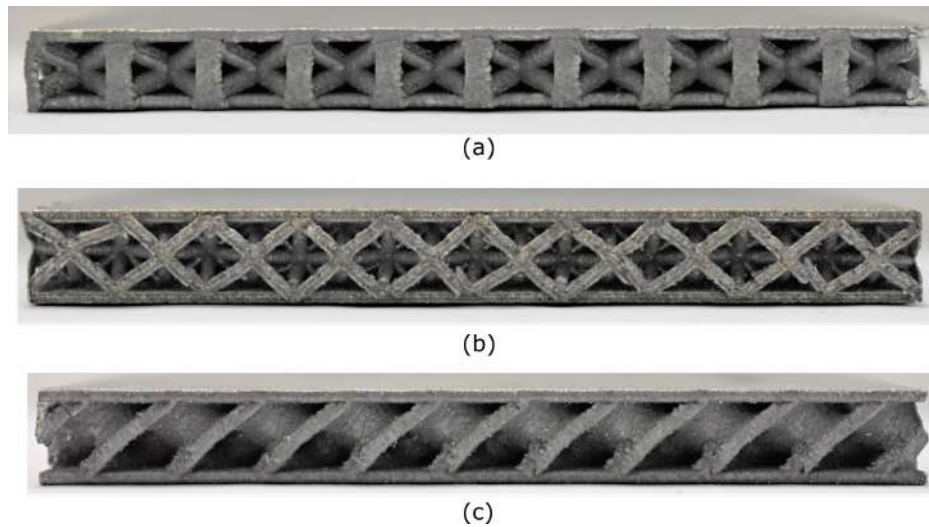


Figure 4.58: Tested sandwich panels: a) Bccz-7-30, b) Oct-7-25 and c) Sch-7-25.

It should be noted that the collapse of the panel with Bccz cell occurs after deformation and breakage due to buckling of the vertical struts. The Octet panels break due to the collapse of the struts at the nodes. However, breaks are concentrated in the conjunction between the core and the skin, where the struts are thinner. There is almost never a break at the central nodes. Finally, the breakage of the panels with Schwartz cell takes place for very high loads mainly due to the progressive disintegration of the core. There is no failure at 45° observed for the specimens due to the thinness of the core.

The stress-strain curves of the tests are presented in Appendix D, in the Figures D.55, D.56 and D.57, while the mechanical results in terms of σ_{\max} , σ_{02} , E , σ_{\max}/ρ , σ_{02}/ρ and E/ρ are resumed in Figures 4.59 and 4.60. The Bccz and Schwartz panels have a wider range of plastic deformation than Octet cells. From the point of view of the σ_{\max} and σ_{02} the best cell is the Schwartz, followed by the Bccz cell and finally by the Octet; from the point of view of the elastic modulus the best cell is the Schwartz, followed by the Oct cell and finally by the Bccz. However, the results

of the Bccz and the Octet are very similar.

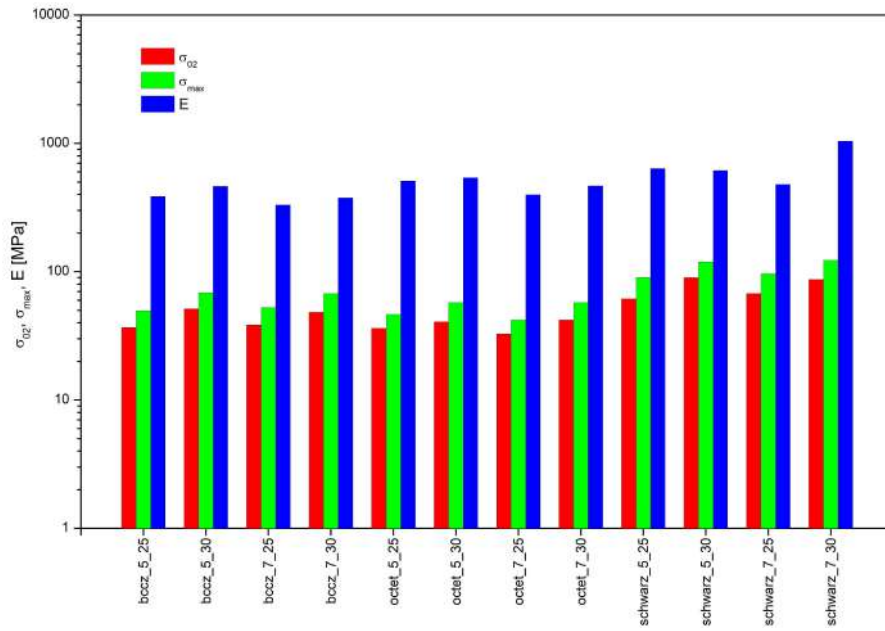


Figure 4.59: Column chart of compression test results on sandwich panels.

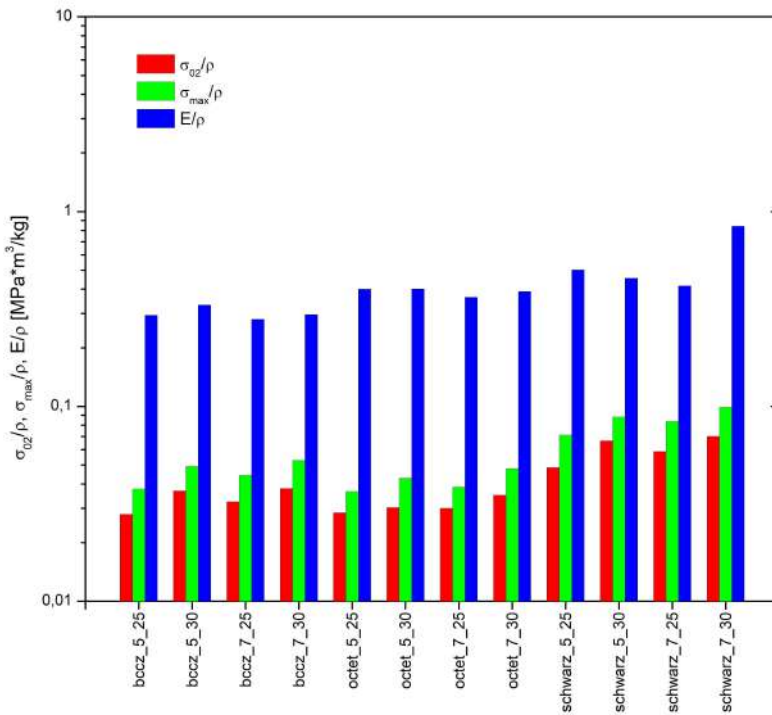


Figure 4.60: Column chart of compression test results on sandwich panels.

For an assessment of the factors that most influenced the results in terms of σ_{\max} , σ_{02} and E , three main effect plots were produced and reported in Figures 4.61, 4.62 and 4.63. As can be seen from the graphs, the most influential factor is the type of cell: the best performance is obtained with the Schwartz cell, followed by the Bccz. However, the Octet cell has a Young modulus greater than the Bccz cell. The second most influential factor is the solid volume fraction: passing from 25 % to 30 % there is an improvement in the mechanical properties, as already seen during the compression on the specimens. The size of the cell does not influence the final result in any way.

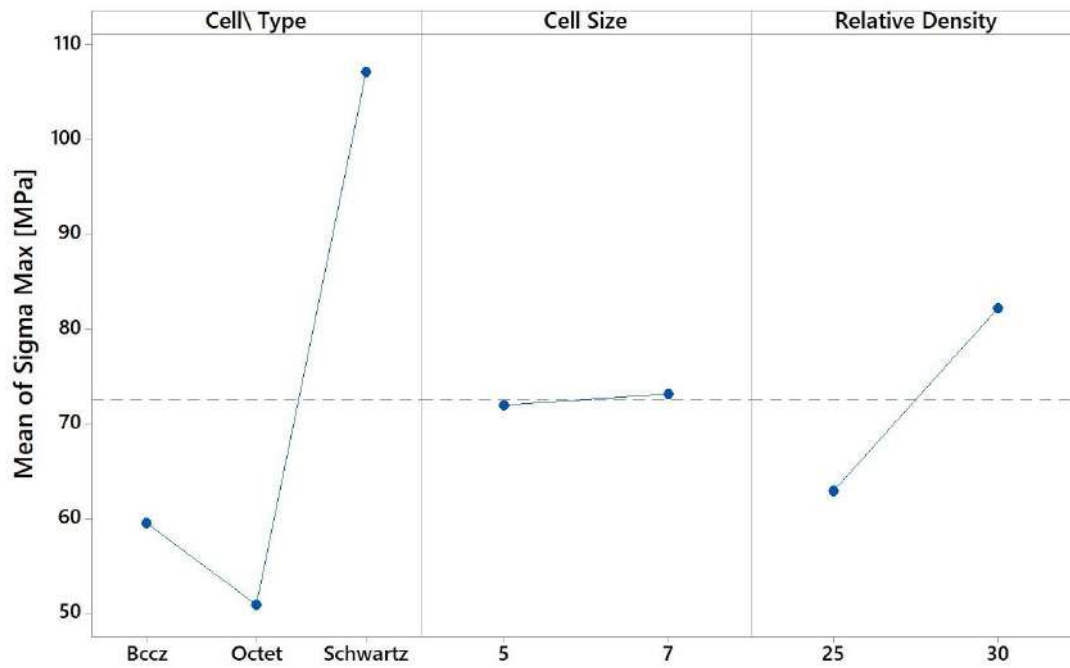


Figure 4.61: Main effect plot for σ_{\max} .

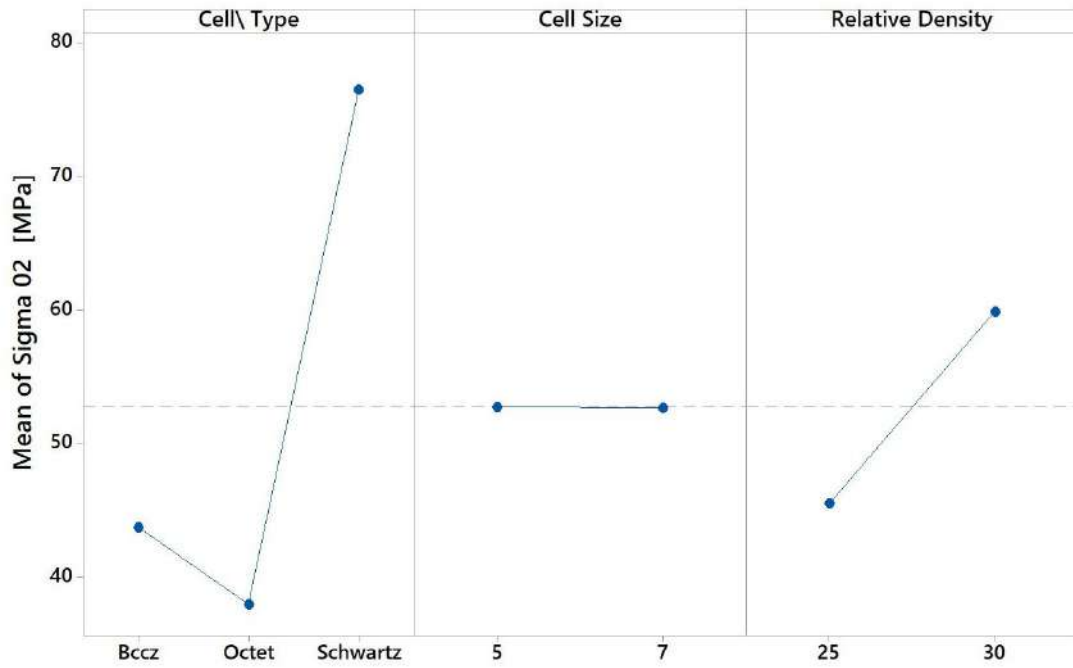


Figure 4.62: Main effect plot for σ_{02} .

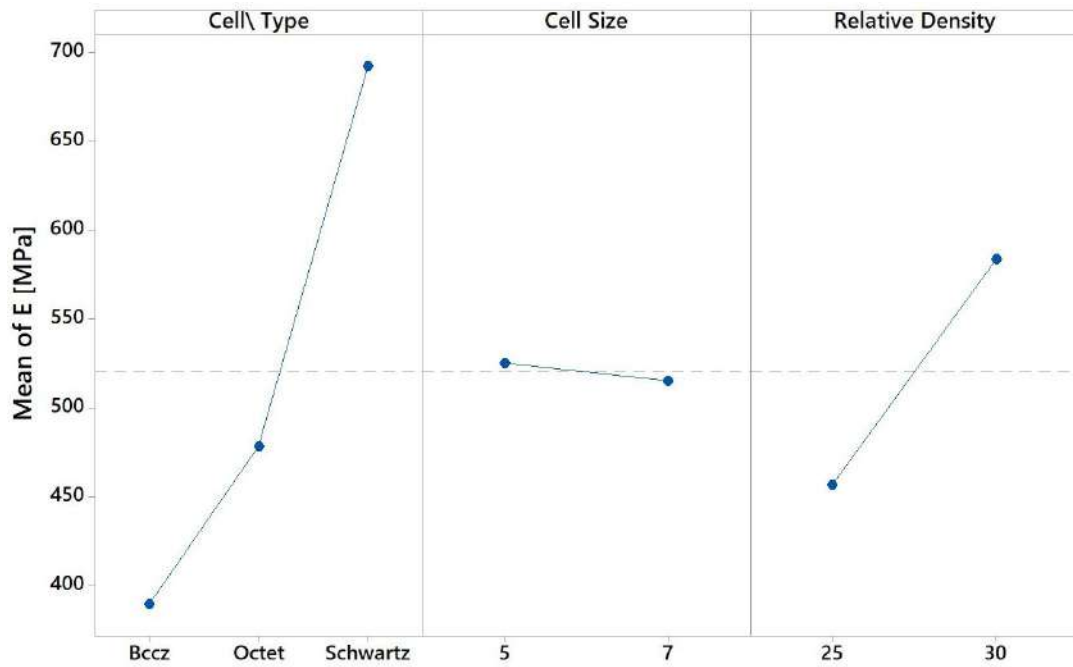


Figure 4.63: Main effect plot for E.

4.6 3-point bending tests on sandwich panels

In this section were analyzed the the 3-point bending tests on the sandwich panels with the same cell types used for the uniaxial compression of the panels: Bccz, Octet-truss and Schwartz diamond, with 5 mm and 7 mm cell size and solid volume fractions of 25 % and 30 %. Two different types of panel designs were chosen. The *long* specimens provide information on the flexural properties of the panels, while the *short* specimens provide information on the shear properties. All the panels are produced in according to the ASTM regulations. All the graphs relating to the bending tests on the panels are reported in Appendix D.

4.6.1 Long sandwich panels

One of the most important aspects to investigate to evaluate the panels for the anti-icing system is the goodness of the junction between the trabeculae that form the core and the panel skins. Trabecular panels are made in one piece, but the connection is the most critical point. The 3-point bending test on the long specimens allow to evaluate the bending behavior of each cell type and to detect the possible detachments between the skins and the trabecular core.

Bccz panels

The long Bccz panels reach break in correspondence with the lower values compared to results obtained for the other cells, as shown in the Table C.9. All the panels break in the same way, with the failure of the external skin, at half the length of the specimen, where the load acts. The failure is net for panels with a 7 mm cell, which are thicker. The crack starts from the outer skin and propagates quickly along the direction perpendicular to the skin. The panels with a 5 mm cell with a solid fraction of 30 % behave like those with a 7 mm cell, but at lower loads. Panels with a 5 mm cell with a solid fraction volume of 25 % have a break that starts from the same point as the 7 mm ones, but the crack proceeds more irregularly, as you can also see from the graph D.70. This is due to the fact that the panel and the struts are very thin. The break modes of two panels are shown in the Figure 4.64. Both the results and the comparison between the curves show that the increase in density leads to an improvement in mechanical performance. The transition from 5 mm to 7 mm improves the results in terms of Facing Stress and F_{yield} , but does not affect F_{ult} . The fact that F_{ult} does not vary means that the breaking properties of the core are similar between the 5 mm and 7 mm cells, as observed already during the compression tests.

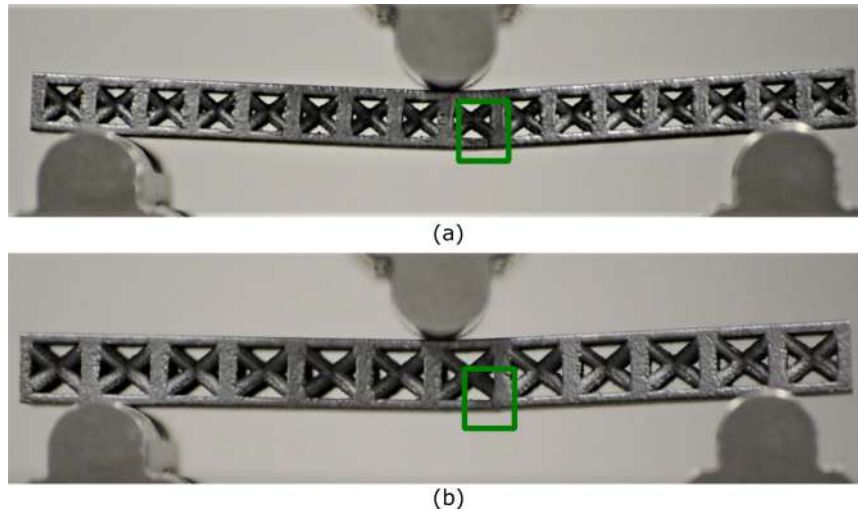


Figure 4.64: Long sandwich panels after 3-point bending test: a) Bccz-5-30-1 and b) Bccz-7-25-2.

Octet-truss panels

The long Octet-truss panels reach break in correspondence with the values higher than Bccz cells, but lower than Schwartz diamond ones, as visible in the Table C.9. As described for the previous cell, the panels break with the failure of the external skin, at half the length of the specimen. The failure is net for all the specimens: the crack starts from the outer skin and propagates quickly along the direction perpendicular to the skin. The break modes of two panels are shown in the Figure 4.65. Both the results and the comparison between the curves show that the increase in density leads to an improvement in mechanical performance. The transition from 5 mm to 7 mm improves the results in terms of Facing Stress and F_{yield} , but does not affect F_{ult} . The fact that F_{ult} does not vary means that the breaking properties of the core are similar between the 5 mm and 7 mm cells, as observed already during the compression tests.

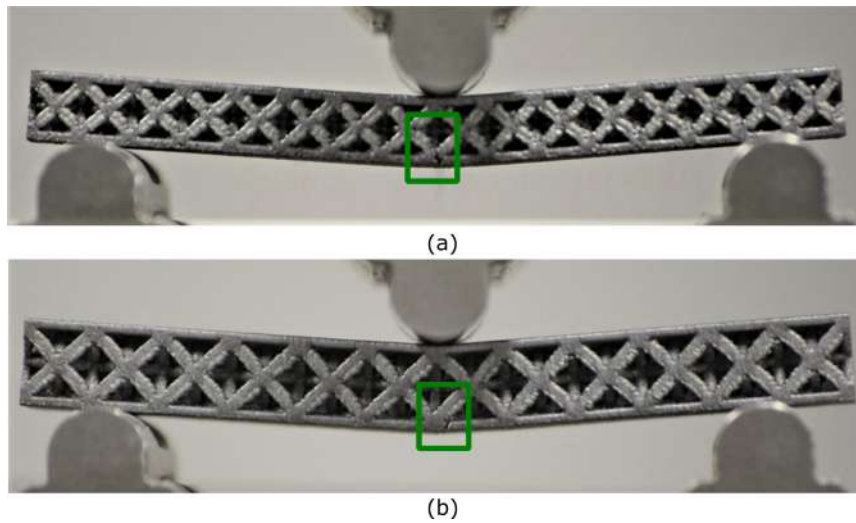


Figure 4.65: Long sandwich panels after 3-point bending test: a) Oct-5-25-1 and b) Bccz-7-30-1.

Schwartz diamond panels

The long Schwartz diamond panels reach break in correspondence with the values higher than all the other cells, as shown in the Table C.9. Also for the this panels type, the break is due the failure of the external skin, at half the length of the specimen. The failure is net for all the specimens: the crack starts from the outer skin and propagates quickly along the direction perpendicular to the skin. The break modes of two panels are shown in the Figure 4.66. Both the results and the comparison between the curves show that the increase in density leads to an improvement in mechanical performance. The transition from 5 mm to 7 mm, in this case, worsens the results in terms of Facing Stress and increases F_{yield} , but does not affect F_{ult} . The fact that F_{ult} does not vary means that the breaking properties of the core are similar between the 5 mm and 7 mm cells, as observed already during the compression tests.

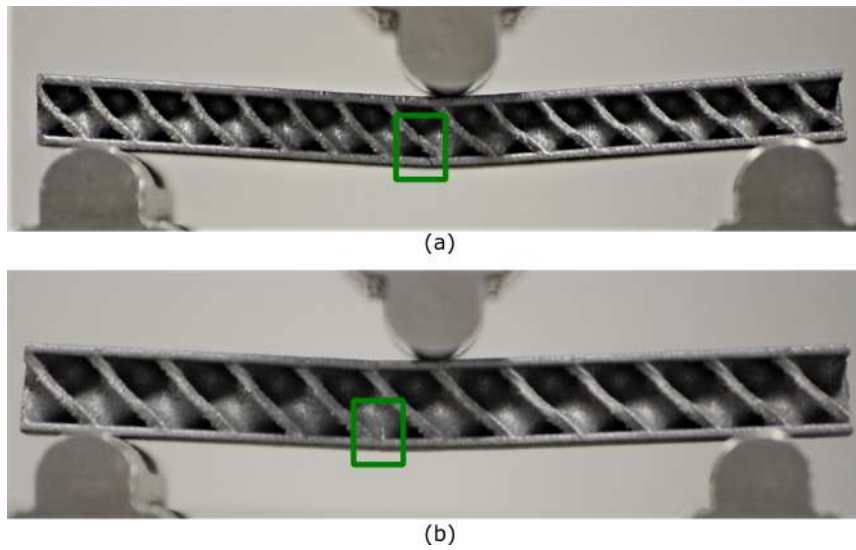


Figure 4.66: Long sandwich panels after 3-point bending test: a) Sch-5-30-2 and b) Sch-7-30-2.

Final evaluation

Comparing the results obtained from the bending tests on the long panels showed that all the panels collapsed in correspondence with the external skin and the crack propagated perpendicularly to the skin: for any type of cell the detachment of the skins from the core occurs. The results indicate that the best mechanical behavior is obtained for the Schwartz diamond cells, followed by the Octet-truss cell and finally by the Bccz. Furthermore, with the cell shape constant, the mechanical results are largely influenced by the solid volume fraction: there is a great difference between the Facing Stress of the 25 % and the 30 %. The cell size, instead, does not influence the final data. For all the geometries except Schwartz, the facing stress is higher for 7 mm cells than for 5 mm cells. The same trend can be observed for F_{yield} . On the other hand, F_{ult} depends on the solid volume fraction and does not vary with the cell size.

4.6.2 Short sandwich panels

The 3-point bending test on the short specimens allows to see the shear behavior of each cell type and to detect the possible detachments between the skins and the trabecular core.

Bccz panels

The short Bccz panels reach break in correspondence with the lower values compared to results obtained for the other cells, as visible in the Table C.8. All the panels break in the same way of the long one, with the failure of the external skin, at half the length of the specimen. Compared to long panels, the cross displacement before breaking is lower. The failure is net for all the specimens: the crack starts from the outer skin and propagates quickly along the direction perpendicular to the skin. The break modes of two panels are shown in the Figure 4.67. Both the results and the comparison between the curves show that the increase in solid volume fraction leads to an improvement in mechanical performance. The transition from 5 mm to 7 mm has different results respect to the data obtained for long panels. The 7 mm panels are thicker and stubby and reach breakage with a smaller bend. For this reason, this occurs at lower Facing Stress values than those for breaking the 5 mm panels. The values of F_{ult} are better for 5 mm panels, due to their better ability to deform in the presence of stress, because they are thinner. The 7 mm panels, being more rigid, have a higher F_{yield} than the value for 5 mm, and closer to the F_{ult} values: in fact, as soon as they start to deform they reach break. The 5 mm panels, instead, have a greater deformation range and therefore F_{yield} is very lower than F_{ult} .

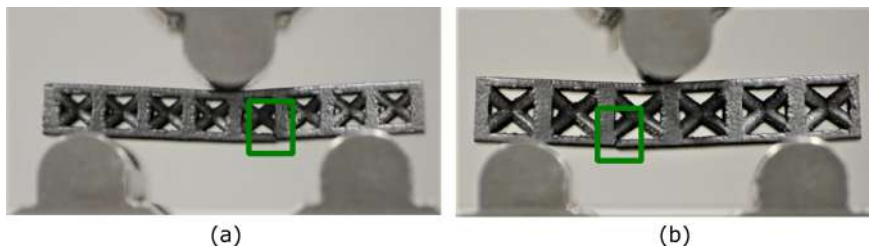


Figure 4.67: Long sandwich panels after 3-point bending test: a) Bccz-5-30- and b) Bccz-7-25-2.

Octet-truss panels

The short Octet panels reach break in correspondence with the values higher than Bccz cells, as shown in the Table C.8. For this type of cell the panels have a different failure mechanism compared to the long ones. The crack for the Octet short panels start from one of the two lower support points and it propagates towards the upper loading point, as shown in the Figure 4.68. Propagation occurs irregularly, as can also be seen from the charts in Appendix D, and compared to long panels, the cross displacement before breaking is lower. Both the results and the comparison between the curves show that the increase in solid volume fraction leads to an improvement in mechanical performance. The transition from 5 mm

to 7 mm has different results respect to the data obtained for long panels. The 7 mm panels are thicker and stubby and reach breakage with a smaller bend. For this reason, occurs at lower Facing Stress values than those for breaking the 5 mm panels. The values of F_{ult} are better for 5 mm panels, due to their better ability to deform in the presence of stress, because they are thinner. The 7 mm panels, being more rigid, have a high F_{yield} , closer to the F_{ult} values: in fact, as soon as they start to deform they reach break. The 5 mm panels, instead, have a greater deformation range and therefore F_{yield} is very lower than F_{ult} .

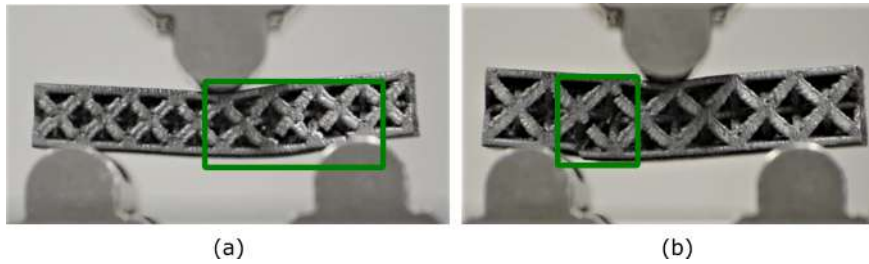


Figure 4.68: Long sandwich panels after 3-point bending test: a) Oct-5-30-2 and b) Oct-7-30-1.

Schwartz diamond panels

The short Schwartz diamond panels reach break in correspondence with the higher values compared to the other cells, as reported in the Table C.8. As seen for Bccz cell, all the panels break in the same way of the long one, but compared to long panels, the cross displacement before breaking is lower. The failure is net for all the specimens: the crack starts from the outer skin and propagates quickly along the direction perpendicular to the skin. The break modes of two panels are shown in the Figure 4.69. Both the results and the comparison between the curves show that the increase in solid volume fraction leads to an improvement in mechanical performance. The transition from 5 mm to 7 mm has different results respect to the data obtained for long panels. The 7 mm panels are thicker and stubby and reach breakage with a smaller bend. For this reason, this occurs at lower Facing Stress values than those for breaking the 5 mm panels. The values of F_{ult} are better for 5 mm panels, due to their better ability to deform in the presence of stress, because they are thinner. The 7 mm panels, being more rigid, have a high F_{yield} , closer to the F_{ult} values: in fact, as soon as they start to deform they reach break. The 5 mm panels, instead, have a greater deformation range and therefore F_{yield} is very lower than F_{ult} .

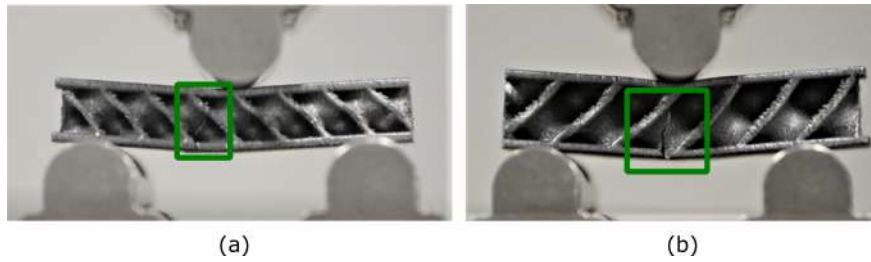


Figure 4.69: Long sandwich panels after 3-point bending test: a) Sch-5-25-1 and b) Sch-7-30-2.

Final evaluation

The short specimens are produced and tested in order to evaluate the shear behaviour of the different cell type cells. For octet panels the failure starts in correspondence of the lower skin, and the crack continues breaking the trabecular core and then the upper skin of the panel. For Bccz and Schwartz diamond specimens the failure occurs in the same way already observed for the long panels: starting from the lower skin e continues perpendicularly to the skins. Also in this case, the best mechanical results were obtained for Schwartz diamond, but followed by the Bccz cell and then by the Octet-truss. In respect to long panels, there is a bigger difference between 5 mm and the 7 mm cell cell size in the Facing Stress, and the values are higher for 5 mm cells than for 7 mm. The solid volume fraction, instead, does not influence these data.

4.7 Fatigue tests

The last mechanical test carried out for trabecular structures was the fatigue test. The cells subjected to this test are the Bccz, the Octet-truss and the Rhombic dodecahedron: the cells composed by struts. This allows us to see how the specimens behave under cyclic loads at the nodes and how the failure mechanisms vary with respect to uniaxial compression tests. The specimens were subjected to cyclic loads in which the maximum load was selected on the basis of the uniaxial compression tests on the specimens. For each type of specimen (cell shape, cell size, solid volume fraction) the average value of the σ_{02} obtained from the compression test was considered. All σ_{02} values obtained from the compression tests are listed in Appendix C. The maximum imposed load for each type of specimens is given by a percentage of the average value of σ_{02} (80 %, 60 %, 40 % and 20 %): in this way the maximum imposed load never exceeds the elastic deformation range of the specimen. The compressive fatigue test was conducted at R=0.1 with a frequency of 50 Hz. The frequency value has no influence on the result of fatigue tests on

lattice structures below 70 Hz [70]. The goal is to realize the Wohler curves for all the analyzed cell types. The Wohler curves show the amplitude of the load, σ_a , for each sample and the number of cycles for which the specimen failure occurs. The fatigue tests were completed for Rhombic dodecahedron and Octet cells, but not for Bccz cells.

4.7.1 Rhombic dodecahedron

The graph in Figure 4.70 shows the Wohler curves for all the Rhombic specimens tested. At the same amplitude of the load the longest fatigue life is that of the 5-30 specimens, followed by the specimens 7-30 and then by 5-25. This suggests that the solid volume fraction has an influence on the fatigue strength of the specimens. A greater solid volume fraction causes greater thicknesses in the rods and nodes, which better withstand the stresses of the test.

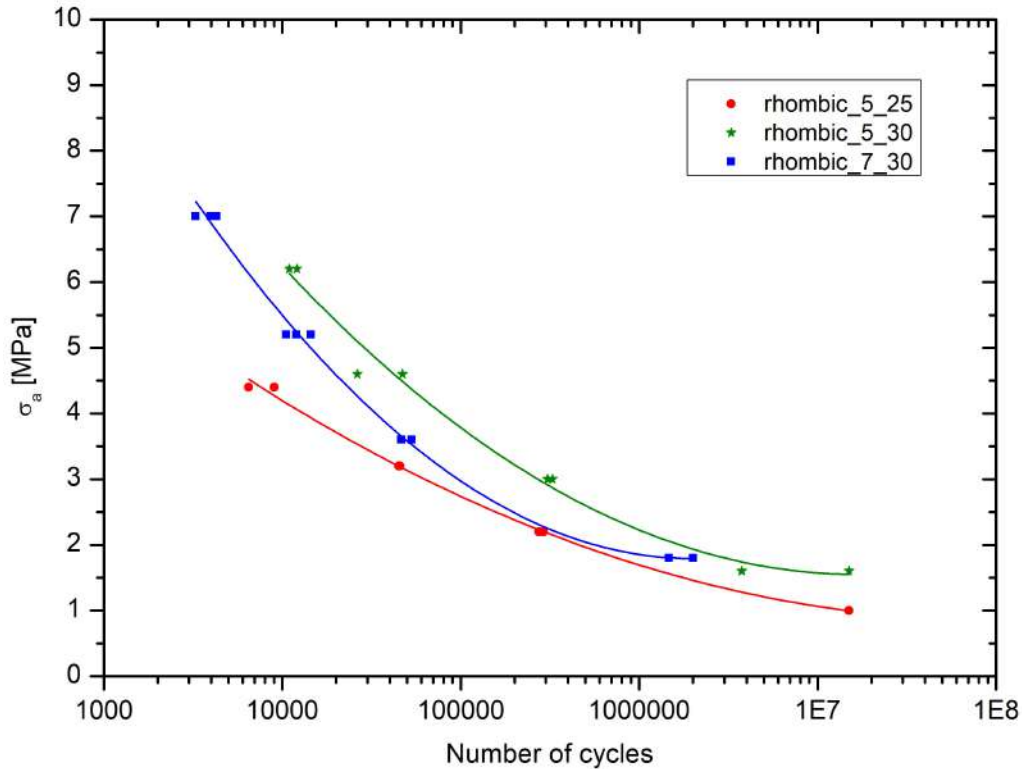


Figure 4.70: Wohler curves for Rhombic dodecahedron specimens.

The comparison between the samples 7-30 and 5-30 is more complex. Specimens 7-30 have a shorter fatigue life, because they are subjected to higher loads. The choice of load depends on the σ_{02} obtained for compression test; for the specimens

with a 7 mm cell the σ_{02} value is a little higher than the value of 5 mm, but the breaking point is slightly higher for the 5 mm cells. In fatigue tests, the slightly higher load amplitude causes fewer cycles for 7 mm specimens. The specimens 5-30 and 5-25 reach the imposed fatigue limit ($1.5 \cdot 10^7$ cycles) without breaking with a maximum load of 20 % of σ_{02} .

The photos of the Rhombic specimens after the fatigue test at different loads are reported in the Figures 4.71, 4.72 and 4.73. It can be seen that the breaking of the specimen is in part similar to that seen for the compression tests. The failure occurs along a 45° plane in respect to Z axis and the failure starts from a corner of the specimen. The deformation before the failure is almost absent; the connections break one by one along the plane until the resistant section becomes so small as to cause the specimen to collapse. From the images it is possible to see that the breaking of the specimens subjected to higher loads (80 % and 60 % of σ_{02}) is more clear and similar to that seen for the compression tests. On the other hand, the breaking of the specimens subjected to lower loads (40 % and 20 % of σ_{02}) is more irregular and acts on several levels causing the final separation of the specimen into more than two pieces. This difference is particularly marked for the 7 mm cells, as visible in the Figure 4.73. For cells with low solid volume fraction, such as 5-25, irregular breaking is already present for higher loads, such as 60 % of σ_{02} , as shown in Figure 4.71.

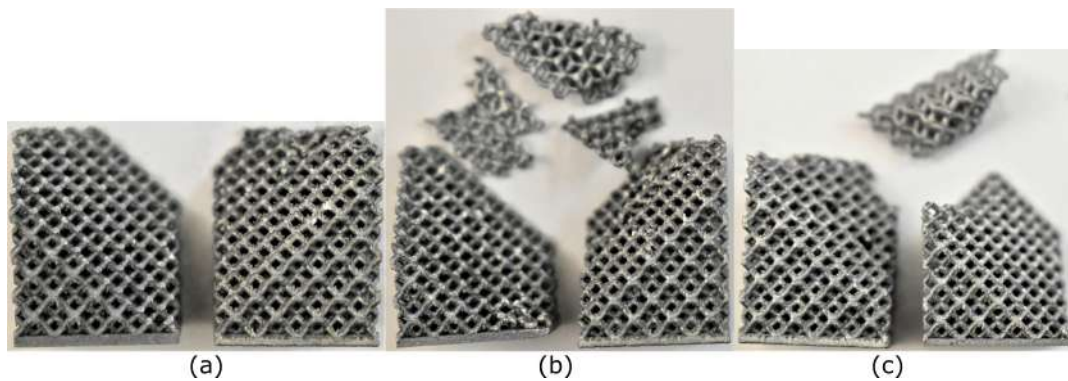


Figure 4.71: Rom-5-25 specimens subjected to fatigue tests with maximum load of: a) 80 % of σ_{02} , b) 60 % of σ_{02} and c) 40 % of σ_{02} .

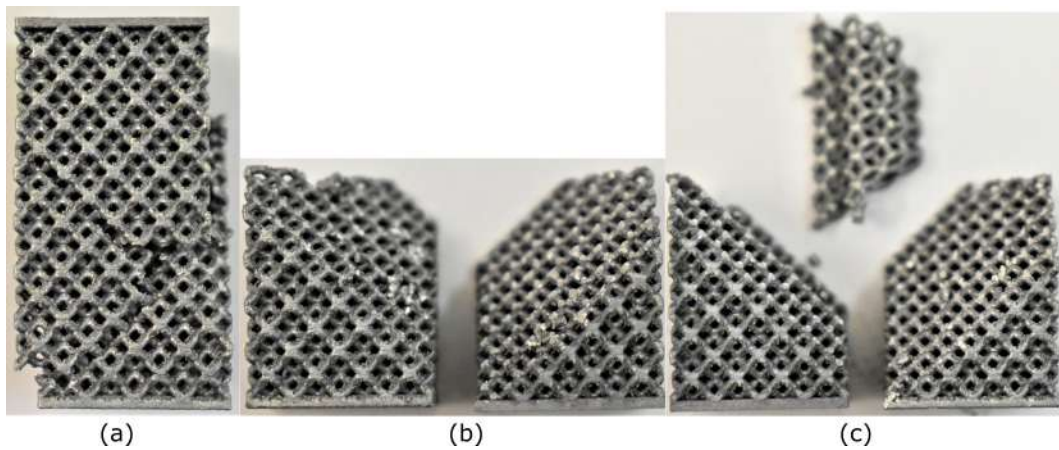


Figure 4.72: Rom-5-30 specimens subjected to fatigue tests with maximum load of: a) 80 % of σ_{02} , b) 60 % of σ_{02} and c) 20 % of σ_{02} .

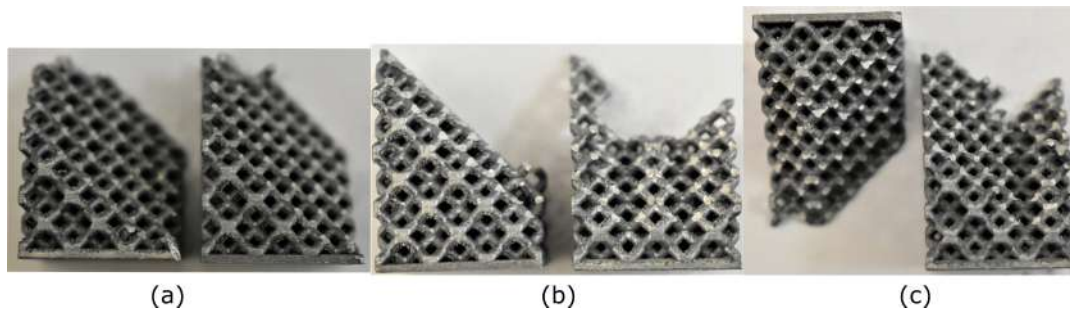


Figure 4.73: Rom-7-30 specimens subjected to fatigue tests with maximum load of: a) 80 % of σ_{02} , b) 40 % of σ_{02} and c) 20 % of σ_{02} .

4.7.2 Octet-truss

The graph in Figure 4.74 reports the Wohler curves for all the Octet-truss specimens tested. At the same amplitude of the load the longest fatigue life is that of the 5-30 specimens, followed by the specimens 7-30 and then by 5-25. This suggests that the solid volume fraction has an influence on the fatigue strength of the specimens. A greater solid volume fraction causes greater thicknesses in the rods and nodes, which better withstand the stresses of the test. Also in this case, the comparison between the samples 7-30 and 5-30 is complex. Specimens 7-30 have a shorter fatigue life, because they are subjected to higher loads. The choice of load depends on the σ_{02} obtained for compression test; for the specimens with a 7 mm cell the σ_{02} value is a little higher than the value of 5 mm, but the breaking point is equal to the 5 mm cells. In fatigue tests, the slightly higher load amplitude

causes fewer cycles for 7 mm specimens. For Octet cells, however, it is possible to see a difference with respect to the Rhombic cells: the curves of the specimens 7-30 and 5-25 intersect. The 7-30 specimens have a longer fatigue life compared to 5-25 at high load amplitudes. At low load amplitudes, however, the specimens 5-25 are more resistant. The specimens 5-30 and 5-25 reach the imposed fatigue limit ($1.5 \cdot 10^7$ cycles) without breaking with a maximum load of 20 % of σ_{02} .

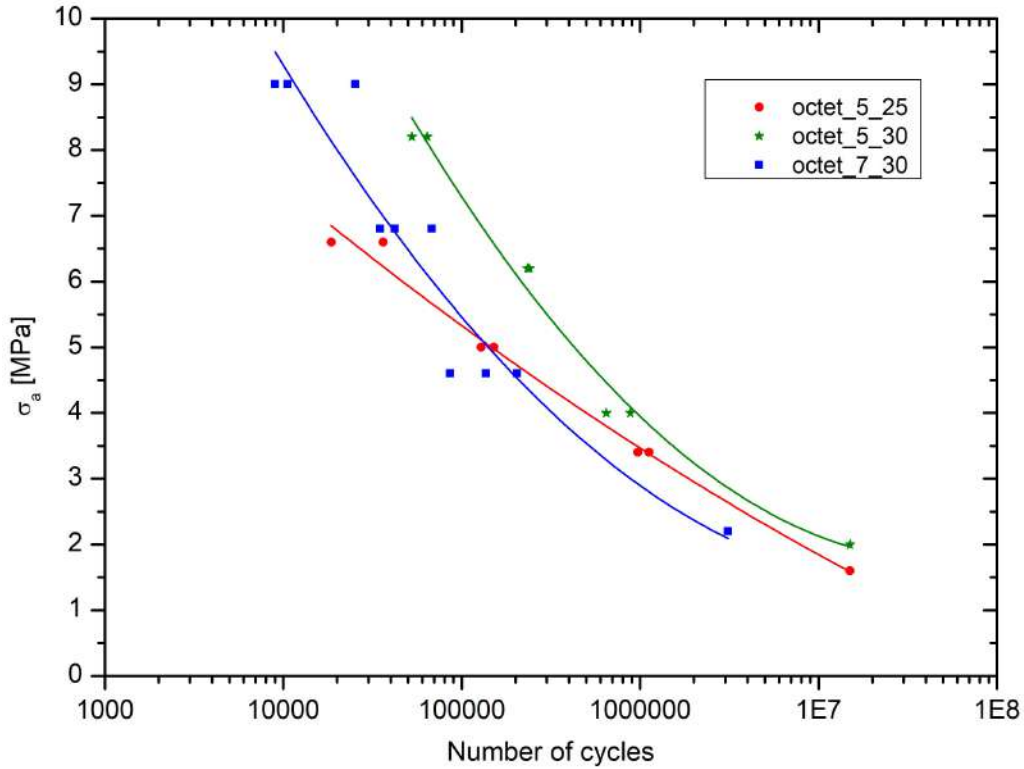


Figure 4.74: Wohler curves for Octet-truss specimens.

The Figures 4.75, 4.76 and 4.77 show the photos of the Octet specimens after the fatigue test at different loads. It can be seen that the breaking of the specimen is in part similar to that seen for the compression tests. The failure occurs along a 45° plane in respect to Z axis and the failure starts from a corner of the specimen. The deformation before the failure is almost absent; the connections break one by one along the plane until the resistant section becomes so small as to cause the specimen to collapse. From the images it is possible to see that the breaking of the 5-30 specimens is more clear and similar to that seen for the compression tests. On the other hand, the breaking of the 5-25 specimens subjected to all loads is more irregular and acts on several levels causing the final separation of the specimen into more than two pieces. For 7-30 specimens the breaking of the samples subjected

to higher loads (80 % and 60 % of σ_{02}) is more clear and similar to that seen for the compression tests. On the other hand, the breaking of the specimens subjected to lower loads (40 % and 20 % of σ_{02}) is more irregular and acts on several levels causing the final separation of the specimen into more than two pieces.

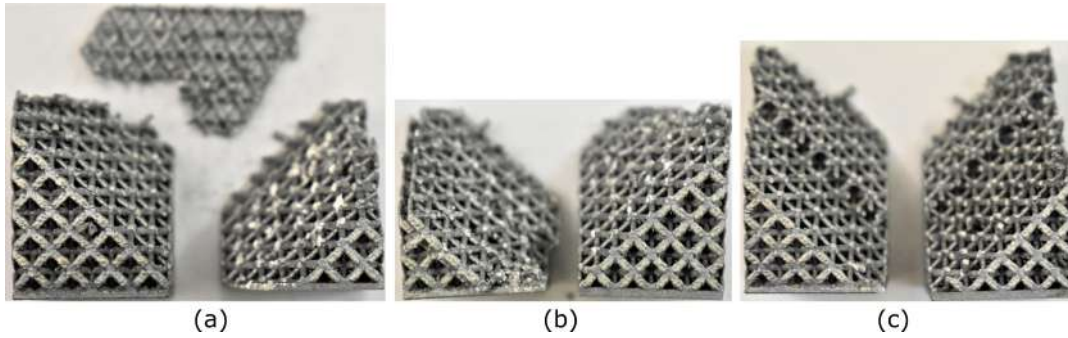


Figure 4.75: Oct-5-25 specimens subjected to fatigue tests with maximum load of: a) 80 % of σ_{02} , b) 60 % of σ_{02} and c) 40 % of σ_{02} .

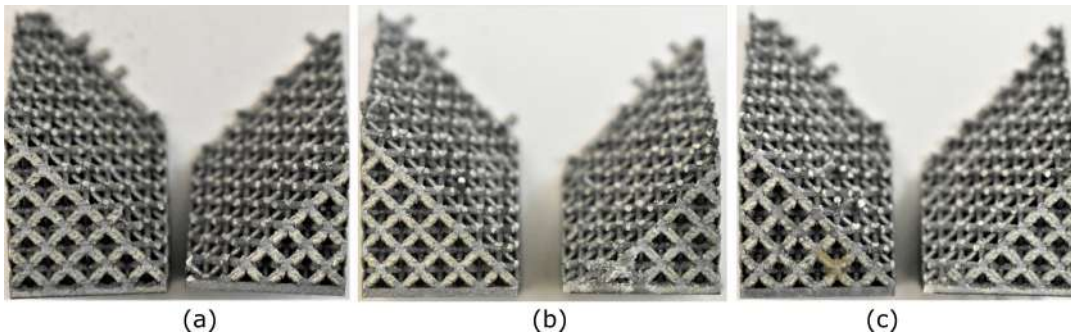


Figure 4.76: Oct-5-30 specimens subjected to fatigue tests with maximum load of: a) 80 % of σ_{02} , b) 40 % of σ_{02} and c) 20 % of σ_{02} .

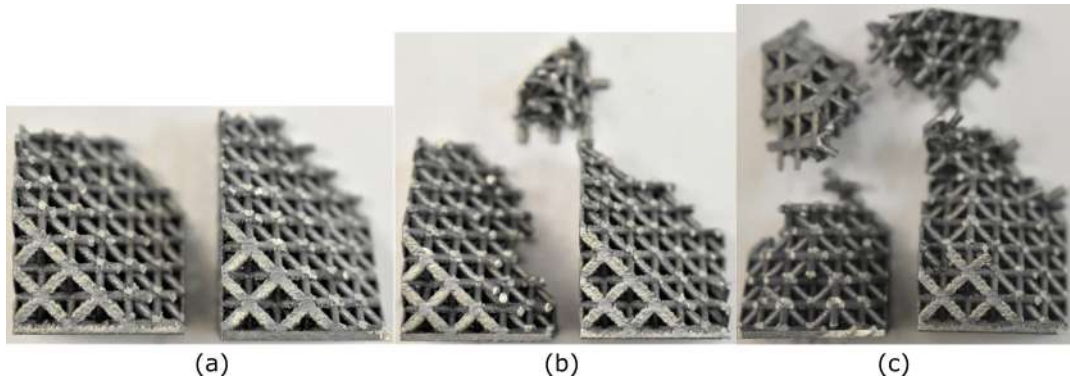


Figure 4.77: Oct-7-30 specimens subjected to fatigue tests with maximum load of: a) 80 % of σ_{02} , b) 40 % of σ_{02} and c) 20 % of σ_{02} .

4.7.3 Bccz

Fatigue tests on Bccz specimens remained incomplete due to the different behavior found. The specimens reach the set limit already at 60 % of the load for the 5 mm cells and 40 % for the 7 mm cells, for this reason it was impossible to realize the Wohler curves. The greatest fatigue resistance of Bccz specimens is given by the vertical struts. During the compression tests the vertical struts deformed and then broke for buckling. In fatigue tests the imposed load is not sufficient for the buckling of the vertical struts. In fact, as visible from the Figure 4.78, the failure of the specimen, when it occurs, is due to the breaking of the struts at the nodes, as seen for Rhombic and Octet. The fracture follows the angle of 45° only in some points, but in most cases there is a sparse and irregular separation of the cells for all cell sizes and for all solid volume fraction values. The fatigue life of the Bccz specimens is much higher than that of the other cells analyzed: the geometry requires the performance of further tests to characterize the fatigue behavior.

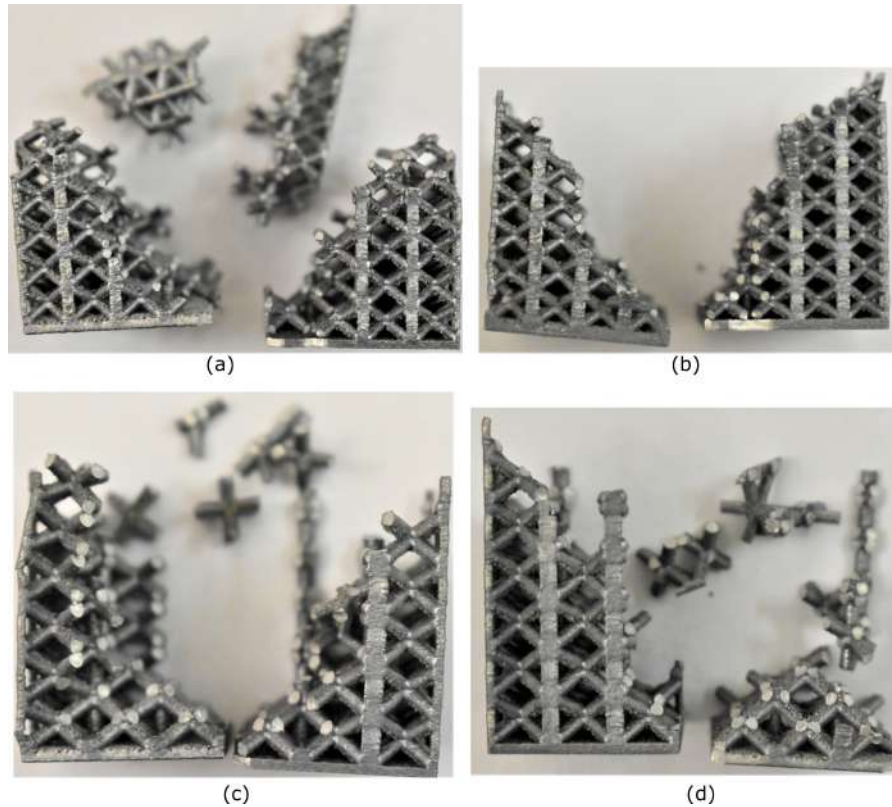


Figure 4.78: Specimens subjected to fatigue tests: a) Bccz-5-25 with 80 % of σ_{02} , b) Bccz-5-30 with 80 % of σ_{02} , c) Bccz-7-30 with 80 % of σ_{02} and d) Bccz-7-30 with 60 % of σ_{02} .

4.8 Thermal tests on the test bench

Based on the three set up previously described the thermal tests were carried out on the panels with Bccz and Rhombic cells. The pressure drop, the temperature drop and the heat transfer were obtained and listed in the Table 4.6. From the recorded values it can be seen that an increase in the solid volume fraction always leads to an increase in pressure drop, for both cells. This is due to the fact that the thicker rods form a major obstacle to the passage of air. It should also be noted that the pressure drop values for Bccz cells are always significantly lower than those found for the Rhombic cells. This effect is due to the presence of preferential passages in the lattice structure. Those passages represent some sort of internal channels that accelerate the flow of air, reducing pressure drops. These passages, due to the topology of the cell, are absent in the Rhombic cells.

The values of temperature drop and heat transfer are connected: greater is the heat transferred, greater is the temperature drop. For Bccz cells an increase in

pressure drop leads to a worsening of the heat exchange. In fact, it can be seen that at 25 % of solid volume fraction there is a greater pressure drop and the values of heat exchange are lower. This could happen because the denser structure hinders more the passage of the air increasing the pressure drop, but it does not create a greater number of turbulences that would help the heat exchange. For Rhombic cells the tendency is the opposite: by increasing the solid volume fraction, and therefore the pressure drop, the heat exchange improves. It can be seen that the values of heat transfer and temperature drop are higher for cells with 25 % solid volume fraction. For Rhombic cells the increase in the density of the structure could lead to an increase in turbulence and therefore to an increase in heat exchange.

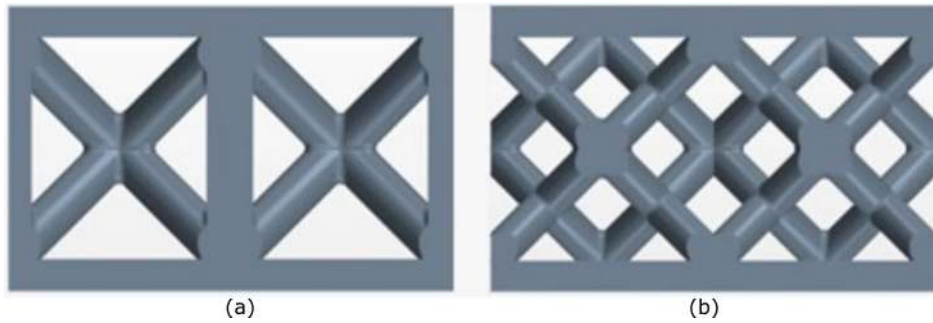


Figure 4.79: Cross section of a) Bccz and b) Rhombic panels.

Table 4.6: Results thermal tests.

Panel type	Test type	Pressure drop [mbar]	Temperature drop [°C]	Heat transfer [J/s]
Bccz - 12.5%	Test 1	43	25	495
Bccz - 12.5%	Test 2	70	15	400
Bccz - 12.5%	Test 3	94	14	425
Bccz - 25%	Test 1	96	19	376
Bccz - 25%	Test 2	155	11	286
Bccz - 25%	Test 3	197	10	299
Rhom - 12.5%	Test 1	80	10	201
Rhom - 12.5%	Test 2	128	5	139
Rhom - 12.5%	Test 3	155	4	121
Rhom - 25%	Test 1	208	14	276
Rhom - 25%	Test 2	310	10	250
Rhom - 25%	Test 3	431	4	137

The Figure 4.79 presents two sections of the tested panels. The Bccz cell has preferential air passages, while Rhombic panel does not present. The high heat

exchange of the Bccz is due to the vertical rods, which form turbulent vortices. As the density increases, less vortices are formed, but the passage of air does not change. For Rhombic cells, instead, an increase in density increases the tortuosity of the path and facilitates heat exchange.

From the graph in Figure 4.80 is possible to see that Bccz panels have always better mechanical performances compared to Rhombic ones and the best heat transfer is for Bccz cell with 12.5 % of solid volume fraction. This solution has many advantages because it has good results in terms of heat exchange, and also a very light structure. Such a low fraction solid volume leads to lower mechanical properties.

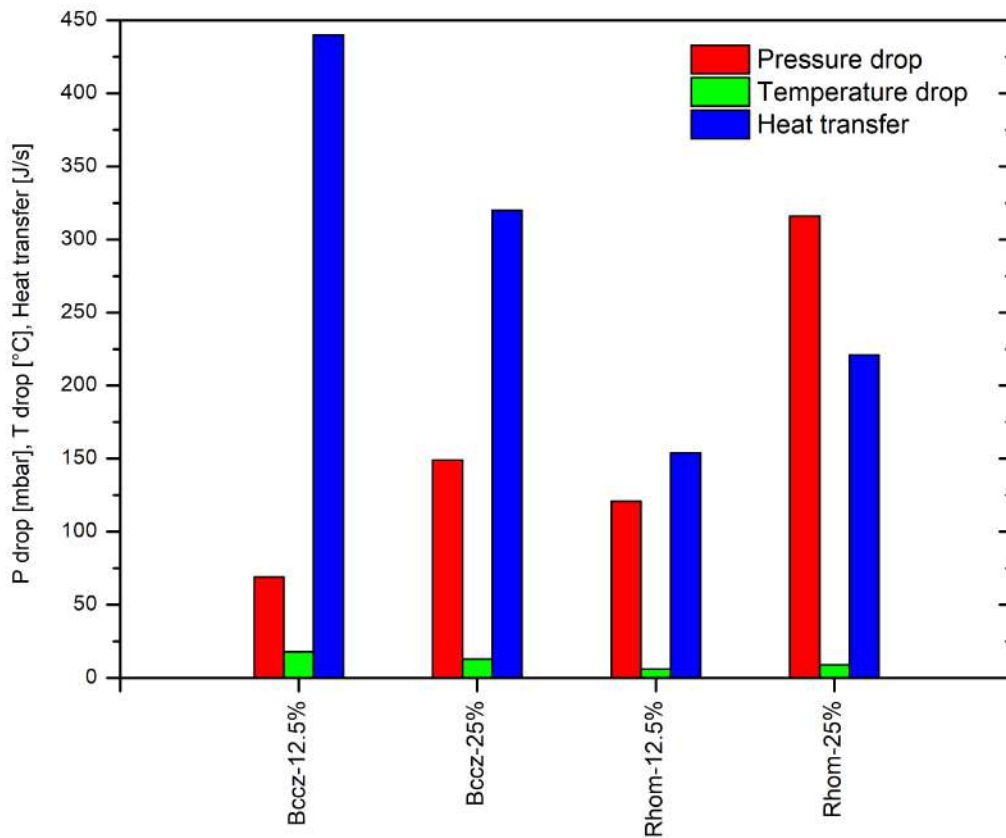


Figure 4.80: Pressure drop, temperature drop and heat transfer for all the panels.

4.9 POC final prototype

The patented anti-ice system is specifically designed for use in small aircraft. This is a much simpler structure than the current applied solutions: it is made in one piece with a considerable reduction in the number of parts, it is integrated in the primary structure of the aircraft, it is more robust and light and it requires much less maintenance than traditional systems. From 2018 the Italian company Piaggio began to collaborate with Politecnico di Torino for the development of an anti-ice system for their aircraft P180. The anti-ice system currently in use for the P180 is shown in the Figure 4.81: it is formed by welded sheets and is not optimized for heat exchange. Hot air is introduced directly between the sheets. Furthermore, the welds can cause cracks over use and worsen reliability.

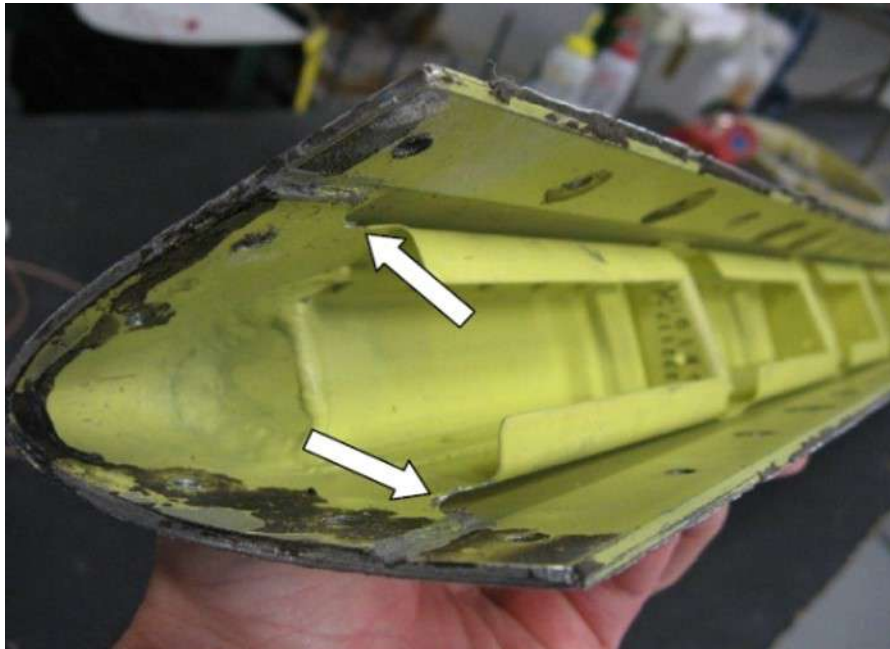


Figure 4.81: Anti-ice system of Piaggio P180 aircraft.

A demonstration mock-up was made from the designs of the leading edge of the wing supplied by Piaggio. The innovative system, shown in the Figure 4.82, eliminates all problems related to welding, improves heat exchange and increases the resistance of the leading edge to impact.

The demonstrator is also the final goal of the PoC, as it is an object able to demonstrate the feasibility of the system produced by the L-PBF technology. The component was initially made only for the 7 mm Octet-truss cell, but it will be produced also in Bccz and Schwartz diamond cells. Its length is 205 mm and weighs 0.53 kg. The traditional anti-ice system of equivalent length has a weight

of 1.15 kg. The simplification of the whole structure and the elimination of the junctions led to a lightening of 46 %.



Figure 4.82: Mock-up of the anti-ice system designed for Piaggio P180 aircraft and produced with L-PBF.

Chapter 5

Conclusions and future developments

5.1 STAMP project and LLA400 machine

The innovative L-PBF machine LLA400 was designed and produced after analyzing the solutions of the L-PBF machines currently on the market. This allowed the demonstrator to respond in the best way to the expectations of companies on machines. To satisfy the need to improve machine productivity, the following innovations were provided: the increase of the working volume ($400 \times 400 \times 600 \text{ mm}^3$), the decreasing of the production times, the improvement of the pre-heating, the increase in process automation and control. All the innovations and operations have been tested separately and in a combined manner to check for problems in the work cycle. The inert gas flushing systems were tested on the machine, and air-knife vents were designed to guarantee a laminar flow on the melted metal in any point of the platform and during the whole work. The aim of the STAMP project is the production of aluminum components and for this reason several AlSi10Mg powders were evaluated as raw material. Morphological and granulometric evaluations were carried out through SEM and image analysis. In particular, the particle size distribution graphs were obtained by measuring the granules diameters in SEM images of a representative amount of powders. Among the 4 powders provided and produced with different atomization techniques, the powder 3 demonstrates the best set of features: good particle size distribution and regular morphology. Despite the objective is the production of Al components, these alloys present different problems during the process and their use require greater care. The commissioning of a prototype leads to various problems and inconveniences that can make the process very complex. For this reason, in the first phase of the use of the LLA400 machine it was decided to exploit a simple material to process. The most suitable material for this purpose is stainless steel: 316L material was chosen because it was already widely used in literature and has a well known behavior in L-PBF.

The gas-atomized stainless steel 316L powders supplied by LPW were used to produce the specimens with the LLA400 machine, after the characterization of the raw material. With the LLA400 machine, the first set of 20x20 mm² single layers with 40 μ m thickness were produced. From this first group some problems to be solved were identified, such as the removal of the fumes and the repeatability of the results in all areas of the plate. The specimens were produced at 300 W of laser power, but showed several holes and surface anomalies at higher speeds. For this reason the power was lowered to 195 W for the second set of specimens and these defects were partly solved. However, the problem of repeatability of results within the platform is not yet solved and will require further analysis before proceeding with the realization of components of many layers.

Future developments for the machine realized within the STAMP project regards the improvement of the process parameters for the 316L as a first step. Subsequently the same characterization work has to be done for all the other materials of interest. The porosity of the multi-layers specimens must be analyzed; in addition, specimens must be produced for mechanical tests, verifying the quality of the results obtained with the machine. At this point the advantages of the innovations introduced, such as the best pre-heating and high productivity, can be evaluated, producing large components (for which the machine has been designed).

5.2 Proof Of Concept and trabecular structures

Trabecular structures are complex geometries that can be produced with AM technologies. They offer different advantages for the many fields; one of this is the aerospace sector. The advantages are the high specific surface area useful for the heat exchange, the structural lightening, the controlled porosity and the custom structural complexity. The application proposed is an aircraft anti-ice system integrated into the leading edge of the wing. The hot-air system uses hot air tapped from the engine to maintain the wing surface at a temperature higher than the water freezing point. An innovative hot-air system patented consists of metal trabecular sandwich with core volume crossed by the heating fluid. The trabecular core acts as a heat exchanger for the hot air used to de-ice the outer layer. The patent of the innovative anti-ice system has been funded by the Proof Of Concept of the Politecnico di Torino. The research activities carried out had the objective of developing a functional prototype, taking the project from an initial state of TRL 1 to a state of TRL 5.

Different mechanical tests were carried out for the trabecular characterization: uniaxial compression tests on the trabecular specimens, uniaxial compression tests on the sandwich panels with trabecular core, bending tests on the sandwich panels and a set of fatigue tests. All the specimens are produced according to the standards with AlSi10Mg and Ti6Al4V with a SLM 500 machine. The specimens are

characterized by six cell shapes, varying three cell sizes and three volume fractions. The mechanical behavior of the specimens was evaluated by the stress-strain curves and by the analysis of the fracture mechanisms. Before the uniaxial compression test, OM analysis were carried out on specimens. It is possible to note an excessive enlargement of the struts of the specimens with a 3 mm cell, that occurs during the process, mainly in the case of Al samples. The very dense structure of the 3 mm cells leads to a difficult dissipation of heat during the process, with a consequent excessive adhesion of the unmelted powder: this causes a large increase in density.

Mechanical tests allowed to identify the best types of cells to be used as sandwich cores in aerospace use. The compression tests on both the core and the panels identified the best cells: Schwartz, Octet and Bccz, with different fracture mechanisms. The first two cell types lead to greater strength, while the last one leads to a more gradual failure. The bending tests showed the goodness of the connection between core and skins as delamination never occurs. Finally, fatigue tests revealed that Bccz cells have a higher fatigue life than Octet and Rhombic cells, and Octet cells have a higher fatigue life than Rhombic cells. Thermal tests were also conducted on the Bccz and Rhombic panels revealing that the Bccz cells have a better heat exchange thanks to the presence of vertical struts that form turbulent whirls of hot air. In conclusion the best cell for the application examined (structurally integrated anti-icing system) is the Bccz one. This cell, in fact, shows good mechanical performance and a deformation before breaking that prevents a sudden and catastrophic failure. Its mechanical behavior, even considering their fatigue resistance, is governed by vertical struts, which also allow an excellent heat exchange with the air.

To complete the set of mechanical and thermal tests it will be necessary to repeat the thermal analysis also on Schwartz geometry cells, complete the fatigue tests on the Bccz and perform them on the Schwartz and on the Gyroid.

With the production of the mock-up the proof of Concept was concluded and thanks to Piaggio it was possible to realize the prototype on a real leading edge of an aircraft. On panels shaped with leading edge it will be necessary to carry out impact tests to observe how the panel behaves in the event of a bird strike.

Appendix A

List of specimens

This section contains all the data on the specimens produced for mechanical tests.

A.1 AlSi10Mg specimens for uniaxial compression test

Data on AlSi10Mg specimens for uniaxial compression tests are listed in the Tables [A.1](#), [A.2](#), [A.3](#) and [A.4](#).

Data on Ti6Al4V specimens for uniaxial compression tests are listed in the Tables [A.5](#) and [A.6](#).

The schemes reported in in Figure [A.1](#) illustrate the correspondence between the specimens and the measures listed in the tables.

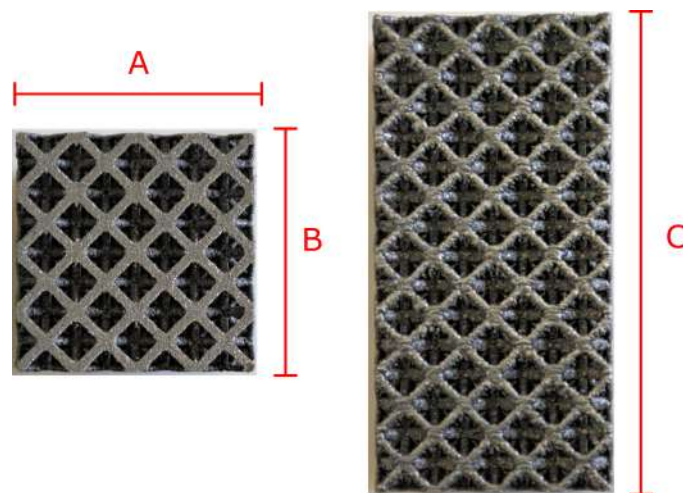


Figure A.1: Measurements of the specimens for compression tests.

Table A.1: AlSi10Mg compression specimens with Bccz cells. The identification code of the specimens is: Celle shape - Cell size - Solid volume fraction (nominal) - Serial number

Id. code	Mass [g]	A [mm]	B [mm]	C [mm]	Density [kg/m ³]	ρ_t/ρ_s
Bccz-3-25-1	19.64	21.35	21.35	38.55	1118	0.42
Bccz-3-25-2	19.36	21.35	21.40	38.60	1098	0.41
Bccz-3-25-3	19.64	21.40	21.35	38.80	1108	0.41
Bccz-3-30-1	21.95	21.35	21.40	38.60	1245	0.47
Bccz-3-30-2	21.77	21.40	21.35	38.55	1236	0.46
Bccz-3-30-3	21.95	21.30	21.40	38.70	1244	0.47
Bccz-3-30-4	22.04	21.35	21.35	38.20	1266	0.47
Bccz-3-35-1	24.42	21.35	21.45	38.55	1383	0.52
Bccz-3-35-2	24.41	21.40	21.45	38.60	1378	0.52
Bccz-3-35-3	24.27	21.40	21.45	38.55	1372	0.51
Bccz-5-25-1	7.45	20.15	20.25	30.40	601	0.22
Bccz-5-25-2	7.46	20.15	20.15	30.40	604	0.23
Bccz-5-25-3	7.42	20.30	20.20	30.30	597	0.22
Bccz-5-25-4	7.43	20.35	20.30	30.05	599	0.22
Bccz-5-30-1	9.46	20.25	20.25	30.25	763	0.29
Bccz-5-30-2	9.51	20.15	20.20	30.50	766	0.29
Bccz-5-30-3	9.50	20.20	20.25	30.30	766	0.29
Bccz-5-35-1	10.88	20.20	20.15	30.35	881	0.33
Bccz-5-35-2	10.86	20.25	20.20	30.45	872	0.33
Bccz-5-35-3	10.83	20.15	20.20	30.15	883	0.33
Bccz-7-25-1	10.55	21.15	21.10	37.05	638	0.24
Bccz-7-25-2	10.57	21.15	21.15	37.25	634	0.24
Bccz-7-25-3	10.55	21.20	21.20	37.30	629	0.24
Bccz-7-30-1	12.53	21.15	21.20	37.20	751	0.28
Bccz-7-30-2	12.51	21.15	21.10	37.20	754	0.28
Bccz-7-30-3	12.52	21.15	21.10	37.25	753	0.28
Bccz-7-35-1	14.81	21.15	21.20	37.20	888	0.33
Bccz-7-35-2	14.81	21.20	21.20	37.30	883	0.33
Bccz-7-35-3	14.79	21.25	21.20	37.15	884	0.33

Table A.2: AlSi10Mg compression specimens with Rhombic dodecahedron cells. The identification code of the specimes is: Celle shape - Cell size - Solid volume fraction (nominal) - Serial number

Id. code	Mass [g]	A [mm]	B [mm]	C [mm]	Density [kg/m ³]	ρ_f/ρ_s
Rhom-3-25-1	21.76	21.20	21.15	38.20	1270	0.48
Rhom-3-25-2	21.71	21.10	21.20	38.02	1277	0.48
Rhom-3-25-3	21.73	21.30	21.35	38.25	1249	0.47
Rhom-3-30-1	24.33	21.30	21.30	38.40	1397	0.52
Rhom-3-30-2	24.22	21.45	21.35	38.40	1377	0.52
Rhom-3-30-3	24.33	21.35	21.25	38.45	1395	0.52
Rhom-3-35-1	27.74	21.35	21.35	38.15	1595	0.60
Rhom-3-35-2	27.84	21.35	21.35	38.15	1601	0.60
Rhom-3-35-3	27.52	21.35	21.30	38.25	1582	0.59
Rhom-5-25-1	10.08	19.95	19.95	39.10	648	0.24
Rhom-5-25-2	10.06	20.00	20.05	39.15	641	0.24
Rhom-5-25-3	10.08	19.90	19.95	39.25	647	0.24
Rhom-5-30-1	12.18	20.05	20.05	39.95	758	0.28
Rhom-5-30-2	12.19	19.95	19.95	39.90	768	0.29
Rhom-5-30-3	12.17	19.95	19.90	39.95	767	0.29
Rhom-5-35-1	14.33	20.05	20.05	39.90	893	0.33
Rhom-5-35-2	14.23	20.05	20.10	39.95	884	0.33
Rhom-5-35-3	14.36	19.95	20.00	39.10	920	0.34
Rhom-7-25-1	9.46	20.95	21.00	34.10	631	0.24
Rhom-7-25-2	9.35	20.95	20.95	33.60	634	0.24
Rhom-7-25-3	9.51	21.00	20.95	34.05	635	0.24
Rhom-7-30-1	11.62	21.00	20.95	34.00	777	0.29
Rhom-7-30-2	11.55	21.00	20.95	34.00	772	0.29
Rhom-7-30-3	11.57	20.95	20.95	34.05	774	0.29
Rhom-7-35-1	13.60	20.95	20.90	33.80	919	0.34
Rhom-7-35-2	13.64	20.95	20.90	34.05	915	0.34
Rhom-7-35-3	13.65	20.95	20.90	34.10	914	0.34

Table A.3: AlSi10Mg compression specimens with Octet-truss cells. The identification code of the specimen is: Celle shape - Cell size - Solid volume fraction (nominal) - Serial number

Id. code	Mass [g]	A [mm]	B [mm]	C [mm]	Density [kg/m ³]	ρ_f/ρ_s
Oct-3-25-1	25.69	21.35	21.40	39.10	1438	0.54
Oct-3-25-2	25.88	21.35	21.35	39.15	1450	0.54
Oct-3-25-3	26.01	21.35	21.35	39.15	1458	0.55
Oct-3-25-4	25.46	21.55	21.60	39.15	1397	0.52
Oct-3-25-5	26.01	21.35	21.35	39.20	1456	0.55
Oct-3-25-6	26.01	21.39	21.41	39.15	1451	0.54
Oct-3-30-1	30.18	21.50	21.40	39.40	1665	0.62
Oct-3-30-2	30.39	21.50	21.45	39.60	1664	0.62
Oct-3-30-3	30.22	21.50	21.45	39.15	1674	0.63
Oct-3-35-1	30.92	21.40	21.40	39.40	1713	0.64
Oct-3-35-2	30.96	21.50	21.55	39.35	1698	0.64
Oct-3-35-3	30.81	21.45	21.48	39.38	1699	0.64
Oct-5-25-1	11.89	19.85	19.90	40.05	752	0.28
Oct-5-25-2	11.81	20.05	19.90	40.20	736	0.28
Oct-5-25-3	11.93	20.10	20.15	40.30	731	0.27
Oct-5-30-1	13.55	19.90	19.90	40.05	854	0.32
Oct-5-30-2	13.86	19.90	19.90	40.20	871	0.33
Oct-5-30-3	13.56	20.15	20.15	40.05	834	0.31
Oct-5-35-1	16.18	19.90	20.05	40.15	1010	0.38
Oct-5-35-2	16.24	19.95	20.05	40.05	1014	0.38
Oct-5-35-3	15.76	20.10	20.10	40.35	967	0.36
Oct-7-25-1	10.78	21.05	21.05	35.10	693	0.26
Oct-7-25-2	10.78	21.05	20.90	35.10	698	0.26
Oct-7-25-3	10.83	21.05	21.15	35.30	689	0.26
Oct-7-30-1	12.55	21.05	20.90	35.15	812	0.30
Oct-7-30-2	12.55	21.05	20.90	35.05	814	0.30
Oct-7-30-3	12.60	21.25	21.15	35.35	797	0.30
Oct-7-35-1	14.56	20.90	21.05	35.10	943	0.35
Oct-7-35-2	14.91	20.90	21.05	35.05	967	0.36
Oct-7-35-3	14.94	21.10	21.05	35.20	956	0.36

Table A.4: AlSi10Mg compression specimens with Auxetic, Gyroid and Schwartz diamond cells. The identification code of the specimens is: Celle shape - Cell size - Solid volume fraction (nominal) - Serial number

Id. code	Mass [g]	A [mm]	B [mm]	C [mm]	Density [kg/m ³]	ρ_t/ρ_s
Aux-3-35-1	26.35	25.90	26.10	37.10	1051	0.39
Aux-3-35-2	26.12	25.90	26.00	37.00	1048	0.39
Aux-3-35-3	26.01	25.80	25.80	36.80	1062	0.40
Aux-3-35-4	26.40	25.50	25.50	37.15	1093	0.41
Aux-3-35-5	26.84	25.65	25.65	37.00	1103	0.41
Aux-3-35-6	26.93	25.70	25.70	37.10	1099	0.41
Aux-3-35-7	26.79	26.05	26.00	37.30	1060	0.40
Aux-3-35-8	26.15	25.90	26.10	37.30	1037	0.39
Aux-3-35-9	25.99	25.60	26.05	36.95	1055	0.40
Aux-5-30-1	11.37	24.60	24.50	35.30	534	0.20
Aux-5-30-2	11.44	24.60	24.60	35.70	530	0.20
Aux-5-30-3	10.99	24.60	24.50	35.50	514	0.19
Aux-5-30-4s	11.51	24.60	24.65	35.60	533	0.20
Aux-5-30-4	11.75	24.70	24.75	36.75	523	0.20
Aux-5-30-5	11.44	24.65	24.65	36.55	515	0.19
Aux-7-25-1	9.01	26.10	26.10	30.70	431	0.16
Aux-7-25-2	9.07	25.90	26.10	30.80	436	0.16
Aux-7-25-3	9.11	26.10	26.20	30.50	437	0.16
Aux-7-25-4	9.22	26.30	26.30	30.10	443	0.17
Aux-7-25-5	9.38	26.25	26.25	30.95	440	0.16
Gyr-3-30-1	15.74	21.85	21.90	39.90	824	0.31
Gyr-3-30-2	16.20	21.95	21.80	40.05	845	0.32
Gyr-3-30-3	15.54	21.95	22.05	40.05	802	0.30
Gyr-5-25-1	10.68	19.80	19.70	39.95	685	0.26
Gyr-5-25-2	10.68	19.90	19.85	39.60	683	0.26
Gyr-5-25-3	10.65	19.75	19.80	39.90	683	0.26
Gyr-7-35-1	12.91	20.05	20.35	32.50	974	0.36
Gyr-7-35-2	12.82	19.95	20.25	32.65	972	0.36
Gyr-7-35-3	12.86	19.95	20.05	32.70	983	0.37
Sch-3-25-1	13.84	21.70	21.90	39.70	734	0.27
Sch-3-25-2	13.93	21.75	21.80	39.70	740	0.28
Sch-3-25-3	13.91	21.85	21.90	39.80	730	0.27
Sch-5-35-1	13.99	19.30	19.25	37.90	994	0.37
Sch-5-35-2	14.15	19.45	19.40	38.05	959	0.37
Sch-5-35-3	13.87	19.45	19.55	38.05	959	0.36
Sch-7-30-1	11.62	20.35	20.35	33.15	846	0.32
Sch-7-30-2	11.53	20.20	20.30	33.20	847	0.32
Sch-7-30-3	11.72	20.25	20.30	33.25	857	0.32

A.2 Ti6Al4V specimens for uniaxial compression test

Table A.5: Ti6Al4V compression specimens with Bccz, Rhombic dodecahedron and Octet-truss cells. The identification code of the specimens is: Celle shape - Cell size - Solid volume fraction (nominal) - Serial number

Id. code	Mass [g]	A [mm]	B [mm]	C [mm]	Density [kg/m ³]	ρ_f/ρ_s
Bccz-3-30-1	21.73	21.20	21.15	37.15	1305	0.30
Bccz-3-30-2	21.34	21.05	21.05	36.75	1310	0.30
Bccz-3-30-3	21.69	21.35	21.30	37.60	1269	0.29
Bccz-5-25-1	12.49	20.10	20.20	29.25	1052	0.24
Bccz-5-25-2	12.37	20.15	20.25	28.90	1021	0.24
Bccz-5-25-3	12.05	20.15	20.20	29.00	1021	0.23
Bccz-7-35-1	24.35	21.20	21.15	35.15	1545	0.35
Bccz-7-35-2	23.66	21.05	21.05	35.55	1502	0.34
Bccz-7-35-3	24.14	21.20	21.20	35.35	1519	0.34
Rhom-3-25-1	18.50	21.20	21.15	38.20	1085	0.25
Rhom-3-25-2	18.92	20.95	20.90	37.95	1139	0.26
Rhom-3-25-3	18.87	21.15	21.15	38.10	1107	0.25
Rhom-5-35-1	24.24	20.05	20.10	38.55	1560	0.35
Rhom-5-35-2	24.80	20.05	20.10	39.15	1572	0.36
Rhom-5-35-3	25.78	20.05	20.05	38.95	1646	0.37
Rhom-7-30-1	22.95	20.85	21.10	34.40	1516	0.34
Rhom-7-30-2	23.14	21.15	20.95	33.85	1543	0.35
Rhom-7-30-3	22.86	20.20	21.25	34.10	1562	0.35
Oct-3-35-1	39.82	21.25	21.25	38.75	2276	0.52
Oct-3-35-2	39.14	21.25	21.25	38.95	2225	0.50
Oct-3-35-3	40.41	21.35	21.40	39.00	2268	0.51
Oct-5-30-1	21.59	20.10	20.05	38.55	1355	0.31
Oct-5-30-2	21.93	20.10	20.15	39.80	1360	0.31
Oct-5-30-3	22.14	20.15	20.15	39.85	1368	0.31
Oct-7-25-1	17.62	21.10	21.15	35.20	1122	0.25
Oct-7-25-2	17.13	21.15	21.15	35.35	1083	0.25
Oct-7-25-3	17.32	21.20	21.15	35.40	1091	0.25

Table A.6: Ti6Al4V compression specimens with Auxetic, Gyroid and Schwartz diamond cells. The identification code of the specimens is: Celle shape - Cell size - Solid volume fraction (nominal) - Serial number

Id. code	Mass [g]	A [mm]	B [mm]	C [mm]	Density [kg/m ³]	ρ_f/ρ_s
Aux-3-35-1	25.39	25.60	25.60	37.35	1037	0.24
Aux-3-35-2	25.97	25.55	25.45	37.35	1069	0.24
Aux-3-35-3	25.92	25.55	25.60	37.50	1057	0.24
Aux-5-30-1	20.17	24.70	24.75	36.10	914	0.21
Aux-5-30-2	20.04	24.60	24.70	36.05	915	0.21
Aux-5-30-3	20.04	24.65	24.75	36.85	891	0.20
Aux-7-25-1	14.89	26.25	26.40	29.60	726	0.16
Aux-7-25-2	14.49	26.20	26.25	29.50	714	0.16
Aux-7-25-3	14.95	26.50	26.55	30.05	707	0.16
Aux-7-25-4	15.88	26.30	26.25	31.05	741	0.17
Aux-7-25-5	15.99	26.35	26.30	30.95	746	0.17
Aux-7-25-6	16.10	26.35	26.35	31.10	746	0.17
Gyr-3-30-1	27.30	22.05	22.10	39.80	1408	0.32
Gyr-3-30-2	27.30	21.85	22.05	39.20	1431	0.32
Gyr-3-30-3	27.21	22.00	22.05	39.20	1431	0.32
Gyr-5-25-1	16.93	19.45	19.55	38.33	1162	0.26
Gyr-5-25-2	16.80	19.55	19.65	38.85	1126	0.26
Gyr-5-25-3	16.79	19.60	19.20	38.10	1171	0.27
Gyr-7-35-1	21.35	20.50	20.55	32.60	1555	0.35
Gyr-7-35-2	21.26	20.05	20.25	33.05	1584	0.36
Gyr-7-35-3	21.19	20.50	20.50	32.70	1542	0.35
Sch-3-25-1	24.05	22.00	22.05	40.05	1238	0.28
Sch-3-25-2	23.68	22.00	21.85	40.15	1227	0.28
Sch-3-25-3	23.63	22.15	22.10	39.95	1208	0.27
Sch-5-35-1	23.55	19.50	19.50	38.35	1615	0.37
Sch-5-35-2	23.53	19.50	19.55	38.30	1612	0.37
Sch-5-35-3	23.51	19.60	19.65	38.55	1583	0.36
Sch-5-35-4	23.54	19.65	19.55	38.35	1598	0.36
Sch-7-30-1	19.39	20.40	20.45	33.25	1398	0.32
Sch-7-30-2	19.36	20.55	20.75	33.10	1372	0.31
Sch-7-30-3	19.10	20.35	20.30	32.00	1445	0.33

A.3 AlSi10Mg sandwich panels for uniaxial compression test

Data on AlSi10Mg sandwich panels for uniaxial compression tests are listed in the table A.7.

The scheme in Figure A.2 illustrates the correspondence between the panels and the measures listed in the table.

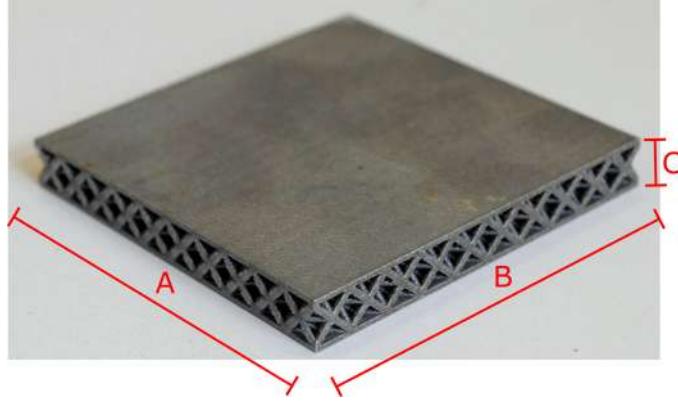


Figure A.2: Measurements of the sandwich panels for compression tests.

Table A.7: AlSi10Mg compression sandwich panels with Bccz, Octet-truss and Schwartz diamond cells. The identification code of the specimens is: Celle shape - Cell size - Solid volume fraction (nominal)

Id. code	Mass [g]	A [mm]	B [mm]	C [mm]	Density [kg/m ³]	ρ_f/ρ_s
Bccz-5-25	19.25	50.75	50.05	5.75	1318	0.49
Bccz-5-30	20.54	49.95	50.80	5.80	1396	0.52
Bccz-7-25	43.20	70.05	70.75	7.35	1186	0.44
Bccz-7-30	46.46	70.00	70.80	7.35	1275	0.48
Oct-5-25	23.12	50.95	50.15	7.10	1274	0.48
Oct-5-30	24.39	50.30	50.75	7.10	1346	0.50
Oct-7-25	49.22	70.00	70.75	9.10	1092	0.41
Oct-7-30	54.14	70.15	70.70	9.10	1200	0.45
Sch-5-25	22.02	49.50	49.95	7.05	1263	0.47
Sch-5-30	23.68	50.00	49.45	7.10	1349	0.51
Sch-7-25	50.99	68.90	69.95	9.05	1160	0.43
Sch-7-30	54.72	69.80	70.00	9.05	1238	0.46

A.4 AlSi10Mg sandwich panels for bending tests

Data on AlSi10Mg sandwich panels for bending tests are listed in the tables [A.8](#) and [A.9](#).

The scheme in Figure [A.3](#) illustrates the correspondence between the specimens and the measures listed in the tables.

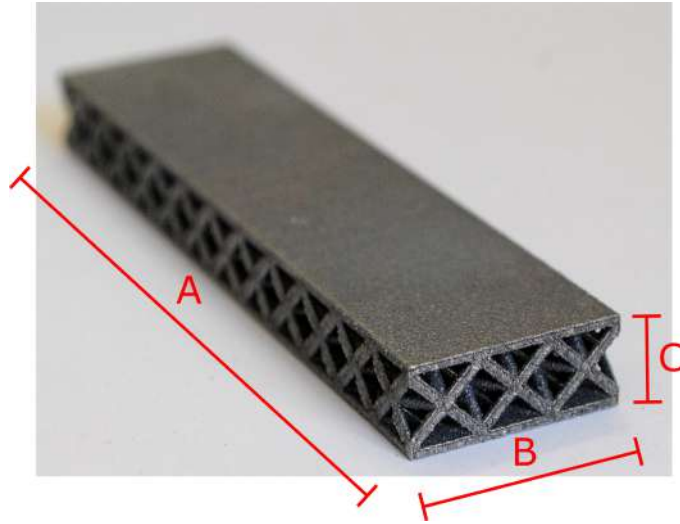


Figure A.3: Measurements of the sandwich panels for bending tests.

Table A.8: AlSi10Mg short sandwich panels for bending test with Bccz, Octet-truss and Schwartz diamond cells. The identification code of the specimens is: Celle shape - Cell size - Solid volume fraction (nominal) - Serial number

Id. code	Mass [g]	A [mm]	B [mm]	C [mm]	Density [kg/m ³]	ρ_f/ρ_s
Bccz-5-25-1	4.62	40.75	15.05	5.85	1288	0.48
Bccz-5-25-2	4.65	40.75	15.10	5.85	1292	0.48
Bccz-5-30-1	5.14	41.95	15.05	5.85	1392	0.52
Bccz-5-30-2	5.06	41.65	15.05	5.80	1392	0.52
Bccz-7-25-1	7.73	42.65	21.00	7.30	1182	0.44
Bccz-7-25-2	7.81	42.80	21.00	7.35	1182	0.44
Bccz-7-30-1	8.34	42.70	21.00	7.35	1265	0.47
Bccz-7-30-1	8.35	42.65	21.05	7.35	1265	0.47
Oct-5-25-1	5.61	40.65	15.15	7.10	1283	0.48
Oct-5-25-2	5.67	40.75	15.25	7.05	1294	0.48
Oct-5-30-1	5.89	40.65	15.10	7.05	1361	0.51
Oct-5-30-2	6.00	40.80	15.25	7.05	1368	0.51
Oct-7-25-1	9.13	42.90	21.20	9.05	1109	0.42
Oct-7-25-2	9.13	42.65	21.05	9.05	1124	0.42
Oct-7-30-1	9.85	42.70	21.15	9.05	1205	0.45
Oct-7-30-1	9.78	42.75	21.15	9.05	1195	0.45
Sch-5-25-1	5.17	39.45	15.05	7.10	1226	0.46
Sch-5-25-2	5.15	39.55	15.00	7.05	1231	0.46
Sch-5-30-1	5.52	39.25	15.00	7.05	1330	0.50
Sch-5-30-2	5.55	39.75	15.00	7.05	1320	0.49
Sch-7-25-1	8.85	41.35	21.00	9.05	1126	0.42
Sch-7-25-2	8.81	41.65	21.00	9.05	1112	0.42
Sch-7-30-1	9.62	41.60	21.00	9.10	1210	0.45
Sch-7-30-2	9.60	41.55	21.00	9.05	1216	0.46

Table A.9: AlSi10Mg long sandwich panels for bending test with Bccz, Octet-truss and Schwartz diamond cells. The identification code of the specimens is: Celle shape - Cell size - Solid volume fraction (nominal) - Serial number

Id. code	Mass [g]	A [mm]	B [mm]	C [mm]	Density [kg/m ³]	ρ_t/ρ_s
Bccz-5-25-1	9.07	80.65	15.00	5.80	1293	0.48
Bccz-5-25-2	9.23	80.80	15.05	5.85	1297	0.49
Bccz-5-30-1	9.64	80.80	15.10	5.80	1362	0.51
Bccz-5-30-2	9.89	80.70	15.10	5.85	1387	0.52
Bccz-7-25-1	15.14	84.70	20.95	7.35	1161	0.43
Bccz-7-25-2	15.41	84.70	21.05	7.35	1176	0.44
Bccz-7-30-1	16.72	85.65	21.05	7.30	1270	0.48
Bccz-7-30-1	16.67	85.65	21.10	7.30	1264	0.47
Oct-5-25-1	11.15	80.75	15.20	7.05	1289	0.48
Oct-5-25-2	10.59	80.70	15.15	7.05	1229	0.46
Oct-5-30-1	11.52	80.75	15.30	7.05	1323	0.50
Oct-5-30-2	11.84	80.80	15.25	7.10	1353	0.51
Oct-7-25-1	17.69	84.65	21.05	9.00	1103	0.41
Oct-7-25-2	18.15	84.80	21.20	9.05	1116	0.42
Oct-7-30-1	19.33	84.65	21.00	9.10	1195	0.45
Oct-7-30-1	19.34	84.75	21.05	9.05	1198	0.45
Sch-5-25-1	10.43	79.15	15.05	7.10	1233	0.46
Sch-5-25-2	10.44	79.65	15.00	7.05	1239	0.46
Sch-5-30-1	11.16	79.20	15.00	7.15	1314	0.49
Sch-5-30-2	11.26	79.30	15.05	7.05	1338	0.50
Sch-7-25-1	17.95	83.65	21.05	9.05	1126	0.42
Sch-7-25-2	17.95	83.40	21.00	9.05	1132	0.42
Sch-7-30-1	19.28	82.40	20.95	9.10	1227	0.46
Sch-7-30-2	19.60	83.55	21.00	9.05	1234	0.46

Appendix B

Images of specimens

This section contains all the images of the specimens produced for mechanical tests.

B.1 AlSi10Mg specimens for uniaxial compression test

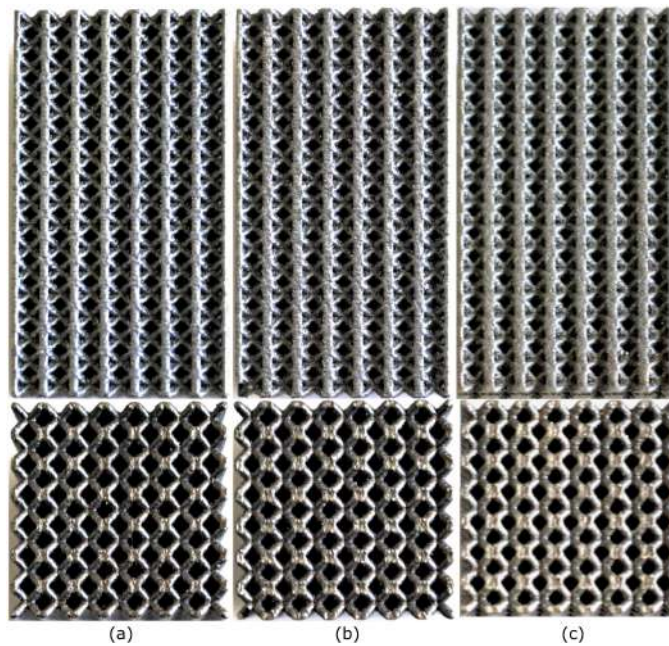


Figure B.1: Lateral and top view of the Bccz AlSi10Mg specimens: a) Bccz-3-25-1, b) Bccz-3-30-2 and c) Bccz-3-35-1.

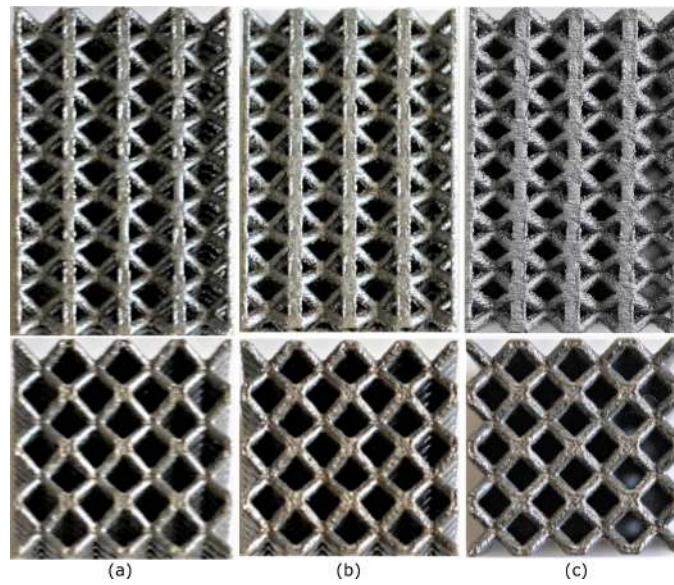


Figure B.2: Lateral and top view of the Bccz AlSi10Mg specimens: a) Bccz-5-25-3, b) Bccz-5-30-1 and c) Bccz-5-35-1.

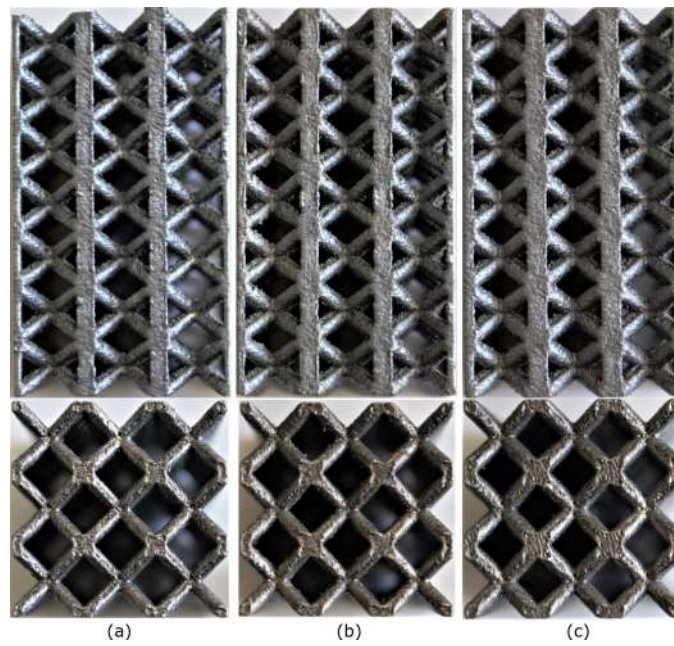


Figure B.3: Lateral and top view of the Bccz AlSi10Mg specimens: a) Bccz-7-25-2, b) Bccz-7-30-1 and c) Bccz-7-35-1.

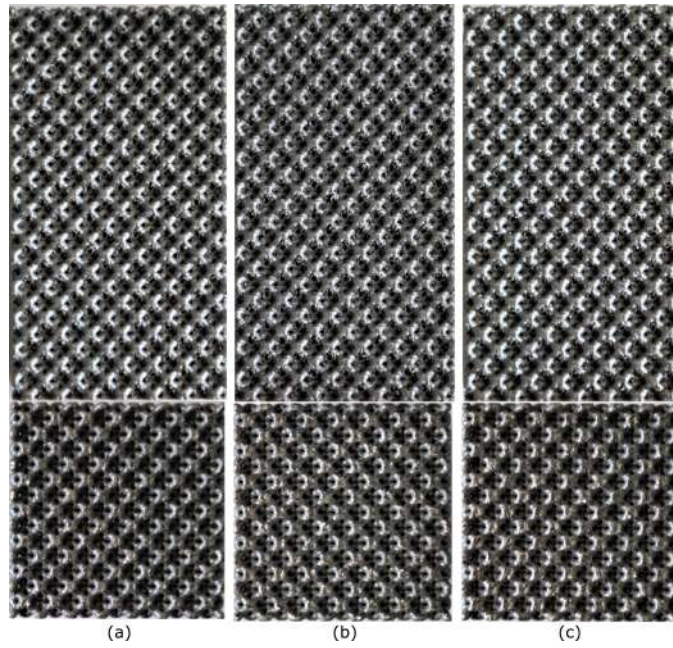


Figure B.4: Lateral and top view of the Rhombic dodecahedron AlSi10Mg specimens: a) Rhom-3-25-1, b) Rhom-3-30-1 and c) Rhom-3-35-1.

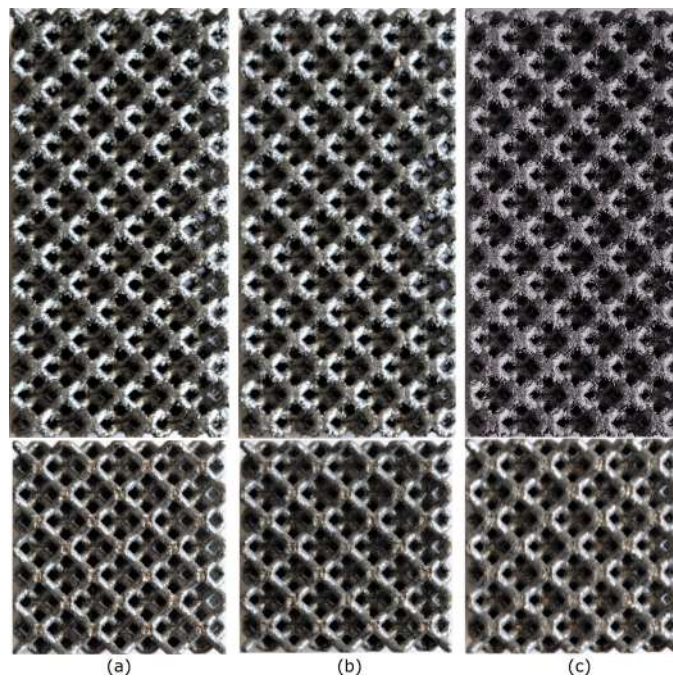


Figure B.5: Lateral and top view of the Rhombic dodecahedron AlSi10Mg specimens: a) Rhom-5-25-1, b) Rhom-5-30-1 and c) Rhom-5-35-1.

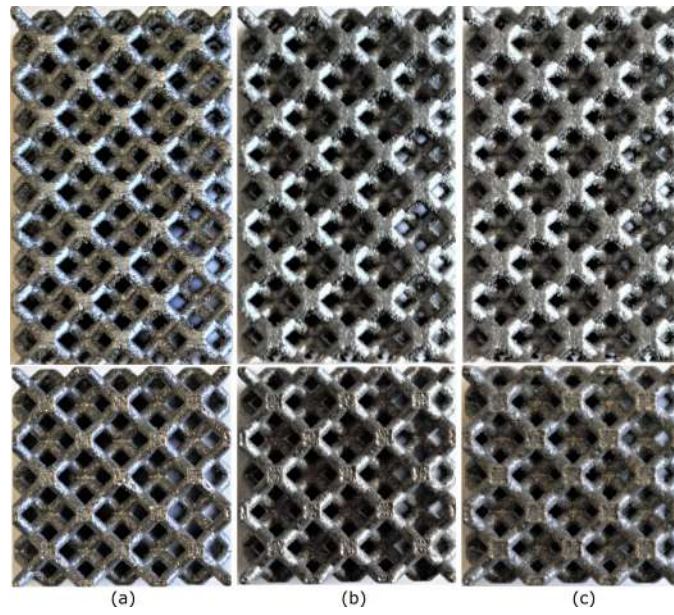


Figure B.6: Lateral and top view of the Rhombic dodecahedron AlSi10Mg specimens: a) Rhom-7-25-2, b) Rhom-7-30-2 and c) Rhom-7-35-1.

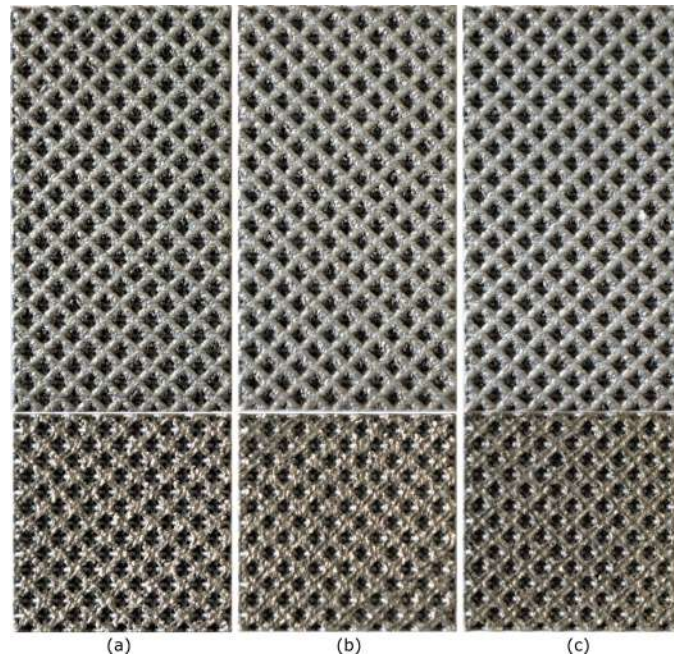


Figure B.7: Lateral and top view of the Octet-truss AlSi10Mg specimens: a) Oct-3-25-6, b) Oct-3-30-3 and c) Oct-3-35-3.

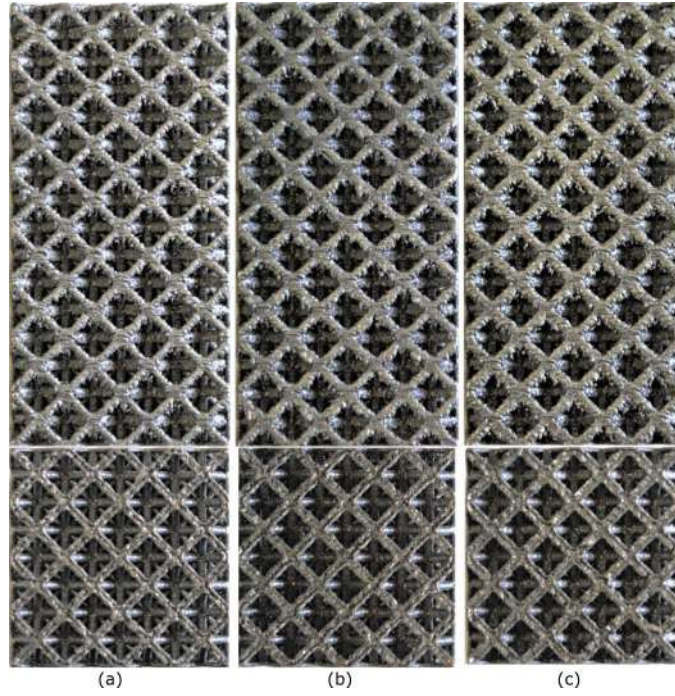


Figure B.8: Lateral and top view of the Octet-truss AlSi10Mg specimens: a) Oct-5-25-1, b) Oct-5-30-1 and c) Oct-5-35-1.

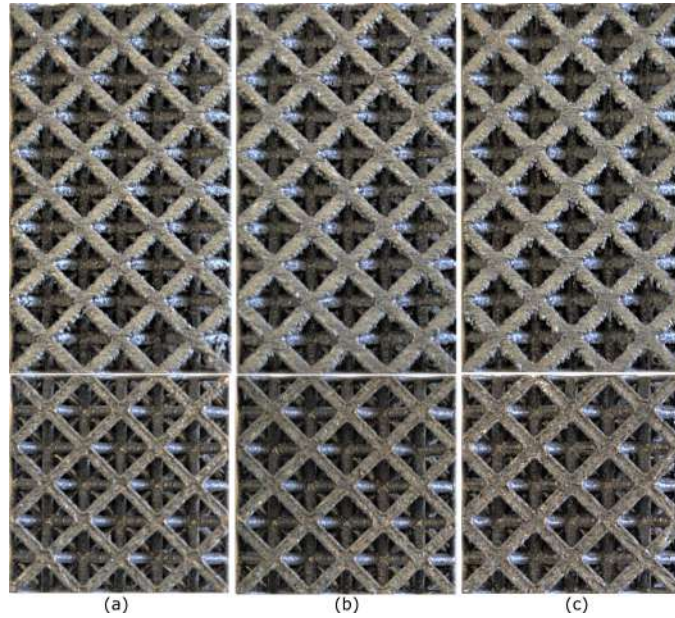


Figure B.9: Lateral and top view of the Octet-truss AlSi10Mg specimens: a) Oct-7-25-1, b) Oct-7-30-1 and c) Oct-7-35-1.

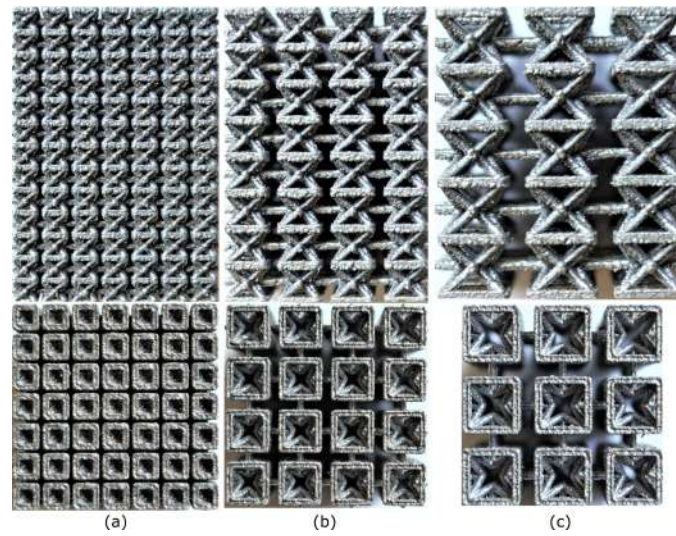


Figure B.10: Lateral and top view of the Auxetic AlSi10Mg specimens: a) Aux-3-35-3, b) Aux-5-30-1 and c) Aux-7-25-1.

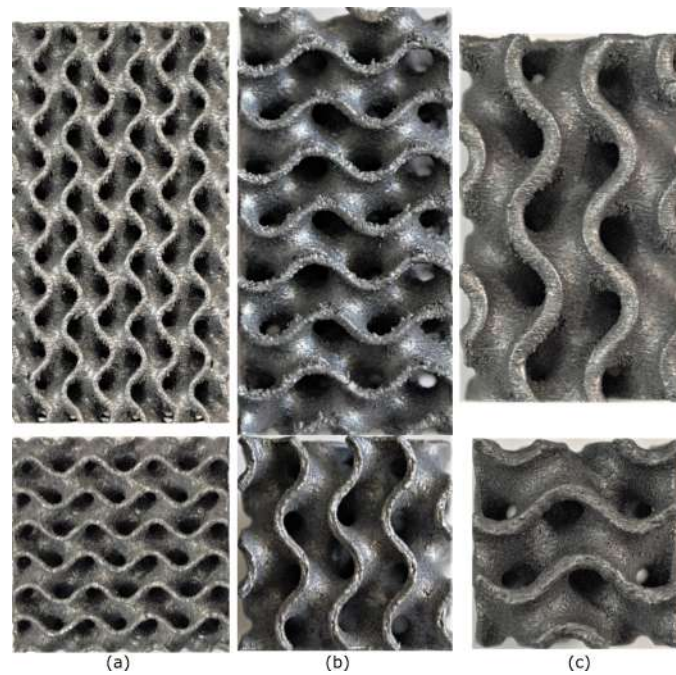


Figure B.11: Lateral and top view of the Gyroid AlSi10Mg specimens: a) Gyr-3-30-3, b) Gyr-5-25-1 and c) Gyr-7-35-2.

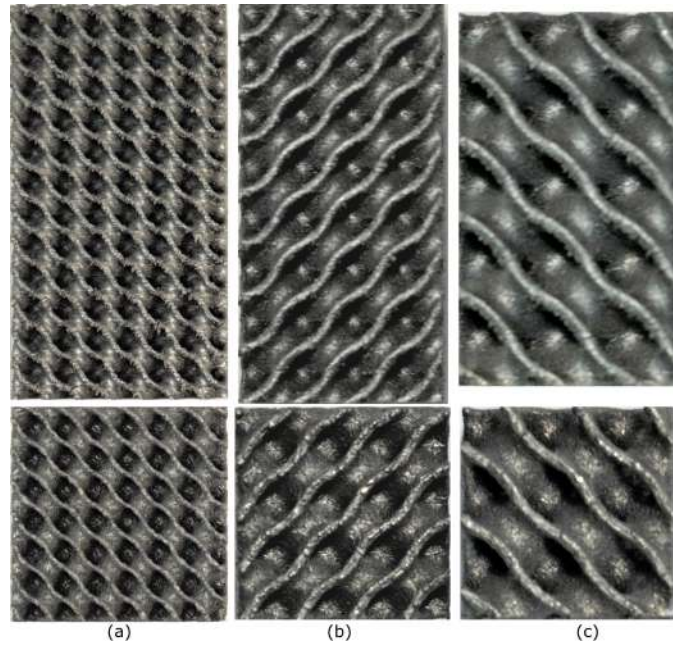


Figure B.12: Lateral and top view of the Schwartz diamond AlSi10Mg specimens: a) Sch-3-25-3, b) Sch-5-35-1 and c) Sch-7-30-2.

B.2 Ti6Al4V specimens for uniaxial compression test

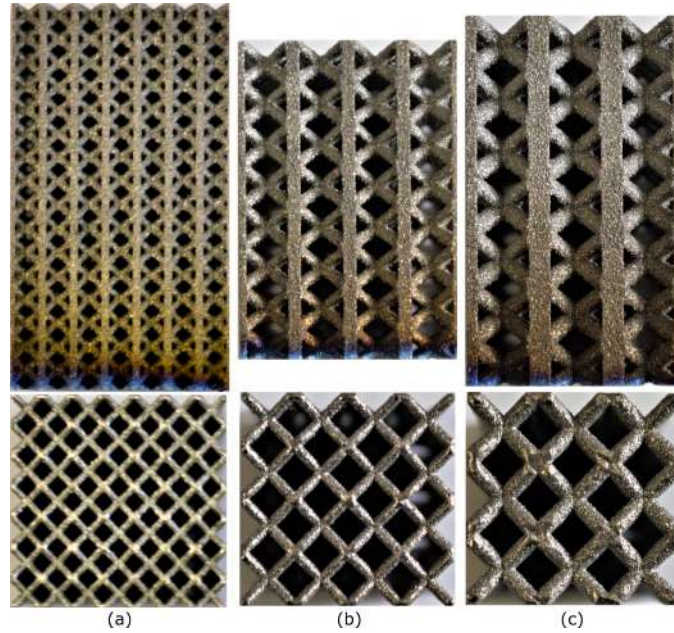


Figure B.13: Lateral and top view of the Bccz Ti6Al4V specimens: a) Bccz-3-30-2, b) Bccz-5-25-1 and c) Bccz-7-35-1.

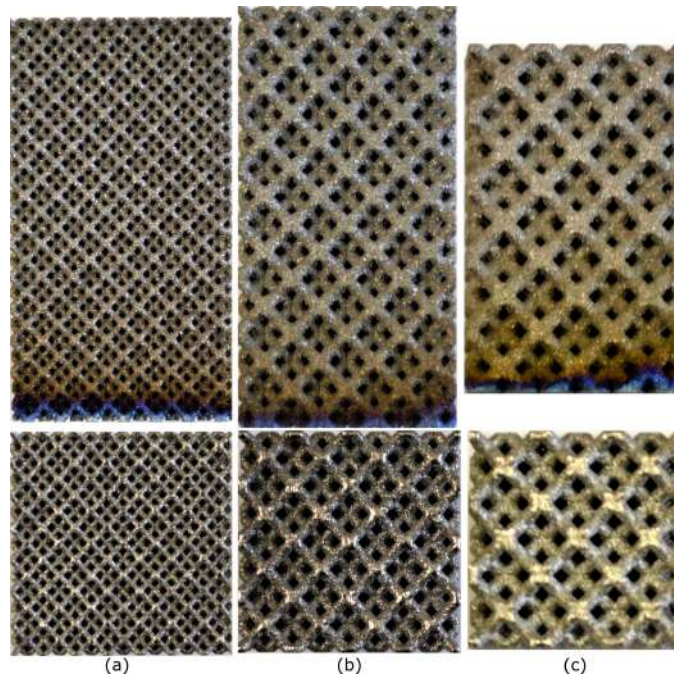


Figure B.14: Lateral and top view of the Rhombic dodecahedron Ti6Al4V specimens: a) Rhom-3-25-3, b) Rhom-5-35-1 and c) Rhom-7-30-3.

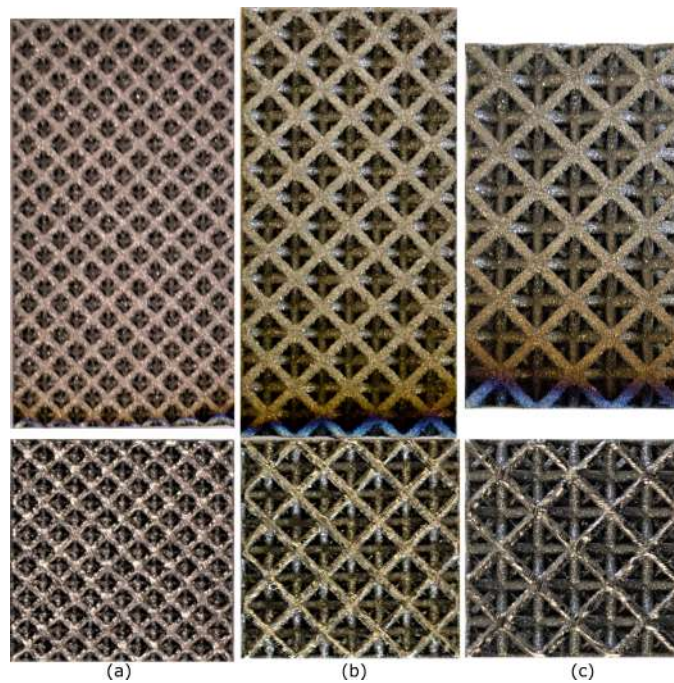


Figure B.15: Lateral and top view of the Octet-truss Ti6Al4V specimens: a) Oct-3-35-3, b) Oct-5-30-3 and c) Oct-7-25-2.

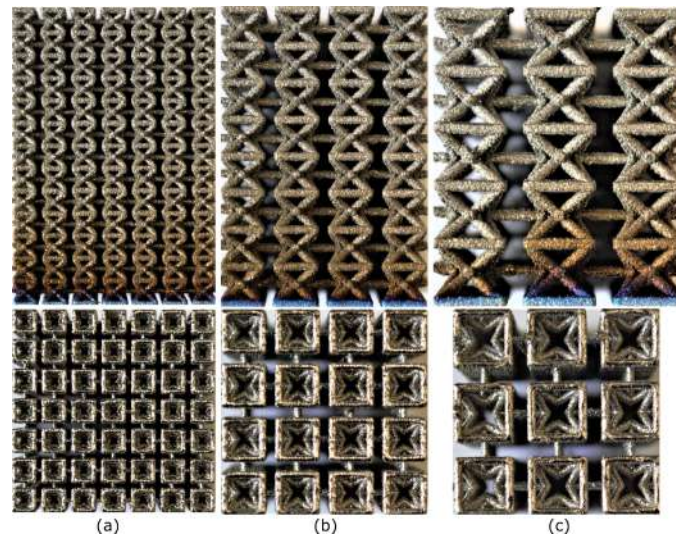


Figure B.16: Lateral and top view of the Auxetic Ti6Al4V specimens: a) Aux-3-35-1, b) Aux-5-30-1 and c) Aux-7-25-4.



Figure B.17: Lateral and top view of the Gyroid Ti6Al4V specimens: a) Gyr-3-30-13, b) Gyr-5-25-1 and c) Gyr-7-35-1.

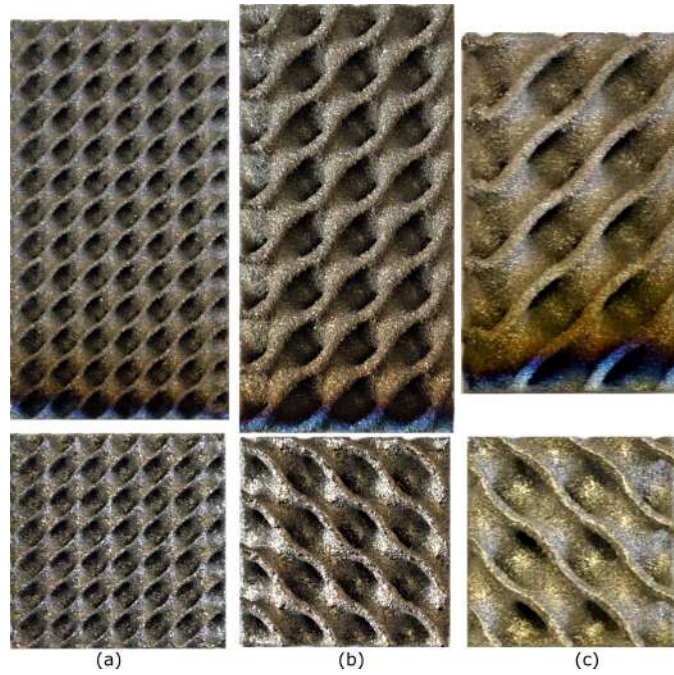


Figure B.18: Lateral and top view of the Schwartz diamond Ti6Al4V specimens: a) Sch-3-25-1, b) Sch-5-35-4 and c) Sch-7-30-1.

B.3 AlSi10Mg sandwich panels for uniaxial compression test

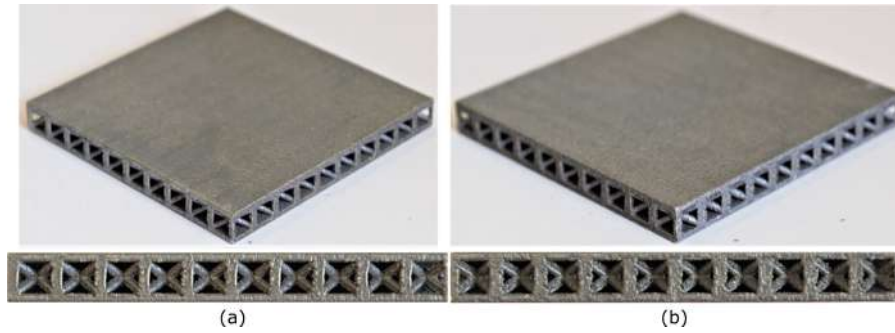


Figure B.19: Lateral and top view of the Bccz AlSi10Mg sandwich panels: a) Bccz-5-25 and b) Bccz-5-30.

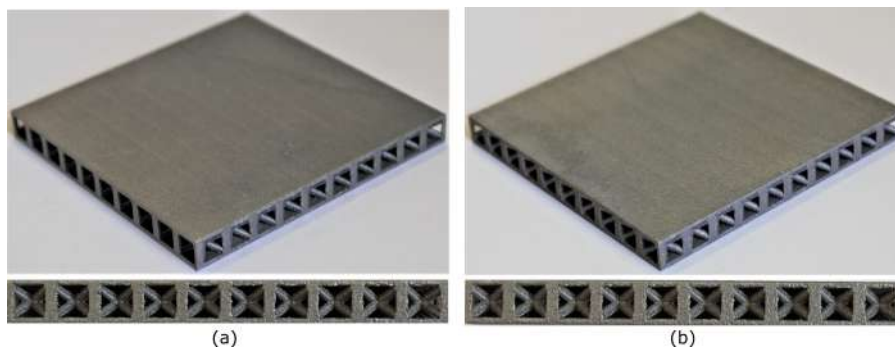


Figure B.20: Lateral and top view of the Bccz AlSi10Mg sandwich panels: a) Bccz-7-25 and b) Bccz-7-30.

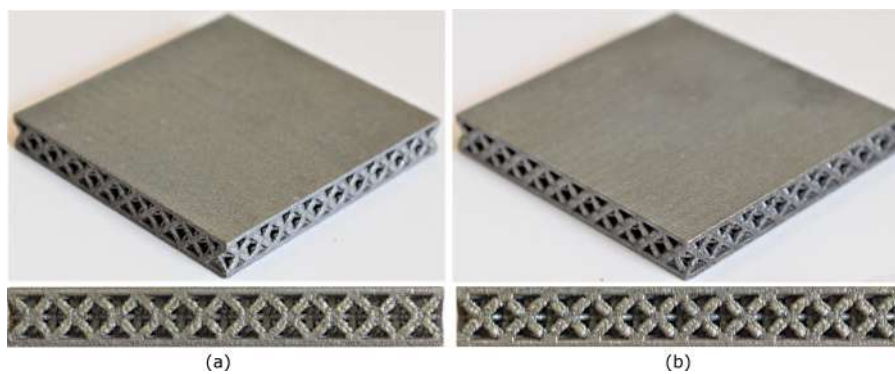


Figure B.21: Lateral and top view of the Octet-truss AlSi10Mg sandwich panels: a) Oct-5-25 and b) Oct-5-30.

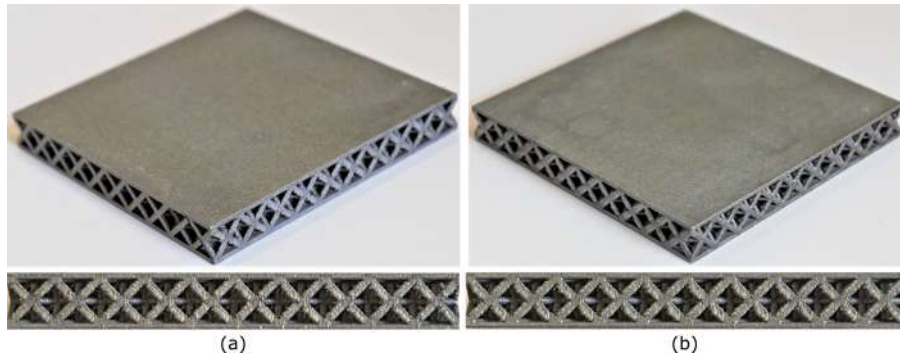


Figure B.22: Lateral and top view of the Octet-truss AlSi10Mg sandwich panels: a) Oct-7-25 and b) Oct-7-30.

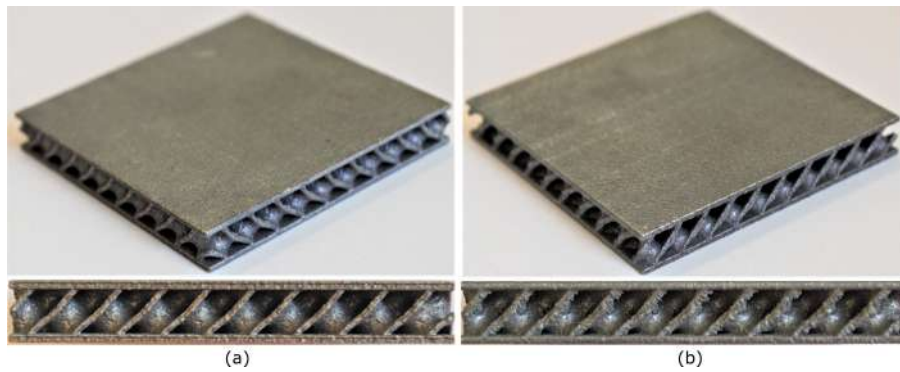


Figure B.23: Lateral and top view of the Schwartz diamond AlSi10Mg sandwich panels: a) Sch-5-25 and b) Sch-5-30.

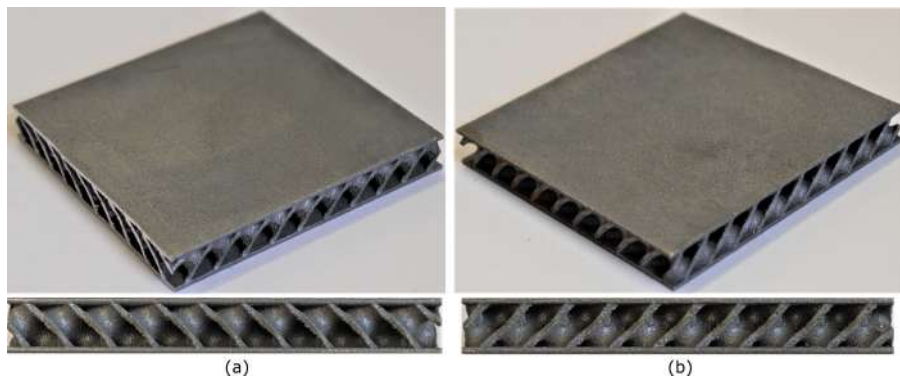


Figure B.24: Lateral and top view of the Schwartz diamond AlSi10Mg sandwich panels: a) Sch-7-25 and b) Sch-7-30.

B.4 AlSi10Mg sandwich panels for bending tests

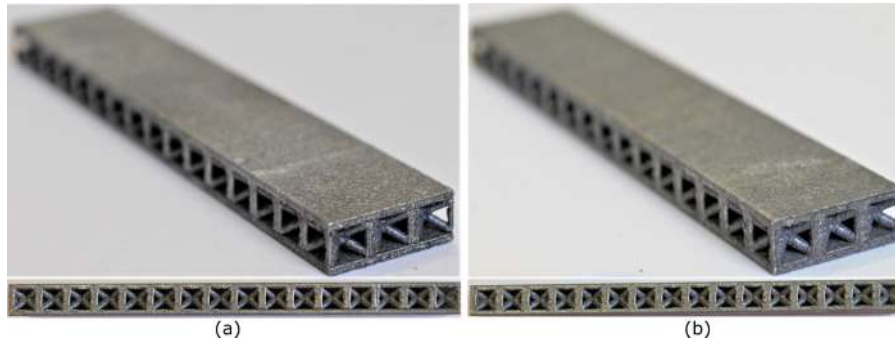


Figure B.25: Lateral and top view of the Bccz AlSi10Mg long sandwich panels: a) Bccz-5-25-2 and b) Bccz-5-30-1.

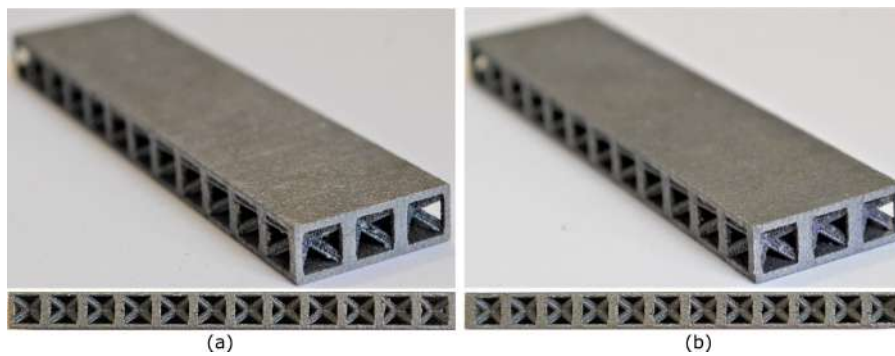


Figure B.26: Lateral and top view of the Bccz AlSi10Mg long sandwich panels: a) Bccz-7-25-1 and b) Bccz-7-30-1.

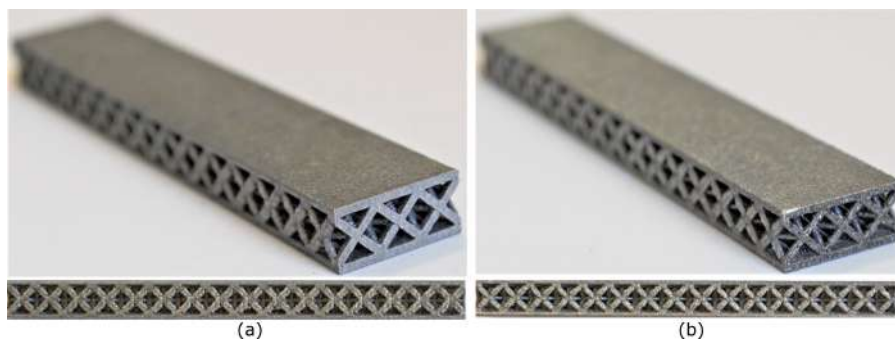


Figure B.27: Lateral and top view of the Octet-truss AlSi10Mg long sandwich panels: a) Oct-5-25-2 and b) Oct-5-30-1.

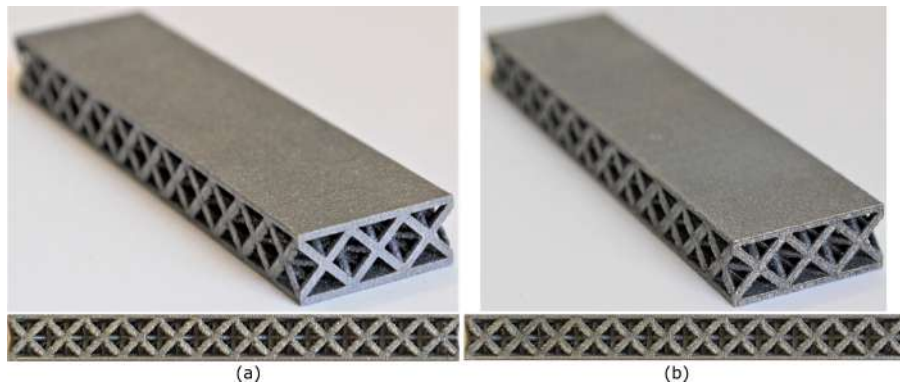


Figure B.28: Lateral and top view of the Octet-truss AlSi10Mg long sandwich panels: a) Oct-7-25-2 and b) Oct-7-30-2.

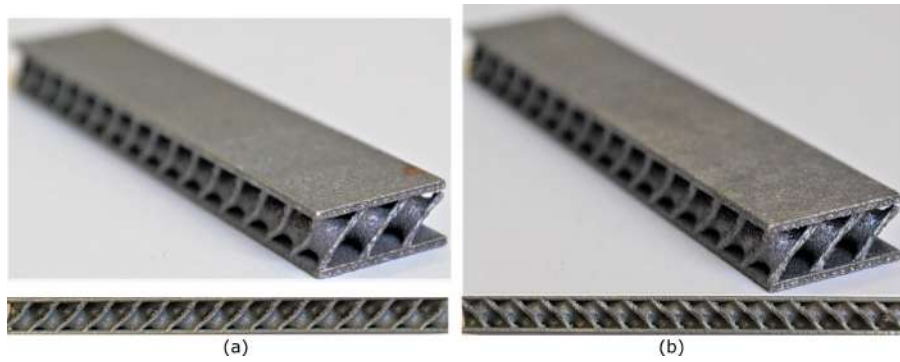


Figure B.29: Lateral and top view of the Schwartz diamond AlSi10Mg long sandwich panels: a) Sch-5-25-2 and b) Sch-5-30-1.

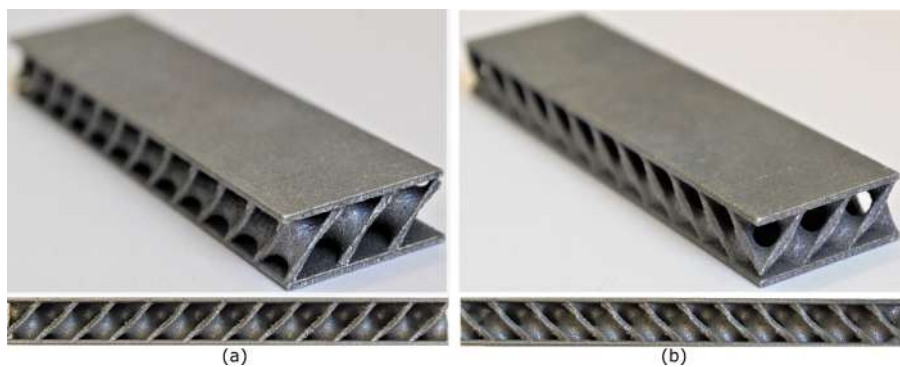


Figure B.30: Lateral and top view of the Schwartz diamond AlSi10Mg long sandwich panels: a) Sch-7-25-1 and b) Sch-7-30-1.

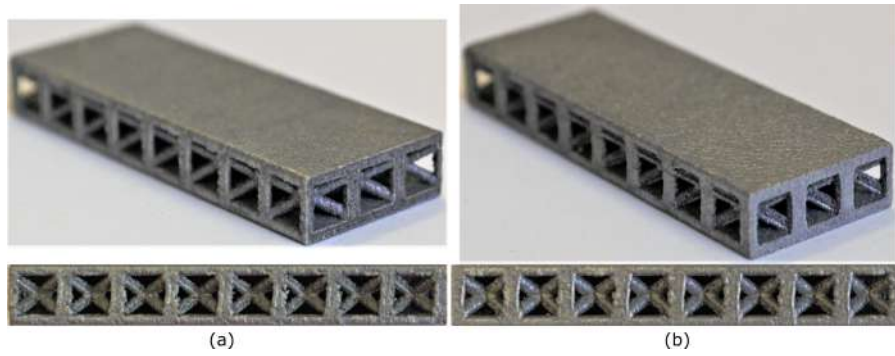


Figure B.31: Lateral and top view of the Bccz AlSi10Mg short sandwich panels: a) Bccz-5-25-1 and b) Bccz-5-30-2.

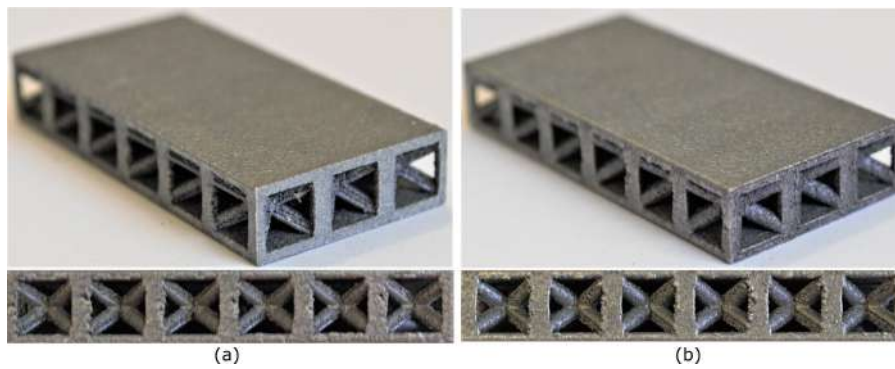


Figure B.32: Lateral and top view of the Bccz AlSi10Mg short sandwich panels: a) Bccz-7-25-1 and b) Bccz-7-30-1.

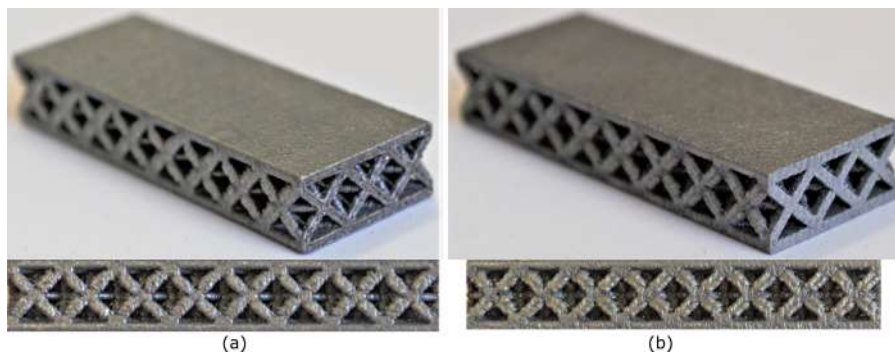


Figure B.33: Lateral and top view of the Octet-truss AlSi10Mg short sandwich panels: a) Oct-5-25-1 and b) Oct-5-30-1.

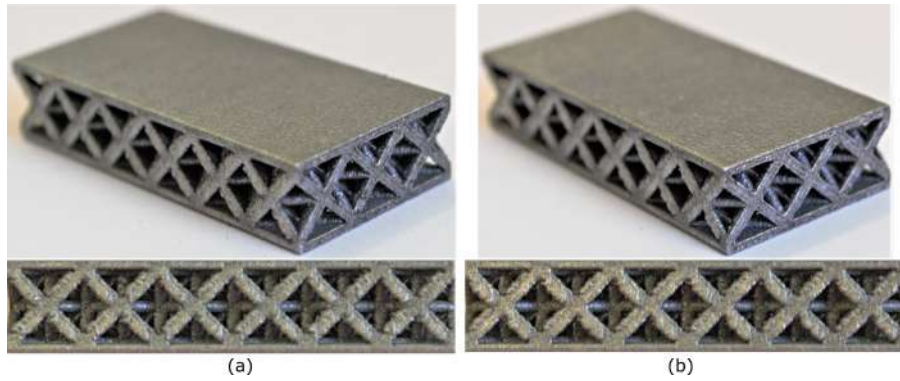


Figure B.34: Lateral and top view of the Octet-truss AlSi10Mg short sandwich panels: a) Oct-7-25-1 and b) Oct-7-30-1.

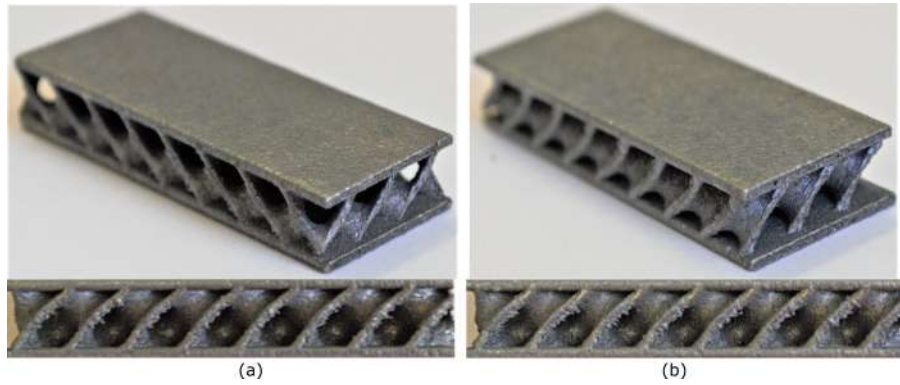


Figure B.35: Lateral and top view of the Schwartz diamond AlSi10Mg short sandwich panels: a) Sch-5-25-2 and b) Sch-5-30-1.

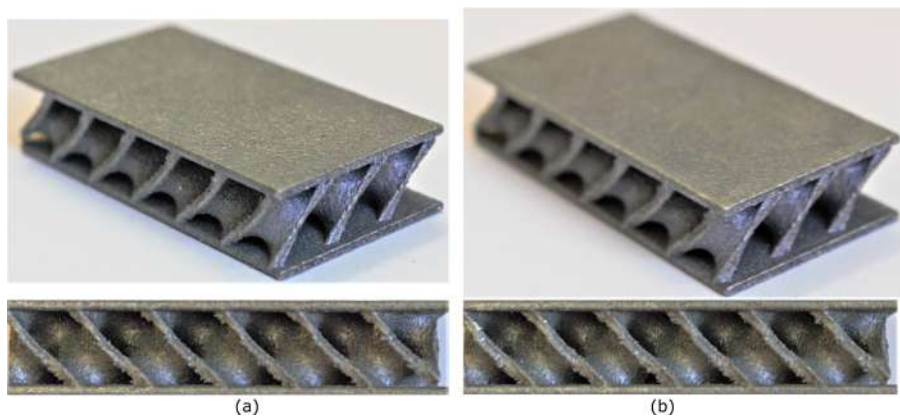


Figure B.36: Lateral and top view of the Schwartz diamond AlSi10Mg short sandwich panels: a) Sch-7-25-2 and b) Sch-7-30-2.

B.5 AlSi10Mg specimens for fatigue tests

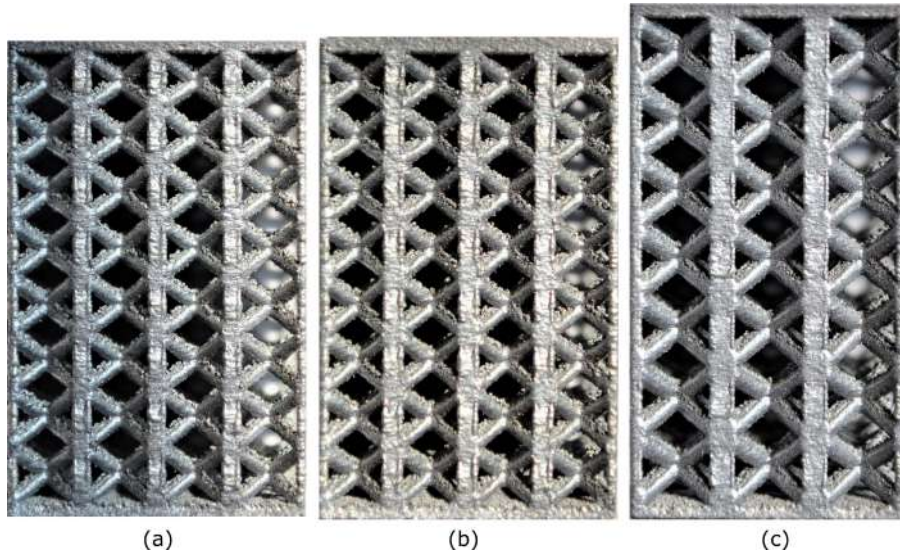


Figure B.37: Lateral view of the Bccz AlSi10Mg specimens for fatigue test: a) Bccz-5-25, b) Bccz-5-30 and b) Bccz-7-30.

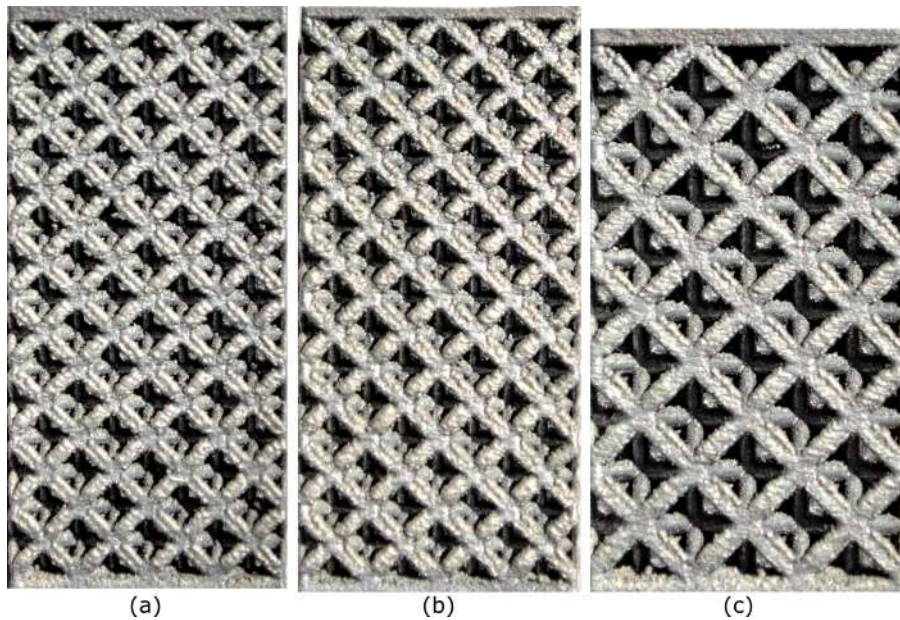


Figure B.38: Lateral view of the Octet-truss AlSi10Mg specimens for fatigue test: a) Oct-5-25, b) Oct-5-30 and b) Oct-7-30.

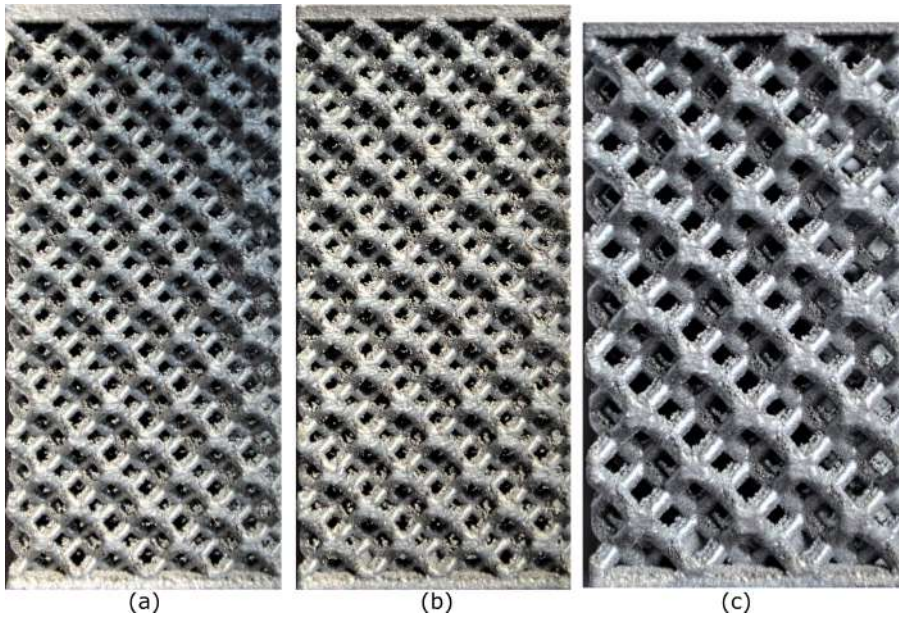


Figure B.39: Lateral view of the Rhombic dodecahedron AlSi10Mg specimens for fatigue test: a) Rhom-5-25, b) Rhom-5-30 and b) Rhom-7-30.

Appendix C

Mechanical tests results

This section contains all the results of mechanical tests carried out on the specimens and the sandwich panels.

C.1 Results of uniaxial compression tests on AlSi10Mg trabecular specimens

The results of uniaxial compression tests on AlSi10Mg specimens are listed in the Tables [C.1](#), [C.2](#), [C.3](#) and [C.4](#).

The results of uniaxial compression tests on Ti6Al4V specimens are listed in the Tables [C.5](#) and [C.6](#).

Table C.1: AlSi10Mg compression specimens with Bccz cells. The identification code of the specimens is: Celle shape - Cell size - Solid volume fraction (nominal) - Serial number

Id. code	σ_{\max} [MPa]	σ_{02} [MPa]	E [MPa]	σ_{\max}/ρ [MPa m ³ /kg]	σ_{02}/ρ [MPa m ³ /kg]	E/ ρ [MPa m ³ /kg]	Valid test
Bccz-3-25-1	95	48	2954	0.0852	0.0428	2.64	yes
Bccz-3-25-2	93	44	2837	0.0848	0.0404	2.58	yes
Bccz-3-25-3	97	47	3000	0.0874	0.0428	2.71	yes
Bccz-3-30-1	-	-	-	-	-	-	no
Bccz-3-30-2	118	55	3804	0.0958	0.0446	3.08	yes
Bccz-3-30-3	118	61	4821	0.0950	0.0490	3.87	yes
Bccz-3-30-4	116	59	3927	0.0913	0.0465	3.10	yes
Bccz-3-35-1	149	77	4315	0.108	0.0558	3.12	yes
Bccz-3-35-2	149	70	4264	0.108	0.0511	3.10	yes
Bccz-3-35-3	144	71	4224	0.105	0.0518	3.08	yes
Bccz-5-25-1	25	15	1322	0.0414	0.0241	2.20	no
Bccz-5-25-2	28	17	1224	0.0463	0.0275	2.03	yes
Bccz-5-25-3	27	16	1233	0.0450	0.0270	2.06	yes
Bccz-5-25-4	28	17	1199	0.0462	0.0284	2.00	yes
Bccz-5-30-1	42	25	1579	0.0556	0.0327	2.07	yes
Bccz-5-30-2	43	26	1565	0.0560	0.0337	2.04	yes
Bccz-5-30-3	43	25	1707	0.0555	0.0326	2.23	yes
Bccz-5-35-1	57	31	2011	0.0642	0.0352	2.28	yes
Bccz-5-35-2	56	30	2020	0.0647	0.0348	2.32	yes
Bccz-5-35-3	56	30	2018	0.0632	0.0342	2.29	yes
Bccz-7-25-1	32	18	1491	0.0496	0.0288	2.34	yes
Bccz-7-25-2	30	20	1282	0.0469	0.0322	2.02	yes
Bccz-7-25-3	32	18	1626	0.0506	0.0284	2.58	yes
Bccz-7-30-1	44	24	1822	0.0579	0.0320	2.43	yes
Bccz-7-30-2	44	25	1826	0.0580	0.0328	2.42	yes
Bccz-7-30-3	41	32	1337	0.0540	0.0422	1.78	yes
Bccz-7-35-1	59	32	2273	0.0660	0.0359	2.56	yes
Bccz-7-35-2	57	28	2251	0.0645	0.0320	2.55	yes
Bccz-7-35-3	58	33	2219	0.0660	0.0373	2.51	yes

Table C.2: AlSi10Mg compression specimens with Rhombic dodecahedron cells. The identification code of the specimens is: Celle shape - Cell size - Solid volume fraction (nominal) - Serial number

Id. code	σ_{\max} [MPa]	σ_{02} [MPa]	E [MPa]	σ_{\max}/ρ [MPa m ³ /kg]	σ_{02}/ρ [MPa m ³ /kg]	E/ ρ [MPa m ³ /kg]	Valid test
Rhom-3-25-1	86	50	2847	0.0680	0.0397	2.24	yes
Rhom-3-25-2	87	51	2823	0.0684	0.0402	2.21	yes
Rhom-3-25-3	86	52	2853	0.0690	0.0414	2.28	yes
Rhom-3-30-1	108	72	4009	0.0777	0.0516	2.87	yes
Rhom-3-30-2	104	68	4254	0.0753	0.0497	3.09	yes
Rhom-3-30-3	106	78	3464	0.0758	0.0562	2.48	yes
Rhom-3-35-1	137	76	4840	0.0858	0.0477	3.03	yes
Rhom-3-35-2	135	80	4641	0.0842	0.0499	2.90	yes
Rhom-3-35-3	135	89	4973	0.0852	0.0562	3.14	yes
Rhom-5-25-1	19	15	1046	0.0287	0.0235	1.62	yes
Rhom-5-25-2	19	15	1001	0.0290	0.0233	1.56	yes
Rhom-5-25-3	19	15	1096	0.0291	0.0234	1.69	yes
Rhom-5-30-1	29	21	1522	0.0383	0.0280	2.01	yes
Rhom-5-30-2	29	22	1526	0.0382	0.0280	1.99	yes
Rhom-5-30-3	29	22	1610	0.0380	0.0285	2.10	yes
Rhom-5-35-1	42	30	2059	0.0470	0.0334	2.30	yes
Rhom-5-35-2	40	29	2006	0.0458	0.0323	2.27	yes
Rhom-5-35-3	42	30	2090	0.0461	0.0322	2.27	yes
Rhom-7-25-1	18	15	955	0.0290	0.0241	1.52	yes
Rhom-7-25-2	17	14	908	0.0276	0.0223	1.43	yes
Rhom-7-25-3	18	15	1008	0.0286	0.0236	1.59	yes
Rhom-7-30-1	28	22	1403	0.0359	0.0285	1.81	yes
Rhom-7-30-2	28	22	1405	0.0361	0.0286	1.82	yes
Rhom-7-30-3	28	23	1440	0.0362	0.0291	1.86	yes
Rhom-7-35-1	40	30	1845	0.0438	0.0328	2.01	yes
Rhom-7-35-2	40	31	1840	0.0439	0.0335	2.01	yes
Rhom-7-35-3	41	31	1899	0.0443	0.0335	2.08	yes

Table C.3: AlSi10Mg compression specimens with Octet-truss cells. The identification code of the specimens is: Celle shape - Cell size - Solid volume fraction (nominal) - Serial number

Id. code	σ_{\max} [MPa]	σ_{02} [MPa]	E [MPa]	σ_{\max}/ρ [MPa m ³ /kg]	σ_{02}/ρ [MPa m ³ /kg]	E/ ρ [MPa m ³ /kg]	Valid test
Oct-3-25-1	111	61	4070	0.0772	0.0425	2.83	no
Oct-3-25-2	112	62	4057	0.0773	0.0426	2.80	no
Oct-3-25-3	-	-	-	-	-	-	no
Oct-3-25-4	107	72	3747	0.0765	0.0513	2.68	yes
Oct-3-25-5	114	55	5907	0.0786	0.0377	4.06	yes
Oct-3-25-6	-	-	-	-	-	-	no
Oct-3-30-1	156	89	5520	0.0936	0.0532	3.32	yes
Oct-3-30-2	-	-	-	-	-	-	no
Oct-3-30-3	-	-	-	-	-	-	no
Oct-3-35-1	161	91	5902	0.0938	0.0534	3.44	yes
Oct-3-35-2	160	84	7321	0.0941	0.0497	4.31	yes
Oct-3-35-3	-	-	-	-	-	-	no
Oct-5-25-1	28	24	1610	0.0377	0.0316	2.14	yes
Oct-5-25-2	28	23	1599	0.0378	0.0306	2.17	yes
Oct-5-25-3	29	22	1741	0.0391	0.0307	2.38	yes
Oct-5-30-1	37	27	1906	0.0433	0.0316	2.23	yes
Oct-5-30-2	41	30	2011	0.0473	0.0341	2.31	yes
Oct-5-30-3	36	27	1922	0.0426	0.0325	2.31	yes
Oct-5-35-1	57	36	2426	0.0565	0.0358	2.40	yes
Oct-5-35-2	56	36	2396	0.0556	0.0356	2.36	yes
Oct-5-35-3	53	35	2321	0.0549	0.0363	2.40	yes
Oct-7-25-1	29	23	1502	0.0420	0.0325	2.17	yes
Oct-7-25-2	28	23	1507	0.0407	0.0328	2.16	yes
Oct-7-25-3	31	23	1595	0.0449	0.0333	2.31	yes
Oct-7-30-1	42	29	1732	0.0522	0.0355	2.13	yes
Oct-7-30-2	42	28	1787	0.0520	0.0350	2.20	yes
Oct-7-30-3	42	29	1691	0.0522	0.0367	2.12	yes
Oct-7-35-1	59	36	2289	0.0623	0.0386	2.43	yes
Oct-7-35-2	58	36	2240	0.0601	0.0371	2.32	yes
Oct-7-35-3	58	37	2260	0.0608	0.0389	2.36	yes

Table C.4: AlSi10Mg compression specimens with Auxetic, Gyroid and Schwartz diamond cells. The identification code of the specimens is: Celle shape - Cell size - Solid volume fraction (nominal) - Serial number

Id. code	σ_{\max} [MPa]	σ_{02} [MPa]	E [MPa]	σ_{\max}/ρ [MPa m ³ /kg]	σ_{02}/ρ [MPa m ³ /kg]	E/ ρ [MPa m ³ /kg]	Valid test
Aux-3-35-1	50	30	1661	0.0472	0.0287	1.58	no
Aux-3-35-2	48	30	1536	0.0456	0.0289	1.47	no
Aux-3-35-3	52	29	1758	0.0491	0.0278	1.66	no
Aux-3-35-4	55	34	1741	0.0506	0.0316	1.59	no
Aux-3-35-5	54	32	1755	0.0488	0.0289	1.59	no
Aux-3-35-6	53	32	1744	0.0482	0.0293	1.59	no
Aux-3-35-7	50	30	2090	0.0469	0.0279	1.97	yes
Aux-3-35-8	53	27	3135	0.0513	0.0262	3.02	yes
Aux-3-35-9	51	30	2050	0.0482	0.0282	1.94	yes
Aux-5-30-1	9	8	562	0.0173	0.0148	1.05	no
Aux-5-30-2	6	5	385	0.0107	0.0087	0.73	no
Aux-5-30-3	-	-	-	-	-	-	no
Aux-5-30-4s	9	8	575	0.0163	0.0149	1.08	yes
Aux-5-30-4	10	8	688	0.0188	0.0153	1.32	yes
Aux-5-30-5	9	8	624	0.0177	0.0152	1.21	yes
Aux-7-25-1	7	6	394	0.0161	0.0129	0.91	no
Aux-7-25-2	6	4	360	0.0141	0.0095	0.83	no
Aux-7-25-3	8	6	369	0.0177	0.0141	0.85	yes
Aux-7-25-4	7	6	368	0.0166	0.0125	0.83	yes
Aux-7-25-5	8	6	379	0.0176	0.0134	0.86	yes
Gyr-3-30-1	58	33	2223	0.0701	0.0404	2.70	yes
Gyr-3-30-2	59	34	2174	0.0703	0.0403	2.57	yes
Gyr-3-30-3	56	32	2184	0.0703	0.0402	2.72	yes
Gyr-5-25-1	44	27	1485	0.0648	0.0392	2.17	yes
Gyr-5-25-2	43	33	1472	0.0635	0.0486	2.16	yes
Gyr-5-25-3	44	28	2063	0.0652	0.0410	3.02	yes
Gyr-7-35-1	67	43	2065	0.0687	0.0439	2.12	yes
Gyr-7-35-2	68	41	2162	0.0698	0.0427	2.22	yes
Gyr-7-35-3	69	43	2146	0.0702	0.0439	2.18	yes
Sch-3-25-1	59	32	2158	0.0799	0.0431	2.94	yes
Sch-3-25-2	59	32	2172	0.0791	0.0428	2.94	yes
Sch-3-25-3	58	31	2208	0.0800	0.0422	3.02	yes
Sch-5-35-1	94	53	3239	0.0948	0.0529	3.26	yes
Sch-5-35-2	94	53	3127	0.0957	0.0534	3.17	yes
Sch-5-35-3	90	52	3217	0.0941	0.0546	3.36	yes
Sch-7-30-1	76	44	2332	0.0896	0.0521	2.76	yes
Sch-7-30-2	76	44	2309	0.0900	0.0517	2.73	yes
Sch-7-30-3	79	44	2293	0.0921	0.0517	2.67	yes

C.2 Results of uniaxial compression tests on Ti6Al4V trabecular specimens

Table C.5: Ti6Al4V compression specimens with Bccz, Rhombic dodecahedron and Octet-truss cells. The identification code of the specimens is: Celle shape - Cell size - Solid volume fraction (nominal) - Serial number

Id. code	σ_{\max} [MPa]	σ_{02} [MPa]	E [MPa]	σ_{\max}/ρ [MPa m ³ /kg]	σ_{02}/ρ [MPa m ³ /kg]	E/ ρ [MPa m ³ /kg]	Valid test
Bccz-3-30-1	134	96	4344	0.103	0.0733	3.33	yes
Bccz-3-30-2	134	90	3983	0.102	0.0685	3.04	yes
Bccz-3-30-3	134	92	4544	0.105	0.0726	3.58	yes
Bccz-5-25-1	98	71	3349	0.0931	0.0677	3.18	no
Bccz-5-25-2	94	69	3251	0.0892	0.0657	3.10	yes
Bccz-5-25-3	93	67	3295	0.0909	0.0660	3.23	yes
Bccz-7-35-1	184	112	3931	0.119	0.0725	2.54	yes
Bccz-7-35-2	180	138	4848	0.112	0.0918	3.23	yes
Bccz-7-35-3	182	136	5288	0.120	0.0895	3.48	yes
Rhom-3-25-1	71	64	1827	0.0659	0.0589	1.68	yes
Rhom-3-25-2	76	66	2304	0.0663	0.0583	2.02	yes
Rhom-3-25-3	74	66	2279	0.0665	0.0594	2.06	yes
Rhom-5-35-1	154	133	4221	0.0987	0.0853	2.71	yes
Rhom-5-35-2	155	132	3630	0.0987	0.0837	2.31	yes
Rhom-5-35-3	160	133	5349	0.0972	0.0809	3.25	yes
Rhom-7-30-1	145	136	3713	0.0959	0.0894	2.45	yes
Rhom-7-30-2	147	141	3746	0.0954	0.0912	2.43	yes
Rhom-7-30-3	149	142	4193	0.0956	0.0909	2.68	yes
Oct-3-35-1	270	222	8402	0.119	0.0976	3.69	yes
Oct-3-35-2	-	-	-	-	-	-	no
Oct-3-35-3	-	-	-	-	-	-	no
Oct-5-30-1	128	110	3637	0.0947	0.0809	2.68	yes
Oct-5-30-2	129	115	3512	0.0951	0.0844	2.58	yes
Oct-5-30-3	128	123	4602	0.0933	0.0897	3.36	yes
Oct-7-25-1	98	95	2716	0.0872	0.0848	2.42	yes
Oct-7-25-2	94	92	2643	0.0871	0.0848	2.44	yes
Oct-7-25-3	92	89	2984	0.0847	0.0813	2.73	yes

Table C.6: Ti6Al4V compression specimens with Auxetic, Gyroid and Schwartz diamond cells. The identification code of the specimens is: Celle shape - Cell size - Solid volume fraction (nominal) - Serial number

Id. code	σ_{\max} [MPa]	σ_{02} [MPa]	E [MPa]	σ_{\max}/ρ [MPa m ³ /kg]	σ_{02}/ρ [MPa m ³ /kg]	E/ ρ [MPa m ³ /kg]	Valid test
Aux-3-35-1	58	48	2076	0.0559	0.0463	2.00	yes
Aux-3-35-2	61	52	2041	0.0569	0.0482	1.91	yes
Aux-3-35-3	57	53	1977	0.0541	0.0497	1.87	yes
Aux-5-30-1	43	38	1370	0.0468	0.0411	1.50	no
Aux-5-30-2	42	37	1365	0.0456	0.0408	1.49	no
Aux-5-30-3	41	37	1417	0.0455	0.0418	1.59	yes
Aux-7-25-1	-	-	-	-	-	-	no
Aux-7-25-2	-	-	-	-	-	-	no
Aux-7-25-3	-	-	-	-	-	-	no
Aux-7-25-4	24	22	574	0.0324	0.0297	0.77	yes
Aux-7-25-5	26	24	788	0.0355	0.0316	1.06	yes
Aux-7-25-6	25	23	822	0.0329	0.0309	1.10	yes
Gyr-3-30-1	171	149	4743	0.122	0.105	3.37	yes
Gyr-3-30-2	175	152	4916	0.122	0.106	3.44	yes
Gyr-3-30-3	172	150	4996	0.120	0.105	3.49	yes
Gyr-5-25-1	129	106	4082	0.111	0.0909	3.51	yes
Gyr-5-25-2	128	112	4361	0.114	0.0991	3.87	yes
Gyr-5-25-3	129	114	4155	0.110	0.0975	3.55	yes
Gyr-7-35-1	200	179	4730	0.129	0.115	3.04	yes
Gyr-7-35-2	207	188	4809	0.131	0.118	3.04	yes
Gyr-7-35-3	199	175	5441	0.129	0.113	3.53	yes
Sch-3-25-1	170	155	5122	0.138	0.125	4.14	yes
Sch-3-25-2	171	153	4877	0.139	0.125	3.97	yes
Sch-3-25-3	164	146	5388	0.135	0.121	4.46	yes
Sch-5-35-1	-	-	-	-	-	-	no
Sch-5-35-2	248	218	6495	0.154	0.135	4.03	yes
Sch-5-35-3	-	-	-	-	-	-	no
Sch-5-35-4	228	189	6246	0.143	0.118	3.91	yes
Sch-7-30-1	208	190	4935	0.148	0.136	3.53	yes
Sch-7-30-2	208	190	5013	0.151	0.138	3.65	yes
Sch-7-30-3	209	182	5169	0.145	0.126	3.58	yes

C.3 Results of uniaxial compression tests on AlSi10Mg sandwich panels

The results of uniaxial compression tests on AlSi10Mg sandwich panels are listed in the table C.7.

Table C.7: AlSi10Mg compression sandwich panels with Bccz, Octet-truss and Schwartz diamond cells. The identification code of the specimens is: Celle shape - Cell size - Solid volume fraction (nominal)

Id. code	σ_{\max} [MPa]	σ_{02} [MPa]	E [MPa]	σ_{\max}/ρ [MPa m ³ /kg]	σ_{02}/ρ [MPa m ³ /kg]	E/ ρ [MPa m ³ /kg]	Valid test
Bccz-5-25	50	37	387	0.0376	0.0279	0.294	yes
Bccz-5-30	69	51	463	0.0492	0.0368	0.332	yes
Bccz-7-25	53	39	332	0.0444	0.0325	0.280	yes
Bccz-7-30	68	48	377	0.0529	0.0379	0.296	yes
Oct-5-25	47	36	510	0.0365	0.0285	0.401	yes
Oct-5-30	58	41	540	0.0428	0.0303	0.401	yes
Oct-7-25	42	33	397	0.0386	0.0300	0.364	yes
Oct-7-30	58	42	466	0.0480	0.0351	0.389	yes
Sch-5-25	90	61	636	0.0714	0.0486	0.503	yes
Sch-5-30	119	90	614	0.0883	0.0666	0.455	yes
Sch-7-25	96	68	478	0.0838	0.0588	0.415	yes
Sch-7-30	123	87	1041	0.0993	0.0703	0.841	yes

C.4 Results of bending tests on AlSi10Mg sandwich panels

The results of bending tests on AlSi10Mg sandwich panels are listed in the tables C.8 and C.9 for short and long specimens, respectively..

Table C.8: AlSi10Mg short sandwich panels for bending test with Bccz, Octet-truss and Schwartz diamond cells. The identification code of the specimens is: Celle shape - Cell size - Solid volume fraction (nominal) - Serial number

Id. code	F _{ult} [MPa]	P _{max} [N]	Facing Stress [MPa]	F _{yield} [MPa]	Valid test
Bccz-5-25-1	20	2866	304	-	yes
Bccz-5-25-2	21	3111	329	12	yes
Bccz-5-30-1	24	3522	374	-	yes
Bccz-5-30-2	22	3229	346	13	yes
Bccz-7-25-1	19	4941	289	12	yes
Bccz-7-25-2	19	5059	294	12	yes
Bccz-7-30-1	20	5431	315	17	yes
Bccz-7-30-1	20	5282	306	15	yes
Oct-5-25-1	22	4004	336	13	yes
Oct-5-25-2	21	3918	329	13	yes
Oct-5-30-1	25	4508	382	15	yes
Oct-5-30-2	24	4518	379	15	yes
Oct-7-25-1	16	5323	242	10	yes
Oct-7-25-2	16	5441	249	10	yes
Oct-7-30-1	19	6376	290	12	yes
Oct-7-30-1	18	6132	279	12	yes
Sch-5-25-1	24	4474	377	14	yes
Sch-5-25-2	24	4442	379	14	yes
Sch-5-30-1	27	4839	413	18	yes
Sch-5-30-2	27	4843	413	19	yes
Sch-7-25-1	20	6661	305	13	yes
Sch-7-25-2	19	6473	297	12	yes
Sch-7-30-1	22	7441	339	15	yes
Sch-7-30-2	23	7669	351	15	yes

Table C.9: AlSi10Mg long sandwich panels for bending test with Bccz, Octet-truss and Schwartz diamond cells. The identification code of the specimens is: Celle shape - Cell size - Solid volume fraction (nominal) - Serial number

Id. code	F_{ult} [MPa]	P_{max} [N]	Facing Stress [MPa]	F_{yield} [MPa]	Valid test
Bccz-5-25-1	9	1261	300	4	yes
Bccz-5-25-2	8	1204	283	4	yes
Bccz-5-30-1	11	1579	374	6	yes
Bccz-5-30-2	10	1526	358	5	yes
Bccz-7-25-1	10	2594	334	5	yes
Bccz-7-25-2	9	2432	312	5	yes
Bccz-7-30-1	11	2889	374	6	yes
Bccz-7-30-1	11	2857	369	6	yes
Oct-5-25-1	11	1932	360	5	yes
Oct-5-25-2	11	1965	368	5	yes
Oct-5-30-1	13	2418	448	6	yes
Oct-5-30-2	13	2448	451	6	yes
Oct-7-25-1	12	3994	407	7	yes
Oct-7-25-2	12	4131	215	8	yes
Oct-7-30-1	12	4204	424	7	yes
Oct-7-30-1	13	4306	436	-	yes
Sch-5-25-1	12	2295	429	5	yes
Sch-5-25-2	14	2456	464	6	yes
Sch-5-30-1	13	2389	444	18	yes
Sch-5-30-2	13	2350	437	19	yes
Sch-7-25-1	12	4178	423	7	yes
Sch-7-25-2	13	4231	429	8	yes
Sch-7-30-1	13	4388	444	8	yes
Sch-7-30-2	12	4222	428	7	yes

C.5 Results of fatigue tests on AlSi10Mg specimens

Table C.10: AlSi10Mg specimens for fatigue test with Bccz cell. The identification code of the specimens is: Celle shape - Cell size - Solid volume fraction (nominal) - Serial number

Id. code	σ_M [MPa]	σ_m [MPa]	σ_a [MPa]	N
Bccz-5-25-1	12.6	1.26	6.9	10178091
Bccz-5-25-2	12.6	1.26	6.9	12441038
Bccz-5-25-3	12.6	1.26	6.9	-
Bccz-5-25-4	9.4	0.94	5.2	15000000
Bccz-5-25-5	9.4	0.94	5.2	15000000
Bccz-5-25-6	9.4	0.94	5.2	-
Bccz-5-25-7	6.3	0.63	3.5	15000000
Bccz-5-25-8	6.3	0.63	3.5	15000000
Bccz-5-25-9	6.3	0.63	3.5	-
Bccz-5-25-10	3.1	0.31	1.7	15000000
Bccz-5-25-11	3.1	0.31	1.7	15000000
Bccz-5-25-12	3.1	0.31	1.7	-
Bccz-5-30-1	20.3	2.03	11.2	654563
Bccz-5-30-2	20.3	2.03	11.2	762810
Bccz-5-30-3	20.3	2.03	11.2	-
Bccz-5-30-4	15.2	1.52	8.4	15000000
Bccz-5-30-5	15.2	1.52	8.4	15000000
Bccz-5-30-6	15.2	1.52	8.4	-
Bccz-5-30-7	10.2	1.02	5.6	15000000
Bccz-5-30-8	10.2	1.02	5.6	15000000
Bccz-5-30-9	10.2	1.02	5.6	-
Bccz-5-30-10	5.1	0.51	2.8	15000000
Bccz-5-30-11	5.1	0.51	2.8	15000000
Bccz-5-30-12	5.1	0.51	2.8	-
Bccz-7-30-1	19.5	1.95	10.7	326837
Bccz-7-30-2	19.5	1.95	10.7	440166
Bccz-7-30-3	19.5	1.95	10.7	326161
Bccz-7-30-4	14.6	1.46	8.0	3362847
Bccz-7-30-5	14.6	1.46	8.0	3331678
Bccz-7-30-6	14.6	1.46	8.0	2249586
Bccz-7-30-7	9.8	0.98	5.4	15000000
Bccz-7-30-8	9.8	0.98	5.4	15000000
Bccz-7-30-9	9.8	0.98	5.4	15000000
Bccz-7-30-10	4.9	0.49	2.7	15000000
Bccz-7-30-11	4.9	0.49	2.7	15000000
Bccz-7-30-12	4.9	0.49	2.7	15000000

Table C.11: AlSi10Mg specimens for fatigue test with Rhombic dodecahedron cell. The identification code of the specimens is: Celle shape - Cell size - Solid volume fraction (nominal) - Serial number

Id. code	σ_M [MPa]	σ_m [MPa]	σ_a [MPa]	N
Rhom-5-25-1	12.1	1.21	6.6	9044
Rhom-5-25-2	12.1	1.21	6.6	6480
Rhom-5-25-3	12.1	1.21	6.6	-
Rhom-5-25-4	9.0	0.9	5.0	45544
Rhom-5-25-5	9.0	0.9	5.0	45031
Rhom-5-25-6	9.0	0.9	5.0	-
Rhom-5-25-7	6.0	0.6	3.3	291522
Rhom-5-25-8	6.0	0.6	3.3	274062
Rhom-5-25-9	6.0	0.6	3.3	-
Rhom-5-25-10	3.0	0.3	1.7	15000000
Rhom-5-25-11	3.0	0.3	1.7	15000000
Rhom-5-25-12	3.0	0.3	1.7	-
Rhom-5-30-1	17.1	1.71	9.4	12100
Rhom-5-30-2	17.1	1.71	9.4	10947
Rhom-5-30-3	17.1	1.71	9.4	-
Rhom-5-30-4	12.8	1.28	7.1	47132
Rhom-5-30-5	12.8	1.28	7.1	26329
Rhom-5-30-6	12.8	1.28	7.1	-
Rhom-5-30-7	8.6	0.86	4.7	327084
Rhom-5-30-8	8.6	0.86	4.7	307454
Rhom-5-30-9	8.6	0.86	4.7	-
Rhom-5-30-10	4.3	0.43	2.4	15000000
Rhom-5-30-11	4.3	0.43	2.4	3755825
Rhom-5-30-12	4.3	0.43	2.4	-
Rhom-7-30-1	17.7	1.77	9.7	4281
Rhom-7-30-2	17.7	1.77	9.7	3281
Rhom-7-30-3	17.7	1.77	9.7	3970
Rhom-7-30-4	13.3	1.33	7.3	14484
Rhom-7-30-5	13.3	1.33	7.3	12010
Rhom-7-30-6	13.3	1.33	7.3	10550
Rhom-7-30-7	8.9	0.89	4.9	53097
Rhom-7-30-8	8.9	0.89	4.9	46449
Rhom-7-30-9	8.9	0.89	4.9	46723
Rhom-7-30-10	4.4	0.44	2.4	1471143
Rhom-7-30-11	4.4	0.44	2.4	2004674
Rhom-7-30-12	4.4	0.44	2.4	-

Table C.12: AlSi10Mg specimens for fatigue test with Octet-truss cell. The identification code of the specimens is: Celle shape - Cell size - Solid volume fraction (nominal) - Serial number

Id. code	σ_M [MPa]	σ_m [MPa]	σ_a [MPa]	N
Oct-5-25-1	18.5	1.85	10.2	18568
Oct-5-25-2	18.5	1.85	10.2	36394
Oct-5-25-3	18.5	1.85	10.2	-
Oct-5-25-4	13.9	1.39	7.6	128641
Oct-5-25-5	13.9	1.39	7.6	151236
Oct-5-25-6	13.9	1.39	7.6	-
Oct-5-25-7	9.3	0.93	5.1	971841
Oct-5-25-8	9.3	0.93	5.1	1119612
Oct-5-25-9	9.3	0.93	5.1	-
Oct-5-25-10	4.6	0.46	2.5	15000000
Oct-5-25-11	4.6	0.46	2.5	15000000
Oct-5-25-12	4.6	0.46	2.5	-
Oct-5-30-1	22.7	2.27	12.5	64099
Oct-5-30-2	22.7	2.27	12.5	52684
Oct-5-30-3	22.7	2.27	12.5	-
Oct-5-30-4	17.0	1.70	9.3	239878
Oct-5-30-5	17.0	1.70	9.3	234151
Oct-5-30-6	17.0	1.70	9.3	-
Oct-5-30-7	11.3	1.13	6.2	880174
Oct-5-30-8	11.3	1.13	6.2	645908
Oct-5-30-9	11.3	1.13	6.2	-
Oct-5-30-10	5.7	0.57	3.1	15000000
Oct-5-30-11	5.7	0.57	3.1	15000000
Oct-5-30-12	5.7	0.57	3.1	-
Oct-7-30-1	22.9	2.29	12.6	10607
Oct-7-30-2	22.9	2.29	12.6	9009
Oct-7-30-3	22.9	2.29	12.6	25343
Oct-7-30-4	17.2	1.72	9.4	42201
Oct-7-30-5	17.2	1.72	9.4	68178
Oct-7-30-6	17.2	1.72	9.4	35084
Oct-7-30-7	11.5	1.15	6.3	136536
Oct-7-30-8	11.5	1.15	6.3	86464
Oct-7-30-9	11.5	1.15	6.3	204722
Oct-7-30-10	5.7	0.57	3.1	3108586
Oct-7-30-11	5.7	0.57	3.1	-
Oct-7-30-12	5.7	0.57	3.1	-

Appendix D

Graphs

This section contains all the data on the specimens produced results of the mechanical tests carried out.

D.1 AlSi10Mg specimens for uniaxial compression test

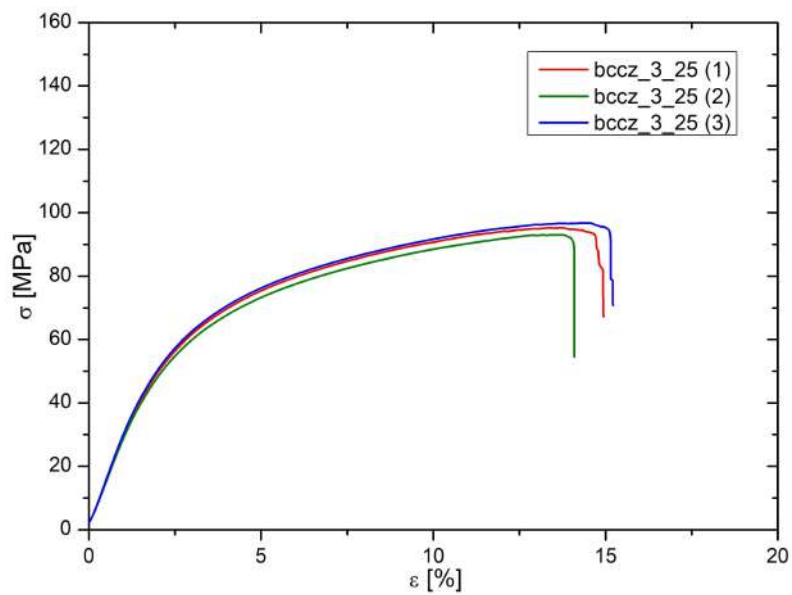


Figure D.1: Stress-strain curves of compression test of Bccz-3-25 specimens.

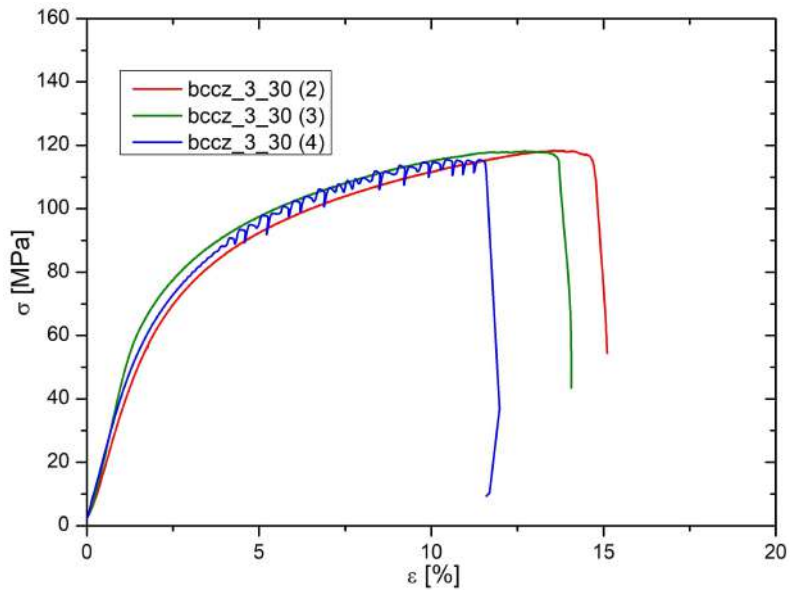


Figure D.2: Stress-strain curves of compression test of Bccz-3-30 specimens.

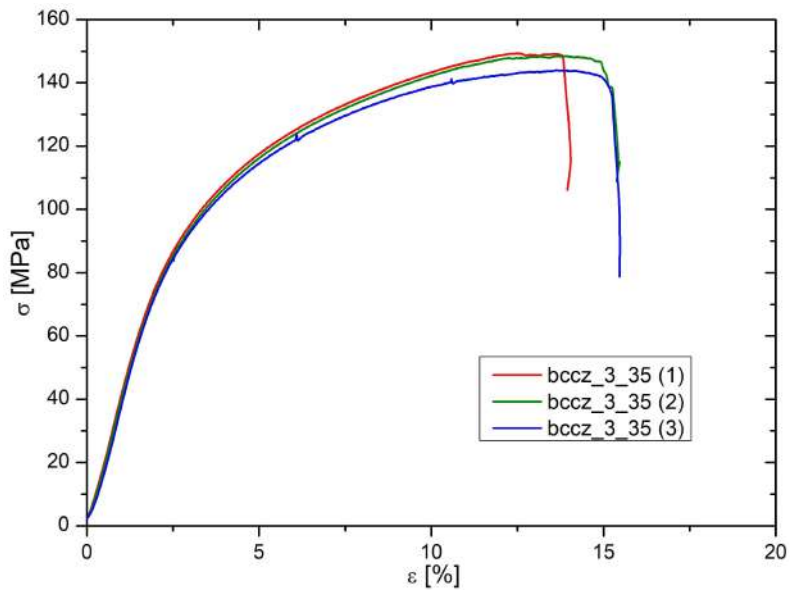


Figure D.3: Stress-strain curves of compression test of Bccz-3-35 specimens.

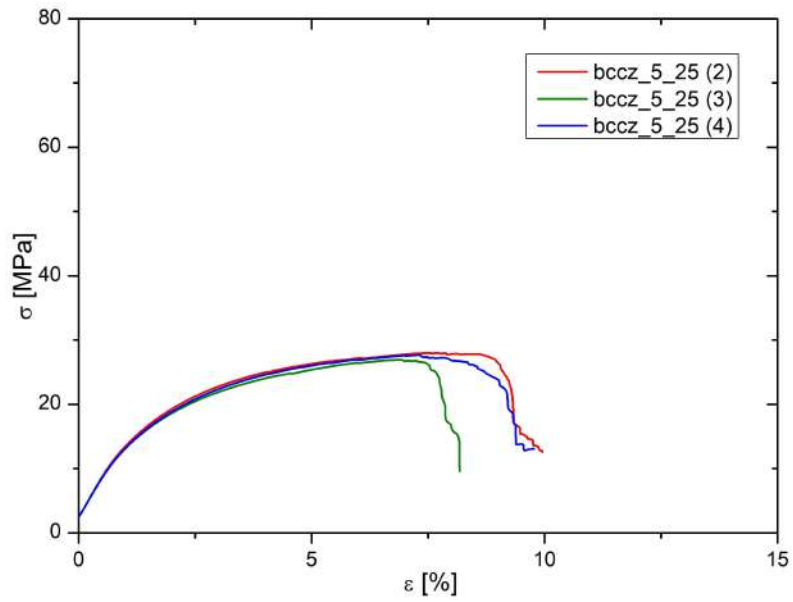


Figure D.4: Stress-strain curves of compression test of Bccz-5-25 specimens.

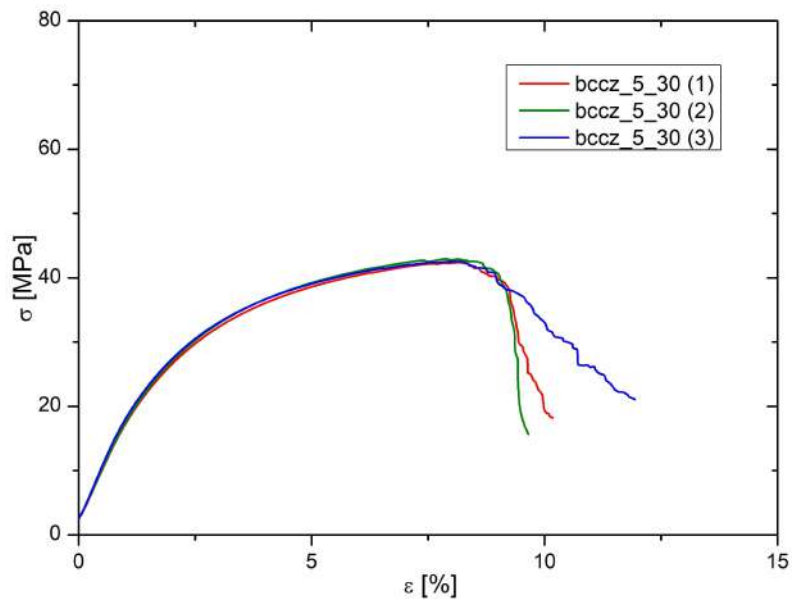


Figure D.5: Stress-strain curves of compression test of Bccz-5-30 specimens.

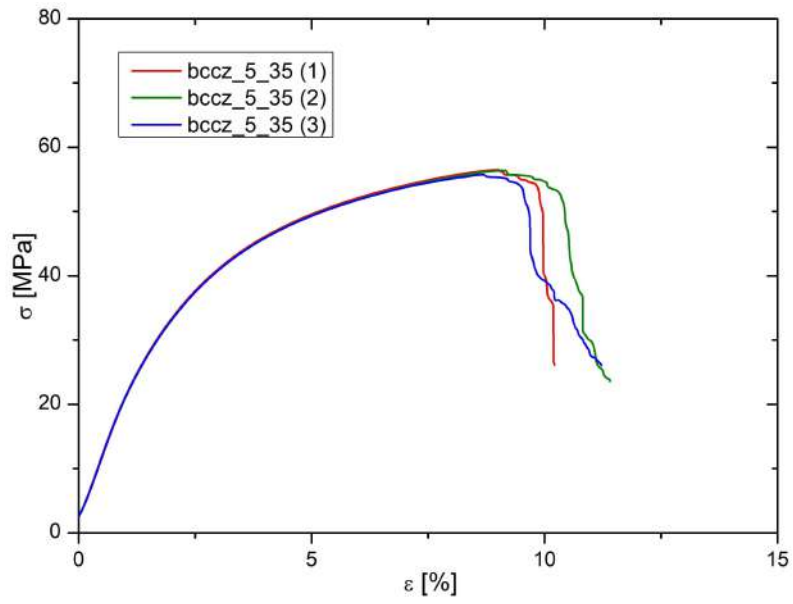


Figure D.6: Stress-strain curves of compression test of Bccz-5-35 specimens.

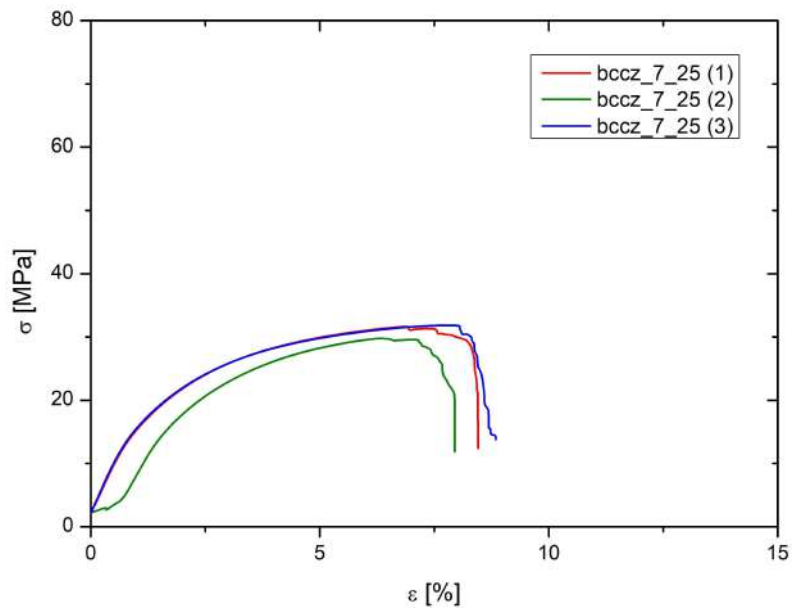


Figure D.7: Stress-strain curves of compression test of Bccz-7-25 specimens.

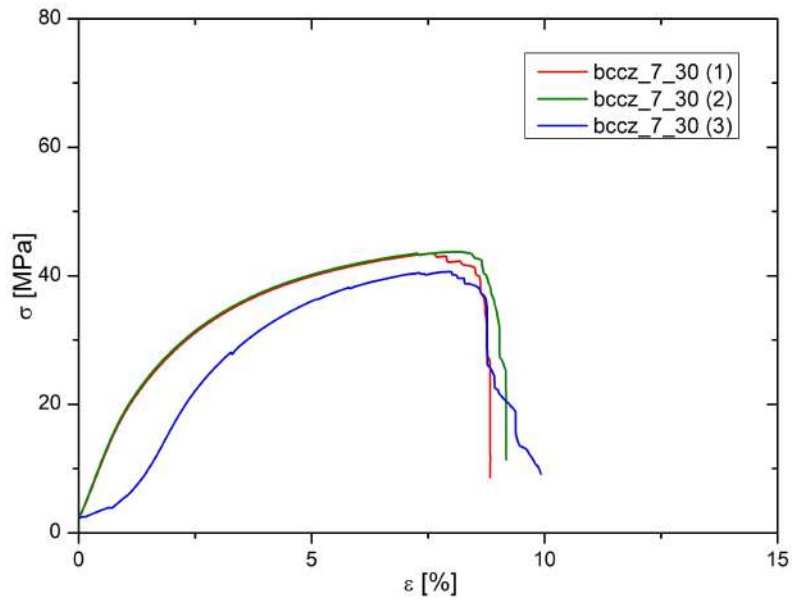


Figure D.8: Stress-strain curves of compression test of Bccz-7-30 specimens.

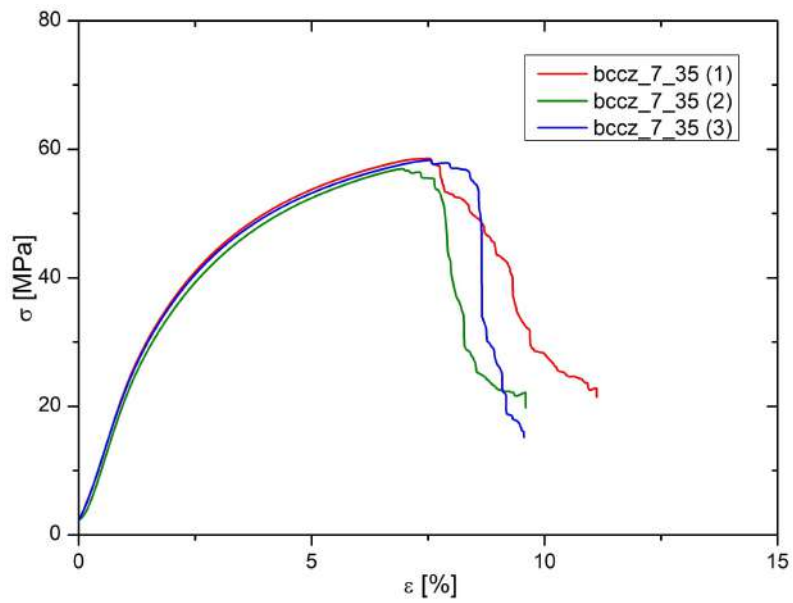


Figure D.9: Stress-strain curves of compression test of Bccz-7-35 specimens.

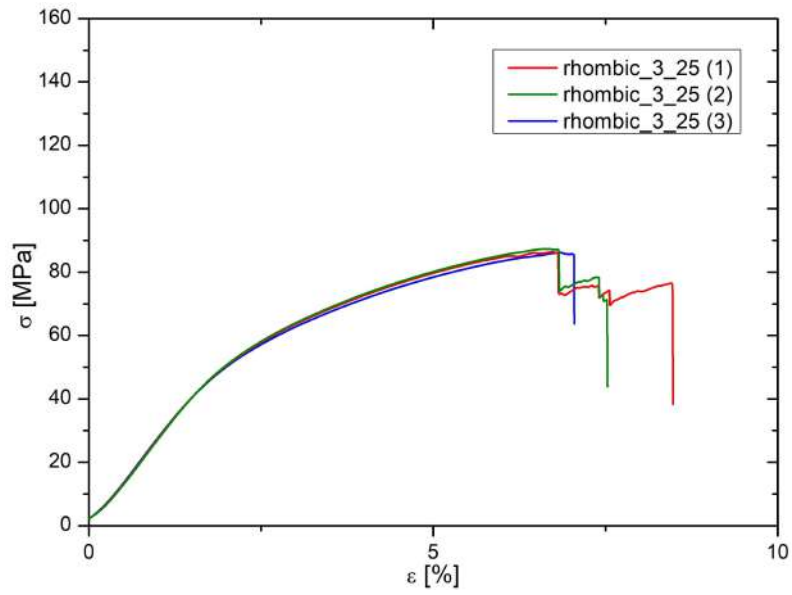


Figure D.10: Stress-strain curves of compression test of Rhom-3-25 specimens.

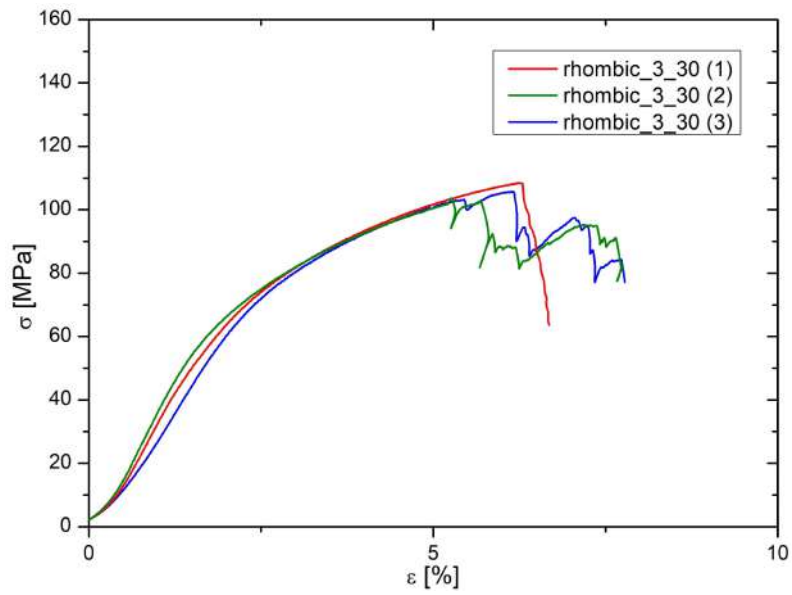


Figure D.11: Stress-strain curves of compression test of Rhom-3-30 specimens.

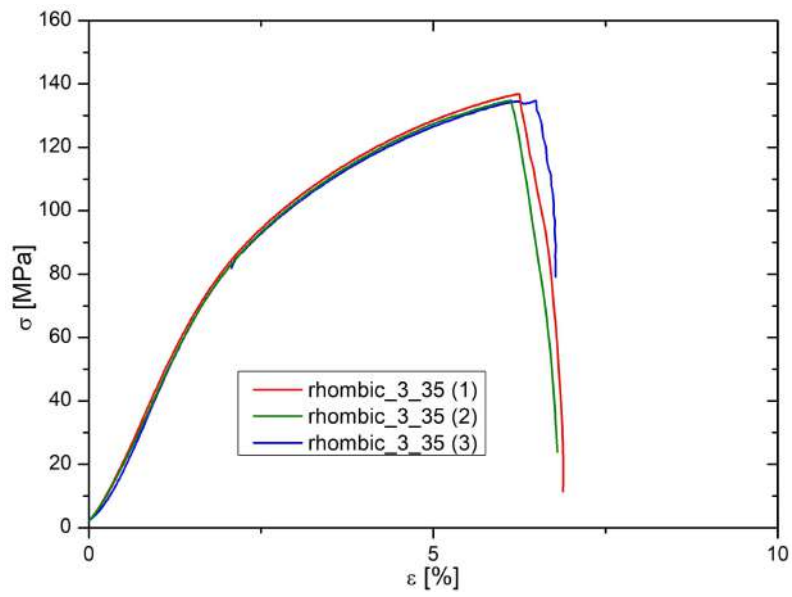


Figure D.12: Stress-strain curves of compression test of Rhom-3-35 specimens.

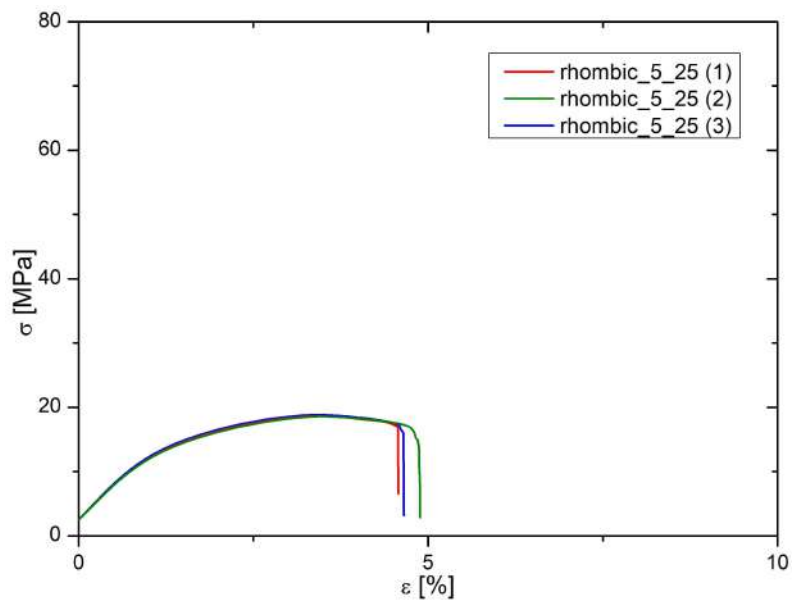


Figure D.13: Stress-strain curves of compression test of Rhom-5-25 specimens.

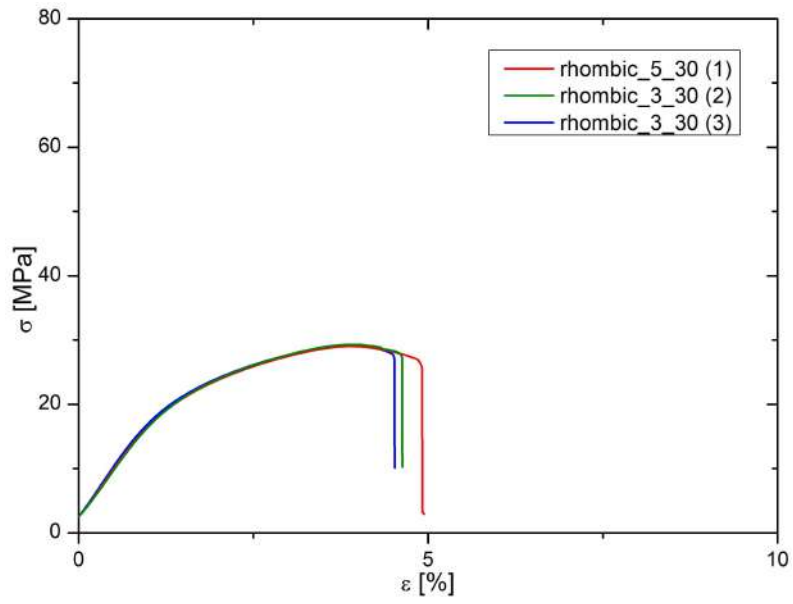


Figure D.14: Stress-strain curves of compression test of Rhom-5-30 specimens.

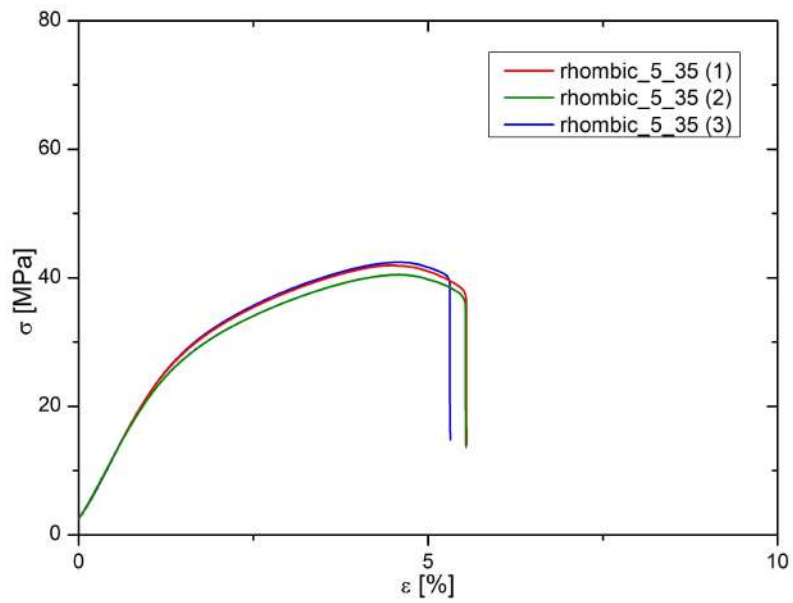


Figure D.15: Stress-strain curves of compression test of Rhom-5-35 specimens.

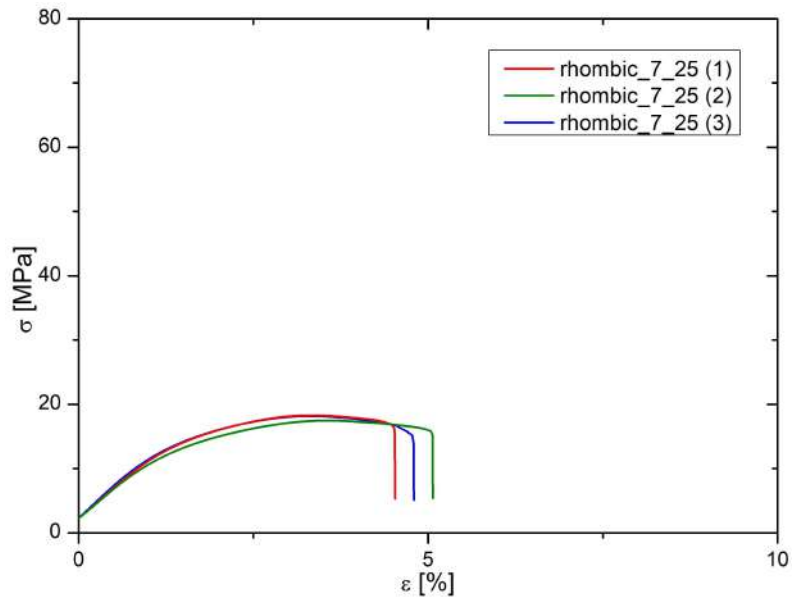


Figure D.16: Stress-strain curves of compression test of Rhom-7-25 specimens.

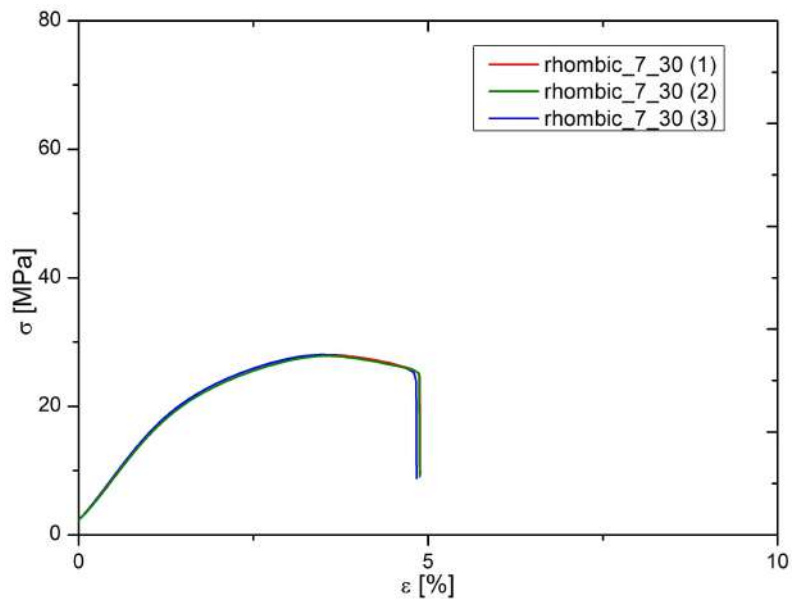


Figure D.17: Stress-strain curves of compression test of Rhom-7-30 specimens.

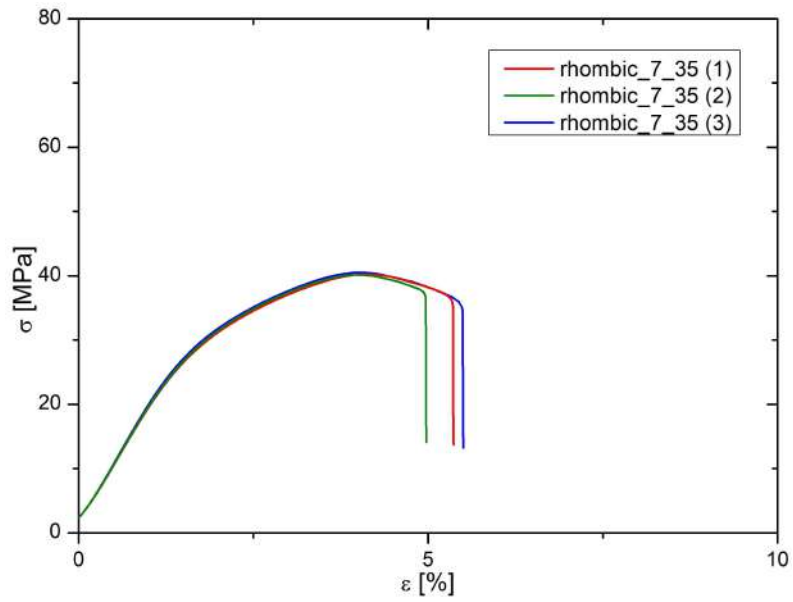


Figure D.18: Stress-strain curves of compression test of Rhom-7-35 specimens.

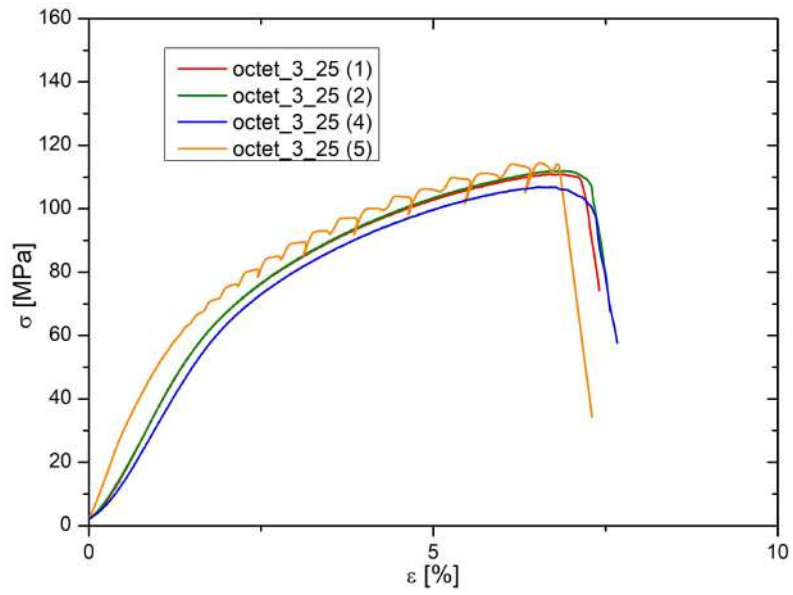


Figure D.19: Stress-strain curves of compression test of Oct-3-25 specimens.

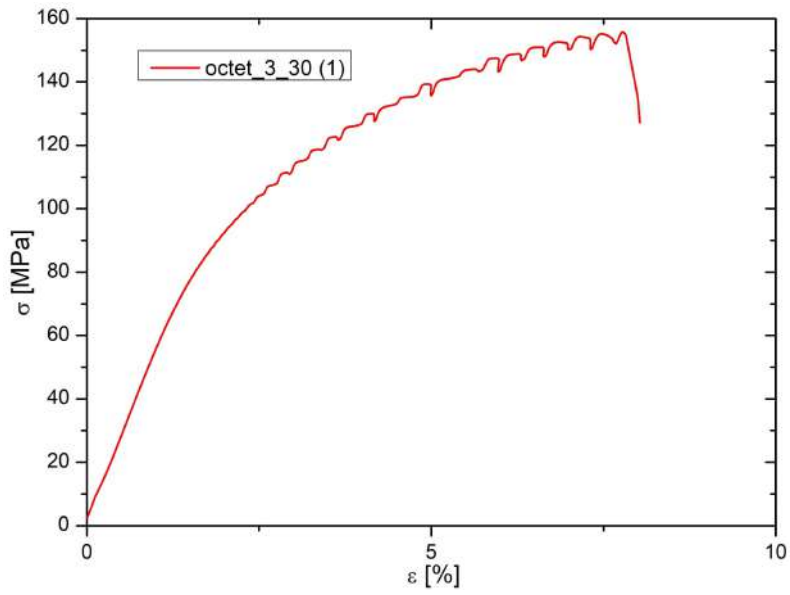


Figure D.20: Stress-strain curves of compression test of Oct-3-30 specimens.

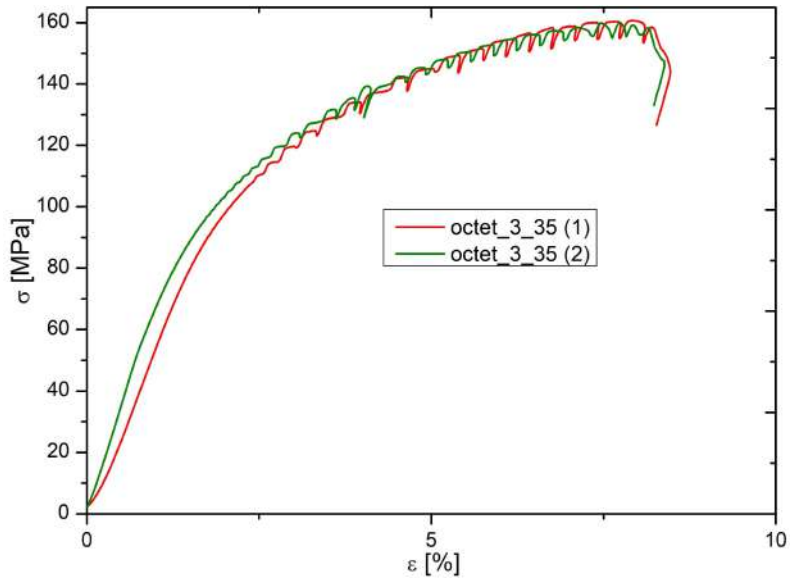


Figure D.21: Stress-strain curves of compression test of Oct-3-35 specimens.

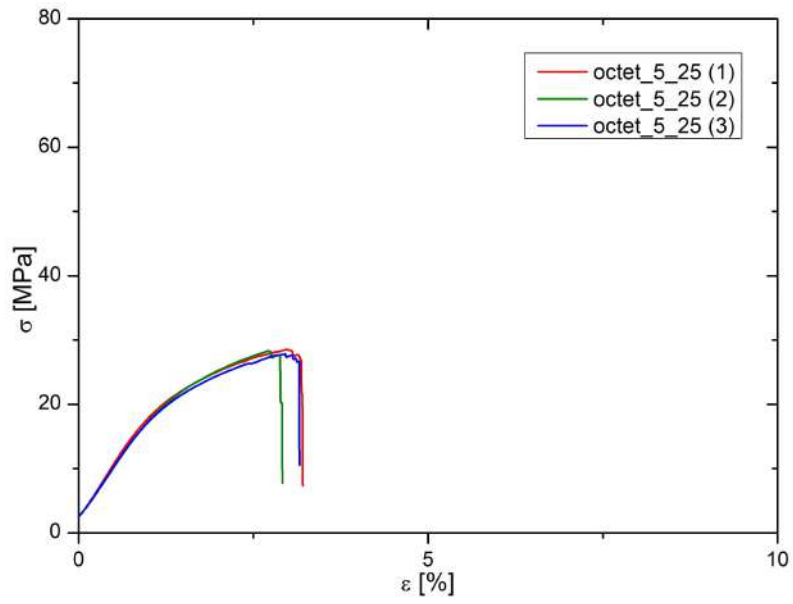


Figure D.22: Stress-strain curves of compression test of Oct-5-25 specimens.

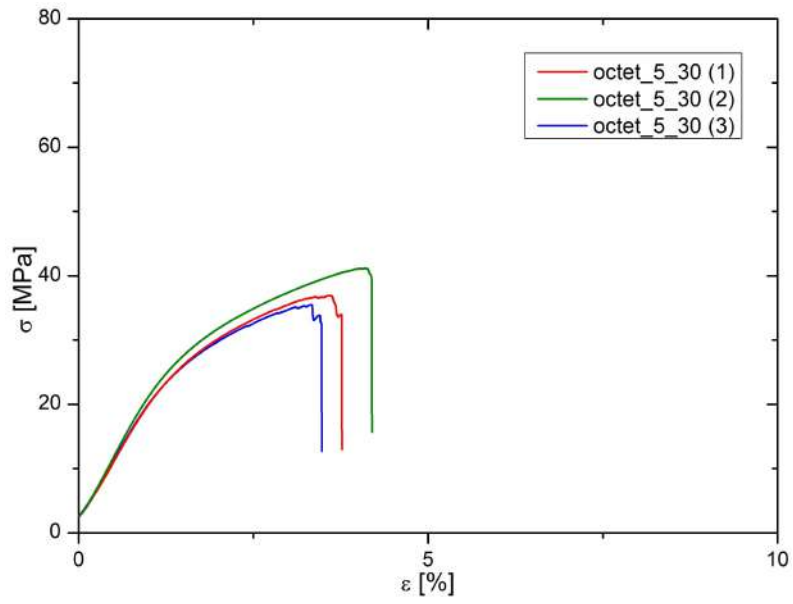


Figure D.23: Stress-strain curves of compression test of Oct-5-30 specimens.

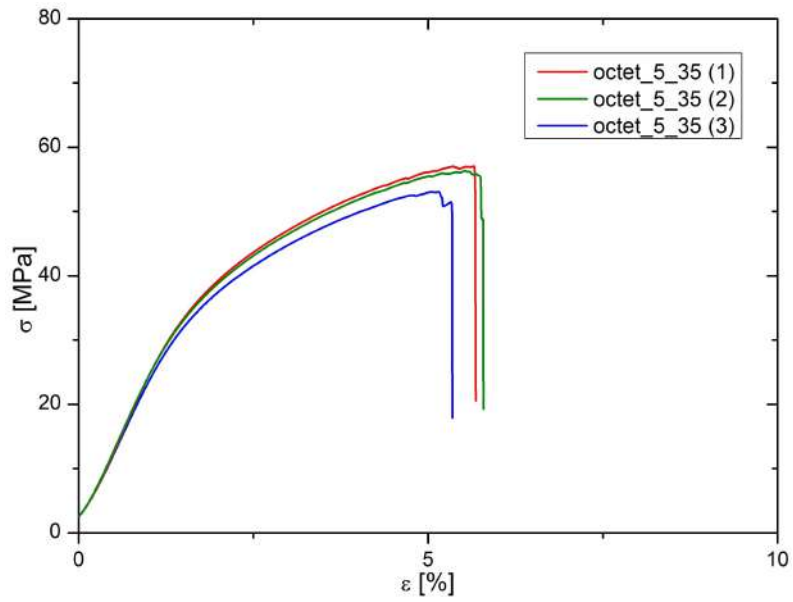


Figure D.24: Stress-strain curves of compression test of Oct-5-35 specimens.

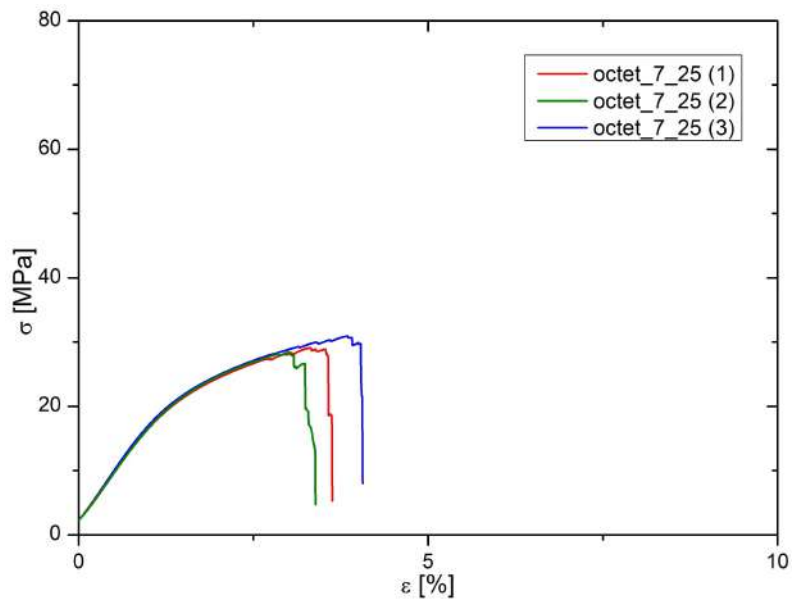


Figure D.25: Stress-strain curves of compression test of Oct-7-25 specimens.

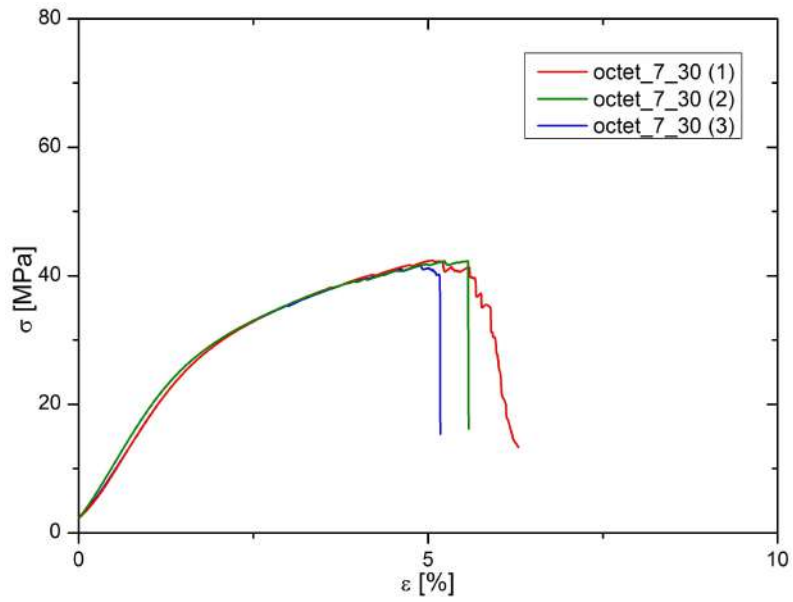


Figure D.26: Stress-strain curves of compression test of Oct-7-30 specimens.

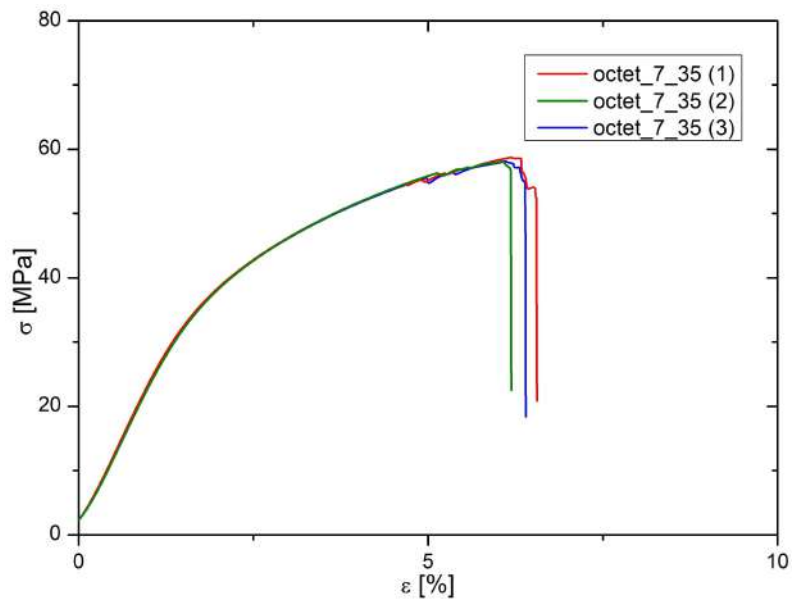


Figure D.27: Stress-strain curves of compression test of Oct-7-35 specimens.

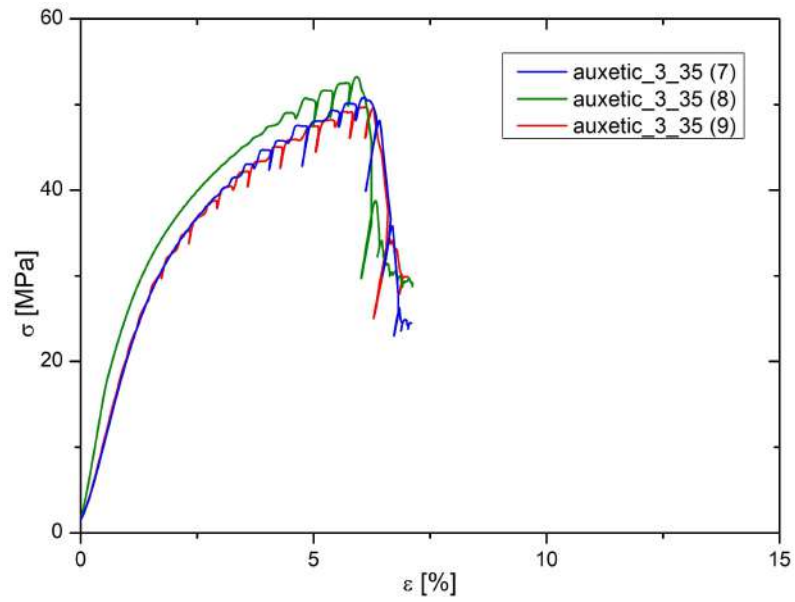


Figure D.28: Stress-strain curves of compression test of Aux-3-35 specimens.

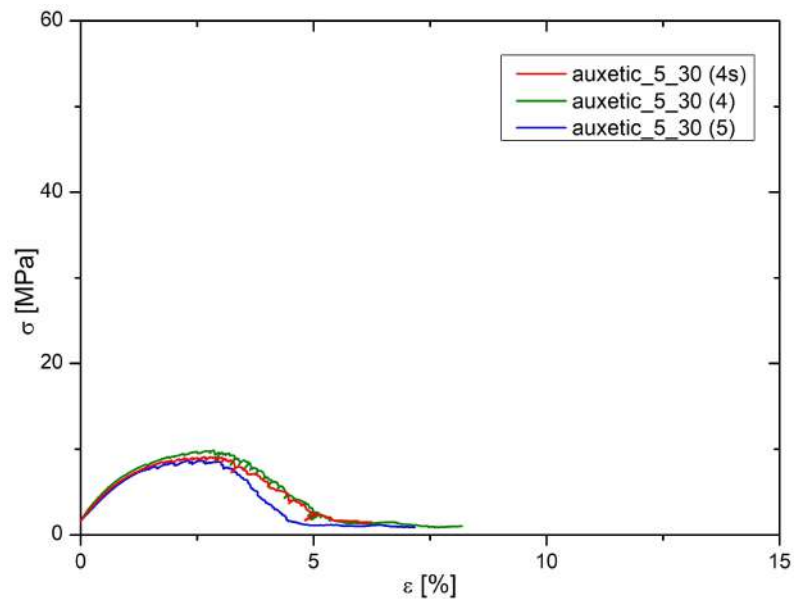


Figure D.29: Stress-strain curves of compression test of Aux-5-30 specimens.

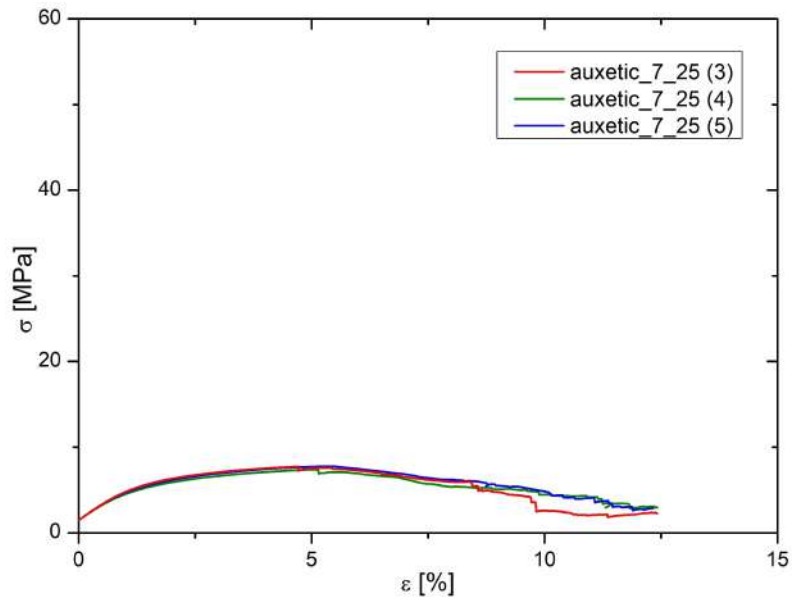


Figure D.30: Stress-strain curves of compression test of Aux-7-25 specimens.

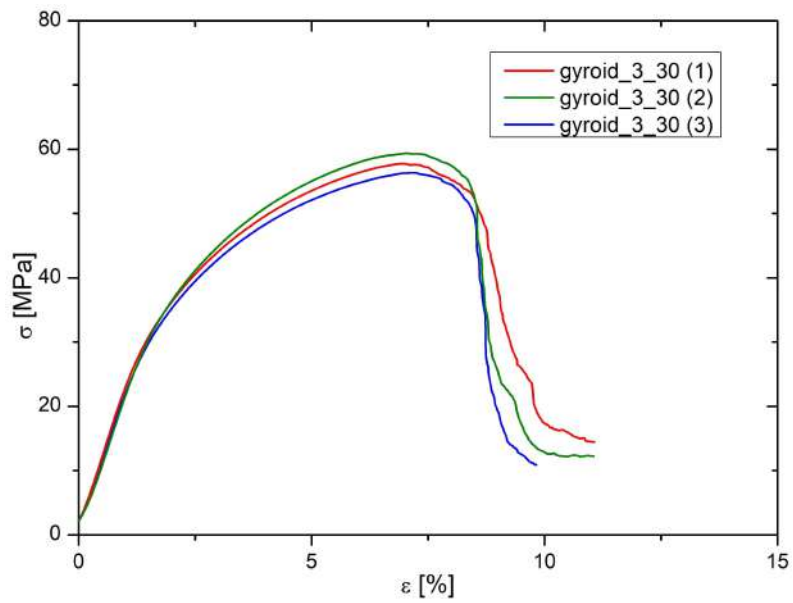


Figure D.31: Stress-strain curves of compression test of Gyr-3-30 specimens.

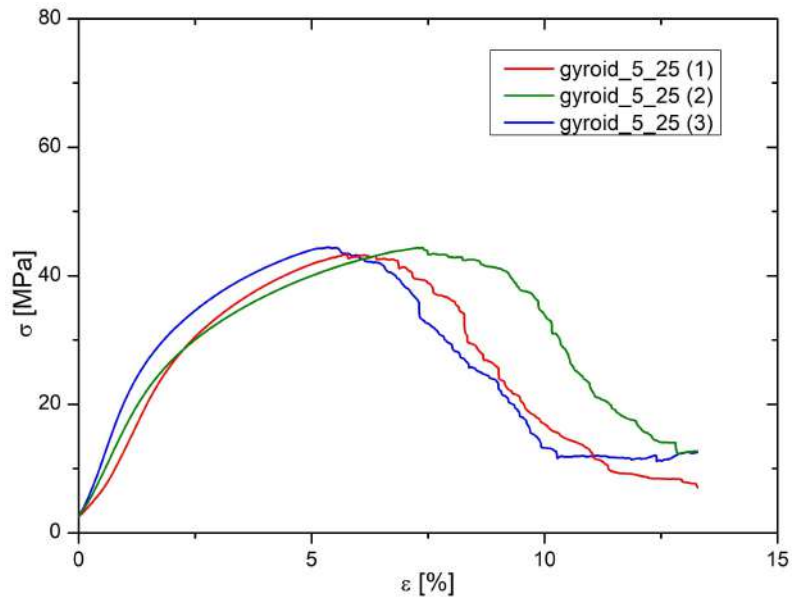


Figure D.32: Stress-strain curves of compression test of Gyr-5-25 specimens.

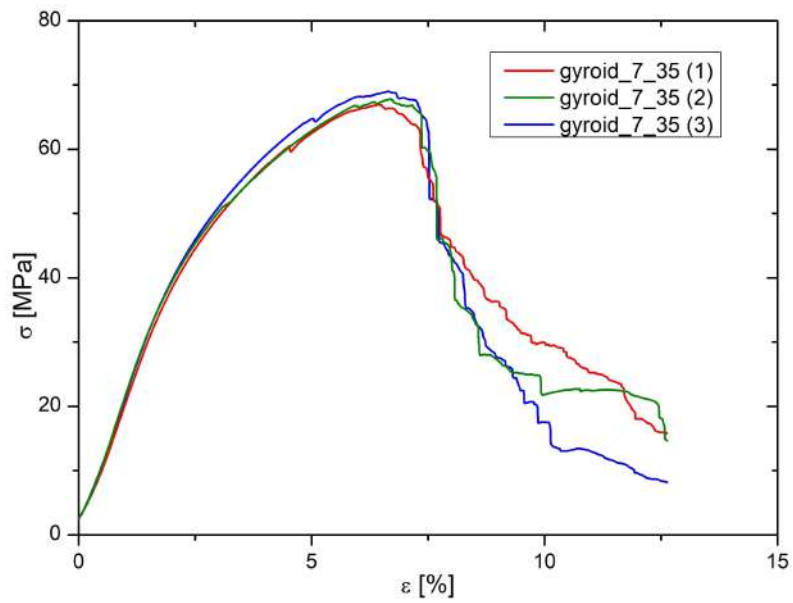


Figure D.33: Stress-strain curves of compression test of Gyr-7-35 specimens.

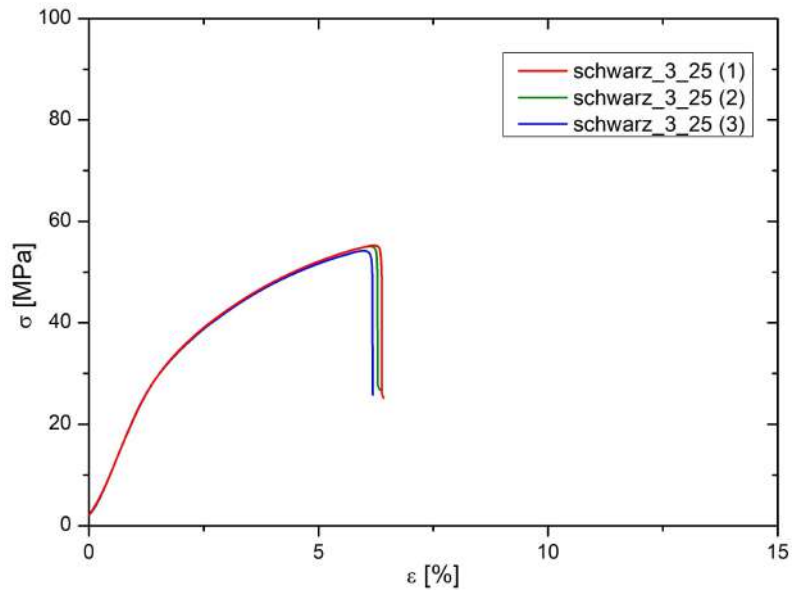


Figure D.34: Stress-strain curves of compression test of Sch-3-25 specimens.

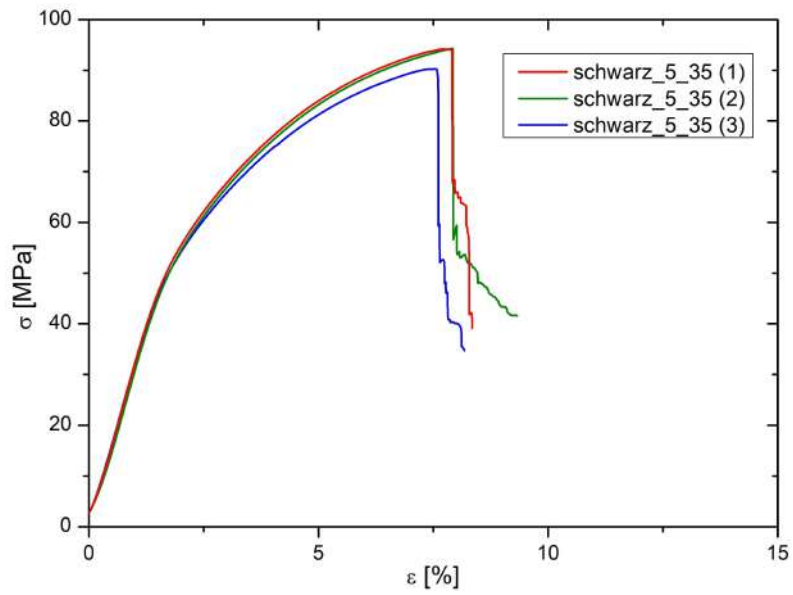


Figure D.35: Stress-strain curve of compression test of Sch-5-35 specimens.

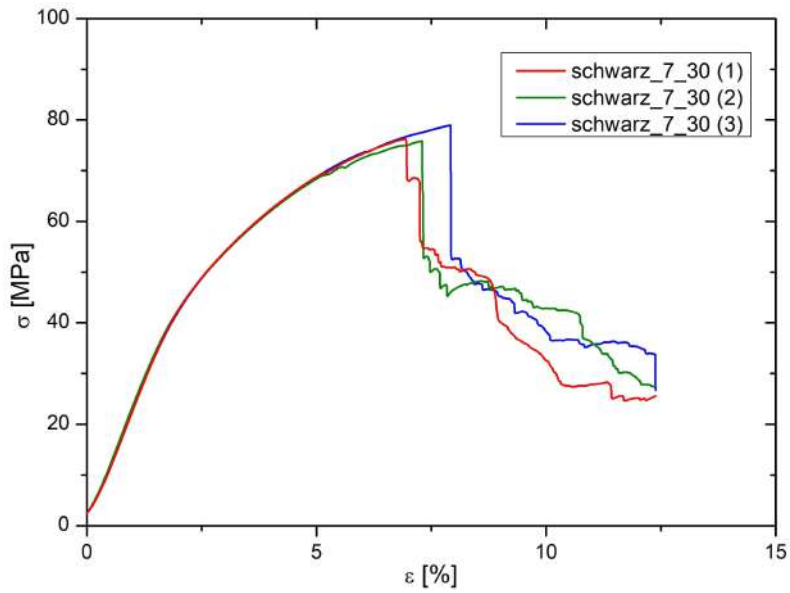


Figure D.36: Stress-strain curves of compression test of Sch-7-30 specimens.

D.2 Ti6Al4V specimens for uniaxial compression test

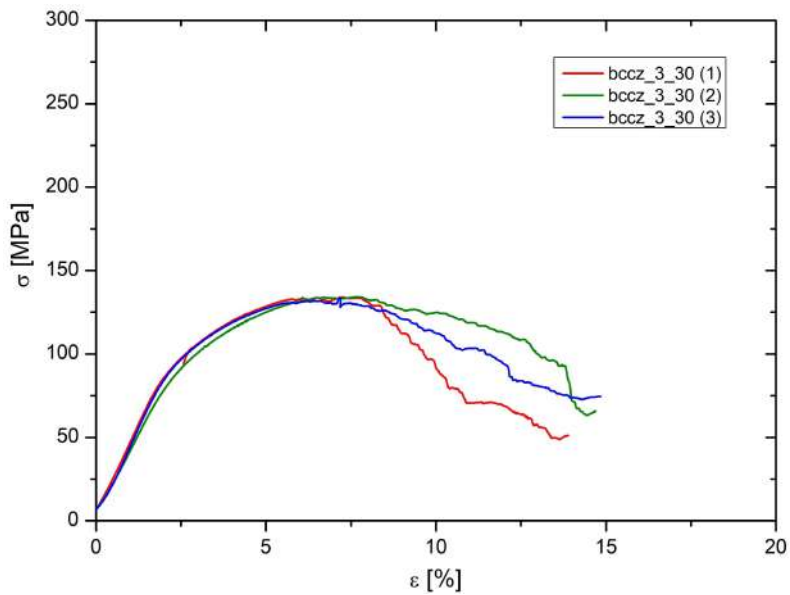


Figure D.37: Stress-strain curves of compression test of Bccz-3-30 specimens.

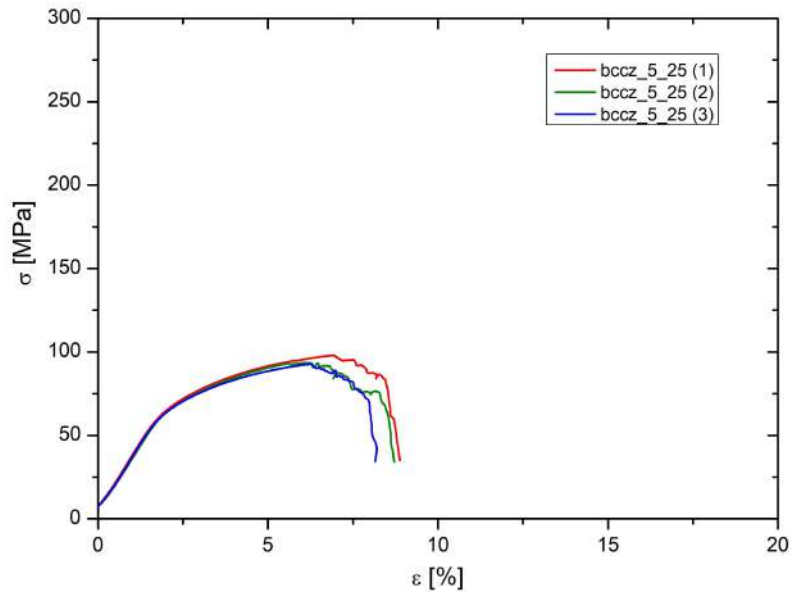


Figure D.38: Stress-strain curves of compression test of Bccz-5-25 specimens.

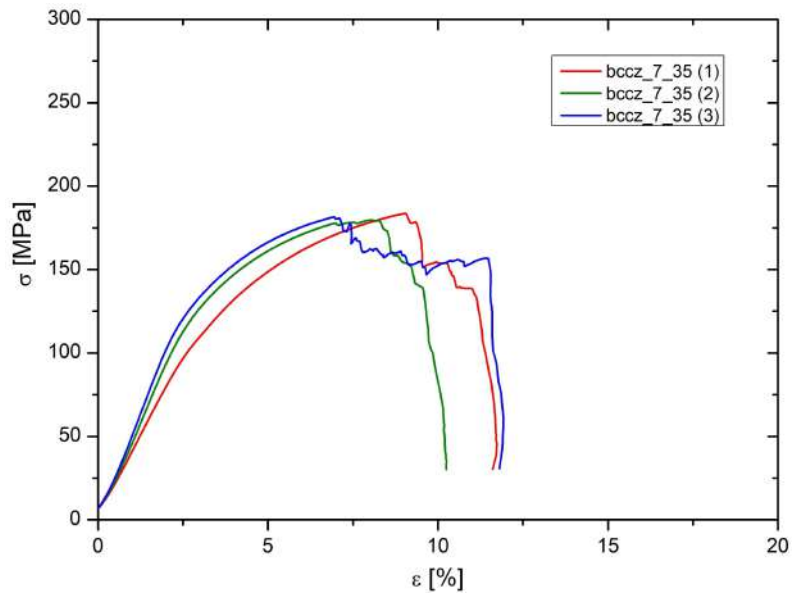


Figure D.39: Stress-strain curves of compression test of Bccz-7-35 specimens.

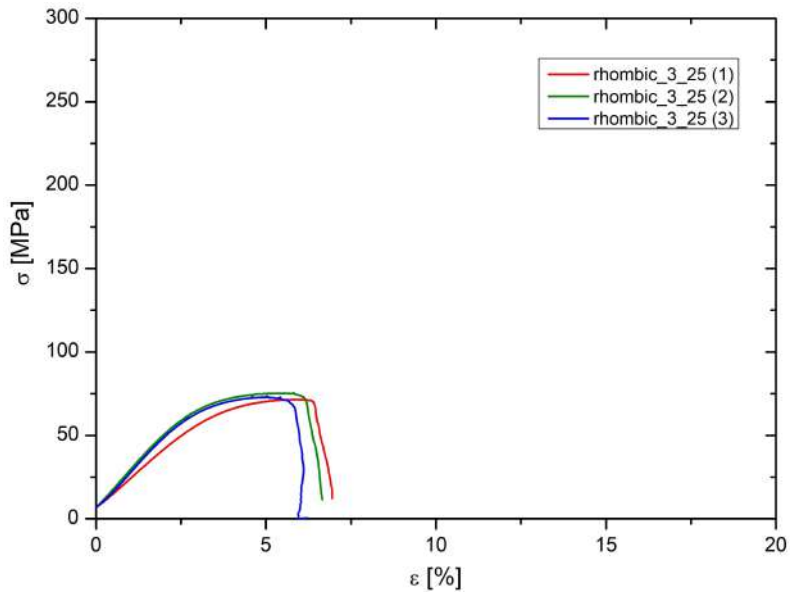


Figure D.40: Stress-strain curves of compression test of Rhom-3-25 specimens.

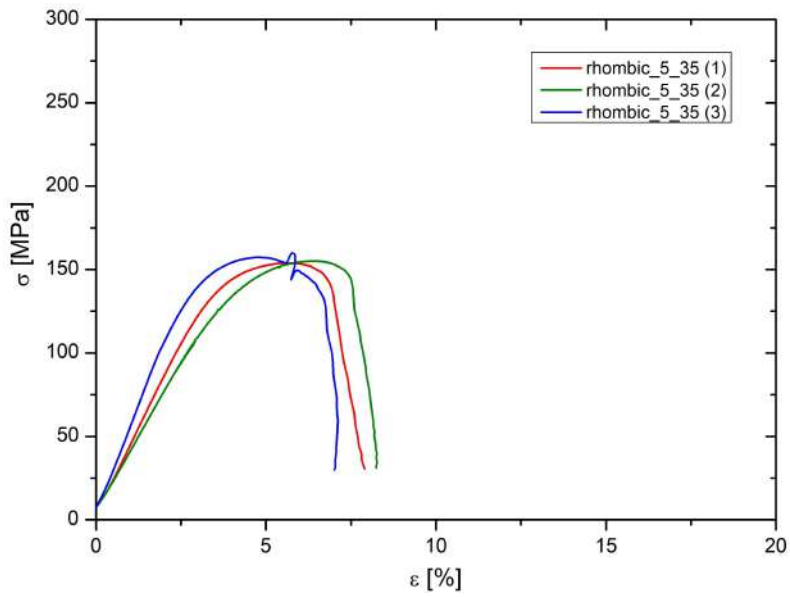


Figure D.41: Stress-strain curves of compression test of Rhom-5-35 specimens.

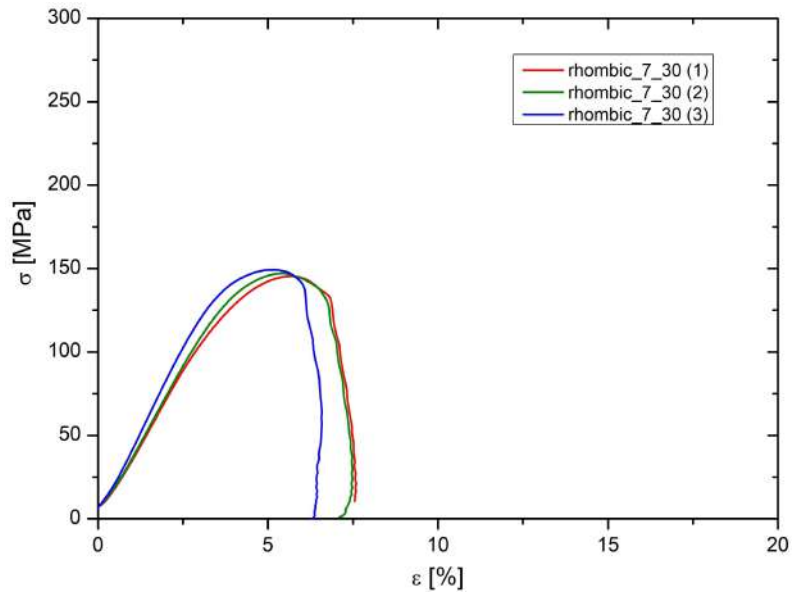


Figure D.42: Stress-strain curves of compression test of Rhom-7-30 specimens.

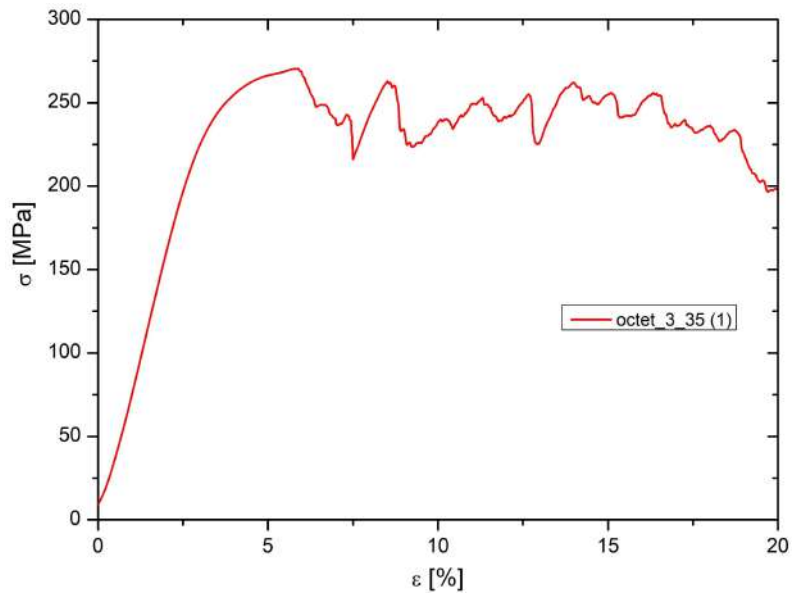


Figure D.43: Stress-strain curves of compression test of Oct-3-35 specimens.

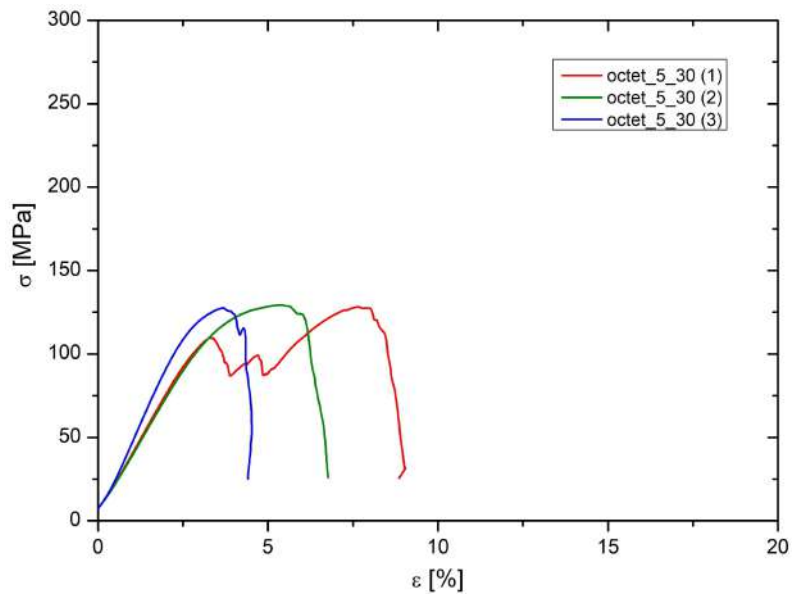


Figure D.44: Stress-strain curves of compression test of Oct-5-30 specimens.

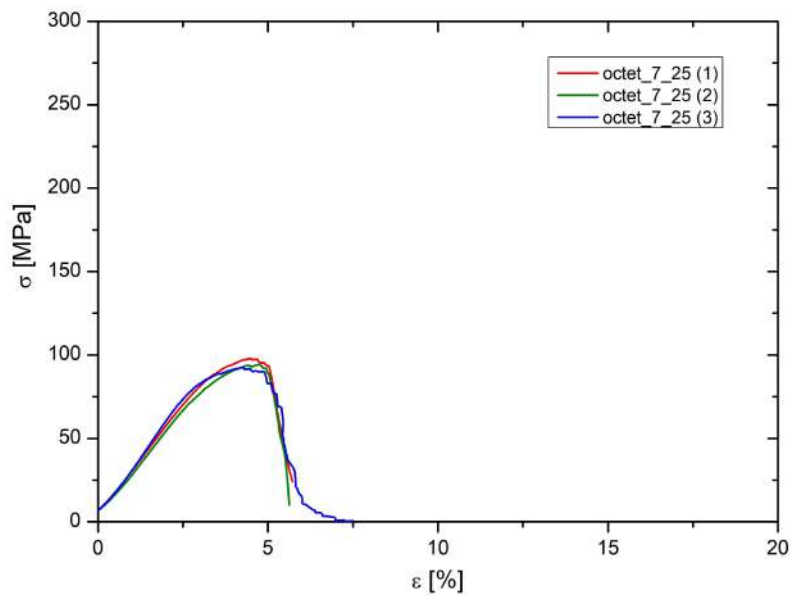


Figure D.45: Stress-strain curves of compression test of Oct-7-25 specimens.

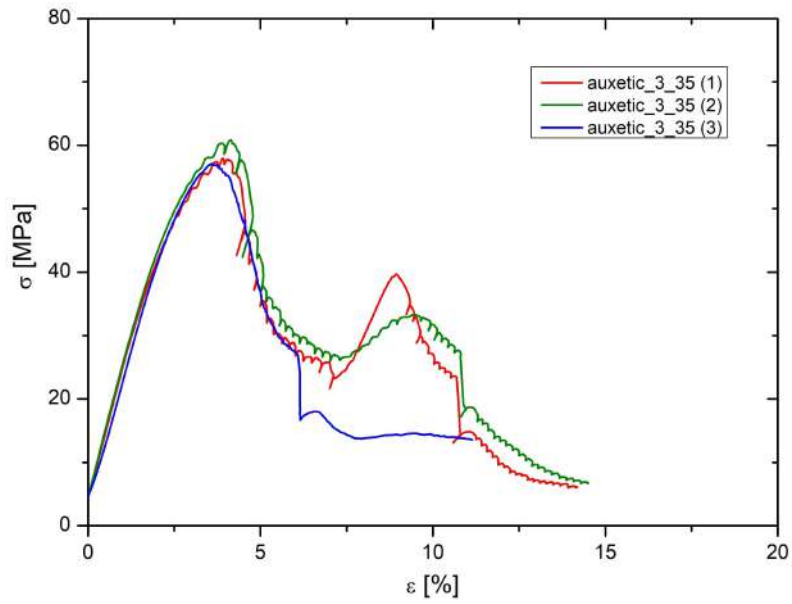


Figure D.46: Stress-strain curves of compression test of Aux-3-35 specimens.

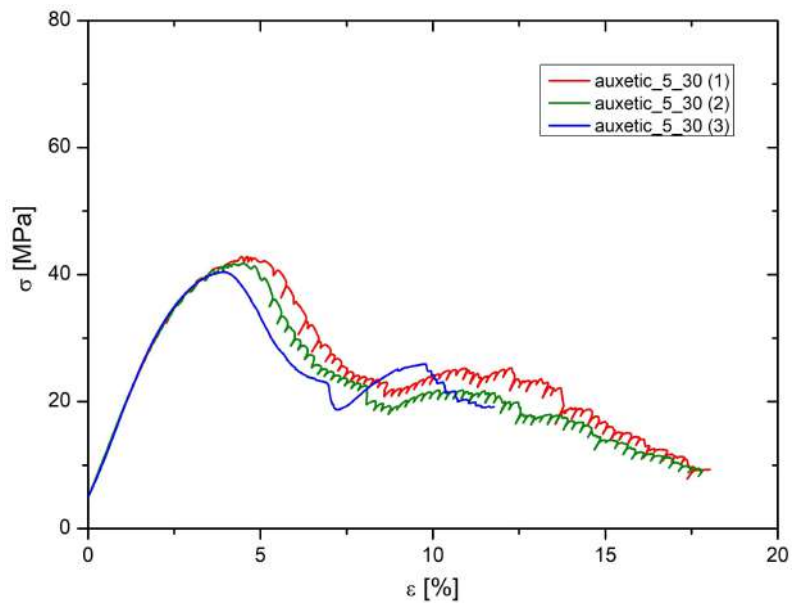


Figure D.47: Stress-strain curves of compression test of Aux-5-30 specimens.

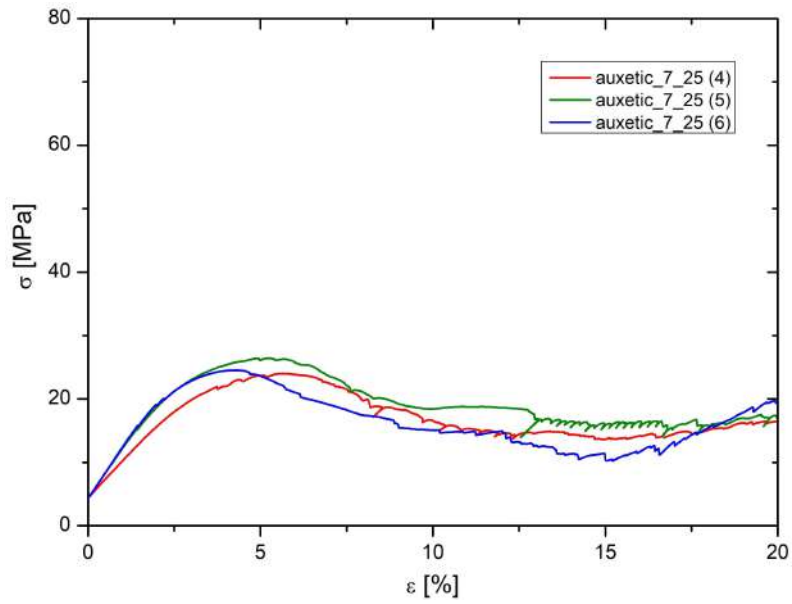


Figure D.48: Stress-strain curves of compression test of Aux-7-25 specimens.

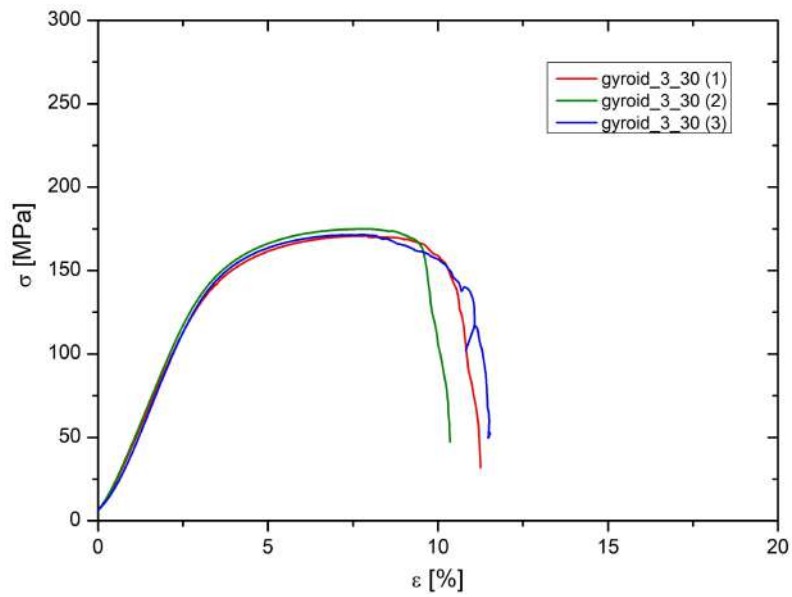


Figure D.49: Stress-strain curves of compression test of Gyr-3-30 specimens.

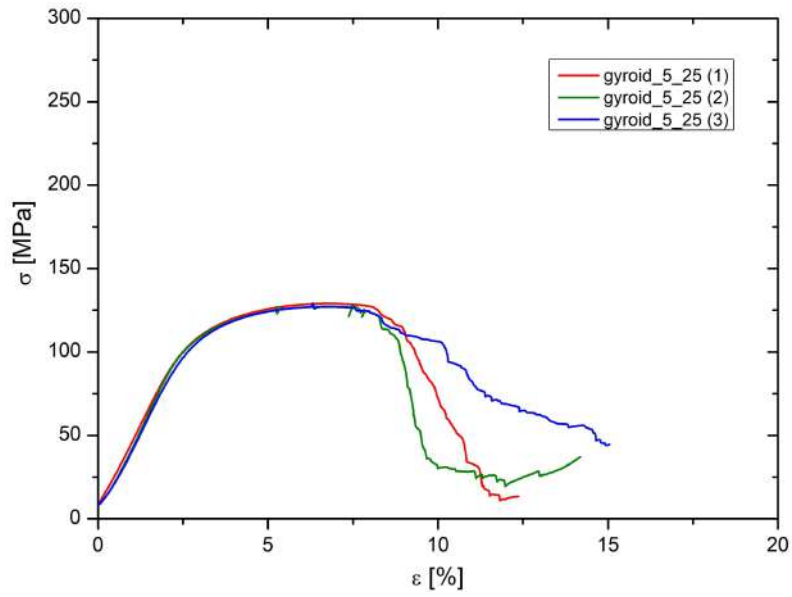


Figure D.50: Stress-strain curves of compression test of Gyr-5-25 specimens.

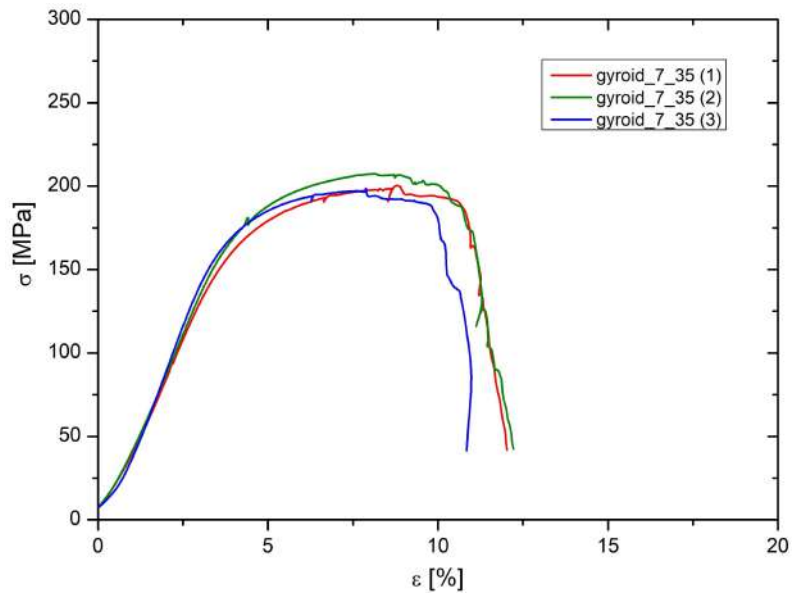


Figure D.51: Stress-strain curves of compression test of Gyr-7-35 specimens.

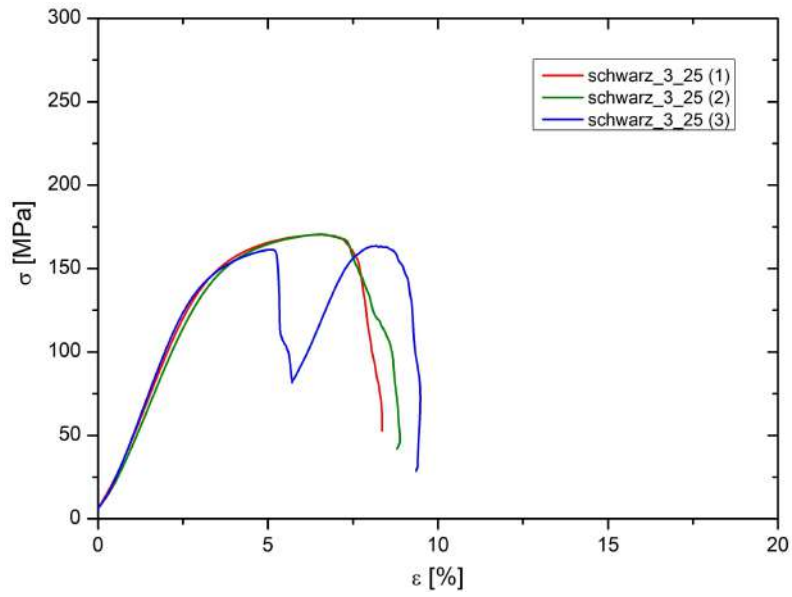


Figure D.52: Stress-strain curves of compression test of Sch-3-25 specimens.

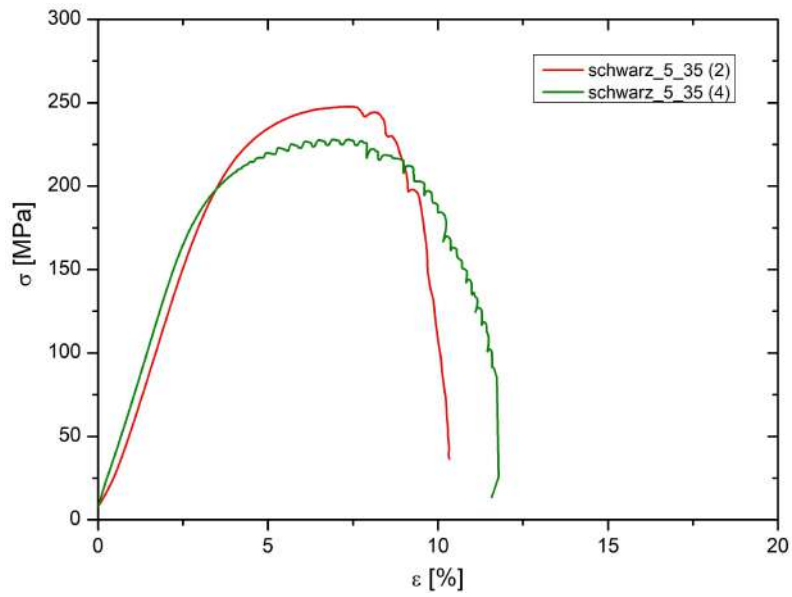


Figure D.53: Stress-strain curves of compression test of Sch-5-35 specimens.

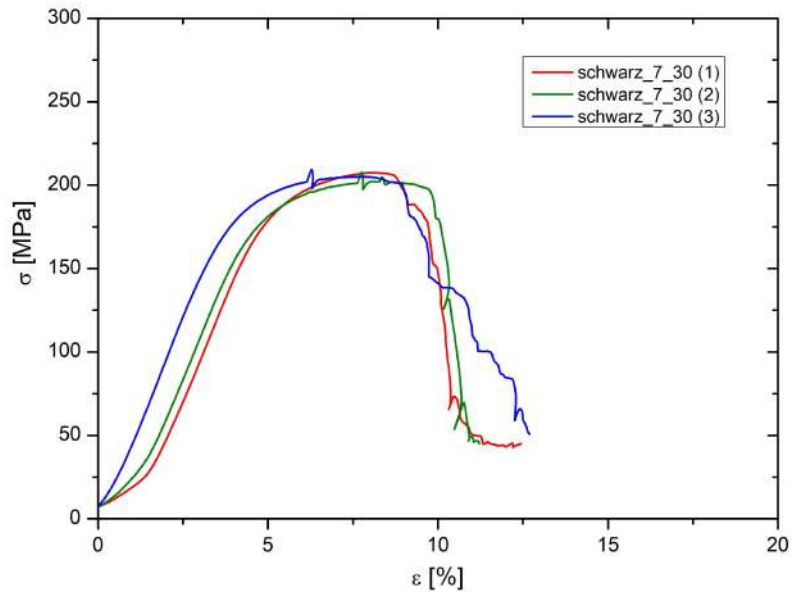


Figure D.54: Stress-strain curves of compression test of Sch-7-30 specimens.

D.3 AlSi10Mg sandwich panels for uniaxial compression test

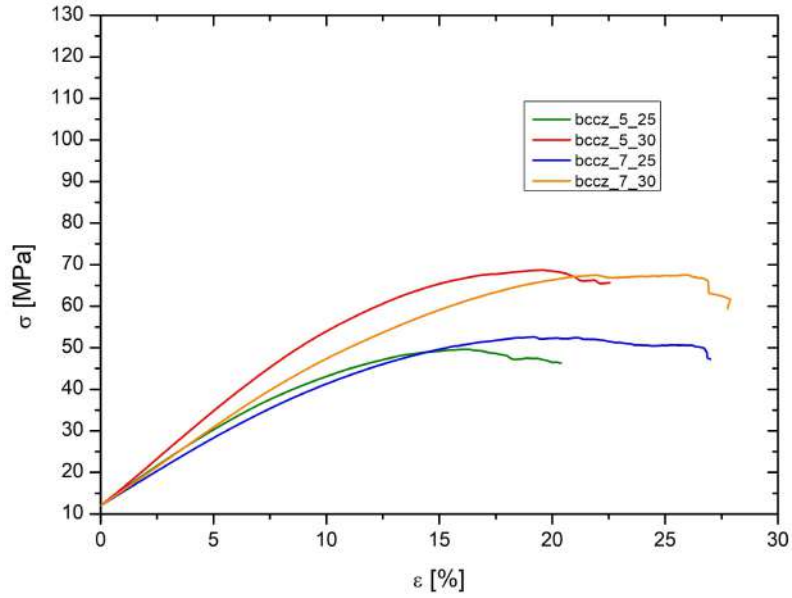


Figure D.55: Stress-strain curves of compression test of Bccz sandwich panels.

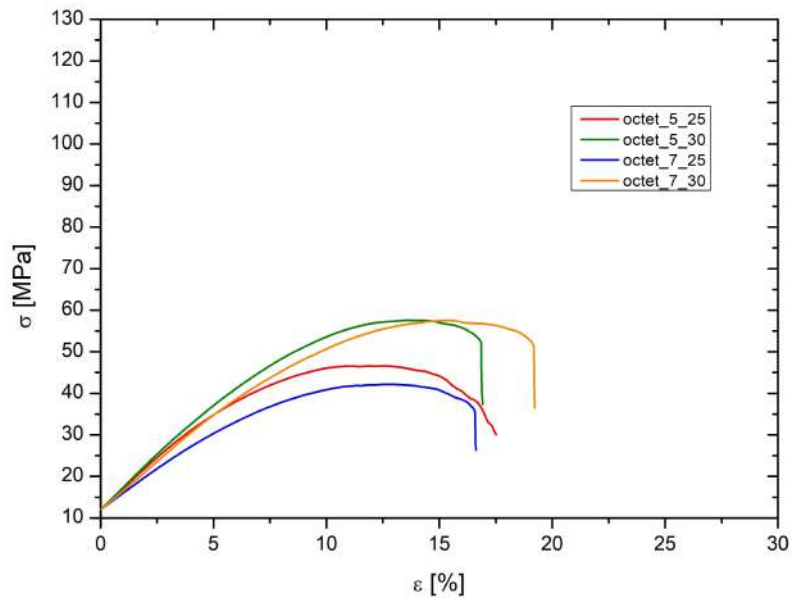


Figure D.56: Stress-strain curves of compression test of Octet-truss sandwich panels.

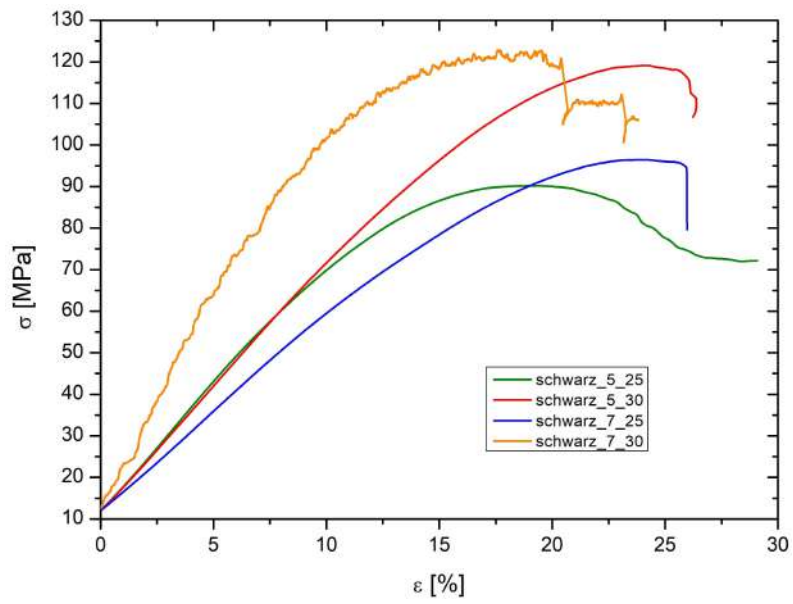


Figure D.57: Stress-strain curves of compression test of Schwartz diamond sandwich panels.

D.4 AlSi10Mg sandwich panels for bending tests

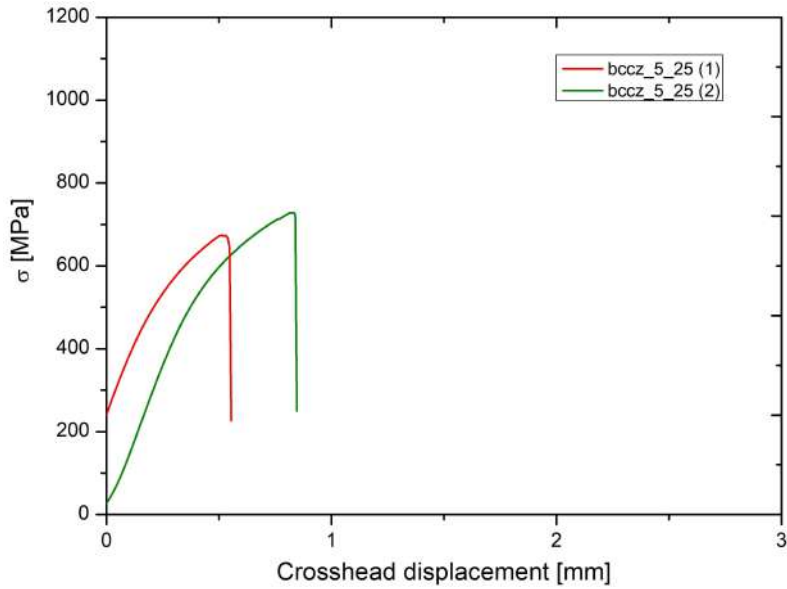


Figure D.58: σ vs crosshead displacement curves of bending test on Bccz-5-25 short sandwich panels.

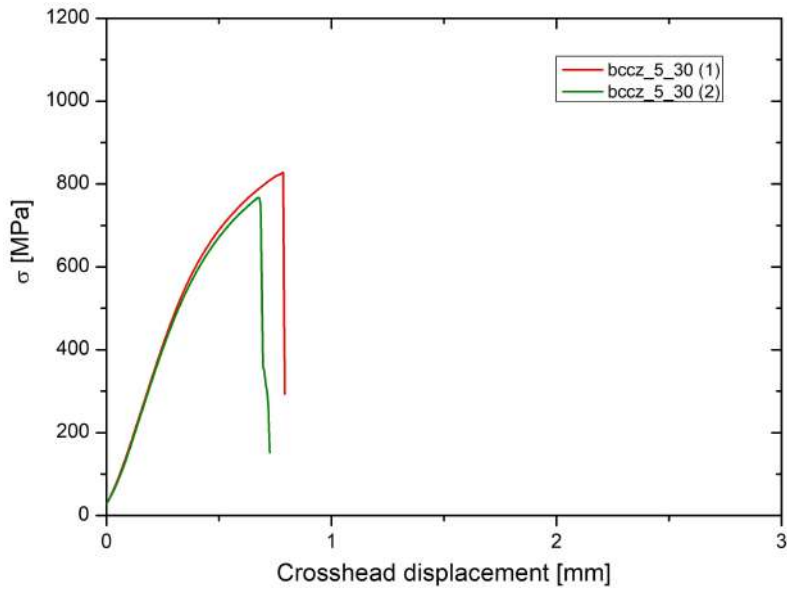


Figure D.59: σ vs crosshead displacement curves of bending test on Bccz-5-30 short sandwich panels.

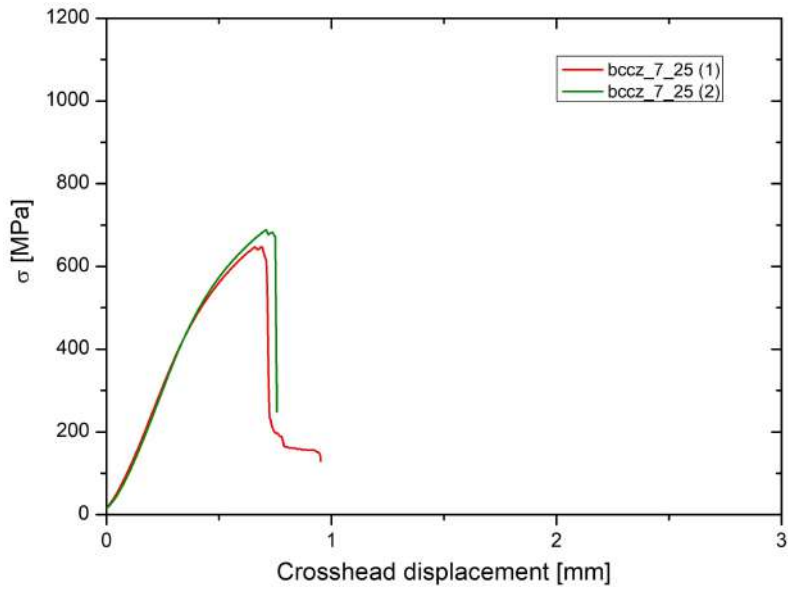


Figure D.60: σ vs crosshead displacement curves of bending test on Bccz-7-25 short sandwich panels.

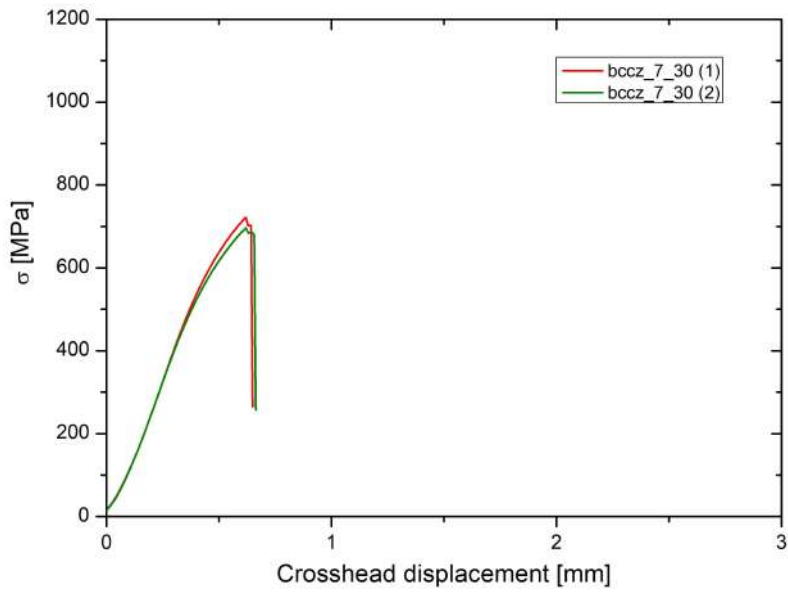


Figure D.61: σ vs crosshead displacement curves of bending test on Bccz-7-30 short sandwich panels.

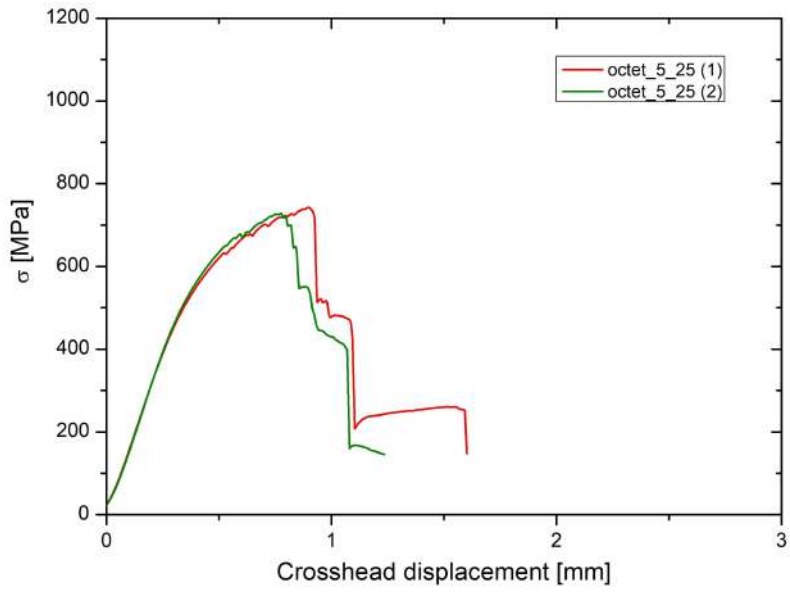


Figure D.62: σ vs crosshead displacement curves of bending test on Oct-5-25 short sandwich panels.

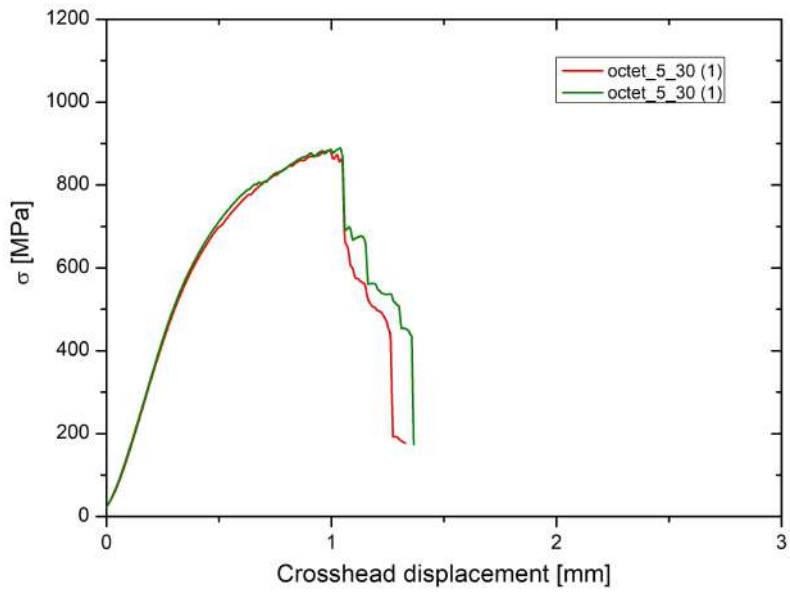


Figure D.63: σ vs crosshead displacement curves of bending test on Oct-5-30 short sandwich panels.

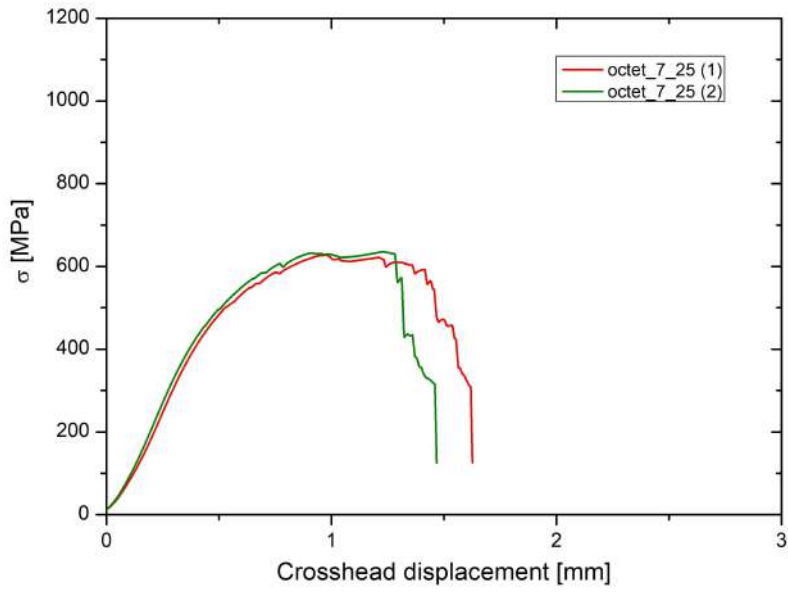


Figure D.64: σ vs crosshead displacement curves of bending test on Oct-7-25 short sandwich panels.

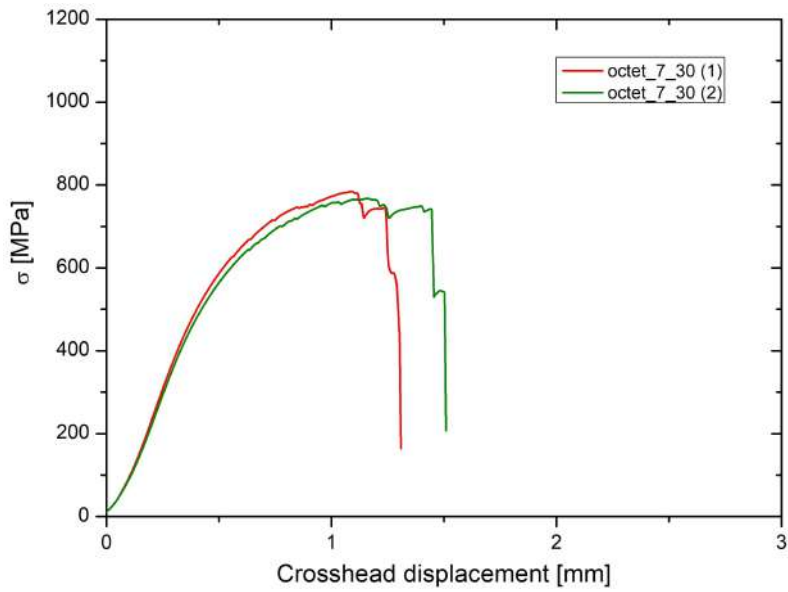


Figure D.65: σ vs crosshead displacement curves of bending test on Oct-7-30 short sandwich panels.

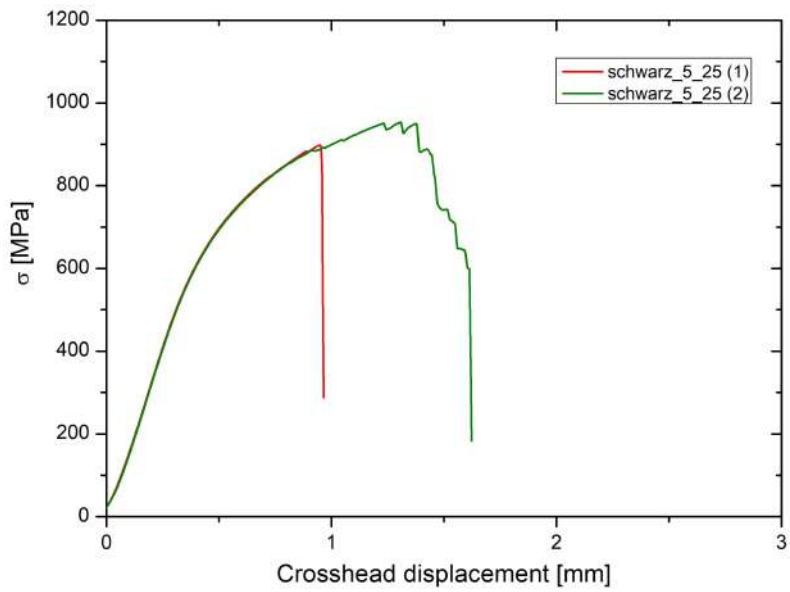


Figure D.66: σ vs crosshead displacement curves of bending test on Sch-5-25 short sandwich panels.

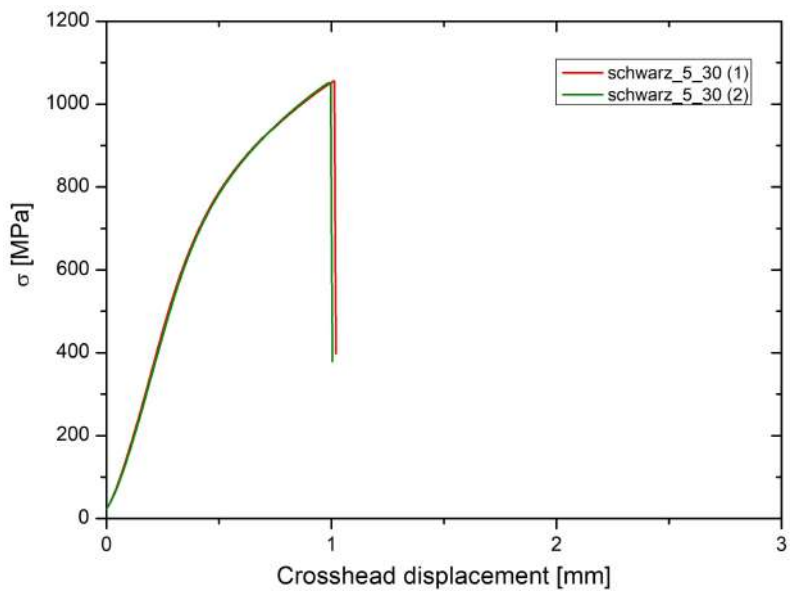


Figure D.67: σ vs crosshead displacement curves of bending test on Sch-5-30 short sandwich panels.

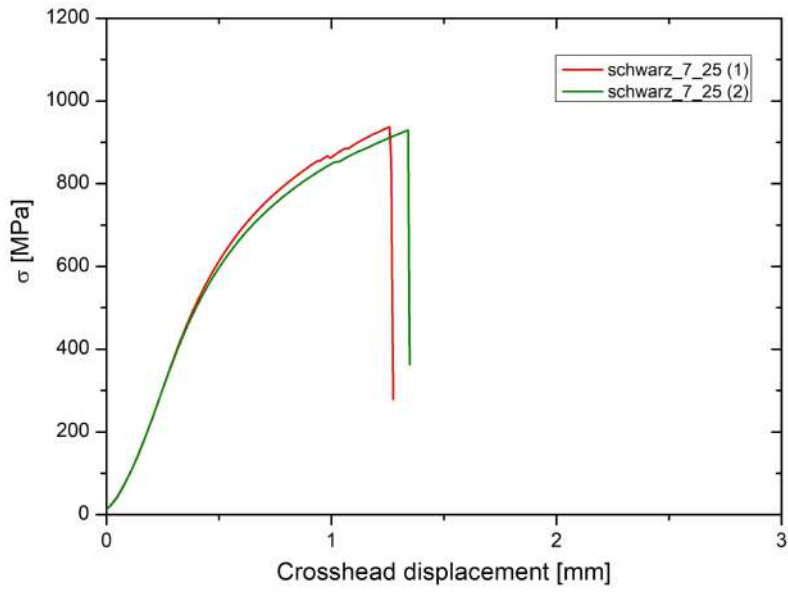


Figure D.68: σ vs crosshead displacement curves of bending test on Sch-7-25 short sandwich panels.

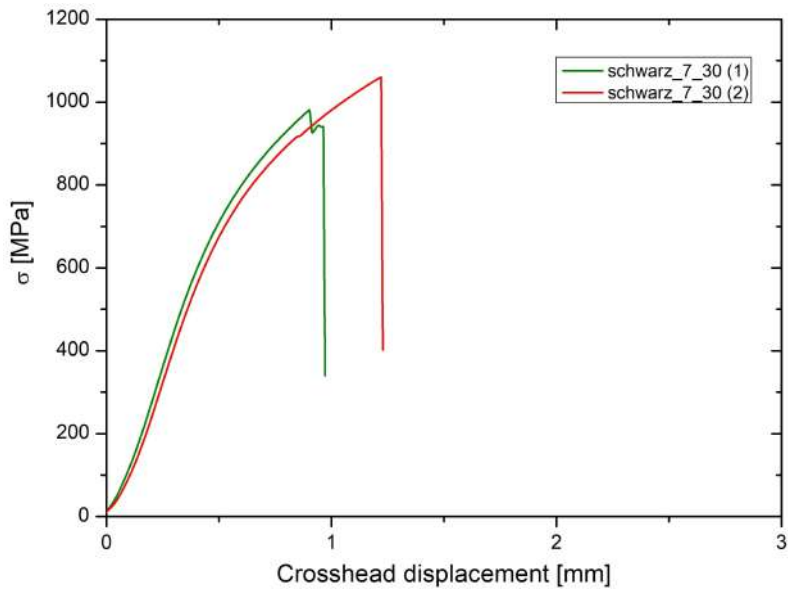


Figure D.69: σ vs crosshead displacement curves of bending test on Sch-7-30 short sandwich panels.

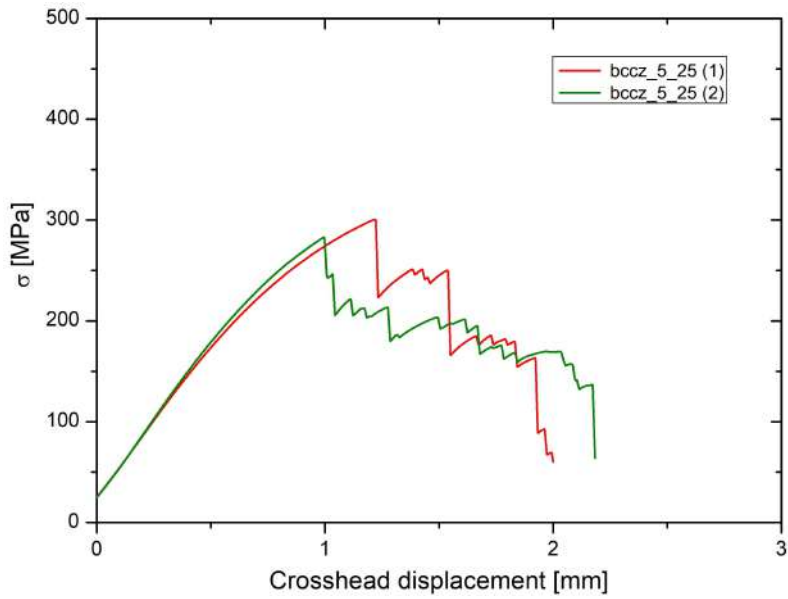


Figure D.70: σ vs crosshead displacement curves of bending test on Bccz-5-25 long sandwich panels.

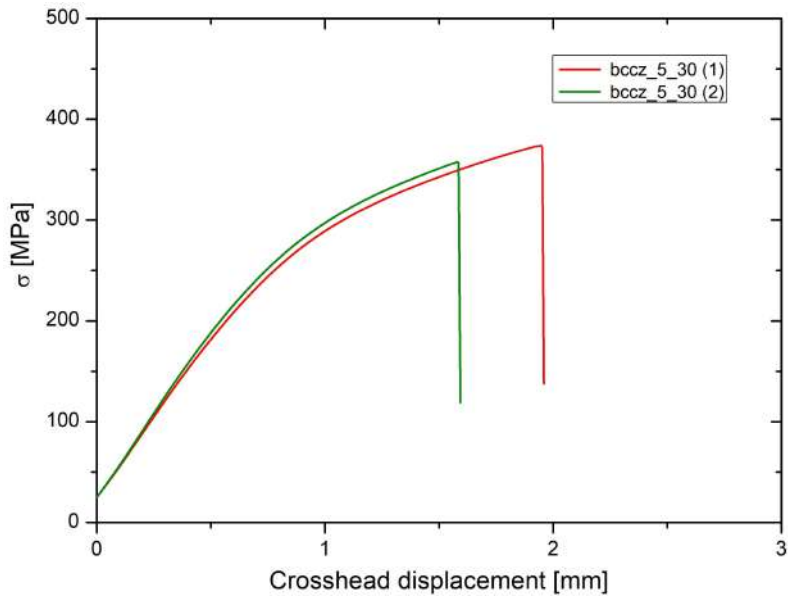


Figure D.71: σ vs crosshead displacement curves of bending test on Bccz-5-30 long sandwich panels.

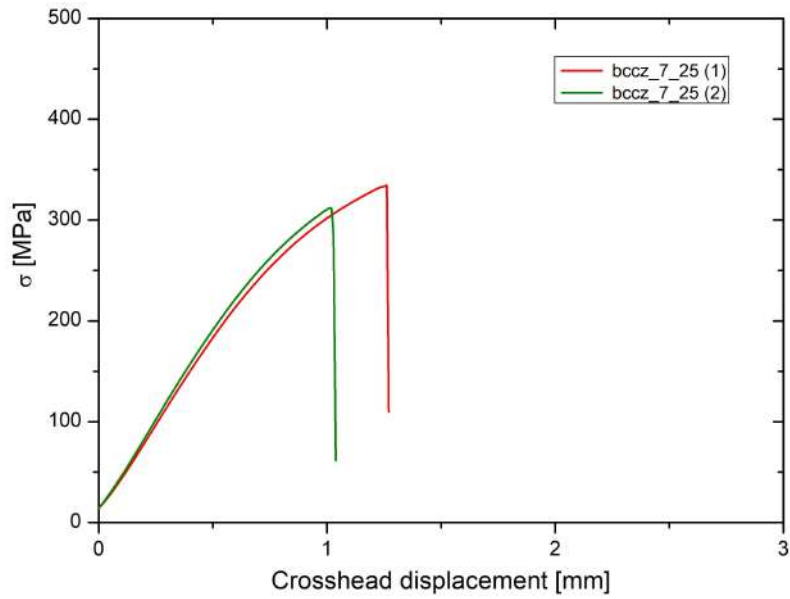


Figure D.72: σ vs crosshead displacement curves of bending test on Bccz-7-25 long sandwich panels.

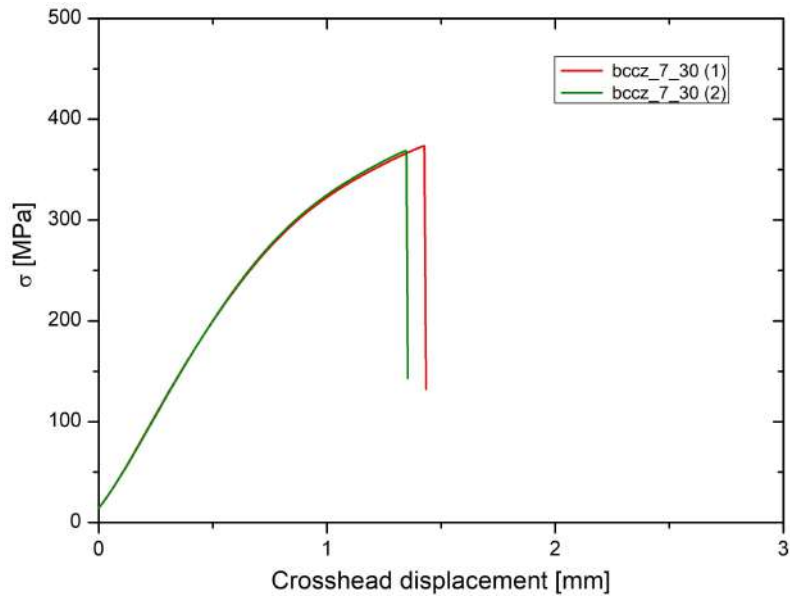


Figure D.73: σ vs crosshead displacement curves of bending test on Bccz-7-30 long sandwich panels.

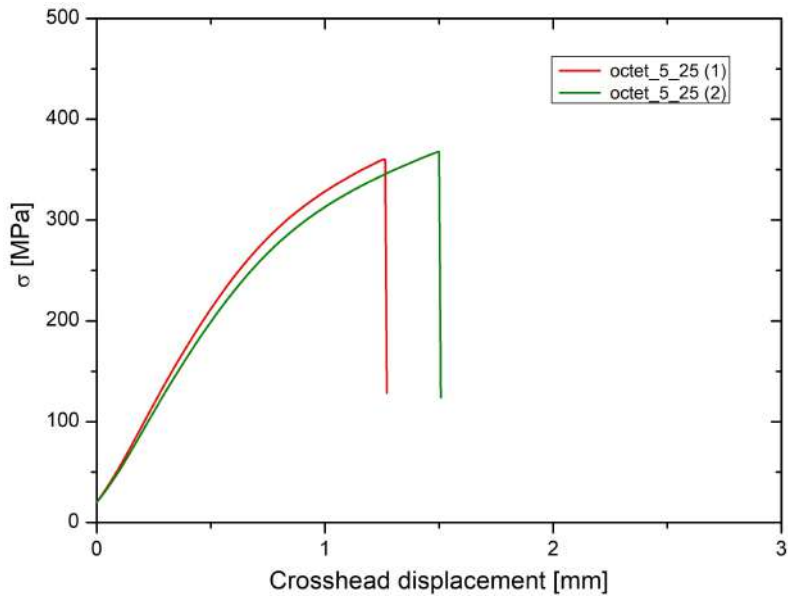


Figure D.74: σ vs crosshead displacement curves of bending test on Oct-5-25 long sandwich panels.

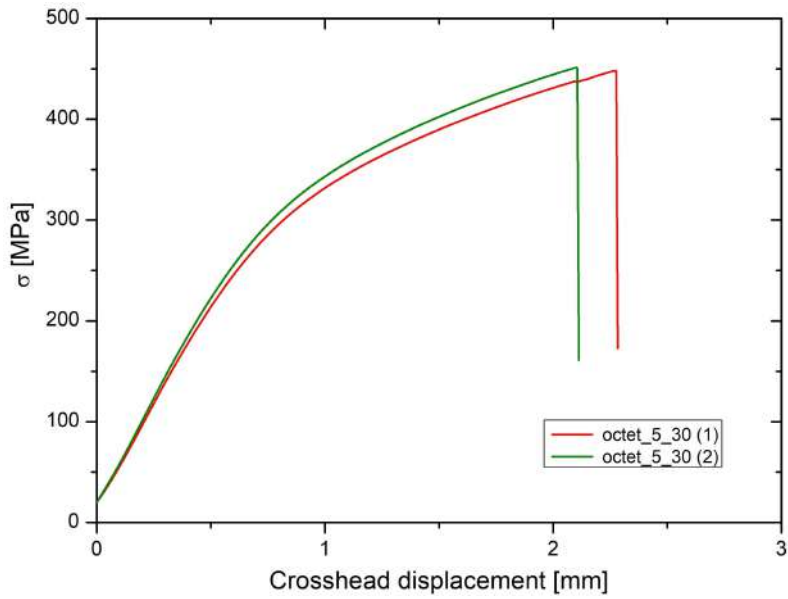


Figure D.75: σ vs crosshead displacement curves of bending test on Oct-5-30 long sandwich panels.

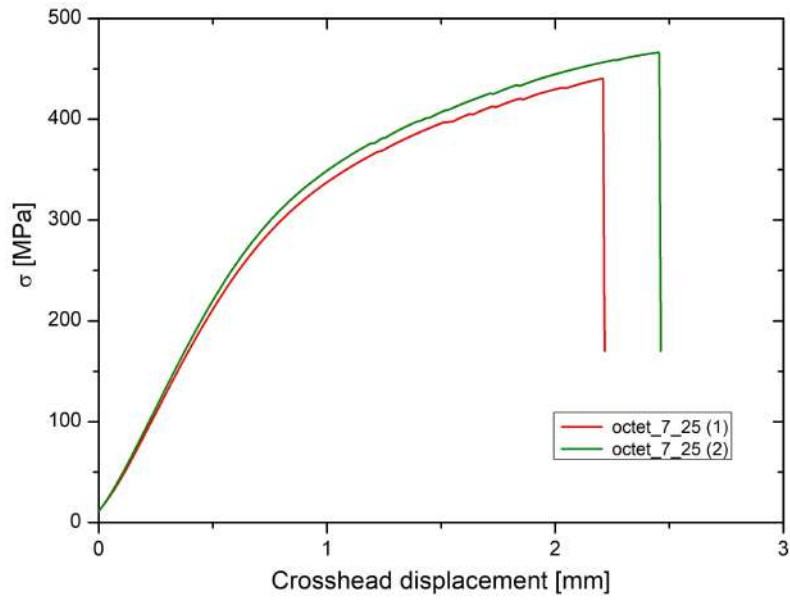


Figure D.76: σ vs crosshead displacement curves of bending test on Oct-7-25 long sandwich panels.

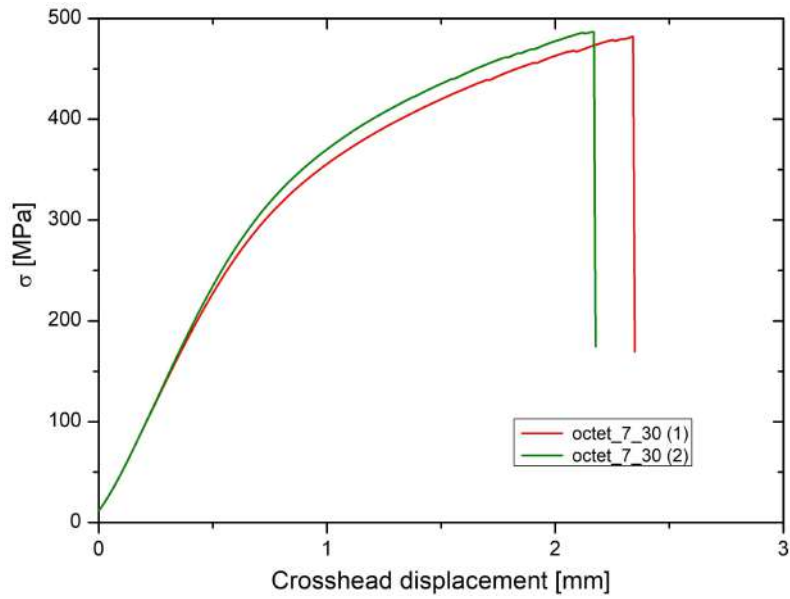


Figure D.77: σ vs crosshead displacement curves of bending test on Oct-7-30 long sandwich panels.

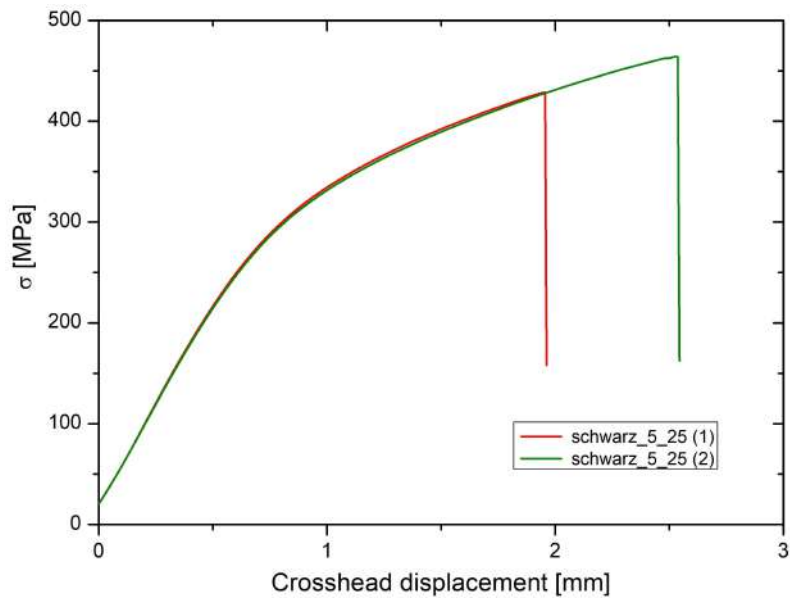


Figure D.78: σ vs crosshead displacement curves of bending test on Sch-5-25 long sandwich panels.

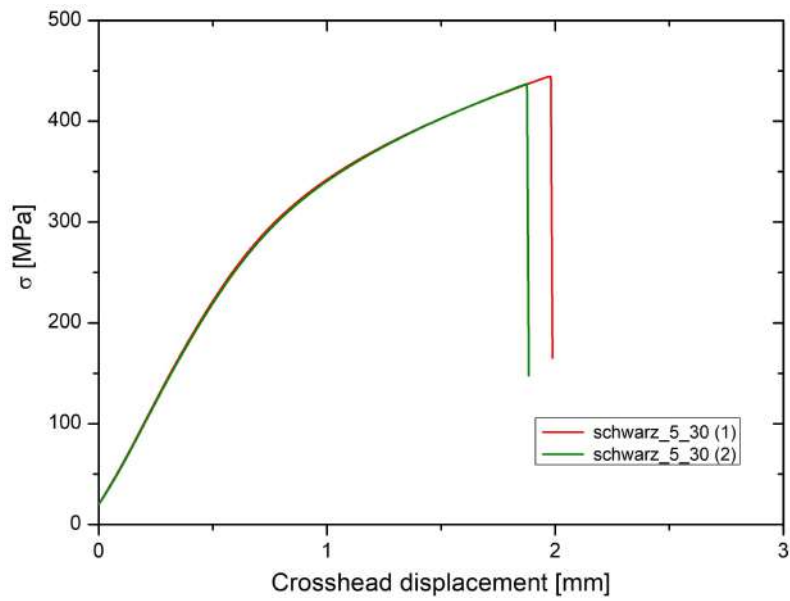


Figure D.79: σ vs crosshead displacement curves of bending test on Sch-5-30 long sandwich panels.

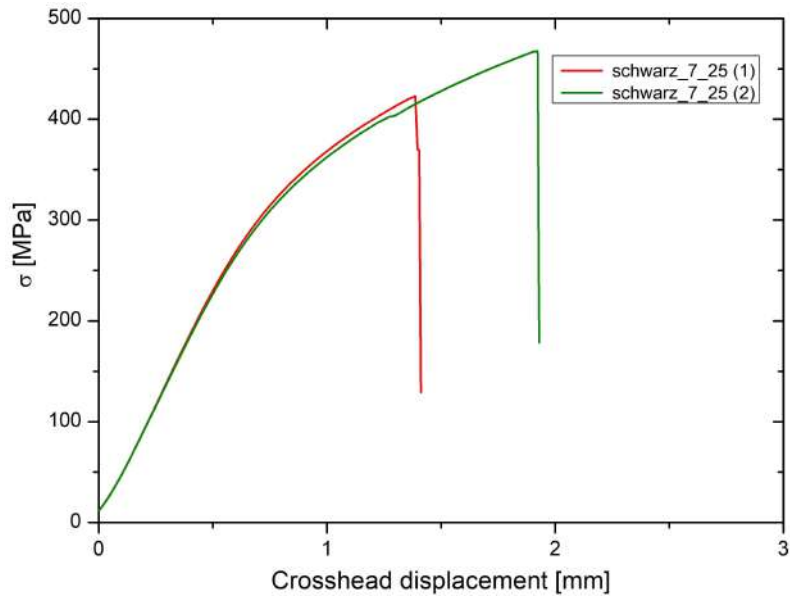


Figure D.80: σ vs crosshead displacement curves of bending test on Sch-7-25 long sandwich panels.

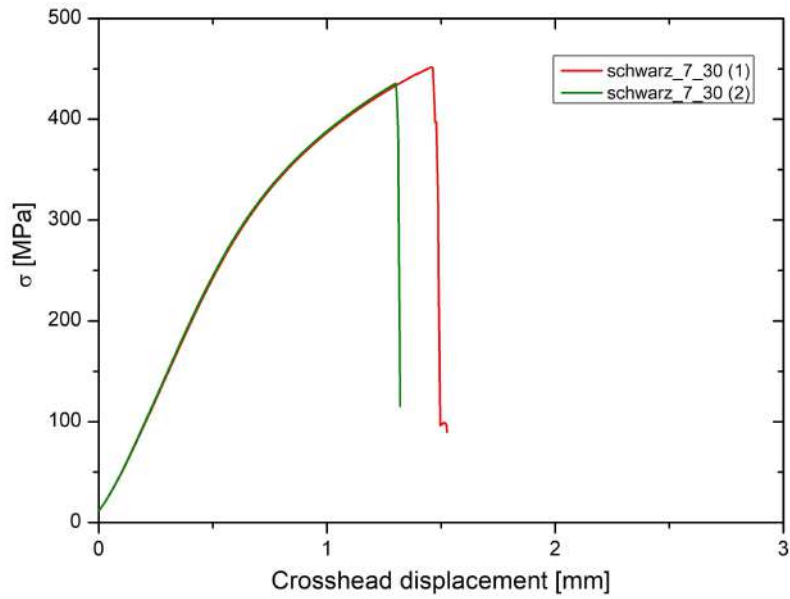


Figure D.81: σ vs crosshead displacement curves of bending test on Sch-7-30 long sandwich panels.

Bibliography

- [1] ASTM F3049 -14. *Standard Guide for Characterizing Properties of Metal Powders Used for Additive Manufacturing Processes*.
- [2] Yu Sun; Rainer J. Hebert; Mark Aindow. “Effect of heat treatments on microstructural evolution of additively manufactured and wrought 17-4PH stainless steel”. In: *Materials and Design* 156 (2018), pp. 429–440.
- [3] *Aircraft Ice Protection Systems*. Sky Brary. URL: https://www.skybrary.aero/index.php/Aircraft_Ice_Protection_Systems (visited on 08/21/2019).
- [4] Cassiopée Galy; Emilie Le Guen; Eric Lacoste; Corinne Arvieu. “Main defects observed in aluminum alloy parts produced by SLM: From causes to consequences”. In: *Additive Manufacturing* 22 (2018), pp. 165–175.
- [5] E. Liverani; A. Fortunato; A. Leardini; C. Belvedere; S. Siegler; L. Ceschini; A. Ascari. “Fabrication of Co-Cr-Mo endoprosthesis ankle devices by means of Selective Laser Melting (SLM)”. In: *Materials and Design* 106 (2016), pp. 60–68.
- [6] *Ashby diagrams*. *Ashby diagrams*. URL: https://downloadfiles.grantadesign.com/pdf/teaching_resource_books/2-Materials-Charts-2010.pdf (visited on 08/26/2019).
- [7] K. Y. G. McCullough; N. A. Fleck; M. F. Ashby. “The stress-life fatigue behaviour of aluminium alloy foams”. In: *Fatigue and Fracture of Engineering Materials and Structures* 23 (1999), pp. 199–208.
- [8] Kavan Hazeli; Behzad Bahrami Babamiri; Joseph Indeck; Andrew Minor; Hesam Askari. “Microstructure-topology relationship effects on the quasi-static and dynamic behavior of additively manufactured lattice structures”. In: *Materials and Design* 176 (2019), p. 107826.
- [9] Ryoya Nishida; Naoki Takata; Makoto Kobashi; Masaki Kato Asuka Suzuki; “Design of laser parameters for selectively laser melted maraging steel based on deposited energy density”. In: *Additive Manufacturing* 28 (2019), pp. 160–168.

- [10] C. Qiu; ShengYue; N.J.E. Adkins; M. Ward; H. Hassanin; P.D.Lee; P.J. Withers; M.M. Attallah. “Influence of processing conditions on strut structure and compressive properties of cellular lattice structures fabricated by selective laser melting”. In: *Materials Science and Engineering A* 628 (2015), pp. 188–197.
- [11] Roland Berger. *Additive Manufacturing - next generation AMnx*. 2016.
- [12] Saurabh Vaidya; Prashant Ambad; Santosh Bhosle. “Industry 4.0 – A Glimpse”. In: *2nd International Conference on Materials Manufacturing and Design Engineering* 20 (2018), pp. 233–238.
- [13] National Transportation Safety Board. *Accident Report: Crash During Approach to Landing Empire Airlines Flight 8284 Avions de Transport Régional Aerospatiale Alenia ATR 42-320, N902FX*. 2009.
- [14] J. D. López-Castro; A. Marchal; L. González; J. Botana. “Topological optimization and manufacturing by Direct Metal Laser Sintering of an aeronautical part in 15-5PH stainless steel”. In: *Procedia Manufacturing* 13 (2017), pp. 818–824.
- [15] Eric Yang; Martin Leary; Bill Lozanovski; David Downing; Maciej Mazur; Avik Sarker; AmirMahyar Khorasani; Alistair Jones; Tobias Maconachie; Stuart Bateman; Mark Easton; Ma Qian; Peter Choong; Milan Brandt. “Effect of geometry on the mechanical properties of Ti-6Al-4V Gyroid structures fabricated via SLM: A numerical study”. In: *Materials and Design* 184 (2019), p. 108165.
- [16] M. Leary; M. Mazur; J. Elambasseril; M. McMillan; T. Chirent; Y. Sun; M. Qian; M. Easton; M. Brandt. “Selective laser melting (SLM) of AlSi12Mg lattice structures”. In: *Materials and Design* 98 (2016), pp. 344–357.
- [17] Martin Leary; Tobias Maconachie; Avik Sarker; Omar Faruque; Milan Brandt. “Mechanical and thermal characterisation of AlSi10Mg SLM block support structures”. In: *Materials and Design* 183 (2019), p. 108138.
- [18] R. Rashid; S. H. Masood; D. Ruan; S. Palanisamy; R. A. Rahman Rashid; M. Brandt. “Effect of scan strategy on density and metallurgical properties of 17-4PH parts printed by Selective Laser Melting (SLM)”. In: *Journal of Materials Processing Tech.* 249 (2017), pp. 502–511.
- [19] R. Rashid; S. H. Masooda; D. Ruana; S. Palanisamy; R. A. Rahman Rashid; J. Elambasseril; M. Brandt. “Effect of energy per layer on the anisotropy of selective laser melted AlSi12 aluminium alloy”. In: *Additive Manufacturing* 22 (2018), pp. 426–439.

- [20] Tobias Maconachie; Martin Leary; Bill Lozanovski; Xuezhe Zhang; Ma Qian; Omar Faruque; Milan Brandt. “SLM lattice structures: Properties, performance, applications and challenges”. In: *Materials and Design* 183 (2019), p. 108137.
- [21] Nicholas Lippiatt; Martine Wevers Brecht Van Hooreweder; Karel Lietaert; Bram Neirinck; “CoCr F75 scaffolds produced by additive manufacturing: Influence of chemical etching on powder removal and mechanical performance”. In: *Journal of the Mechanical Behavior of Biomedical Materials* 70 (2017), pp. 60–67.
- [22] Tatiana Mishurova; Katia Artzt; Jan Haubrich; Guillermo Requena; Giovanni Bruno. “New aspects about the search for the most relevant parameters optimizing SLM materials”. In: *Additive Manufacturing* 25 (2019), pp. 325–334.
- [23] ASTM C365/C365M-16. *Standard Test Method for Flatwise Compressive Properties of Sandwich Cores*. 2016.
- [24] ASTM C393/C393M-16. *Standard Test Method for Core Shear Properties of Sandwich Constructions by Beam Flexure*. 2016.
- [25] Carlo Giovanni Ferro; Sara Varetti; Fabio Vitti; Paolo Maggiore; Mariangela Lombardi; Sara Biamino; Diego Manfredi; Flaviana Calignano. “A Robust Multifunctional Sandwich Panel Design with Trabecular Structures by the Use of Additive Manufacturing Technology for a New De-Icing System”. In: *Technologies* 5(2) (2017), p. 35.
- [26] Carlo Giovanni Ferro; Sara Varetti; Paolo Maggiore; Mariangela Lombardi; Sara Biamino; Diego Manfredi; Flaviana Calignano. “Design and characterization of trabecular structures for an anti-icing sandwich panel produced by additive manufacturing”. In: *Journal of Sandwich Structures and Materials* doi: <https://doi.org/10.1177/1099636218780513> (2018), pp. 1–21.
- [27] Shohei Higashiyama; Kuniharu Ushijima; Masahiro Motosuke; Wesley J Cantwell. “Evaluation of heat dissipation and structural response of a cellular panel as a heat exchanger”. In: *Journal of Sandwich Structures and Materials* DOI: [10.1177/1099636217749274](https://doi.org/10.1177/1099636217749274) (2018), pp. 1–24.
- [28] S. K. Thomas; R. P. Cassoni; and C. D. MacArthur. “Aircraft anti-icing and de-icing techniques and modeling”. In: *J. Aircr.* 33.5 (1996), pp. 841–854.
- [29] D. Champvillair. *Numerical and experimental validation of an innovative anti ice panel by means of computational fluid dynamics*. 2018.
- [30] Syed A.M. Tofail; Elias P. Koumoulos; Amit Bandyopadhyay; Susmita Bose; Lisa O’Donoghue; Costas Charitidis. “Additive manufacturing: scientific and technological challenges, market uptake and opportunities”. In: *Materials Today* 21.1 (2018), pp. 22–37.

- [31] Xibing Gong; Ted Anderson; Kevin Chou. “Review on powder-based electron beam additive manufacturing technology”. In: *Manufacturing Review* 1.2 (2014).
- [32] BEA Bureau d’Enquêtes et d’Analyses pour la sécurité de l’aviation civile. *Final report On the accident on 1st June 2009 to the Airbus A330-203 registered F-GZCP operated by Air France flight AF 447 Rio de Janeiro - Paris*. 2012.
- [33] *Cloud Classification. Cloud Classification*. URL: <https://public.wmo.int/en/WorldMetDay2017/classifying-clouds> (visited on 08/20/2019).
- [34] Ksawery Szykiedans; Wojciech Credo. “Mechanical properties of FDM and SLA low-cost 3-D prints”. In: *The 20th International Conference: Machine Modeling and Simulations, MMS 2015* 136 (2016), pp. 257–262.
- [35] V. Alcácer; V. Cruz-Machado. “Scanning the Industry 4.0: A Literature Review on Technologies for Manufacturing Systems”. In: *Engineering Science and Technology, an International Journal* - in press (2019), pp. -.
- [36] ASTM D7249/D7249M-18. *Standard Test Method for Facesheet Properties of Sandwich Constructions by Long Beam Flexure*. 2018.
- [37] ASTM D7250/D7250-16. *Standard Practice for Determining Sandwich Beam Flexural and Shear Stiffness*. 2016.
- [38] M. DanZenkert. “Tension, compression and shear fatigue of a closed cell polymer foam”. In: *Compos. Sci. Technol.* 69.6 (2009), pp. 785–792.
- [39] Simon Ford; Melanie Despeisse. “Additive manufacturing and sustainability: an exploratory study of the advantages and challenges”. In: *Journal of Cleaner Production* 137 (2016), pp. 1573–1587.
- [40] C. Dunsky. “Process monitoring in metal powder bed fusion”. In: (2015).
- [41] Michael Dawoud; Iman Taha; Samy J. Ebeid. “Mechanical behaviour of ABS: An experimental study using FDM and injection moulding techniques”. In: *Journal of Manufacturing Processes* 21 (2016), pp. 39–45.
- [42] Sebastian Hällgren; Lars Pejryd; Jens Ekengren. “(Re)Design for Additive Manufacturing”. In: *26th CIRP Design Conference* 50 (2016), pp. 246–251.
- [43] Dirk Herzog; Vanessa Seyda; Eric Wycisk; Claus Emmelmann. “Additive manufacturing of metallic components – Process, structure and properties”. In: *Acta Materialia* 117 (2016), pp. 371–392.
- [44] European Powder Metallurgy Association EMPA. *Introduction to Additive Manufacturing technology, 1st edition*. 2015.
- [45] EOS. *Aluminium AlSi10Mg Datasheet*. 2011.
- [46] EOS. *EOS Corporate Presentation. Krailling (DE): EOS*. 2015.

- [47] EOS. *EOS M100 Technical datasheet*. 2015.
- [48] EOS. *EOS M290 Technical datasheet*. 2014.
- [49] EOS. *EOS M400 Technical datasheet*. 2016.
- [50] EOS. *Titanium Ti6Al4V Datasheet*. 2011.
- [51] Ernst and Young. “Global 3D Printing Report”. In: (2016).
- [52] *Example of topology optimization. Case study: aeronautical bracket*. URL: https://www.3dmpmag.com/magazine/article/?/2018/10/29/Designing_for_Additive_Manufacturing_Brings_with_It_Design_Freedom (visited on 07/21/2019).
- [53] Federal Aviation Administration FAA. *Aviation maintenance technician handbook airframe*. 2012.
- [54] Federal Aviation Administration FAA. *Ice and rain protection*. 2011.
- [55] V. Gunenthiram; P. Peyre; Matthieu Schneider; Morgan Dal; Frédéric Coste; Imade Koutiri; Rémy Fabbro. “Experimental analysis of spatter generation and melt-pool behavior during the powder bed laser beam melting process”. In: *Journal of Materials Processing Technology* 251 (2018), pp. 376–386.
- [56] Valérie Gunenthiram; Patrice Peyre; Matthieu Schneider; Morgan Dal; Frédéric Coste; Rémy Fabbro. “Analysis of laser-melt pool-powder bed interaction during the selective laser melting of a stainless steel”. In: *Journal of Laser Applications* 29.2 (2017), p. 022303.
- [57] Dengbao Xiao; Xiaoqi Chen; Ying Li; Wenwang Wu; Daining Fang. “The structure response of sandwich beams with metallic auxetic honeycomb cores under localized impulsive loading-experiments and finite element analysis”. In: *Materials and Design* 176 (2019), p. 107840.
- [58] Tomas Forsman. “Laser Welding of Aluminium Alloys”. In: *Doctoral thesis* (2000).
- [59] E. Liverani; S. Toschi; L. Ceschini; A. Fortunato. “Effect of selective laser melting (SLM) process parameters on microstructure and mechanical properties of 316L austenitic stainless steel”. In: *Journal of Materials Processing Tech.* 249 (2017), pp. 255–263.
- [60] Lucas Santos Dalenogare; Guilherme Brittes Benitez; Néstor Fabián Ayala; Alejandro Germán Frank. “The expected contribution of Industry 4.0 technologies for industrial performance”. In: *International Journal of Production Economics* 204 (2018), pp. 383–394.
- [61] William E. Frazier. “Metal Additive Manufacturing: A Review”. In: *Journal of Materials Engineering and Performance* 23.6 (2014), pp. 1917–1928.

- [62] José Fuentes, José A. Rodríguez-Ortiz, and E J. Herrera. “ROTURA DE PROBETAS SINTERIZADAS DE Al AM CON ADICIÓN DE SILICIO”. In: (2001).
- [63] Julien Gardan. “Additive manufacturing technologies: state of the art and trends”. In: *International Journal of Production Research* 54.10 (2016), pp. 3118–3132.
- [64] Germain Sossou; Frédéric Demoly; Ghislain Montavon; Samuel Gomes. “An additive manufacturing oriented design approach to mechanical assemblies”. In: *Journal of Computational Design and Engineering* 5 (2018), pp. 3–18.
- [65] Terry Wohlers; Tim Gorne. *History of additive manufacturing, Wohlers Report*. 2016.
- [66] Terry Wohlers; Tim Gornet. “History of additive manufacturing”. In: (2016).
- [67] Robert D. Grace. “Chapter Six - Special Services in Well Control”. In: *Blowout and Well Control Handbook (Second Edition)* (2017), pp. 259–301.
- [68] C. Li; Z.Y. Liu; X.Y. Fang; Y.B. Guo. “Residual Stress in Metal Additive Manufacturing”. In: *4th CIRP Conference on Surface Integrity (CSI 2018)* 71 (2018), pp. 348–353.
- [69] Mahdi Pourbagian; Wagdi G. Habashi. “Aero-thermal optimization of in-flight electro-thermal ice protection systems in transient de-icing mode”. In: *International Journal of Heat and Fluid Flow* 54 (2015), pp. 167–182.
- [70] I. Maskery; N.T. Aboulkhair; A.O. Aremu; C.J. Tuck; I.A. Ashcroft; R.D. Wildman; R.J.M. Hague. “A mechanical property evaluation of graded density Al-Si10-Mg lattice structures manufactured by selective laser melting”. In: *Materials Science and Engineering A* 670 (2016), pp. 264–274.
- [71] Nesma T. Aboulkhair; Marco Simonelli; Luke Parry; Ian Ashcroft; Christopher Tuck; Richard Hague. “3D printing of Aluminium alloys: Additive Manufacturing of Aluminium alloys using selective laser melting”. In: *Progress in Materials Science* (2019), in press.
- [72] Fazil O. Sonmez; H. Thomas Hahn. “Thermomechanical analysis of the laminated object manufacturing (LOM) process”. In: *Rapid Prototyping Journal* 4.1 (1998), pp. 26–36.
- [73] Fikret Caliskan; Chingiz Hajiyev. “A review of in-flight detection and identification of aircraft icing and reconfigurable control”. In: *Progress in Aerospace Sciences* 60 (2013), pp. 12–34.
- [74] Lai-Chang Zhang; Yujing Liu; Shujun Li; Yulin Hao. “Additive Manufacturing of Titanium Alloys by Electron Beam Melting: A Review”. In: *Advanced Engineering Materials* 20 (2018).
- [75] Jr. Harold E. Addy. *Ice accretions and icing effects for modern airfoils*. 2000.

- [76] Dakota Morgan; Emmanuel Agba; Chris Hill. “Support Structure Development and Initial Results for Metal Powder Bed Fusion Additive Manufacturing”. In: *45th SME North American Manufacturing Research Conference, NAMRC 45, LA, USA 10* (2017), pp. 819–830.
- [77] P. L. Narayana; Cheng-Lin Lia; Seong-Woong Kim; Seung-Eon Kim; A. Marquardt; C. Leyens; N. S. Reddy; Jong-Taek Yeom; Jae-Keun Hong. “High strength and ductility of electron beam melted β stabilized γ -TiAl alloy at 800 °C”. In: *Materials Science and Engineering A* 756 (2019), pp. 41–45.
- [78] Tuan D. Ngo; Alireza Kashani; Gabriele Imbalzano; Kate T.Q. Nguyen; David Hui. “Additive manufacturing (3D printing): A review of materials, methods, applications and challenges”. In: *Composites Part B* 143 (2018), pp. 172–196.
- [79] *Ice Classification. Ice Classification*. URL: https://www.aviationweather.ws/050_Structural_Icing.php (visited on 08/20/2019).
- [80] *Icing. Icing*. URL: https://www.weather.gov/source/zhu/ZHU_Training_Page/icing_stuff/icing/icing.htm (visited on 08/20/2019).
- [81] Oliver Parent; Adrian Ilinca. “Anti-icing and de-icing technoques for wind turbines: critical review”. In: *Cold Regions Science and Technology* 65 (2011), pp. 88–96.
- [82] *In-flight Icing Encounter and Loss of Control Simmons Airlines d.b.a. American Eagle Flight 4184 Avions de Transport Regional (ATR) Model 72-212, N401AM. National Transportation Safety Board*. URL: <https://www.ntsb.gov/investigations/AccidentReports/Pages/AAR9601.aspx> (visited on 08/20/2019).
- [83] N. Inoue. *Anti-icing system, wing, aircraft and anti-icing method*. 2013.
- [84] Kim Lynge Srensen; Mogens Blanke; Tor Arne Johansen. “Diagnosis of wing icing through lift and drag coefficient change detection for small unmanned aircraft”. In: *IFAC - Papers OnLine* 48.21 (2015), pp. 541–546.
- [85] C. J. Johnson. *Anti Icing Duct*. 1943.
- [86] Paul O’Regan; Paul Prickett; Rossi Setchi; Gareth Hankins; Nick Jones. “Metal based additive layer manufacturing: variations, correlations and process control”. In: *20th International Conference on Knowledge Based and Intelligent Information and Engineering Systems* 96 (2016), pp. 216–224.
- [87] Christopher Pleass; Sathiskumar Jothi. “Influence of powder characteristics and additive manufacturing process parameters on the microstructure and mechanical behaviour of Inconel 625 fabricated by Selective Laser Melting”. In: *Additive Manufacturing* 24 (2018), pp. 419–431.

- [88] S. Raghavendra; A. Molinari; V. Fontanari; V. Luchin; G. Zappini; M. Benedetti; F. Johansson; J. Klarin. “Tensile and compression properties of variously arranged porous Ti-6Al-4V additively manufactured structures via SLM”. In: *Procedia Structural Integrity* 13 (2018), pp. 149–154.
- [89] C. Körner. “Additive manufacturing of metallic components by selective electron beam melting - a review”. In: *International Materials Reviews* 61.5 (2016), pp. 361–377.
- [90] Y. Z. H. G. D. A. Lados. “Microstructure, static properties, and fatigue crack growth mechanisms in Ti-6Al-4V fabricated by additive manufacturing: LENS and EBM”. In: *Eng. Fail. Anal.* 69 (2016), pp. 3–14.
- [91] J.L. Laforte; M.A. Allaire; J. Laflamme. “State of the art of power line de-icing”. In: *Atmospheric research* 46 (1998), pp. 143–158.
- [92] N. Contuzzi; S.L. Campanelli; C. Casavola; L. Lamberti. “Manufacturing and Characterization of 18Ni Marage 300 Lattice Components by Selective Laser Melting”. In: *Materials* 6.8 (2013), pp. 3451–3468.
- [93] Concept Laser. *M2 Cursing Technical datasheet*. 2014.
- [94] Concept Laser. *Mlab Cusing 200R Technical datasheet*. 2012.
- [95] Concept Laser. *X Line 2000R Technical datasheet*. 2015.
- [96] A. W. Gebisa; H. G. Lemu. “Design for manufacturing to design for Additive Manufacturing: Analysis of implications for design optimality and product sustainability”. In: *Manufacturing Engineering Society International Conference 2017, MESIC 2017, 28-30 June 2017, Vigo (Pontevedra), Spain* 13 (2017), pp. 724–731.
- [97] Changhao Pei; Dong Shi; Huang Yuan; Huaixue Li. “Assessment of mechanical properties and fatigue performance of a selective laser melted nickel-base superalloy Inconel 718”. In: *Materials Science and Engineering A* 759 (2019), pp. 278–287.
- [98] Decheng Kong; Xiaoqing Ni; Chaofang Dong; Liang Zhang; Jizheng Yao; Cheng Man; Li Wang; Kui Xiao; Xiaogang Li. “Anisotropic response in mechanical and corrosion properties of hastelloy X fabricated by selective laser melting”. In: *Construction and Building Materials* 221 (2019), pp. 720–729.
- [99] Zhichao Dong; Yabo Liu; Weibin Wen; Jingran Ge; Jun Liang. “Effect of Hatch Spacing on Melt Pool and As-built Quality During Selective Laser Melting of Stainless Steel: Modeling and Experimental Approaches”. In: *Materials* 12(1).50 (2019), DOI:10.3390/ma12010050.

- [100] Sara Varetti; Carlo Giovanni Ferro; Andrea Emanuele Maria Casini; Andrea Mazza; Paolo Maggiore; Mariangela Lombardi. “Sandwich panel with lattice core for aircraft anti-ice system made by Selective Laser Melting”. In: *2nd International Conference on 3D Printing Technology and Innovations. International Journal of Advancements in Technology*. (2018).
- [101] J. Wu; X. Q. Wang; W. Wang; M. M. Attallah; M. H. Loretto. “Microstructure and strength of selectively laser melted AlSi10Mg”. In: *Acta Materialia* 117 (2016), pp. 311–320.
- [102] Carlo Giovanni Ferro; Sara Varetti; Fabio Vitti; Paolo Maggiore. *An aircraft equipped in a single piece structurally integrated de-icing system and its method of realization*. 2016.
- [103] Yasin Amani; Sylvain Dancette; Pauline Delroisse; Aude Simar; Eric Maire. “Compression behavior of lattice structures produced by selective laser melting: X-ray tomography based experimental and finite element approaches”. In: *Acta Materialia* 159 (2018), pp. 395–407.
- [104] *Manufacturing Guide. Stereolithography*. URL: <https://www.manufacturingguide.com/en/stereolithography-sla> (visited on 07/16/2019).
- [105] *Manufacturing Guide. Fused Deposition Modelling (FDM)*. URL: <https://www.manufacturingguide.com/en/fused-deposition-modeling-fdm> (visited on 07/16/2019).
- [106] *Manufacturing Guide. Laminated Object Manufacturing (LOM)*. URL: <https://www.manufacturingguide.com/en/laminated-object-manufacturing-lom> (visited on 07/16/2019).
- [107] *Manufacturing Guide. Selective laser Melting (SLM)*. URL: <https://www.manufacturingguide.com/en/direct-laser-metal-sintering-dmls> (visited on 07/16/2019).
- [108] *Manufacturing Guide. Electron Beam Melting (EBM)*. URL: <https://www.manufacturingguide.com/en/electron-beam-melting-ebm> (visited on 07/16/2019).
- [109] *Manufacturing Guide. Direct Energy Deposition (DED)*. URL: <https://www.manufacturingguide.com/en/laser-cladding-3d-lc3d> (visited on 07/16/2019).
- [110] Diana Popescu; Aurelian Zapciu; Catalin Amza; Florin Baciu; Rodica Marinescu. “FDM process parameters influence over the mechanical properties of polymer specimens: A review”. In: *Polymer Testing* 69 (2018), pp. 157–166.
- [111] A. Rosochowski; A. Matuszak. “Rapid tooling: the state of the art”. In: *Journal of Materials Processing Technology* 106.1-3 (2000), pp. 191–198.

- [112] Michele Bici; Salvatore Brischetto; Francesca Campana; Carlo Giovanni Ferro; Carlo Seclì; Sara Varetti; Paolo Maggiore; Andrea Mazza. “Development of a multifunctional panel for aerospace use through SLM additive manufacturing”. In: *11th CIRP Conference on Intelligent Computation in Manufacturing Engineering, CIRP ICME 17* 67 (2018), pp. 215–220.
- [113] Christoph Klahn; Bastian Leutenecker; Mirko Meboldt. “Design Strategies for the Process of Additive Manufacturing”. In: *CIRP 25th Design Conference Innovative Product Creation* 36 (2015), pp. 230–235.
- [114] Myriam Orqu era; S ebastien Campocasso; Dominique Millet. “Design for additive manufacturing method for a mechanical system downsizing”. In: *27th CIRP Design 2017* 60 (2017), pp. 223–228.
- [115] S. Zhao; S.J.Li; W.T.Hou; Y.L.Hao; R.Yang; R.D.K. Misra. “The influence of cell morphology on the compressive fatigue behavior of Ti-6Al-4V meshes fabricated by electron beam melting”. In: *Journal of the mechanical behavior of biomedical materials* 59 (2016), pp. 251–264.
- [116] Mohsin Talib Mohammed. “Mechanical Properties of SLM-Titanium Materials for Biomedical Applications: A Review”. In: *Materials Today: Proceedings - ICMPC 2018* 5 (2018), pp. 17906–17913.
- [117] Mahesh Mani; Brandon M. Lane; M. Alkan Donmez; Shaw C. Feng; Shawn P. Moylan. “A review on measurement science needs for realtime control of additive manufacturing metal powder bed fusion processes”. In: (2017).
- [118] Miguel Zavala-Arredondo; Nicholas Boone; Jon Willmott; David T.D. Childs; Pavlo Ivanov; Kristian M. Groom; Kamran Mumtaz. “Laser diode area melting for high speed additive manufacturing of metallic components”. In: *Materials and Design* 117 (2017), pp. 305–315.
- [119] Ray Y. Zhong; Xun Xu; Eberhard Klotz; Stephen T. Newman. “Intelligent Manufacturing in the Context of Industry 4.0: A Review”. In: *Engineering* 3 (2017), pp. 616–630.
- [120] Jukka-Pekka J arvinen; Ville Matilainen; Xiaoyun Li; Heidi Piili; Antti Salminen; Ismo M akel a; Olli Nyrhil a. “Characterization of effect of support structures in laser additive manufacturing of stainless steel”. In: *8th International Conference on Photonic Technologies LANE 2014* 56 (2014), pp. 72–81.
- [121] Douglas McLaren; William W. Orr. “Thermal anti-icing system for aircraft”. In: *The Boeing Company* US 5011098 A (1991).
- [122] Patrik Stenlund; Shingo Kurosu; Yuichiro Koizumi; Felicia Suska; Hiroaki Matsumoto; Akihiko Chiba; Anders Palmquist. “Osseointegration Enhancement by Zr doping of Co-Cr-Mo Implants Fabricated by Electron Beam Melting”. In: *Additive Manufacturing* 6 (2015), pp. 6–15.

- [123] A. Tridello; J. Fiocchi; C. A. Biffi; G. Chiandussi; M. Rossetto; A. Tuissi; D. S. Paolino. “VHCF response of Gaussian SLM AlSi10Mg specimens: Effect of a stress relief heat treatment”. In: *International Journal of Fatigue* 124 (2019), pp. 435–443.
- [124] Alberta Aversa; Mandanà Moshiri; Erica Librera; Mehdi Hadi; Giulio Marchese; Diego Manfredi; Massimo Lorusso; Flaviana Calignano; Sara Biamino; Mariangela Lombardi; Matteo Pavese. “Single scan track analyses on aluminium based powders”. In: *Journal of Materials Processing Tech.* 255 (2018), pp. 17–25.
- [125] Faraz Deirmina; Bandar AlMangour; Dariusz Grzesiak; Massimo Pellizzari. “H13-partially stabilized zirconia nanocomposites fabricated by high-energy mechanical milling and selective laser melting”. In: *Materials and Design* 146 (2018), pp. 286–297.
- [126] J. A. Slotwinski; E. J. Garboczi; P. E. Stutzman; C. F. Ferraris; S. S. Watson; M. A. Peltz. “Characterization of Metal Powders Used for Additive Manufacturing”. In: *Journal of Research of the National Institute of Standards and Technology* 119 (2014), pp. 460–493.
- [127] Shahriar Afkhami; heidi Piili; Antti Salminen; Timo Bjork. “Effective parameters on the fatigue life of metals processed by powder bed fusion technique: A short review”. In: *Procedia Manufacturing - 17th Nordic Laser Material Processing Conference (NOLAMP17), 27-29 August 2019* 36 (2019), pp. 3–10.
- [128] A.M. Vilardell; A. Takezawa; A. du Plessis; N. Takata; P. Krakhmalev; M. Kobashi; I. Yadroitsava; I. Yadroitsev. “Topology optimization and characterization of Ti6Al4V ELI cellular lattice structures by laser powder bed fusion for biomedical applications”. In: *Materials Science and Engineering A* 766 (2019), p. 138330.
- [129] Anton du Plessis. “Effects of process parameters on porosity in laser powder bed fusion revealed by X-ray tomography”. In: *Additive Manufacturing* 30 (2019), p. 100871.
- [130] *Pneumatic de-ice system. De-ice*. URL: https://www.eoas.ubc.ca/courses/atasc113/flying/met_concepts/03-met_concepts/03g-Icing/index.html (visited on 08/21/2019).
- [131] D. D. Gu; W. Meiners; K. Wissenbach; R. Poprawe. “Laser additive manufacturing of metallic components: materials, processes and mechanisms”. In: *International Materials Reviews* 57 (2013), pp. 133–164.
- [132] QYR. *Machinery and Equipment Research Center*. 2016.

- [133] C. Yan; L. Hao; A. Hussein; S.L. Bubb; P. Young; D. Raymont. “Evaluation of light-weight AlSi10Mg periodic cellular lattice structures fabricated via direct metal laser sintering”. In: *Journal of Materials Processing Technology* 214.4 (2014), pp. 856–864.
- [134] M. S. Duval-Chaneac; S. Han; C. Claudin; F. Salvatore; J. Bajolet; J. Rech. “Characterization of maraging steel 300 internal surface created by selective laser melting (SLM) after abrasive flow machining (AFM)”. In: *8th CIRP Conference on High Performance Cutting (HPC 2018)* 77 (2018), pp. 359–362.
- [135] Renishaw. *AM250 Technical datasheet*. 2012.
- [136] Renishaw. *AM400 Technical datasheet*. 2015.
- [137] Renishaw. *AM500 Technical datasheet*. 2015.
- [138] Wohlers Report. *3D Printing and Additive Manufacturing State of the Industry, Annual Worldwide Progress Report*. 2016.
- [139] *Rhombic dodecahedron*. *Rhombic dodecahedron*. URL: https://en.wikipedia.org/wiki/Trapezo-rhombic_dodecahedron (visited on 07/30/2019).
- [140] J. P. Bruggemann; L. Risse; G. Kullmer; B. Schramm; H. A. Richard. “Fracture mechanical investigation on selective laser melted Ti6Al4V”. In: *Procedia Structural Integrity - ECF22 - Loading and Environmental effects on Structural Integrity* 13 (2018), pp. 317–321.
- [141] P. Ponnusamy; S. H. Masood; S. Palanisamy; R. A. Rahman Rashid; D. Ruan. “Characterization of 17-4PH alloy processed by selective laser melting”. In: *Materials Today: Proceedings* 4 (2017), pp. 8498–8506.
- [142] P. K. C. Rudolph. *Anti-icing system for aircraft*. 1992.
- [143] P. K. C. Rudolph. *Leading edge slat/anti-icing system and method for airfoil*. 2001.
- [144] Gary K. Lewis; Eric Schlienger. “Practical considerations and capabilities for laser assisted direct metal deposition”. In: *Materials and Design* 21 (2000), pp. 417–423.
- [145] D. D. Schwarze. *Selective Laser Melting - Eine produktive Fertigungstechnologie*. Lübeck: *SLM Solutions GmbH*. 2015.
- [146] Timothy Gutowski; Sheng Jiang; Daniel Cooper; Gero Corman; Michael Hausmann; Jan-Anders Manson; Timo Schudeleit; Konrad Wegener; Matias Sabelle; Jorge Ramos-Grez; Dusan P. Sekulic. “Note on the Rate and Energy Efficiency Limits for Additive Manufacturing”. In: *Journal of Industrial Ecology* 21.S1 (2017).

- [147] X. J. Wang; L. C. Zhang; M. H. Fang; T. B. Sercombe. “The effect of atmosphere on the structure and properties of a selective laser melted Al-12Si alloy”. In: *Materials Science and Engineering A* 597 (2014), pp. 370–375.
- [148] Jinliang Zhang; Bo Song; Qingsong Wei; Dave Bourell; Yusheng Shi. “A review of selective laser melting of aluminum alloys: Processing, microstructure, property and developing trends”. In: *Journal of Materials Science and Technology* 35 (2019), pp. 270–284.
- [149] J. A. Cherry; H. M. Davies; S. Mehmood; N. P. Lavery; S. G. R. Brown; J. Siens. “Investigation into the effect of process parameters on microstructural and physical properties of 316L stainless steel parts by selective laser melting”. In: *International Journal of Advanced Manufacturing Technology* 76 (2015), pp. 869–879.
- [150] Sisma. *MySint 100 Technical datasheet*. 2014.
- [151] Sisma. *MySint 300 Technical datasheet*. 2016.
- [152] SLD. *Supercooled Large Droplets*. URL: https://www.faasafety.gov/gslac/ALC/course_content.aspx?cID=33%5C&sID=155%5C&preview=true (visited on 08/21/2019).
- [153] H. Alsalla; L. Hao; C. Smith. “Fracture toughness and tensile strength of 316L stainless steel cellular lattice structures manufactured using the selective laser melting technique”. In: *Materials Science and Engineering A* 669 (2016), pp. 1–6.
- [154] Slm Solution. *SLM 125 Technical datasheet*. x.
- [155] Slm Solution. *SLM 280 Technical datasheet*. x.
- [156] Slm Solution. *SLM 500 Technical datasheet*. 2012.
- [157] Stanislav Lagutkin; Lydia Achelis; Sheikhal Sheikhaliev; Volker Uhlenwinkel; Vikas Srivastava. “Atomization process for metal powder”. In: *Materials Science and Engineering A* 383 (2004), pp. 1–6.
- [158] Hengfeng Gu; Haijun Gong; Deepankar Pal; Khalid Rafi; Thomas Starr; Brent Stucker. “Influences of Energy Density on Porosity and Microstructure of Selective Laser Melted 17-4PH Stainless Steel”. In: *24th Annual International Solid Freeform Fabrication Symposium* (2013).
- [159] Ian Gibson; David Rosen; Brent Stucker. “Additive Manufacturing Technologies”. In: *Springer* (2014).
- [160] *Supercooled Water Droplets*. Sky Brary. URL: https://www.skybrary.aero/index.php/Supercooled_Water_Droplets (visited on 08/21/2019).
- [161] B. Ferrar; L. Mullen; E. Jones; R. Stamp; C.J. Sutcliffe. “Gas flow effects on selective laser melting (SLM) manufacturing performance”. In: *Journal of Materials Processing Technology* 212 (2012), pp. 355–364.

- [162] 3D System. *ProX DMP 100 Technical datasheet*. x.
- [163] 3D System. *ProX DMP 200 Technical datasheet*. x.
- [164] 3D System. *ProX DMP 300 Technical datasheet*. x.
- [165] 3D System. *ProX DMP 320 Technical datasheet*. x.
- [166] W. Zhang T. DebRoy; H.L. Wei; J.S. Zuback; T. Mukherjee; J.W. Elmer; J.O. Milewski; A.M. Beese; A. Wilson-Heid; A. De d. “Additive manufacturing of metallic components - Process, structure and properties”. In: *Progress in Materials Science* 92 (2018), pp. 112–224.
- [167] *Tetrakaidecahedron*. *Tetrakaidecahedron*. URL: <https://en.wikipedia.org/wiki/Tetradecahedron> (visited on 07/30/2019).
- [168] Nima Shamsaei; Aref Yadollahi; Linkan Bian; Scott M. Thompson. “An overview of Direct Laser Deposition for additive manufacturing; Part II: Mechanical behavior, process parameter optimization and control”. In: *Additive Manufacturing* 8 (2015), pp. 12–35.
- [169] Lin Cheng; Albert To. “Part-scale build orientation optimization for minimizing residual stress and support volume for metal additive manufacturing: Theory and experimental validation”. In: *Computer-Aided Design* 113 (2019), pp. 1–23.
- [170] T. Toeppel. *3D analysis in laser beam melting based on real-time process monitoring*. 2016.
- [171] Melik Dolen Ugur M Dilberoglu; Bahar Gharehpapagh; Ulas Yaman. “The role of additive manufacturing in the era of Industry 4.0”. In: *27th International Conference on Flexible Automation and Intelligent Manufacturing, FAIM2017, 27-30 June 2017, Modena Italy*. 11 (2017), pp. 545–554.
- [172] Maria L. Montero-Sistiaga; Saeid Pourbabak; Jan Van Humbeeck; Dominique Schryvers; Kim Vanmeensel. “Microstructure and mechanical properties of Hastelloy X produced by HP-SLM (high power selective laser melting)”. In: *Materials and Design* 165 (2019), p. 107598.
- [173] Mostafa Yakout; M. A. Elbestawi; Stephen C. Veldhuis. “A study of thermal expansion coefficients and microstructure during selective laser melting of Invar 36 and stainless steel 316L”. In: *Additive Manufacturing* 24 (2018), pp. 405–418.
- [174] *Waire and Phelan structure*. *Waire and Phelan structure*. URL: https://en.wikipedia.org/wiki/Waire%5C%E2%80%93Phelan_structure (visited on 07/30/2019).

- [175] Ruidi Li; Jinhui Liu; Yusheng Shi; Li Wang. “Balling behavior of stainless steel and nickel powder during selective laser melting process”. In: *International Journal of Advanced Manufacturing Technology* 59 (2012), pp. 1025–1035.
- [176] Yuchao Bai; Di Wang; Yongqiang Yang; Hao Wang. “Effect of heat treatment on the microstructure and mechanical properties of maraging steel by selective laser melting”. In: *Materials Science and Engineering A* 760 (2019), pp. 105–117.
- [177] J. A. Gonzalez; J. Mireles; S. W. Stafford; M. A. Perez; C. A. Terrazas; R. B. Wicker. “Characterization of Inconel 625 fabricated using powder-bed-based additive manufacturing technologies”. In: *Journal of Materials Processing Tech.* 264 (2019), pp. 200–210.
- [178] Apinya Laohaprapanon; Pongnarin Jeanwatthanachai; Marut Wongcumchang; Nattapon Chantarapanich; Surapon Chantawerod; Kriskrai Sitthiseripratip; Sirikul Wisutmethangoon. “Optimal Scanning Condition of Selective Laser Melting Processing with Stainless Steel 316L Powder”. In: *Advanced Materials Research* 341-342 (2012), pp. 816–820.
- [179] Dexing Qi; Huabin Yu; Ming Liu; Han Huang; Shucui Xu; Yong Xia; Guian Qian; Wenwang Wu. “Mechanical behaviors of SLM additive manufactured octet-truss and truncated-octahedron lattice structures with uniform and taper beams”. In: *International Journal of Mechanical Sciences* 163 (2019), p. 105091.
- [180] Yihua Cao; Zhenlong Wu; Yuan Su; Zhongda Xu. “Aircraft flight characteristics in icing conditions”. In: *Progress in Aerospace Sciences* 74 (2015), pp. 62–80.
- [181] Scott M. Thompson; Linkan Bian; Nima Shamsaei; Aref Yadollahi. “An overview of Direct Laser Deposition for additive manufacturing; Part I: Transport phenomena, modeling and diagnostics”. In: *Additive Manufacturing* 8 (2015), pp. 36–62.
- [182] Nkutwane Washington Makoana; Ina Yadroitsava; Heinrich Möller; Igor Yadroitsev. “Characterization of 17-4PH Single Tracks Produced at Different Parametric Conditions towards Increased Productivity of LPBF Systems-The Effect of Laser Power and Spot Size Upscaling”. In: *Metals* 8 (2018), doi:10.3390/met8070475.
- [183] Li Xin; Bai Junqiang; Hua Jun; Wang Kun; Zhang Yang. “A spongy icing model for aircraft icing”. In: *Chinese Journal of Aeronautics* 27.1 (2014), pp. 40–51.

- [184] Goraj Zdobyslaw. “An overview of Deicing and antiicing technologies with prospects for the future”. In: *24th International Congress of the Aeronautical Sciences* (2004).
- [185] Zhiheng Hu; Haihong Zhu; Hu Zhang; Xiaoyan Zeng. “Experimental investigation on selective laser melting of 17-4PH stainless steel”. In: *Optics and Laser Technology* 87 (2017), pp. 17–25.
- [186] Zhen Wang; Zhiyu Xiao; Ying Tse; Chuanshou Huang; Weiwen Zhang. “Optimization of processing parameters and establishment of a relationship between microstructure and mechanical properties of SLM titanium alloy”. In: *Optics and Laser Technology* 112 (2019), pp. 159–167.
- [187] C. Yan; L. Hao; A. Hussein; P. Young; J. Huang; W. Zhu. “Microstructure and mechanical properties of aluminium alloy cellular lattice structures manufactured by direct metal laser sintering”. In: *Materials Science and Engineering A* 628 (2015), pp. 238–246.
- [188] Yang Gao; Dongyun Zhang; Ming Cao; Runping Chen; Zhe Feng; Reinhard Poprawe; Johannes Henrich Schleifenbaum; Stephan Ziegler. “Effect of δ phase on high temperature mechanical performances of Inconel 718 fabricated with SLM process”. In: *Materials Science and Engineering A* 767 (2019), p. 138327.
- [189] Ryan M. Latture; Ricardo X. Rodriguez; Larry R. Holmes Jr.; Frank W. Zok. “Effects of nodal fillets and external boundaries on compressive response of an octet truss”. In: *Acta Materialia* 149 (2018), pp. 78–87.

This Ph.D. thesis has been typeset by means of the T_EX-system facilities. The typesetting engine was pdfL^AT_EX. The document class was `toptesi`, by Claudio Beccari, with option `tipotesi=scudo`. This class is available in every up-to-date and complete T_EX-system installation.